Synthesis and Characterisation of Electron Conducting Mesoporous Ti and Ta Oxide for Use as Potential Electrode Materials in Lithium Ion Batteries

By

Luke Anthony Charles Smith

A submission presented in partial fulfilment of the requirements of the University of South Wales/Prifysgol De Cymru for the degree of Doctor of Philosophy

October 2016

Graduate Research Office

Swyddfa Ymchwil Graddedigion

Declaration of previous publication

This thesis contains two papers that have been previously published in peer reviewed journals and three papers that are in preparation for publication.

Thesis Chapter	Article title/citation	Publication status
Chapter 2	Luke A.C. Smith[a], Frederik Romer[b],Michel L. Trudeau[c], Rosa M. Souto Maior[d], Mark E. Smith[e], John V. Hanna[b], David M. Antonelli[a], Synthesis and electrochemical properties of mesoporous titanium oxide with polythiophene nanowires in the pores. *Microporous and Mesoporous Materials.* **2014**, (194) 52–59	Published
Chapter 3	Luke A. C. Smith[1,*], Frederick Romer[2],Dr. Michel L. Trudeau[3], Dr. Mark E. Smith[4], Dr. John V. Hanna[2] and Prof. David M. Antonelli[1,*]. Effect of Synthesis Parameters on the Electrochemical Properties of High-Surface-Area Mesoporous Titanium Oxide with Polypyrrole Nanowires in the Pores. *ChemElectroChem.* **2014,** *1*(12), 2153-2162	Published
Chapter 4	Luke A. C. Smith[1,*], Frederick Romer[2],Dr. Michel L. Trudeau[3], Dr. Mark E. Smith[4], Dr. John V. Hanna[2] and Prof. David M. Antonelli[1,*].UV-Initiated Synthesis of Electroactive High Surface Area Ta and Ti Mesoporous Oxides Composites with Polypyrrole Nanowires within the Pores. ChemNanoMat. **2015** 1(4), 276–284	Published
Chapter 5	Luke A.C. Smith,[a*] Michel L. Trudeau, [b] Mark E. Smith,[c] and David M. Antonelli.[a, *]. Low Temperature Synthesis and Electrochemical Properties of Mesoporous Titanium Oxysulfides. *ChemElectroChem.* **2015,** 3(2), 256-265	Published
Chapter 6	Morris. L., Smith. L. A. C., Trudeau. M. L., Reed. D., Book, D., Antonelli. D. M. Electorchemical and Hydrogen Storage Properties of Vanadium(IV) Hydride.' *J. Phys. Chem. C*, **2016**, *120* (21), pp 11407–11414	Published

Abstract

Mesoporous titanium oxide with a pore size of 20-30 Å was impregnated with conducting polythiophene nanowires in order to improve conductivity to take advantage of the ca. 1000 m^2/g surface areas for possible applications in charge storage in devices requiring fast Li^+ insertion kinetics. Pristine mesoporous titanium oxide produced a peak capacity of 301 mAh/g at current densities of 0.2 $mA.cm^{-2}$ and 187 mAh/g at 1 $mA.cm^{-2}$. The conductivity of the composite improved from 3.56 x 10^{-2} $mS.cm^{-1}$ to 5.79 $mS.cm^{-1}$ but significantly reduced capacity. This was attributed to pore blocking and a significant increase in the weight of the sample preventing Li^+ diffusion into the pores of the material. An investigation of variation in polymer loading level and pore size using polypyrrole nanowires was then undertaken in order to improve performance. The best synthesis conditions were achieved using 5% polymer loading and host materials with the largest pore size. Excessive polymer loading and smaller pore sizes lead to decreased performance due to inhibition of Li^+ transport. The C_{18} templated TiO_2 composite produced the best capacity retention at 58% retention, and the C_{12} composite produced the highest initial capacity of 170 mAh/g using a current density of 1 $mA.cm^{-2}$. To improve the interface between the polymer and host materials a synthesis was adapted using a catalyst-free UV initiated polymerisation of vapour-loaded pyrrole monomer with mesoporous Ti and Ta oxides. The best materials showed improved conductivity for both the Ti and Ta oxides as well as improved Li^+ capacity (190 mAh/g) relative to the pristine material (128 mAh/g) and superior capacity retention (49% as compared to 22%) for the Ti composites. The retention in surface area was 87% compared to 49% reported previously for analogous materials synthesised by catalyst-initiated method. This yielded Li^+ capacities of 170 mAh/g further highlighting the superiority of this new photochemical approach. Since polymer doping seemed to improve conductivity while inhibiting Li^+ transport an alternative approach using hexamethyldisilathiane (HMDST) to exchange Ti-O units with Ti-S at the surface of the mesopore channels to reduce the band gap between the valance band and the conduction

band, increasing the conductivity while retaining the porosity and thermal stability. Lower temperatures generally yielded materials with superior properties and although conductivity was improved using higher loading levels of HMDST, this produced a significant drop in initial capacity (137 – 41 mAh/g), but superior retention on cycling. The best performing material was synthesised using large amounts of regent (3.5 mL) at lower heating temperatures (100 °C) to maximise the combination of surface area, initial capacity, conductivity, and capacity retention (76%). Finally a vanadium hydride gel was prepared by thermal treatment of tetraphenylvanadium(IV) followed by hydrogenation. This V(III)-based material is redox active and the hydride ligand very light relative to oxide and phosphate supporting ligands normally used in V(III)-based battery materials. For this reason it could potentially lead to greater Li^+ insertion capacities, so electrochemical evaluation was warranted. The best material demonstrated a peak capacity of 131 mAh/g, at a discharge rate of 1 $mA.cm^{-2}$. After repeated charge discharge cycling for 50 cycles, the material retained 36% of its capacity.

Acknowledgments

Firstly I would like to thank my supervisor, Professor David Antonelli for the huge amount of support and guidance that has been given to me over the course of my PhD. Thank you for your enthusiasm of the last 4 years and for always answering any questions quickly and efficiently and for always being available to contact when needed. I am grateful for having been given the opportunity to be part of an active, high standard research group and been able to contribute to a number of publications.

This project would not have been possible without the help of a number of a number of collaborators. Firstly I would like to thank the help and guidance of Michel Tredeau, who carried out a significant proportion of the material characterisation for this project. Thank you for the

many analyses and characterisation experiments that you undertook on my behalf, as well as helping me by answering queries on the interpretation of data when it was required. You have always been a pleasure to work with and thank you for the number of occasions we have been able to network over the years. Other collaborators I must thank are Frederik Romer and Dr John Hana for conducting Solid State NMR on a large number of my samples and helping to contribute to the NMR sections of my publications.

I must also thank current members of the research group: Dr Peter Jenkins, Leah Morris and Jonathan Turley. Thank you also to Dr Peter Jenkins for proof reading some of this thesis.
I would also like to thank my friends and family, especially my parents who have been a big support to me over the duration of my PhD and who have made a large number of sacrifices in order for me to get to where I am today. They gave me the best chances possible to achieve my maximum potential by helping me both emotionally through hard times and financially throughout my time at university.

Lastly, my biggest thank you goes to Kirsty who has been with me on this journey for the last 3 ½ years. Thank you for your help in proof reading my work, being there for me when I am struggling and for being the most supportive partner anyone could ask for. I have shared this journey with someone who understands what doing a PhD entails. Thank you for always being there for me and never letting me give up hope.

Table of Contents

List of Figures

List of Tables

List of Schemes

Abbreviations

AC	Alternating Current
BET	Brunauer, Emmett and Teller
BG	Band Gap
BSE	Back Scattered Electrons
$C^{+\cdot}$	Carbocation Radical
CB	Conduction Band
CNF	Carbon Nanofibre
CNT	Carbon Nanotube
CPMAS NMR	Cross Polarisation Magic Angle Spinning Nuclear Magnetic Resonance
CV	Cyclic Voltammogram
DTA	Differential Thermal Analysis
EDLC	Electric Double Layer Capacitor
EELS	Electron Energy Loss Spectroscopy
EIS	Electrochemical Impedance Spectroscopy
EV	Electric Vehicle
FTIR	Fourier Transform Infrared
HEV	Hybrid Electric Vehicle
HOMO	Highest Occupied Molecular Orbital
JT	Jahn Teller Effect

LUMO	Lowest Unoccupied Molecular Orbital
MAS NMR	Magic Angle Spinning Nuclear Magnetic Resonance
MO	Molecular Orbital
NMR	Nuclear Magnetic Resonance
PXRD	Powder X-Ray Diffraction
R_{el}	Electrolyte Resistance
R_{ct}	Charge Transfer Resistance
SCE	Saturated Calomel Electrode
SEM	Scanning Electron Microscopy
SE	Secondary Electrons
SEI	Solid Electrolyte Interface
SHE	Standard Hydrogen Electrode
STEM	Scanning Transmission Electron Microscopy
TEM	Transmission Electron Microscopy
TGA	Thermogravimetric Analysis
TM	Transition Metal
TMO	Transition Metal Oxide
TMS	Trimethylsilane
VB	Valance Band
W	Warburg Impedance

XPS	X-Ray Photoelectron Spectroscopy
Z	Real Impedance
Z’	Imaginary Impedance

Chapter 1 : Introduction

1.1 Motivation and Objective of the Thesis

As the world's population continues to increase and technology becoming more advanced, the demands on energy are becoming more severe. With volatile oil prices, places heavy reliance on fossil fuels and political influence on the world energy market, this means that the need for alternative energy storage materials to replace the declining supply of fossil foils is of high significance. Furthermore, the use of more renewable energy sources would help reduce further damage to the environment. One method to achieve this is through utilising chemical energy to produce renewable electricity by the development and optimisation of electrochemical energy storage.[1] However, in addition to the current overall energy demand, constant developments in technology necessitates energy storage units capable of supplying larger amounts of power (>100 kW)[2] for extended time periods. The desired properties for the ideal energy storage material for such devices are that they must be low cost,[1] made with materials that are highly abundant[3] and possess a long cycle lifetime with the ability to be recycled thousands of times without significant loss in performance.[4,5] Two important alternative energy storage devices to internal combustion are those of batteries and capacitors. These devices use physical and chemical interactions to produce energy without the by-products of internal combustion. These materials can be regenerated after use, making them renewable and therefore reduces the issue of limited supply of fossil fuels.

The most promising batteries currently in use are Li^+ batteries. These are typically made out of $LiCoO_2$ and $LiFePO_4$ and possess high capacities (150-160 mAh/g) and the ability to store large amounts of energy (200-400 Watt hours/litre (Wh/L)).[6] However, due to kinetic restraints on the redox processes batteries can only produce small currents, limiting the power density (200-430 W/kg).[6] Capacitors typically made from high surface area carbon materials possess fast reaction kinetics leading to an instantaneous release of energy as a large pulse of current resulting in high power densities (1-2 MW/kg).[6] However these materials are unable to store large amounts of energy (5-15 Wh/l)[6] as they only retain charge at the surface of the material. Nevertheless, because of the promise shown by batteries and capacitors alike, there has been significant research to improve performance. The ideal material would possess the advantages of batteries and capacitors without loss of performance during long-term use.

Presently such devices are significantly less efficient compared to those based on fossil fuel combustion, which possesses very high energy densities (>12 kWh/l),[6] and so we are currently not able to replace them.

In the more recently explored phenomenon of pseudocapacitance, energy is stored by Faradaic redox reactions as in battery materials, but the energy release kinetics are nearly instantaneous. The difference in pseudocapacitance is that reactions take place at or close to the surface of the material. This enables the fast release and capture of ions with little or no energy barrier. This combination for fast kinetics and chemical energy storage enables the material to store large amounts of energy in addition to producing large currents when required without the loss of capacity performance as seen in traditional battery materials.

Intrinsic pseudocapacitive materials such as RuO_2 are materials which possess pseudocapacitive properties regardless of structure morphology and particle size. Extrinsic pseudocapacitive materials only possess pseudocapacitive properties when the material has optimised particle size, morphology and structure, which minimise the kinetic restrictions of the diffusion process. These materials can be produced by reducing particle size to increase active surface area, thus increasing the number of surface sites and reducing the diffusion path length of the ions inserted into the material. Well orientated diffusion pathways and high electron conductivity provides easy ion transport throughout the material and the internal pore channels. This topic receives a significant amount of research interest aiming to synthesise materials with the correct combination of properties to optimise the energy storage properties.

In the 1990's Antonelli and Ying synthesised redox active TiO_2 with surface areas >1000 m^2/g.[7] Due to the high Li^+ storage performance achieved previously by high surface area porous oxides,[8] it was anticipated that these new materials may have significant potential to exploit pseudocapacitance in charge transfer processes. However, these mesoporous oxides possess low conductivity compared to their crystalline equivalents due the amorphous nature of the pore walls,[9] thus limiting the kinetics of the redox reactions within the material. Initial attempts to improve conductivity utilised doping with bis(benzene) chromium,[10] which proved to be air sensitive, and alkali fullerides which despite improving the conductivity limited the Li^+ diffusion properties through the material.[11]

The most common method to improve the electron conductivity of a material is by combining them with conducting additives such as carbon, conducting polymers, or molecular wires. These materials passively improve the electron conductivity by providing a conducting pathway for the electrons to be transported throughout the material without leading to an increase in SEI formation. However these additives increase the weight of the material which leads to a decrease in the energy density. Other alternatives are to combine the material with a small percentage of another element to either positively (P-doping) or negatively (N-doping) dope the material. This creates a degree of electron deficiency or electron rich nature within the material which can be exploited to provide charge carriers and improves the charge transport. Alternatively the material can be doped with elements of similar electronic structure but with larger orbitals encouraging greater orbital overlap. This reduces the energy needed to transfer electrons between bands. These approaches are typically used in semiconductors resulting in a reduced band gap between the conduction and valence bands.

This thesis has investigated the synthesis of a series of composites to improve the electron conductivity of high surface area mesoporous transition metal oxides using a combination of conducting polymers and sulphur doping methods. This was carried out in order to assess its potential for applications as a potential Li^+ battery electrode material.

1.2. Electrochemical Energy Storage

There are various devices and materials currently being investigated to store and supply electrical energy, but there is always a compromise that must be made which affects the performance properties of the material. For example some materials are capable of producing large amounts of power, but for only a short period of time. Other devises supply power for many hours, but are only able to produce a very low current.[12] Thus, it is difficult for any one material to provide all the requirements needed to make the ideal energy storage material. There are three main performance characteristics used to compare materials, which are listed below. These define how useful a material is at storing and supplying electrical energy and for which applications they are best suited.

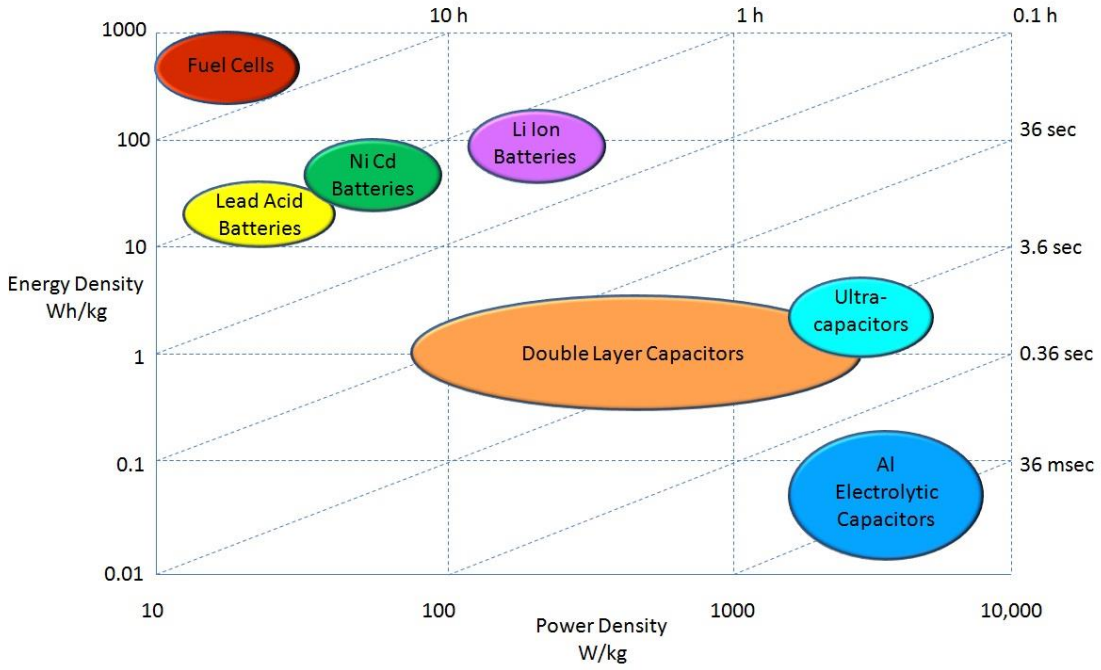

Figure 1.1: Ragone plot demonstrating energy densities vs power densities for different energy storage devices

(1) Energy density: The overall energy capable of being stored within a set mass or volume of the material. This is essential for a material to sustain the release of energy for long periods of time. The key factors that determine the energy density of a material are the potential difference in the cell and the capacity of the material according to Equation 1.1 for electronic potential energy.

Equation 1.1 $E = \frac{1}{2} CV^2$

Where E = Energy, C is capacity/capacitance and V is the electric potential

(2) Power density: The amount of energy that can be efficiently released to produce high currents per mass/volume of material. A larger power density will result in more charge being released efficiently to provide energy for higher loads when necessary. This is essential for materials that need to instantly provide large amounts of energy for high power applications. Key factors that affect power density are the reaction and diffusion kinetics of ions involved in the charge storage mechanism.

(3) Reversibility: The ability of a material to be discharged and recharged repeatedly with no significant drop in performance. For a material to be of any use it must be reusable (up to 1000's of times) representative of daily use over the course of a

number of years. The key factors effecting recyclability are the reversibility of the reactions taking place and the stability of the material during recycling.

There are a number of devices currently in use that utilise different charge storage mechanisms. What follows is a description of the devices and the mechanisms they use to store and release charge (Figure 1.1).

1.2.1 Capacitors

Capacitors are devices that consist of two conducting electrodes and an electrolyte. These types of devices store charge at the electrode/electrolyte interface (Figure 1.2).[13,14] The charges are stored via an electrostatic interaction between the ions present within the electrolyte and the charge present on the electrode surface. This electrostatic interaction leads to the ions within the electrolyte being attracted towards the electrode surface possessing the opposite charge until the maximum capacitance has been reached, this is known as a double layer.

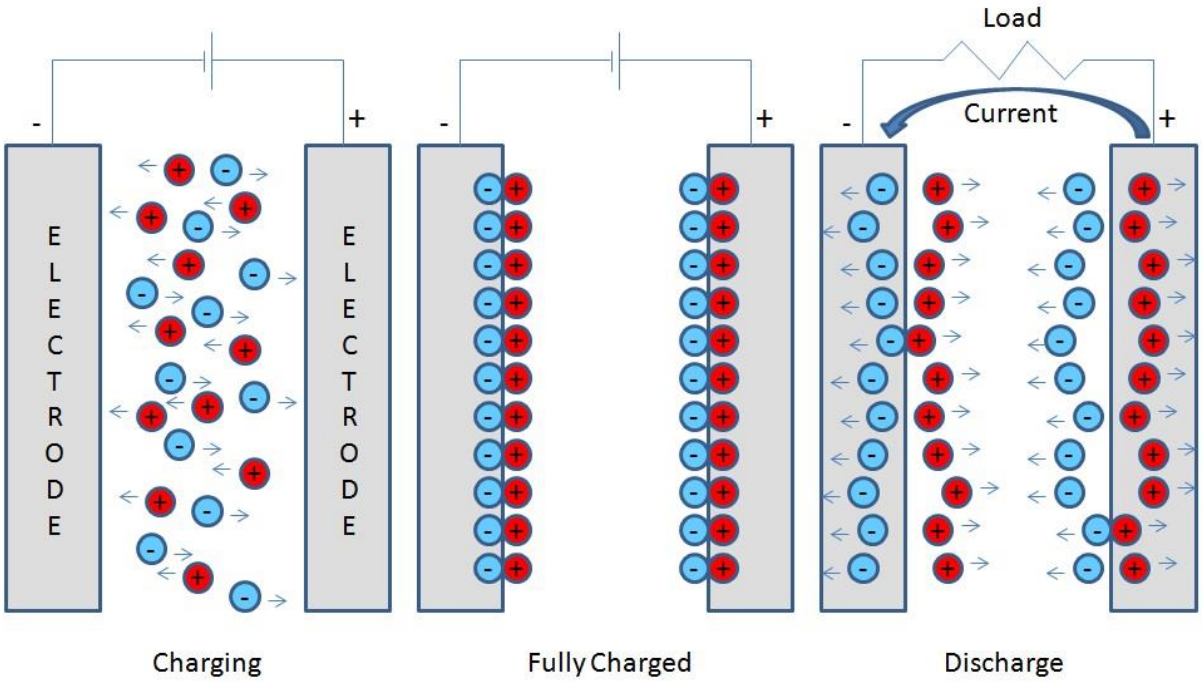

Figure 1.2: Schematic Diagram of an electric double layer capacitor. When the device discharges the ions are released from the surface of the electrode, generating a current which supplies the load with electricity.[14]

Traditional electric double layer capacitors (EDLC's) are able to produce large amounts of power due to their ability to release large amounts of charge instantaneously thus producing a high current.[15,16] This property makes them useful as power supplies in small handheld

devices. Because of the manner in which they store energy, EDLC's are typically made using very high surface area (>1000s m^2/g) carbon materials.[13,17] As the charge is stored on the electrode/electrolyte interface, it possesses a high surface area that provides a larger area on which to store electrostatic charge.[18]

1.2.2 Redox Batteries

Batteries are devices that operate using a different mechanism to EDLC's. Redox batteries consist of four separate components, the anode (negative electrode), cathode (positive electrode), insulating separator and the electrolyte. During the discharge process, redox batteries use redox driven insertion reactions of ions from the anode into the cathode (Equation 1.2). This reaction takes place in the reverse direction during the charging process and is known as deinsertion (Figure 1.3),[19]

In these reactions the anode oxidises to produce positive ions. These ions are transferred towards the cathode by means diffusion through the electrolyte. The ions reach the cathode and cause the cathode itself to become reduced to accommodate the newly inserted positive charges. The separator within the battery only allows the diffusion of positive charges through the electrolyte. The separator itself is electronically insulating but allows for the Li^+ salts in the electrolyte to diffuse through. This causes electrons to be forced through an external circuit via electron conducting wires where they are harvested and used to supply electricity. They then pass towards the cathode where they counteract the positive charges that have transferred from the anode.[19]

Common types of batteries in the past have included lead acid batteries, which are still used in cars today.[20] Advances made in safety and performance later resulted in the development of nickel hydride and more recently Li^+ batteries. Batteries have very different properties to those of EDLC's, because they utilise Faradaic redox reactions to store charges[19] and possess much higher energy densities then EDLC's.[12,21] Battery materials are able to store charge throughout the bulk material rather than only at the surface, increasing the amount of the material utilised for charge storage. However the kinetics of the charge transfer is a limiting factor.[21,22] This limitation means that batteries are not able to produce the high current possible in EDLC and hence have limited power densities due to the slow kinetics for insertion and deinsertion of ions.[21]

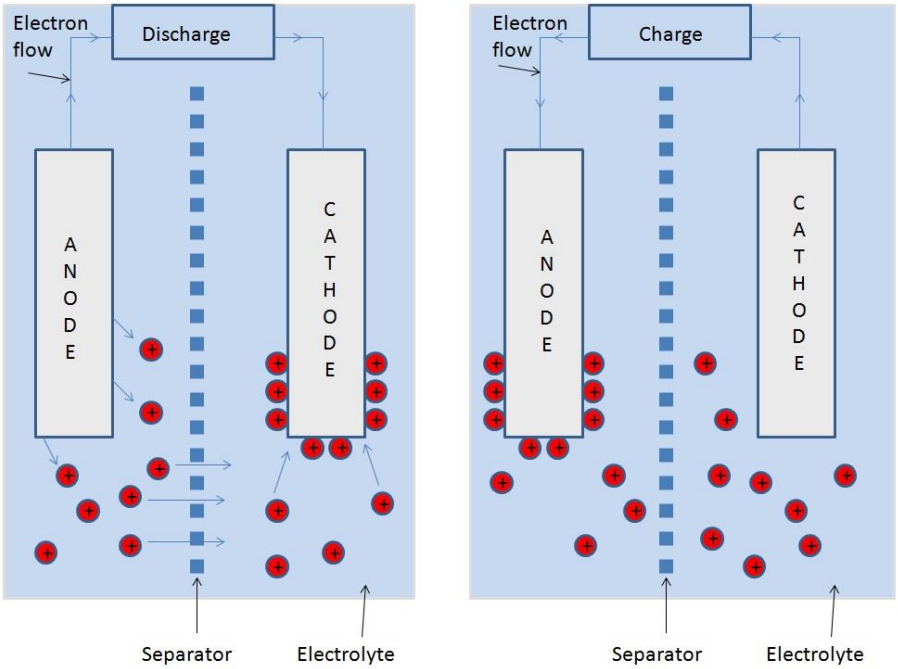

Figure 1.3: Schematic diagram for generic redox battery cell

Equation 1.2 $M + xA + xe^- \underset{\text{Charge}}{\overset{\text{Discharge}}{\rightleftharpoons}} A_xM$

1.2.3 Pseudocapacitance

Another type of electrochemical energy storage material is that of the pseudocapacitor. These devices utilise charge storage in a mechanism that combine those of both redox batteries and EDLC's in an attempt to utilise the advantages offered from both mechanisms.[23–25] Typically the materials utilise chemical redox reactions to store energy. However unlike traditional redox batteries, the reaction takes place on or close to the surface of the material where the active material is in contact with the electrolyte.[26–28] This causes the redox reactions taking place to have little or no kinetic barrier allowing large amounts of energy to be stored but with the fast kinetics typically observed in EDLC's. This mechanism is referred to as pseudocapacitance. Current research has developed pseudocapacitive materials that can operate in both aqueous[29] and organic electrolytes.[30]

It has been demonstrated that the development of materials with advanced networks of organised porous structures and/or high surface area are important to enable a material to show a pseudocapacitive nature.[27,31,32]

Depending on how the materials performance is affected by changes in particle size and morphology, there are two subcategories to pseudocapacitive materials.

(1) **Intrinsic materials:** These types of materials display pseudocapacitive character across a range of different structures, morphologies and particle sizes. Therefore they are almost always pseudocapacitive and not dependant on the structure and morphology of the material, for example $RuO_2(0.5H_2O)$.[33]

(2) **Extrinsic materials:** These types of materials do not exhibit pseudocapacitive characteristics when present in the bulk state. This is due to phase transitions and the kinetic restrictions when insertion reactions are taking place. For these materials to become pseudocapacitive, the material must be tailored to optimise morphology and porosity to minimise kinetic barriers for ion diffusion and maximise surface area to enable pseudocapacitive energy storage.[34]

Pseudocapacitive materials are desirable because they enable the possibility of producing materials capable of possessing both a high energy and power density for high power applications. The best pseudocapacitive materials are able to fully charge or discharge within 10 minutes without significant losses in their capacity performance. The reasons these materials are capable of undergoing fast redox reactions are.

(1) **High electron conductivity:** This allows for fast recombination of charges upon the de/intercalation of ions into and out of the host material, allowing better performance at high discharge rates.

(2) **Fast ion diffusion:** This allows for fast kinetic intercalation reactions to take place so the performance of materials is not limited by the diffusion of ions at high discharge rates.

(3) **High surface area:** Increasing surface area allows more active material to be situated near the surface so the distance needed to diffuse through active material before

reaching the electrolyte is less, reducing one of the key limiting factors in redox reaction kinetics.[31]

Recent research has suggested three mechanisms that account for the pseudocapacitive behaviour shown in these energy storage materials (Figure 1.4).

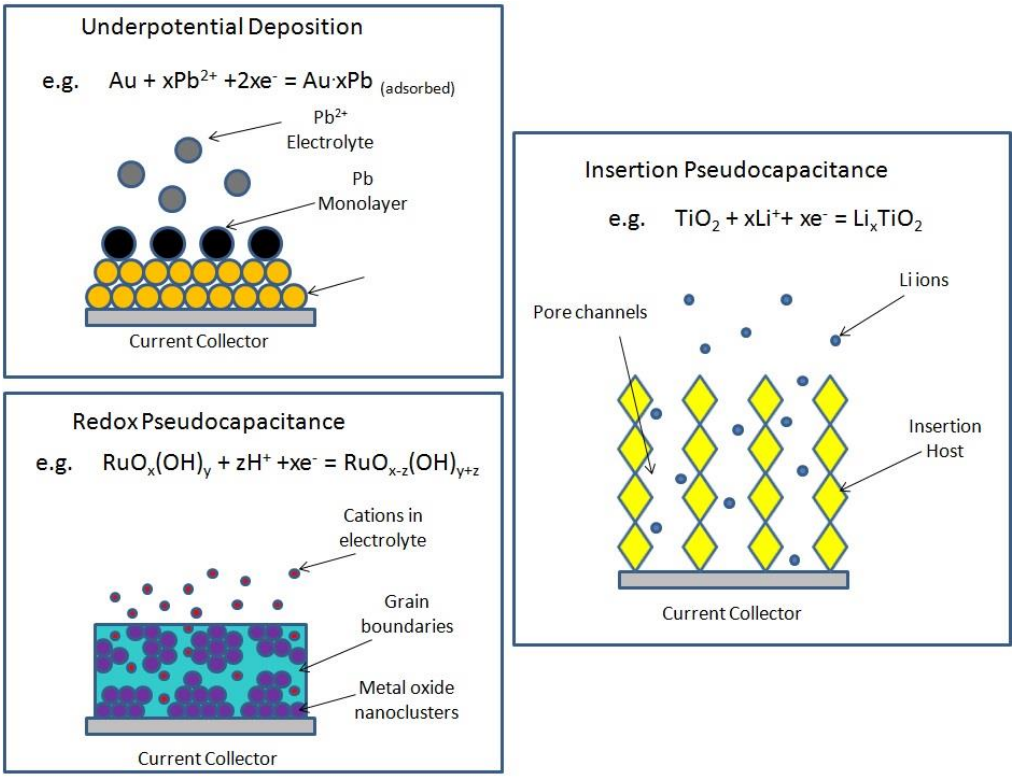

Figure 1.4: Depictions and Examples of different pseudocapacitance mechanisms[35]

1) **Redox pseudocapacitance:** When the ions present within the electrolyte electrochemically adsorb onto the surface of a material e.g. hydrogen ions in redox capacitors.[33]

2) **Intercalation pseudocapacitance:** Takes place when there is an intercalation reaction and a positive ion, such as Li^+ is being inserted into the active material. There is little or no phase changes taking place with no significant kinetic barrier unlike in bulk intercalation, allowing pseudocapacitive speeds for storage and release of charges.[35]

3) **Underpotential deposition:** Where a metal monolayer forms on the surface of another metal with a significantly higher redox potential, leading to a rapid release of current on discharge. e.g. lead particles present on top of gold particles.[33,35]

Mechanisms 1 and 2 are most common, with the first being the most useful in redox capacitors, and the second being the most useful in high performance Li^+ ion batteries.

1.3 Lithium Ion Batteries

At present the lithium ion battery industry is expanding dramatically, taking up a significant proportion of the battery market.[26] This has been due to the development of the technology since its initial discovery.[13,15] However at present the commercial applications of such technologies are limited. This is due to the expense of producing such batteries for commercial applications[19] and the limited performance compared to the requirements of modern devices. Currently Li^+ batteries are very commonly used in smartphones, tablets and other small electronic devices.[36] The main issues are safety concerns, the need for high power output and the expenses of mass production.[37] Despite possessing high energy densities, commercial lithium ion batteries are continuing to be developed in order to supply enough power to operate some of the emerging essential technologies for future such as hybrid electric vehicles (HEV's), electronic vehicles (EV's). Batteries need to improve their current energy densities significantly before being able to compete with internal combustion.[6]

A typical commercial lithium battery at present contain a cathode comprised of a lithium based metal oxide such as $LiCoO_2$,[38–40] whereas the standard anode material is usually low cost graphite[41] with a semi permeable insulating separator and electrolytes containing lithium salts such as $LiPF_6$.[42]

A lithium ion battery works using the same principle as any other redox battery, using the transfer of Li^+ ions and electrons to convert chemical energy to electrical energy. The process is reversed upon charging by applying external current it forces the ions back to their original location ready to be discharged again. During the discharge process Li^+ is supplied by the anode and diffuses through the electrolyte to the cathode. This causes the anode to be oxidised and the cathode to be reduced, as seen in the schematic diagram Figure 1.5.[43] The electrolyte contains lithium salts such as $LiPF_6$ dissolved in organic solvents typically carbonates.[44] This

allows the Li^+ to pass through the semi permeable insulating separator but prevents the passage of electrons. The electrons are forced to pass through an external circuit. This ensures charge transport separation and prevents the cell from shorting. Despite this charge separation it is essential that both charges are able to access the active materials as a redox reaction cannot take place without the ability for charges to balance on both sides of the cell. Therefore the material must be able to be transport both ions and electrons to be an effective electrode.[45] Many electrochemically active materials possess poor electron conductivity, so require the aid of additives such as carbon black to improve their performances, as well as polymeric binders to hold them together. For this reason electrodes are attached to a respective current collector to aid electron transport to and from the active materials (Figure 1.5).

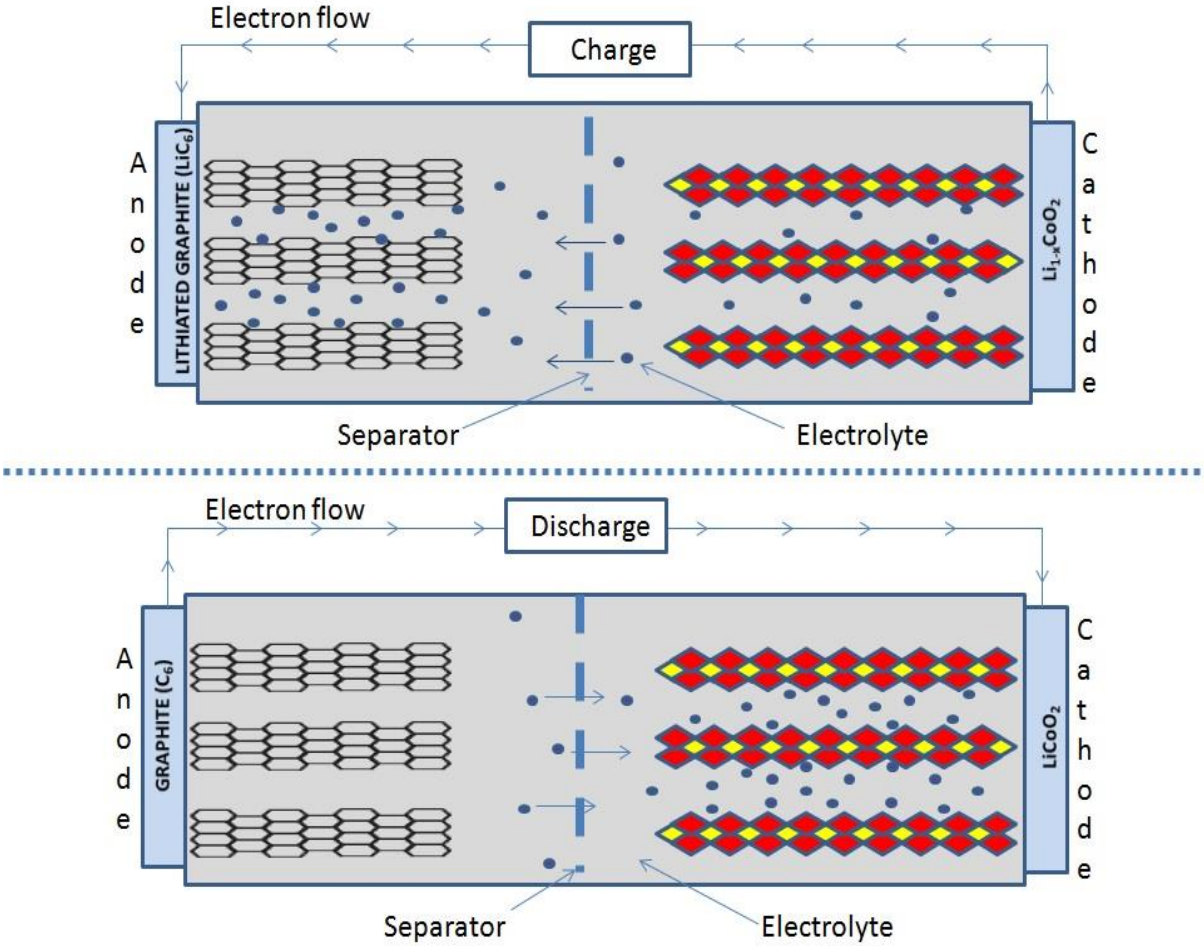

Figure 1.5: Schematic diagram of Li^+ battery using $LiCoO_2$ (Li = Blue, Co = Yellow and Oxygen = Red)[43]

In common commercial batteries the Li^+ is initially present within the cathode material in its discharged state, therefore the battery must first be charged before it can be used. The charging process involves the delithiation of the cathode extracting lithium by applying a reverse current, forcing the Li^+ out of the cathode and into the graphite anode. This produces a Li^+ rich anode

and a Li^+ deficient cathode material. When discharged the current is reversed and the opposite process occurs which causes the Li^+ to migrate back to the cathode (lithiation). This allows the electrons to pass through the external circuit to balance out the charge migration of lithium towards the cathode and returning redox chemistry of the electrodes back to their initial state.[46] The redox reaction taking place can be seen in Equation 1.3.

Equation 1.3

$$\underset{\text{Anode}}{Li} \rightleftharpoons \underset{\text{Cathode}}{Li^+ + e^-}$$

The performance of a battery is mainly assessed on four properties.

(1) Capacity: The higher the capacity the longer it will be able to supply energy.

(2) Potential window: Batteries that operate at a higher and wider potential are able to supply more energy.

(3) Charge transfer kinetics: The rate at which ions and electrons can transfer into and out of the material determines how effective they are at higher discharge rates, minimising capacity loss.

(4) Recyclability: How well the capacity of the battery can be regenerated after each use and for how many cycles the battery can be used before it has lost a significant proportion of its capacity.

1.3.1 Anode Materials

Anode materials make up the negative electrode of the lithium ion battery cell. They are the source of electrons and lithium ions during the discharge process. The most common material for use in commercial lithium battery anodes is graphite[47] due to its good recyclability and a long cycle life which are highly beneficial and desired for an electrode.[48] Good recyclability demonstrates that the material is able to reversibly release and recapture lithium ions during the charging and discharge process, enabling the retention of its capacity throughout cycling. The cycle life capabilities demonstrate the stability for a vast number of cycles. Graphite materials are relatively inexpensive to produce which is vital for the commercialisation process of batteries. They possess good electron conductivity[49] allowing the speedy insertion and

extraction of large quantities of electrons able to potentially produce high power densities. Graphite material possess the advantage of having a very low working potential compared to most other anode materials shown in Figure 1.6 higher only then lithium metal.[50] This allows for a much larger operating potential then other anode materials allowing the maximum possible energy density to be achieved.

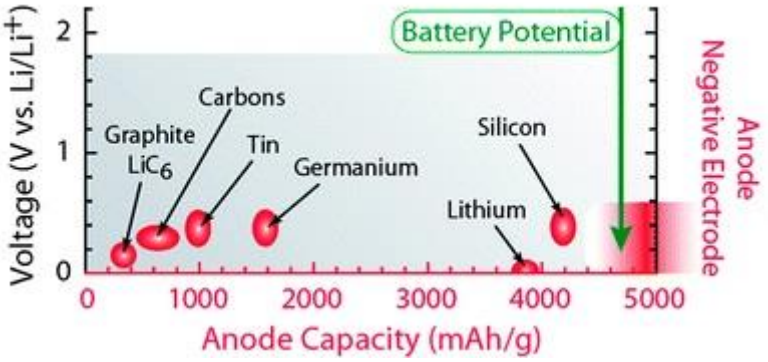

Figure 1.6: Potential vs capacity diagram of various anode materials[50]

Despite these positives, graphite has drawbacks as an anode material. Studies show that only one Li^+ is able to be inserted per 6 carbon atoms in the graphite electrode as can be seen in Equation 1.4.

Equation 1.4 $C_6 + {}_xLi^+ + {}_xe^- = Li_xC_6$ [47]

This limits the potential capacity of the material as a lithium insertion compound compared to high capacity anode materials such as tin oxide.[51] The maximum capacity of graphite is estimated to be around 370 mAh/g.[52,53] This is a higher capacity than most anode materials but still limits the potential capacity of the battery. The other main issue with the use of graphite as a lithium ion anode material is poor lithium diffusion capabilities.[54] The limited speed at which lithium is able to intercalate and deintercalate into the graphite restricts the performance at high discharge rates, despite the high conductivity. Materials must possess both good electron conductivity and lithium diffusion capabilities for the rapid separation and recombination of charges to achieve the best rate capability. Current research aims to produce anodes that possess higher capacities and rate capabilities as well as the retention of capacity and cycle life capabilities.

Initially batteries used lithium metal as the anode back in the 1970's. It possesses the advantages of having the lowest possible operating potential (-3.04 V vs SHE) and the highest theoretical capacity of 3860 mAh/g.[55] This provides both the maximum potential difference between the anode and the cathode with the largest obtainable capacity. However there are a large number of drawbacks to using lithium metal, its reactivity makes it very dangerous and it can easily catch fire. Due to the continuous removal and recoating of lithium onto the surface of the electrode during recycling, particularly at higher discharge rates, the electrodes have tendencies to form branches of lithium protruding out of the surface of the electrode rather than coating evenly across the surface. These branches of lithium are known as dendrites.[56,57] These dendrites can either break off and float around in the electrolyte solution or can puncture the separator of the battery leading to short circuiting and heating of the electrolyte. Heating causes an increase in the reaction rate which leads to thermal runaway within the cell,[58] a common cause of fires in lithium batteries.

Lithium battery anode materials that have been investigated are those such as other carbonaceous materials such as carbon nanotubes (CNT's), nanofibers (CNF's), graphene, porous carbons and transition metal oxides (TMO's).[59,60] These materials have all managed to achieve superior capacities compared to graphitic carbon but each in turn possesses its own drawbacks.

Looking at the present anode materials available, excluding lithium metal, we are able to place the majority into three main groups of materials.

(1) De/intercalation materials: Materials that utilise the intercalation of lithium within the structure to store and supply charge. These include materials such as graphitic carbon and $LiTiO_2$.[60] They possess good cycle life, high rate capabilities and are relatively safe and inexpensive.[61] However they typically possess low capacities, coupled with a higher redox potential (e.g. $LiTiO_2$ = 1.75 V vs Li/Li^+), with the exception of graphite (<0.2 V vs Li/Li^+) meaning that the operating potential difference is greatly reduced despite being safer.[62] Both of these factors significantly lower the energy density of the material.

(2) **De/Alloy materials:** Material that are typically coated with lithium metal to store the charge nearer to the surface allows for high specific capacities and high energy density materials.[63] However these materials demonstrate poor recyclability and irreversible capacity loss.[64] Both are essential for electrode materials for effective secondary batteries.

(3) **Conversion materials:** Structure such as Li_2O that store lithium at the anode and upon discharge covert to produce Li^+ and then back to form Li_2O upon recharging. These materials provide high capacity and a high operation potential difference due to their low operating potential. These materials are low in cost to maintain and are environmentally friendly.[47] However the materials suffer from poor columbic efficiency and therefore have poor cycling performance due to loss in capacity. The materials have a very unstable SEI formation which leads to poor performance as it prevents access for ions to be de/intercalated from the structures when undergoing charge and discharge.[65]

1.3.2 Cathode Materials for Lithium Batteries

Cathode materials are one of the most essential components of a lithium ion battery. The properties of the cathode typically determine the potential difference of the cell as most batteries currently use graphite as the standard anode material. At approximately 49% of the total cost the most expensive component of the battery is usually the cathode material, followed by the electrolyte at 23% with all other components costing around 10% or less.[66] In the ideal lithium battery cathode, there are a number of properties that the material should possess.[45]

(1) **A redox active ion:** There should be an active component able to undergo reversible redox reactions. This is typically a transition metal ion such as Co, Ti or Fe capable of changing oxidation states to compensate for Li^+ being incorporated into the structure.

(2) **Reversible Li intercalation:** The redox active ion should undergo reversible reactions with Li^+. This reversibility enables the active material to be converted back to its original state upon extraction of the Li^+, without leading to a permanent change in structure or morphology.

(3) Good electron conductivity: This is essential for high performance cathode materials as it allows for easy transport of electrons between the transition metal centres via the external circuit needed to counteract the reduction caused by Li^+ insertion. High electron conductivity provides quick access to all redox active centres producing a much greater power density and minimises the need for conducting additives which lower the energy density.

(4) Cycling stability: The cathode must be stable under cycling enabling the battery to be used repeatedly (>1000 cycles) without a significant decay in capacity. This ensures that the battery does not need to be regularly replaced and can be used daily for a number of years.

(5) High energy of reaction: The energy produced by a battery is determined by two properties, firstly the operating potential of the cell, secondly the Li^+ storage capacity. The ideal cathode would operate at the highest possible working potential (currently around 4 V) and be able to store large amount of Li^+ (at least 1 Li^+ per transition metal). Some examples of cathode potentials can be seen in Figure 1.7.

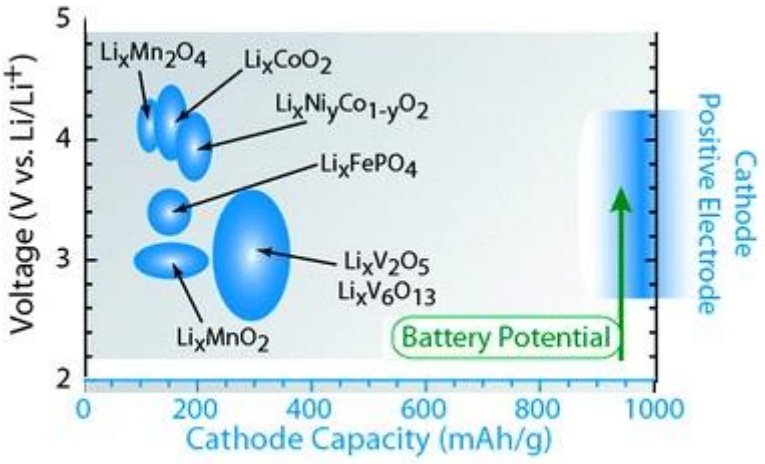

Figure 1.7: Potential vs capacity diagram of various cathode materials[50]

(6) Fast Li^+ diffusion kinetics: Fast diffusion kinetics allows Li^+ to quickly diffuse into and out of the cathode material allowing for the quick uptake and release of charge. This enables the material to produce large current without a significant loss in capacity.

(7) Environmentally benign: The materials should not be hazardous to the environments or harmful to people who are working with the material as dangerous and harmful materials will not be permitted for large scale battery applications.

(8) Low Cost: The price of the materials is very important from a commercial perspective as it will not be possible to upscale and mass produce materials if they are expensive. Therefore such materials would not be viable as a useful alternative to fossil fuel sources.

At present there are three main types of cathode materials that have undergone vast amounts of research, these categories are:

(1) Layered transition metal oxides ($LiMO_2$)
(2) Spinel Oxides (LiM_2O_4)
(3) Olivine Phosphates ($LiFePO_4$)
(M= Ni, Co, and Mn)

1.3.2.1 Layered Transition Metal Oxides:

Layered transition metal oxides are the most common commercial Li^+ battery cathode materials. The parent compound $LiCoO_2$ exists in two possible structure configurations, a cubic spinel or layered trigonal hexagonal structure. The layered hexagonal structure is the most useful as a Li^+ battery cathode material as it produces the best capacities.[41]

In $LiCoO_2$ the cobalt and lithium are situated in the octahedral sites with oxygen atoms close packed in ABC-ABC stacked layers either side of the cobalt as shown in Figure 1.8. When Li^+ is extracted from the structure, the cobalt ions are oxidised from Co^{+3} to Co^{+4} to compensate for the removal of Li^+ from the structure. However after the lithium extraction exceeds a certain concentration ($x<0.5$) this leads to the formation of a different crystal structure. This changes the materials electrochemical properties and damages the performance. For this reason despite having a theoretical capacity of 280 mAh/g the maximum obtainable capacity is 140 mAh/g before it is forced to lose its structural integrity and electrochemical performance.[67]

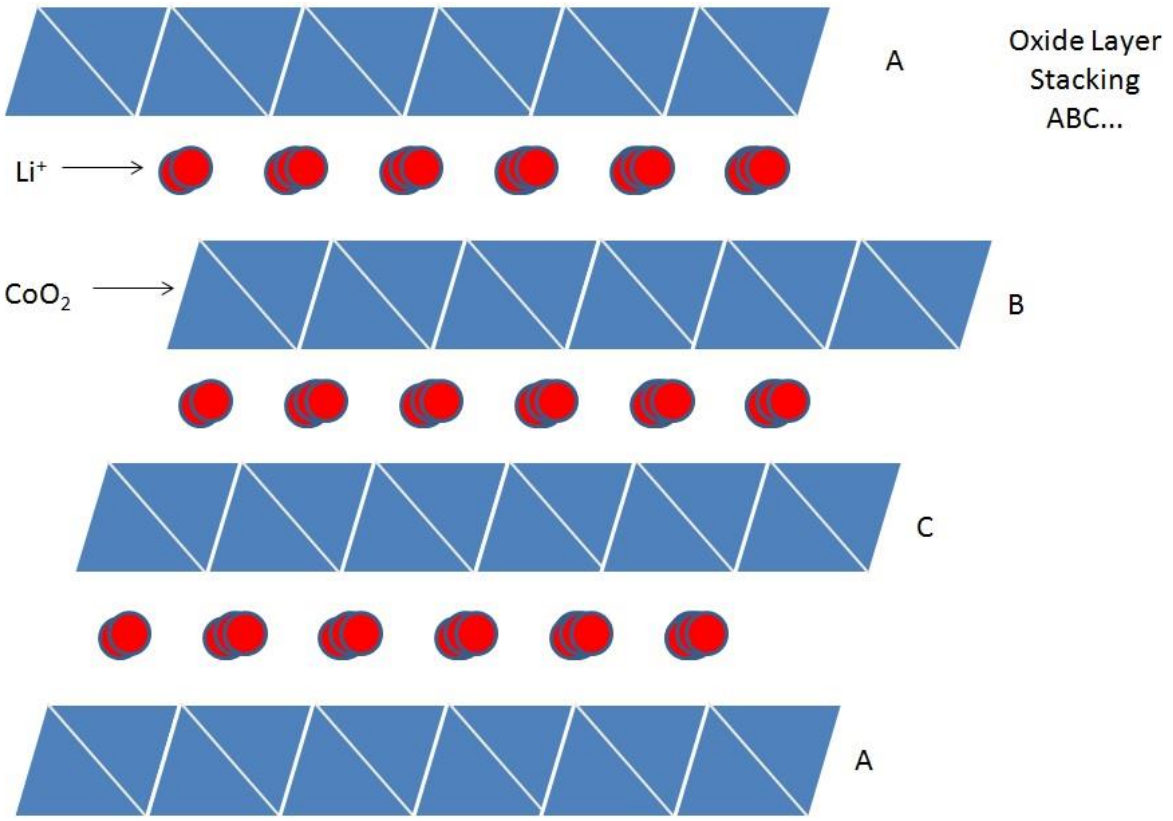

Figure 1.8: Layered trigonal hexagonal structure ($LiMO_2$)[68]

This low practical capacity and the expense of cobalt initiated the development and investigation of other transition metal oxides such as Ni and Mn with similar structures. The nickel analogue to cobalt oxide shows a very similar structure and has the advantage of being much cheaper than cobalt whilst producing a higher capacity. However the Ni layered oxide possesses its own setbacks due to the difficulty obtaining the perfect crystalline structure. There is a tendency for the Ni to locate itself within the Li^+ layer leading to limitations of lithium ion transport within the material. This is referred to as Li/Ni disorder and is detrimental to its performance as a cathode material.[69,70]

Due to the difficulties suffered by Ni and Co oxides, researchers created mixed transition metal oxides to overcome the problems suffered by the individual metal oxides. Mixing Ni and Mn at a 50:50 ratio produced an effective cathode material with the Ni^{+2} and Mn^{+4} states present. The Ni^{2+} species is the only electrochemically active constituent with the Mn having only a passive role.[71,72] During the charge and discharge process the Ni is exchanged between the Ni^{2+} and Ni^{4+} oxidation states whilst the Mn stays constantly at Mn^{4+}. The cell operates within the Ni redox transition window situated at a fairly high potential window of 3.5-4.4 V.[72]

Though the manganese itself is not directly involved in the electrochemical reaction, its presence is intended to stabilise the structure during cycling. Both metals are present within the TM layer of the layered oxides with lithium staying predominantly to the interstitial layers as seen in the cobalt oxides. However there are still traces of Li/Ni disorder within these structures but sufficiently less than pure $LiNiO_2$. The energy density of these Ni/Mn materials is significantly higher than that of the cobalt analogue, achieving capacitates as high of 200 mAh/g.[73] The material undergoes only slight capacity fading over the first 100 cycles. However the issue of Li/Ni disorder remains present in long term stability. To improve lithium transport and recycling performance, research has been carried out to synthesise materials which contain minimal Li/Ni disorder. One of the best materials to date has achieved as low as 4% disorder for mixed Ni/Mn oxide.[74]

Building upon these successes, scientists started to develop materials containing up to three transition metals to improve the performance of the material while minimising the problems produced by the single transition metal oxides. Some of the best results have achieved capacities of 160 mAh/g with excellent recyclability between potentials of 2.5-4.4 V. This increases to 200 mAh/g when the window is increased up to 4.6V.[75] The structure now contains both Co and Ni as electrochemically active constituents, whilst the Mn remains present to assist the stability during cycling. This compound is the most thermally stable layered oxide which is able to reach temperatures of up to 500 °C. The maximum cut off voltage of this material is 4.7 V because once the compounds exceeds 4.5 V there is oxygen loss due to the slight overlap between the manganese 3D orbital's and the oxygen 2P orbital's when it is present in the Mn^{3+} and Mn^{4+} states. This causes the extraction of electrons form the oxygen to the transition metal ions[76]

1.3.2.2 Spinel Oxides LiM_2O_4

Another type of material used as a lithium battery cathode is that of the spinel oxide structures which were first proposed in the 1980's. These are considerably cheaper, safer and more environmentally friendly than layered oxide materials[77] which makes them more attractive for commercial use. These materials typically offer a 3D diffusion pathway due to the vacancies of large numbers of octahedral sites left vacant by M^+ ions with Li^+ in the structure occupying tetrahedral sites as shown in Figure 1.9. These allow easy Li^+ diffusion and high rate capability. They do suffer from poor recycling stability as it is quite common to observe capacity fading,

especially at higher temperatures. These materials produce lower capacities than their respective layered oxides, lowering the energy density. There are two reasons that have been suggested for capacity fading in spinel oxides are:

(1) The dissolution of transition metal ions in the acidic electrolyte damaging the structure

(2) Changes in crystal structural taking place within the materials, e.g. a change from spinel to a tetragonal structure brought about due to the Jan Teller distortion ($LiMnO_2$).[78,79]

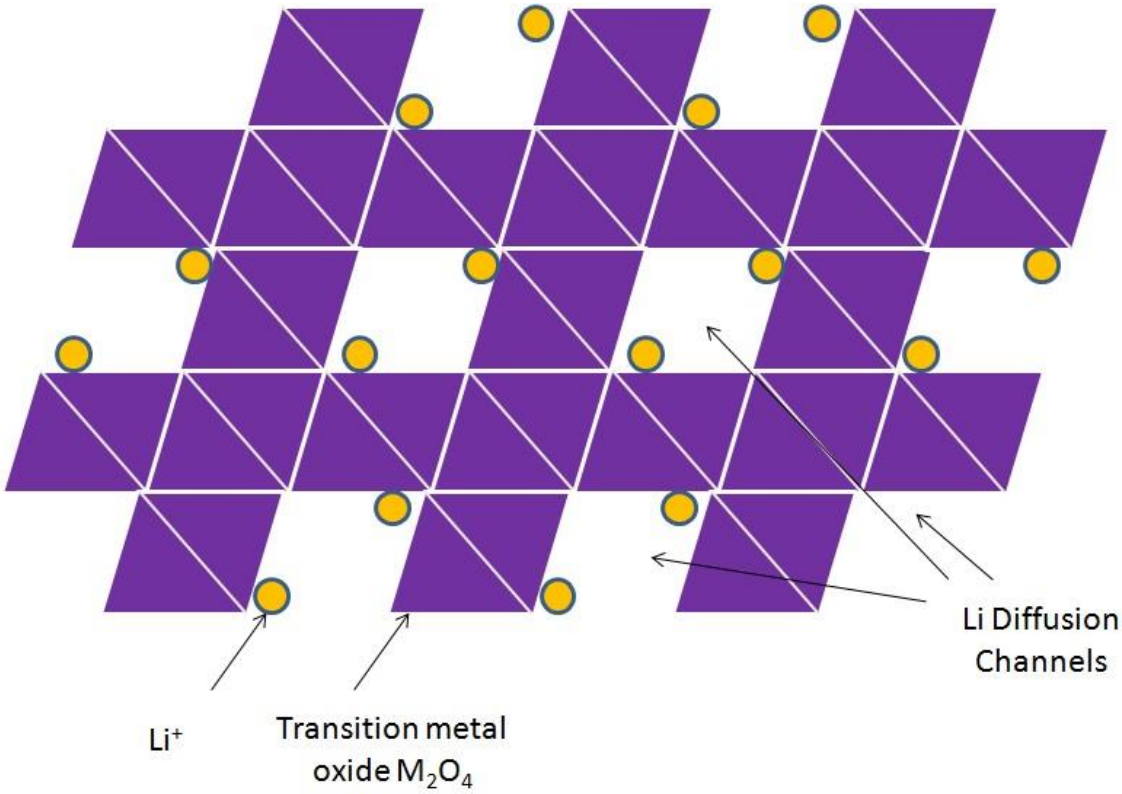

Figure 1.9: Structural diagram for spinel oxides: MO_8 (purple) Li^+ (yellow)[80]

To suppress Jahn Teller (JT) distortion, doping with other metals is used to minimise structure changes during cycling. One investigation demonstrated that doping Mn oxides with Ni at a ratio of 3:1 produced the best performance. This was attributed to the presence of a disordered structure where the metal ions are randomly occupied making it possible for the Li^+ to migrate through the structure via octahedral sites. However, when the structure is more ordered and crystalline, the ordering of the Mn and Ni leads to the inhibition of Li^+ transport throughout the

structure.[81] In addition to stabilising the structure to morphology changes, the incorporation of Ni extends the top of the potential window due to the locations of the Ni^{3+} to Ni^{4+} redox couple up to 4.7 V increasing the energy density.

These mixed materials achieve close to their theoretical capacity unlike many of the layered materials, showing superior cycling performance compared to pure spinel oxides. The incorporation of Cr into the $LiNi_{0.5}Mn_{1.5}O_2$ promotes the formation of a disordered structure in place of the ineffective ordered structure.[82] As the Ni content of Mn oxides increased, the cycling stability of the materials improves. Due to the potential window being situated at higher potential than the undoped oxides, there is a higher degree of electrolyte decomposition taking place at the cathode surface. This induces the formation of a solid electrolyte interface (SEI) leading to the detriment of performance in the long term.

1.3.2.3. Olivine Phosphates ($LiMPO_4$)

Another type of material that has received much research attention is the olivine phosphate materials such as $LiFePO_4$.[83] There are numerous advantages and disadvantages offered by such materials.

Advantages

(1) Low cost: Materials such as Fe are relatively inexpensive and highly abundant unlike Ru, V and Co materials. This enables them to be produced inexpensively and ensures that there is a large supply of metal with which to mass produce devices upon commercialisation.

(2) Low toxicity: They are not harmful to the environment or people and are therefore a much safer alternative battery material. This is important in commercialisation and up scaling production as it does not complicate the procedures.

(3) High specific capacities: Capacities up to 170 mAh/g have been achieved using a relatively high operating potential window (≈ 3.5 V vs Li/Li^+),[45] both essential to producing materials which possess high energy density.

(4) **Low volume expansion:** When Li^+ is incorporated the material does not expand significantly, preventing dramatic changes to the morphology or structure of the material, which would normally damage performance.

(5) **Little capacity fading:** The materials are able to be used repeatedly without significant loss of capacity ensuring that they can be used on a daily basis over a number of years without need of replacement.

Disadvantages

(1) **Low conductivity:** The material is not effective at transporting electrons to and from the transition metal centres. This slows down the kinetics of the reactions and increases the difficulty in the access to the bulk material.[84,85]

(2) **Poor rate capability:** The slow charge transfer kinetics leads to the prevention of charge separation and recombination at high discharge rates. This prevents the material from releasing large amounts of energy efficiently to produce high currents leading to large reductions in capacity at high discharge rates.

Li^+ and Fe^{2+} occupy the octahedral sites with the phosphorous atoms occupying tetrahedral sites within the structure. Oxygen atoms arrange in a hexagonal close packed arrangement around the phosphorous atoms. This arrangement leads to the slow migration of Li^+ through the structure(Figure 1.10) and separation of the FeO_6 octahedra by phosphate[86] which greatly reduces the conductivity of the material due to restricted electron hopping.[87] This is one of the key properties affecting performance especially at high discharge rates.

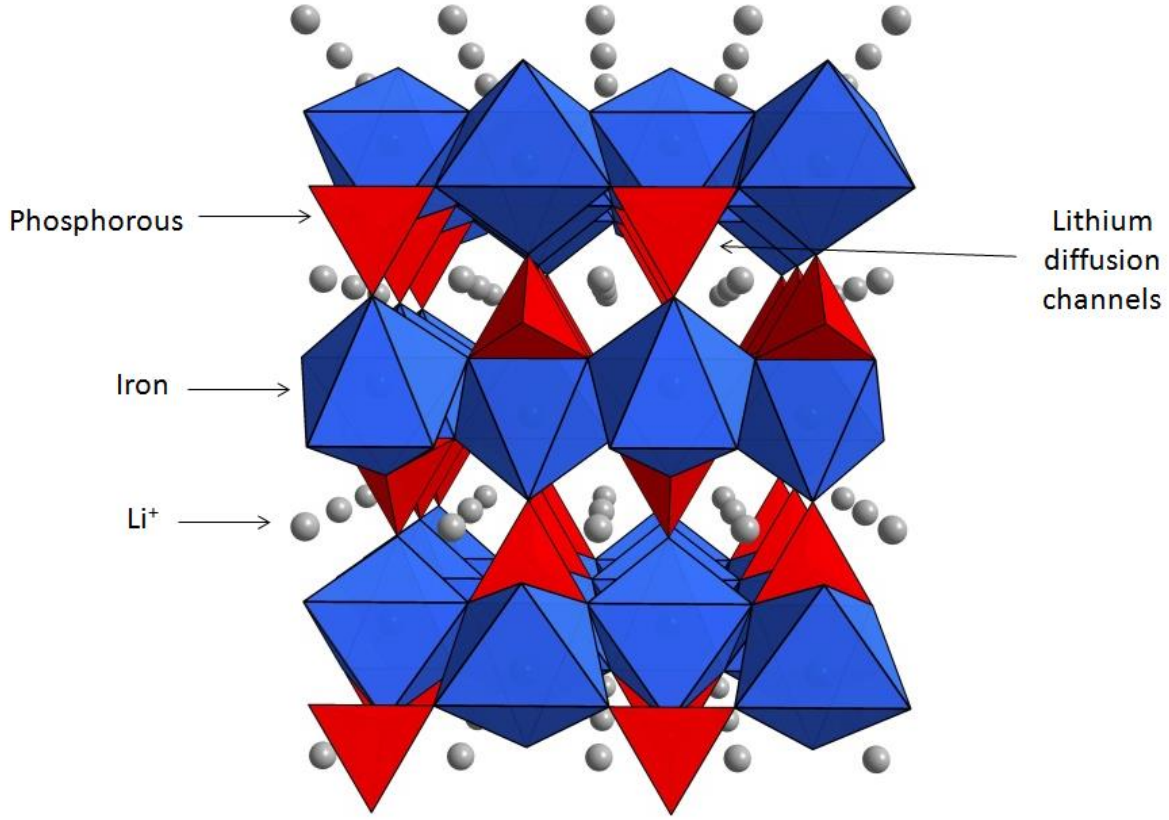

Figure 1.10: Structural diagram of typical olivine phosphates e.g. $LiFePO_4$[88]

Olivine phosphates such as $LiFePO_4$ have a voltage plateau situated at approximately 3.5 V which is lower than those of layered and spinel oxide materials (4.5 V). This lowers the overall energy density meaning that such materials require higher capacities in order to compensate of the lower operating potential.

1.4.1. The Importance of Pseudocapacitive Materials in Li^+ Batteries

The main challenges facing current Li^+ batteries are those of limited power density and poor rate performance. This poor performance is caused by slow Li^+ diffusion kinetics within the material,[21] loss of performance on upscaling, the costs of materials[89] and the poor capacity retention of materials due to the instability of the materials during cycling[90]. The advantages of high electron conductivity, fast Li^+ diffusion and high surface areas[35] offered by pseudocapacitive materials are all key features that would improve these current weak points of the performance of battery materials. The development of electrode materials that utilise pseudocapacitance is therefore a potential solution in the development of modern higher performances devices.

Pseudocapacitance in the field of Li^+ batteries typically involves the use of reversible Faradaic reactions of redox active material in order to store Li^+ near to or on the surface of the electrode. Because the storage of Li^+ takes place near the surface, the Li^+ diffusion kinetics of the material, which are normally the rate limiting step in the reaction and an important factor in the performance of the material, are significantly improved.[28] The shorter distance the Li^+ must travel allows a more efficient release and capture of charge and minimises the loss of efficiency. This means the kinetics within the material no longer become limited by the Li^+ diffusion through the material and instead become limited only by the surface effects of the material.[91] The capacity of the material becomes more independent of the discharge rate and reduces the voltage offset when the material is cycled between the charge and discharge process at high discharge rates due to the faster uptake and release of charge.

In addition to the more common phenomenon of surface redox pseudocapacitance, commonly utilised in redox capacitors, there is also the mechanism of intercalation pseudocapacitance. In this mechanism Li^+ intercalates into the bulk of the electrode material from the electrolyte rather than only at the surface. This is usually made possible because of the crystalline network that is present within the material which provides a 2D pathway that enables fast transport of Li^+ ions throughout the structure, producing negligible or no structural or phase changes within the material.[28] Because of this fast Li^+ transport the rate limiting process is no longer diffusion but that of the surface processes. This means that it does not suffer from the limitations of poor diffusion kinetics seen in typical intercalation materials and its behaviour appears capacitive in nature.

The difference between traditional intercalation materials and those of pseudocapacitive materials is best demonstrated by the responses to electrochemical analysis. Firstly the relationship between current and sweep rate in cyclic voltammetry and secondly the charge discharge profiles for the different types of materials. When carrying out cyclic voltammetry it is possible to separate the contributions of the different charge storage mechanisms towards the total charge stored in the material according to Equation 1.5 commonly used in battery research.[31]

Equation 1.5 $I = a\nu^b$

Equation 1.6 $\log I = b \log \nu + \log a$

In this equation I is peak current (A), ν is the scan rate (mV/s), a and b are adjustable parameters.

When this equation is rearranged to give Equation 1.6 a plot of log peak current versus log sweep rate it is possible to calculate the value of b from the gradient.[31] When the b value produced from the analysis are approximately 0.5, the material is limited by the diffusion of ions thorough the bulk of the material the current produced is proportional to the square root function of the increase in sweep rate.[92] For values of b that are closer to 1, this indicates that the material is limited by surface controlled processes as current increase proportionally to that of the sweep rate (Figure 1.11).[91] The reason for this is that as the material is cycled faster the surface controlled reactions are more capable of releasing the charge fast enough to keep up with the changing potential. The limited rate of diffusion controlled processes leads to a loss in the efficiency of the reaction and a delay in the release of ions leading to smaller currents and often larger peak separation as the sweep rate is increased. Materials that are pseudocapacitive are therefore capable of producing significantly higher capacities at higher discharge rates as they are more able to efficiently release the charge.

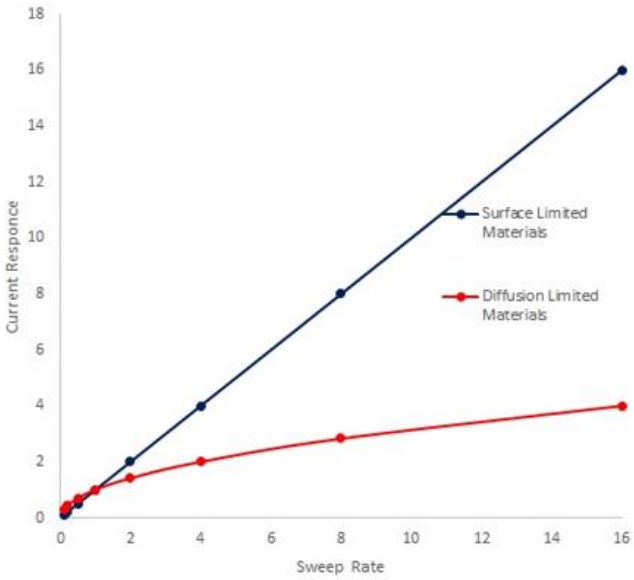

Figure 1.11: Current response comparison between (blue) surface limited and (red) Diffusion limited materials as a function of sweep rate in cyclic voltammetry.

When looking at the different types of discharge profiles (Figure 1.12), it is also possible to observe the different characteristics of the storage mechanisms. During this analysis materials are discharged at a variety of different rates, these are done according to C ratings, where 1 C

is a discharge current that would produce complete discharge of a materials theoretical capacity in one hour. The higher the C rating the faster the rate of discharge, 2 C being ~ 1/2 hour, 4 C ~ 1/4 hour etc.[93] The pseudocapacitive mechanism (Figure 1.12(a)) is similar to that of the Li^+ intercalation mechanism in batteries (Figure 1.12(b)) however its profile appears to show a more linear shape typically seen for surface controlled storage kinetics demonstrated by capacitors (Figure 1.12(c)). Pseudocapacitive materials also retain the shape of their profiles better at higher C rates than traditional insertion materials.

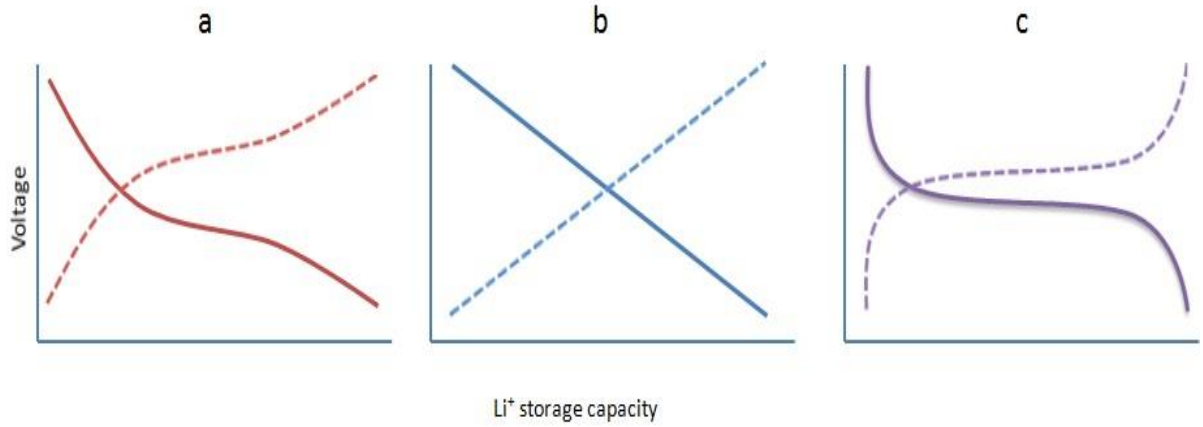

Figure 1.12: Charge (broken lines)discharge(solid lines) profiles of materials that utilise (a) pseudocapacitive, (b) capacitive and (c) Li^+ intercalation charge storage mechanisms [94]

1.4.2. Pseudocapacitance Effects on Battery Performance.

One of the simplest strategies to make a material pseudocapacitive is to reduce the size of the materials down to nanoscales in order to increase the size of active surface area. Increasing the amount of active material present on the surface enhances the rate of the transport kinetics and increases the contribution of pseudocapacitance towards the energy storage of the materials.[91] This was demonstrate by Wang *et al*. who by reducing the sizes of TiO_2 nanoparticles from 30 nm to 7 nm the contribution to energy storage from pseudocapacitance increases from 15 % to 55 %.[31] This demonstrates that as materials approach nanoscale size the surface charge transport mechanism becomes the more dominant.[31]

When looking at the battery specific side of intercalation pseudocapacitance, the objective is not only to increase the amount of material present near the surface but to allow for increased Li^+ storage in the bulk of the material. However during Li^+ intercalation pseudocapacitance the rate is limited by the surface redox processes of the material.[28] This is very rare however as most insertion materials are limited by the poor kinetics of Li^+ diffusion throughout the material.

1.4.3. Intercalation Pseudocapacitance Materials

One example of a material that achieved intercalation pseudocapacitance was that of an amorphous TiO_2 graphene composite, the material was able to produce capacities as high as 182 mAh/g at a discharge rate of 10 C after 100 cycles.[95] This demonstrates excellent storage performance when compared to a similar nanoscale material which does not demonstrate intercalation pseudocapacitance which only achieved a capacity of 50 mAh/g at the same discharge rate.[96] This demonstrating that these materials show significant potential as a high performance Li^+ battery material.

This was attributed to the intercalation pseudocapacitance and was confirmed by the assessment using the b values calculated using Equation 1.5. The materials produced values of between 8.3-9.4, demonstrating a surface storage mechanism being the more dominant process, the capacitive contributions to charge storage were also calculated to be approximately 72%.[95] The intercalation pseudocapacitive behaviour was achieved due to its high porosity and disordered surface structure combined with the defects created by doping it with graphene.[97,98] This enabled the facilitation of fast ion transport throughout the material due to the porosity allowing increased electrolyte access and the surface structure providing increased surface reactions allowing the quicker intake and release of Li^+ at the higher discharge rates.

Other methods of achieving intercalation pseudocapacitance with TiO_2 were achieved using doping with other transition metal oxides such as Nb,[99] this aides conductivity due to the Nb pushing the Fermi level up to the bottom of the conduction band of the Ti aiding charge transport within the material. By doping the material with Nb the capacitive charge storage contributions increased from 50% to 65%, despite the surface area of the material decreasing after doping.[99] The doped materials possessed a significantly improved performance at higher discharge rates producing a capacity of 105 and 88 mAh/g at 29 C and capacities of 48 and 27 mAh/g at 86 C for the doped and non-doped material respectively.[99] These results demonstrated the importance of improving electron conductivity and Li^+ diffusion kinetics and surface effects are more important in intercalation pseudocapacitance than surface area in order to improve charge storage.

Recently research into TiO_2 (B) (Bronze) has produced significantly larger capacities, up to 335 mAh/g,[100] then those achieved using the other forms of TiO_2 Anatase and Rutile 220mAh/g.[101] The excellent performance of this material at high rates indicates that it has different intercalation kinetics to the other forms of TiO_2.[101] This was further corroborated by the shape of the discharge profile which appeared to be more of a steady slope similar to those typically seen for pseudocapacitive materials (Figure 1.12(a)). The reason for this was because the material utilises the intercalation pseudocapacitance mechanism.[94] Nanostructuring causes the shift towards surface charge transfer becoming the dominant charge storage mechanism, and this combines the surface distortions of the material which act as a solid state solution through which the Li^+ can be transported throughout the structure. All of these features allow enhanced and facile Li^+ transport producing pseudocapacitive characteristics and enhanced capacities and cycle rate performance.[94]

Another material that has shown promise as a pseudocapacitive battery material is that of MoS_2.[102] When the material was tailored to optimise morphology and structure the peak current increased in proportion with sweep rate demonstrating its surface process are the main storage mechanism.[102] The fast intercalation was ascribed to the increased spacing between layers which decreases the barrier to Li^+ transport in addition to variation in site energies caused by the structural disorder. The final materials exhibited 70% of its capacity produced at 1C at a discharge rate of 20C, exhibiting excellent rate capability.[102]

All of these materials have demonstrated the advantages offered by pseudocapacitance to the field of Li^+ battery research and how in the future development of high performance Li^+ batteries these types of materials will be taking a key role in enhancing the performance at the higher discharge rates demanded by electronic vehicles and modern technology.

1.5. State of the Art Li Batteries Research

Due to the high power requirements for batteries to be used in modern electronic devices and vehicles (200 Wh kg^{-1} and 300 Wh L^{-1})[103] and the need to be cycled over thousands of cycles with ≥80 % of its initial capacity. The current Li^+ batteries are unable to supply the demands to provide prolonged use over a period of years.

High energy density materials have been created however they have produced their own drawbacks. In order for batteries to meet these demands research has been focussed around overcoming the three main challenges suffered from current battery technology.

1. **Low ionic and electronic conductivity:** Low conductivity reduces the ability to utilise redox sites therefore such materials typically require the use of conducting additives to enhance conductivity and performance.[104]

2. **Changes to morphology during cycling:** Changes to morphology significantly hinder performance as it causes aggregation and loss of electrical contact between particles. Changes to morphology can also lead to the formation of an irreversible SEI causing permanent capacity loss.[105,106]

3. **Volume changes:** Changes in volume causes a strain on the electrode material that eventually leads to structure loss and isolation from the current collector causing a dramatic decrease in cycling performance and caused a large fade in capacity.[90]

State of the art research is focused on improving current high performance materials and overcoming these challenges. This has been approached by both fine tuning and improving previously investigated materials and by researching new materials and strategies.

1.5.1 Approaches to Improving Current Materials

There have been six general strategies used to improve the performance of these materials all of which have produced a mixture of successes and failures. The benefits of these strategies to the materials are listed in Table 1.1

All of these strategies have lead to the improved performance the of previously studied Lithium battery electrode materials. One of the strategies that has received significant interest is that of reduction in materials dimensions to the nanoscale.[107–109]

Strategy for Improvement	Advantages Offered by Approach
Reduction in The Dimensions of The Material (Nanoscale)	• Faster ion and electron transport • Higher surface reactivity • Relief of stress and improved mechanical stability.
Formation of Composite Materials	• Conductive media • Mechanical Structural support
Doping and Functionalisation of Materials	• Faster Ion and electron transport • Improved chemical & thermal stability.
Morphology Control	• Improved structural stability • Faster ion and electron transport • Modified reactivity
Coating and Encapsulating Materials	• Protection from electrolyte • Prevention of electrolyte decomposition • Stabilisation of surface reactions. • Conductive media
Modification of Electrolyte	• Formulation of passivation layers on the surface of the electrode • Controlled solubility of active materials and decomposition products.

Table 1.1: Different strategies used to improve the performance of Li^+ battery electrodes

A significant amount of development in electrode materials is focused around nanotechnology. Nanoscale materials can lead to increased capacities and improved rate performance due to the increased rate of transfer of electrons and Li^+ to and from the electrodes.[110] By reducing the size of the material it increases the surface area which provides easier access to active sites with shorter diffusion path lengths. The larger surface area reduces the polarisation of the electrode during cycling, this enables the power density to increase as it possesses faster diffusion kinetics and more redox active species available for storage at higher discharge rates.[110] Reducing the size of the structures down to nanoscale gives the materials more mechanical stability, and makes them more resistant to structural damage during the phase changes that typically take place that during the lithiation/delithiation process.[111] The structure of the materials can be tuned in order to reduce issues caused by large volume changes (up to 300 %)[112] that can take place during the lithiation/delithiation either by accommodating it or by inhibiting the process.[113,114] There has also been examples where reducing the dimensions

of materials to the nanoscale has allowed materials that were previously inactive to become active materials for energy storage.[115] Part of the reasoning for this is due to the formation of partially bonded atoms with higher surface energies making them more reactive.

However this strategy has its disadvantages, producing materials at the nanoscale leads to a higher inter-particle resistivity meaning that the resistance for current transferring between two separate particles is increased, decreasing the electrical conductivity between separate particles. In addition to this they are more prone to side reactions and agglomeration which causes significant decrease in their storage capacity over the course of cycling.[116] There are a number of strategies used that are attempting to overcome these issues such as synthesising materials in the form of nanoclusters where several nano particles are linked together.

It is typical for a combination of these strategies to be used rather than only using a single approach. Further increases in performance is achieved as the synergic effects of a combination of strategies reduces the disadvantages produced by the single approaches used alone.[117]

The next section discusses materials produced in state of the art research and how the use of the previously mentioned strategies has improved the results of materials that have been studied previously. This will then be followed by the latest new materials and strategies used to improve the performance of Li^+ ion batteries.

1.5.1.1. Anode Material Enhancements

1.5.1.1.1. Intercalation Materials

Graphene is a material that has been investigated thoroughly since its discovery in 2004 and possesses a number of advantages such as excellent conductivity, high mechanical stability and a large contact area to interact with the electrolyte. It is itself a redox active material and is capable of storing Li^+.[118,119] One example where graphene oxide is reduced producing a material with a more open and porous structure, enabled increase access of electrolyte to provide improved Li^+ diffusion kinetics within the material and its performance at higher discharge rates.[119]

Another example of graphene as an effective electrode material is when graphene is doped with different atoms such as nitrogen, boron and phosphorous.[120–122] The doping causes a change in the electronic structure of the material improving the energy storage on the surface. Such materials have been able to produce capacities almost double that of the traditional graphite material at high discharge rates.[119] Graphene has also been frequently used as a conducting additive and a support for other material in order to utilise the synergic effects of both materials.

However, despite these improvements due to the advantages of higher energy density offered by conversion compounds redox chemistry more attention has been focused around these materials

1.5.1.1.2. Conversion Materials

Conversions materials offer very large theoretical capacities (>1000 mAh/g)[89] due to their ability to store more than one Li^+ per transition metal (Equation 1.6).[123] However, these materials suffer issues due to the large volume expansion (up to 300%)[112] that takes place during the lithiation/delithiation process. This causes issues with capacity loss either due to loss of electrical contact, side reactions or loss of structure causing increase in SEI formation and side reactions.

Equation 1.6 $MxOy + 2yLi^+ + 2ye^- = xM + yLi_2O$

The typical strategies used to overcome the issues of these compounds are to synthesizing them at the nanoscale, to control the degree of volume changes that take place within the material. This is often coupled with void space engineering where the materials are designed with an internal void space to accommodate volume expansion without damaging the structure.[124] The alternative strategy is to synthesis a protective coating around the outside of the material to help improve the stability of the material during cycling.

Transition metal sulphides such as Co_3S_4 and Ni_3S_4 are materials that are traditionally hindered by volume changes and side reactions and poor cycling stability.[125] When synthesised in nanotubes onto graphene, the conductivity of Co_3S_4 was significantly improved, the porosity inhibited anion dissolution into the electrolyte allowing improved cycling performance of the material.[126] Ni_3S_4 and annealed doped with graphene nanoparticles, was able to achieve a

capacity of 1323 mAh/g after 100 cycles at a discharge rate of 0.2 C compared to 494 mAh/g for the un-doped material. This improvement was attributed to the favourable Li^+ diffusion caused by improved conductivity and increased in the amount of amount of Li^+ stored per molecule.[127]

In order to overcome issue with volume and structural change during cycling, controlled morphology, protective coatings, transition metal doping and void space engineering has been employed.

Good results were achieved by silicon based anode materials created using the synthesis of nanoparticles in clusters within an external shell coating, coupled with an internal void space within the external coating.[111] This void space ensured that the volume change of the nanoclusters during cycling has no effect on the size of the overall particle and the formation of the SEI on the external coating surface. This improved cycling retention of 97% capacity retention after 1,000 cycles and enables the materials to maintain conductivity.[111]

Selenium nanoparticles doped with cobalt onto the core shell. The nanoparticles enabled the conductivity of the material to increase making more redox sites accessible to Li^+ storage. This was then protected with a cobalt coating to prevent direct reaction with the electrolyte. This composite materials were made on a graphene support that allows the volume expansion to be tolerated during the lithiation/delithiation process without damaging the structure.[118] This combination provided capacity retention of almost 100% and capacities of 1615 mAh/g after 100 cycles compared to <400 mAh/g of the standard oxide material.[118]

1.5.1.2 Cathode Material Enhancements

Typical issues of Cathode materials are that they suffer from slow Li^+ diffusion kinetics that limit their power densities[128]

1.5.1.2.1. Layered

When materials such as $LiCoO_2$ have been doped with metal elements such as Al and Cr [129,130] this has enabled them to overcome the issues of thermal and chemical stability and limited capacity but with limited success. Mixed metal oxides such as $LiNiMnCoO_2$ have improved

their capacity by synthesising a material that is macroporous, producing a material with capacities as high as 234 $mAh.g^{-1}$, whilst also maintaining its cycling stability at elevated temperatures up to 50 °C.[131] However the best performance improvement for layered oxide materials has been achieved from the use of protective coatings. $LiNi_{0.68}Co_{0.18}Mn_{0.18}O_2$ was synthesised creating a Ni rich core possessing the stoichiometry of $LiNi_{0.8}Co_{0.1}Mn_{0.1}O_2$ combined with a more Ni deficient outer layer comprising of $LiNi_{0.46}Co_{0.23}Mn_{0.31}O_2$.[132] This combination of different compositions within the same material provides two advantages. First a higher energy density as the Ni rich core allows more higher Li^+ extraction, secondly the higher Mn and Co content in the outer layer increases the stability of the material.[132] The overall effect is to provide higher energy and power density without structural deterioration during cycling to provide increase capacity and better cycle life.

1.5.1.2.1. Phosphates

A frequent strategy to overcome the poor electron conductivity of olivine phosphates such as $LiFePO_4$ has been the reduction in particle size. This increases the rate of the lithiation/delithiation process and as a result the capability of the material to perform at higher discharge rates.[133,134] However this has a detrimental effect on Li^+ diffusion properties throughout the material. The increased surface area also causes an increase in the number of side reactions with the electrolyte leading to increasing in SEI, which in turn leads to greater capacity fading. These issues are currently being investigated with development of modern electrode materials. $LiFePO_4$ has also been doped by replacing Fe or Li with other elements (e.g. La, Ce, Nd, Mn, Co, Ni)[135] which increases the rate performance of the material due to improved conductivity.

The addition of conductive coatings such as carbon and conducting polymers produces greatly improved conductivity[136] (up to 10^7 times)[137] improving the rate performance without the increase in SEI formation seen with increase in surface area. This combination of Ni and carbon doping enabled the materials to produce capacities of 150 and 130 mAh/g at discharge rates of 10 and 15 C respectively and were able to maintain nearly 100% of their initial capacity after 1000s of cycles, demonstrating outstanding rate performance.[137] This approach has its own disadvantages, by adding additives and coatings to the material this both increases the weight and volume without adding additional capacity. Although the rate performance improves, the energy density per gram or volume will decrease. Therefore it is necessary to compensate

between improvements in conductivity with loss of energy density caused by the increase in weight.

1.5.2. Next Generation Electrode Materials

1.5.2.1. Nanoarray Used for Li^+ Batteries

1.5.2.1.1. Fundamentals of Nanoarrays as Li^+ Battery Electrodes:

One of the essential properties of Li^+ battery materials is that of volumetric and gravimetric capacity, both of which are essential when it comes to the design of storage materials for commercial applications. The main objective is to maximise the amount of energy per unit of weight area and volume, with the objective being to store as much Li^+ as possible per unit.

The development of conversion materials such as vanadium, iron, nickel and mixed transition metal oxides means there is an opportunity to create materials with significantly larger capacities due to their ability to store multiple Li^+ ions per transition metal (Equation 1.6).

As mentioned in section 1.2.3.1, nanostructuring has been used to increase surface area and improve charge transfer reaction kinetics. However these materials still suffer a number of problems such as high intrinsic impedance caused by poor electron conductivity between adjacent particles,[116] and irreversible capacity loss due to the decomposition of electrolytes and SEI formation on the surface of the material. These factors continue to hinder the materials preventing them from fully optimising their Li^+ storage potential.

One strong candidate, for future high performance Li^+ battery materials, is self-supported metal oxide nanoarrays.[104] These remove the need for electrodes materials to be made into pastes and coated onto copper or aluminium foil. The traditional paste based method of making electrodes provides less electrical contact between the active material and the current collector which increases resistance due to grain boundaries between adjacent particles. In self-supported nanoarrays the active material is grown directly onto the current collector therefore removing the need for electrically insulating binders. They have adverse effects on conductivity and Li^+ storage capacity as well as the need for conducting additives such as carbon black which decrease the energy density of the material.[138,139] Typically conducting substrates are made from Ti, Al, Ni or Cu and are used to support the synthesis of the nanoarrays. The choice of current collector is typically dependent upon the conditions required to synthesis the

nanoarrays, e.g. Ti substrates are suitable for acidic synthesis conditions, whereas Cu and Ni are well suited to alkaline conditions.[140]

There are a number of advantages offered by the use of self-supported nanoarrays for use as Li^+ battery electrode materials.

1) **Nanostructure active materials:** Synthesising nanoscale materials reduces the Li^+ diffusion path length and increases the active surface area of the material. This provides increased interaction between the electrolyte and the active material through increased access leading to improved rate capabilities due to accelerated transfer kinetics and increased access for Li^+ storage sites.[141,142]

2) **Direct pathways for electron transport**: Due to the materials being grown directly on the current collector substrate, the interface resistance at the grain boundaries is significantly reduced. This gives the material highly efficient electron transport throughout the entire structure improving the conductivity[143,144] and enables fast electron release and capture to and from the external circuit thus producing higher performance at higher discharge rates.

3) **Tuneable free space within the nanoarrays:** Due to the issued caused by volume expansion, typically observed during the discharge process of conversion materials, the ability to introduce enough free space is highly desirable. Introducing void space to the interior of these nanoarrays in addition to interspaces between the arrays themselves provides a useful way to ease the strain caused to the material by large volume change.[145] This avoids damage to the structure and the separation of the active material from the substrate and enhances cycling stability and capacity retention.

4) **Controlled morphology:** The performance of a material is largely dependent on the structural morphology.[47] The synthesis of self-supported nanoarrays is easily modified by adjusting one of a number of different synthesis parameters. Nanoarrays can be functionalised or fine tuned to encourage features such as porosity or using multiple oxides synthesised through multiple stages of reactions to give the desired properties and characteristics.[140]

5) **Tuneable structure of conducting substrates:** In addition to the nanoarrays it is also possible to fine tune the substrate current collector.[140] For example self-supported nanoarrays on a 2D substrate exhibit excellent capacity retention at high discharge rates however they suffer from restricted capacity due to the limited loading that is obtainable on a 2D substrate. The use of 3D porous substrates offer a higher loading densities and increased electrolyte access.

In the next section different types of nanoarrays are discussed and their effect on the Li^+ storage properties of the material.

1.5.2.1.2. 1D and 2D Nanoarray Materials

1D nanoarrays are obtained by the synthesis of structures such as nanowires, nanotubes and nanorods on a planar substrate. One example of a 1D nanoarrays as a Li^+ battery anode is SnO_2. These materials showed significantly increased capacity performance compared to the standard nanorods and nanoparticles.[146] The capacity retention was superior producing a capacity of 580 mAh/g after 100 cycles compared to previously reported samples that achieved only 300 mAh/g after 30 cycles at 0.1 C. The nanoarray also produced a capacity of 350 mAh/g at a discharge rate of 5 C after cycling, displaying excellent rate capability.[146] Another example of a 1D nanoarray as an effective electrode material is CuO which is usually subjected to a large volume change of approximately 170% during cycling.[147] By synthesising a nanorods on a Cu substrate it was able to achieve a capacities of 650 and 450 mAh/g after 100 cycles at discharge rates of 0.5 C and 2 C respectively exhibiting improved rate capability and high capacity retention.[147]

One example of a nanoarray used as a Li^+ battery cathode material is that of V_2O_5 nanobelts.[148] By synthesising these nanoarrays on a titanium substrate, the materials were able to achieve capacities of 255 mAh/g after 50 cycles a significant capacity retention within the material given the theoretical capacity is 294 mAh/g.[148]

1.5.2.1.3. Hierarchical Nanoarrays.

Hierarchical nanoarrays consist of materials structures made using the assembly from the combination of various reactions using different building blocks to produce different structural features and functionalities at different sizes and scales.[149] Using this strategy it is possible to construct a material with all the desired features through careful selection of different reactions. For example small particles with a large surface area could first be synthesised, followed subsequently by the introduction of additional features such as porosity and void space.[140] These additional features enable increased advantages over the synthesis of simple nanoarrays.

The anode material Co_3O_4 typically suffers from large irreversible capacity loss and large volume expansion reducing its capacity retention performance.[126] By synthesising nanowire arrays grown on Ti foil, combined later with reactions that introduced porosity to further enhance the performance of the materials. This was demonstrated by its capacity values of 700 and mAh/g after 20 cycles at discharge rates of 1 C compared to the non supported nanowires producing only 350 mAh/g.[150] The nanoarrays also showed rate capabilities of 450 and 240 mAh/g after 20 cycles at discharge rates of 20 and 50 C respectively, demonstrating excellent rate performance.[150]

The cathode material $LiCoO_2$ was synthesised into nanoarrays by first synthesising nanoarrays of Co_3O_4, followed by lithiation and subsequent treatment to produce $LiCoO_2$ arrays with high porosity and were capable of retaining 90% of their initial capacity after 50 cycles compared to the non supported nanowires retaining only 68%.[151] In addition the material was able to produce capacities of 103 mAh/g after cycling at a discharge rate of 10 C, showing significant improvement in its capacity retention and rate performance.[151]

1.5.2.1.4. Heterostructured Nanoarrays

One of the remaining issues with hierarchical nanoarrays are that, despite successful synthesis strategies, the materials still suffer from the same weaknesses inherited from the metal oxide from which they are made.[152] For this reason the use of heterostructured nanoarrays offers the ability to utilise a combination of different materials, combining metal oxides and other materials such as carbon. They supplement each other to further improve their performance while also reducing the weaknesses offered by a single material.

One example of an effective heterostructured nanoarray is the use of $Li_4Ti_5O_{12}$ in conjunction with MnO_2.[153] $Li_4Ti_5O_{12}$ undergoes negligible volume expansion and possesses excellent cycling performance but possesses a low capacity,[154] whereas MnO_2 possesses high capacity and poor cycling performance.[155] By combining the two together, it creates a material with improved performance. TiO_2 nanoarrays were created as the scaffold, these were coated with carbon before nanoparticles of MnO_2 were attached onto the surface of the nanoarrays. This material possessed considerable improved capacity increasing from 130 to 170 and 352 mAh/g for TiO_2 only, carbon coated TiO_2 and the TiO_2/MnO_2 composite materials respectively.[153] The composite material was able to achieve a capacity of 130 mAh/g after 100 cycles at 30 C.

1.5.2.1.5. 3D Nanoarrays

The development of nanoarrays has since progressed to the creation of 3D porous substrates upon which to synthesis the metal oxide nanoarrays. This offers further advantages to the previously mentioned 1D and 2D nanoarrays. The main advantage of 3D substrates over 2D is the ability to accommodate a higher loading of active material onto the substrate.[140] This gives the opportunity to increase the gravimetric and volumetric capacity of the material. The porosity of these 3D substrates offers more pathways for the electrolyte to penetrate through the material increasing the number of reactions taking place at the surface of the nanoarrays and improving the Li^+ diffusion kinetics.

One example of an effective 3D nannoary is hetrostructured CuO/CoO nanoarrays were created by Zhang *et al.*[156] by first creating $Cu(OH)_2$ nanorods prepaired on copper foam. Co nanosheets where fabricated uniformly on top of the nanorods and these were finally calcined to form CuO/CoO core shell heterostructured nanoarrays. These materials were able to achieve capacities of 1364 mAh/g after completing 50 cycles at lower discharge rates of 100 mA/g.[156]At high discharge currents of 4 A/g the material was able to achieve 342 mAh/g displaying excellent rate capability compared to standard arterials.

1.5.2.2. Li^+ Rich Layered Oxides

The development of Li^+ rich layered oxides for high voltage cathodes is another strategy currently being investigated for future higher performance Li^+ batteries. These Li^+ rich metal oxide materials such as Li_2MnO_3 are of high interest because they can store up to two Li^+ per

transition metal centre. The capacities achieved are significantly higher (> 270 mAh/g) with the working potentials situated at high potential values(2.4-4.7 V).[157] The combination of both properties means these materials possess superior energy densities to that of traditional layered materials which typically possess either a high capacity or a high working potential. On example of a Li^+ rich layered oxide $Li(Li_{0.2}Mn_{0.54}Ni_{0.13}Co_{0.13})O_2$ was able to achieve capacities as high as 295 mAh/g.[158] The only difference is the presence of Li^+ in the transition metal layer.

The excess Li^+ is situated within the transition metal layers and causes the ordering of cations present within the structure. Crystalline structures of these materials are of a rock salt structure with symmetry similar to layered oxide materials. This ordering causes the creation of a new phase within the material.[15] However when the materials are charged beyond 4.4 V, Li^+ is extracted from the transition metal layer, damaging the cation ordering within the structure. For this reason best cycling performance is achieved when the cut off potential does not exceed 4.4 V. In addition the materials suffer from poor kinetics and large voltage decay during cycling.

Research using these battery materials is ongoing in order to determine methods of maximising the performance of such materials.

1.6 High Surface Area Mesoporous Transition Metal Oxides

1.6.1 Background and Development

The first synthesis of highly ordered mesoporous oxides was carried out in the 1990's in research carried out by Mobil into the formation of porous aluminosilicate structures such as MCM 41[159] and MCM 48.[160] These structures were synthesised using what is referred to as a liquid crystal templating mechanism shown in Scheme 1.1, sometimes referred to as a surfactant templating mechanism. This uses surfactants which bond with the precursors before forming micelles, the micelles are left to arrange into hexagonal rods and then calcined enabling the silanol groups to form silicon-oxygen bridges into shape around the cylindrical micelles.[159] During the calcination process the organic template becomes oxidised and is removed to leave a hollow crystalline structure with well-formed pores, a narrow distribution

of pore sizes and very high surface areas (≥1500 m^2/g). These kinds of structures can be used as templates themselves making them very desirable.

.

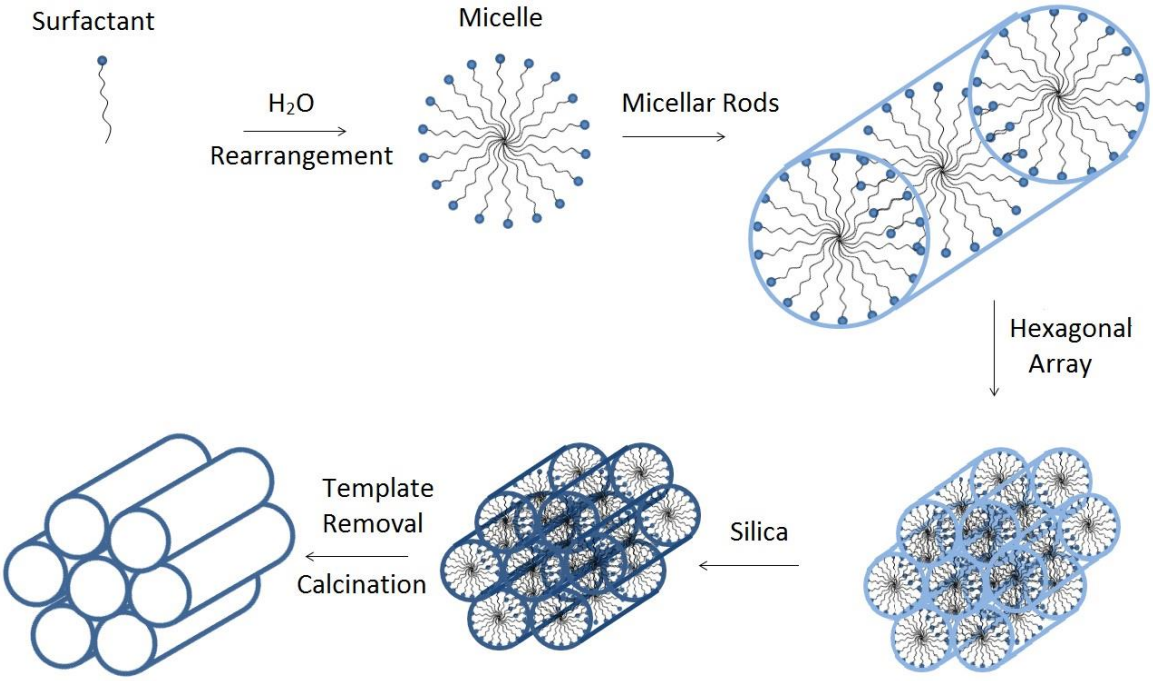

Scheme 1.1: Scheme depicting the synthesis procedure of MCM-41 [161]

Once these materials had been successfully synthesised, changes were made to the templates and it was discovered that the materials can be tailored to give specific pore sizes (between 1 nm-10µm)[162] and different structures depending on the synthesis conditions used.

Once the development of these mesoporous silica had been completed, the focus moved towards the development of similar materials using transition metal oxides. The advantages offered by the variable oxidation states offered by the transition metals as well as their interesting optical and electronic properties. Transition metals would allow for all types of redox and catalytic applications. Antonelli and Ying in 1996 made the first high surface area mesoporous oxide that was stable after template removal.[163] Previously materials made from tungsten and lead oxides were unstable and lost their structure once the template was removed. After the synthesis of niobium oxide this was proceeded by high surface area mesoporous oxides made using Ti, Ta, Mo and Zr.[163–167]

These materials could not be calcined similar to those of mesoporous silica because heating above certain temperatures caused the materials to lose their mesostructure. Once the synthesis mixture is aged to a peak temperature, the template is removed by the addition of organic acids and ample washings with methanol dissolve and wash out the template. The final material is a highly porous amorphous transition metal oxide with very high surface area (>1000 m^2/g). The manganese oxide material synthesised was the first material of its this kind to show semiconducting properties, as all other materials are insulating due to the amorphous nature of the pore walls.[9]

Over the years various investigations have been carried out with these materials in order to fully optimise their potential in a variety of different applications.

1.6.2 Applications in Photocatalysis

There has been a considerable amount of interest in the use of mesoporous transition metal oxides for use in the capture of various gasses (e.g. CO_2).[168] This is needed to lower the effects of combustion of the greenhouse effect and the degradation of hazardous compounds such as organic pollutants into less harmful compounds via catalysis and the conversion of water into hydrogen and oxygen. These types of reactions occur as a product of photocatalysis. Initially mesoporous Nb and Ti oxides were investigated due to the possible advantages offered by the photoactivity, high surface areas and controlled porosity of the material. Titanium based materials are cheaper and show effective electron hole separation causing it to be an effective electron acceptor.[169] The results of studying these amorphous materials showed the materials possessed lower photoactivity than seen in the lower surface area crystalline materials. This was attributed to the amorphous pore walls resulting in low conductivity. Therefore for the materials to be an effective photocatalyst, the conductivity of the walls must first be improved in order to increase the photocatalytic activity.

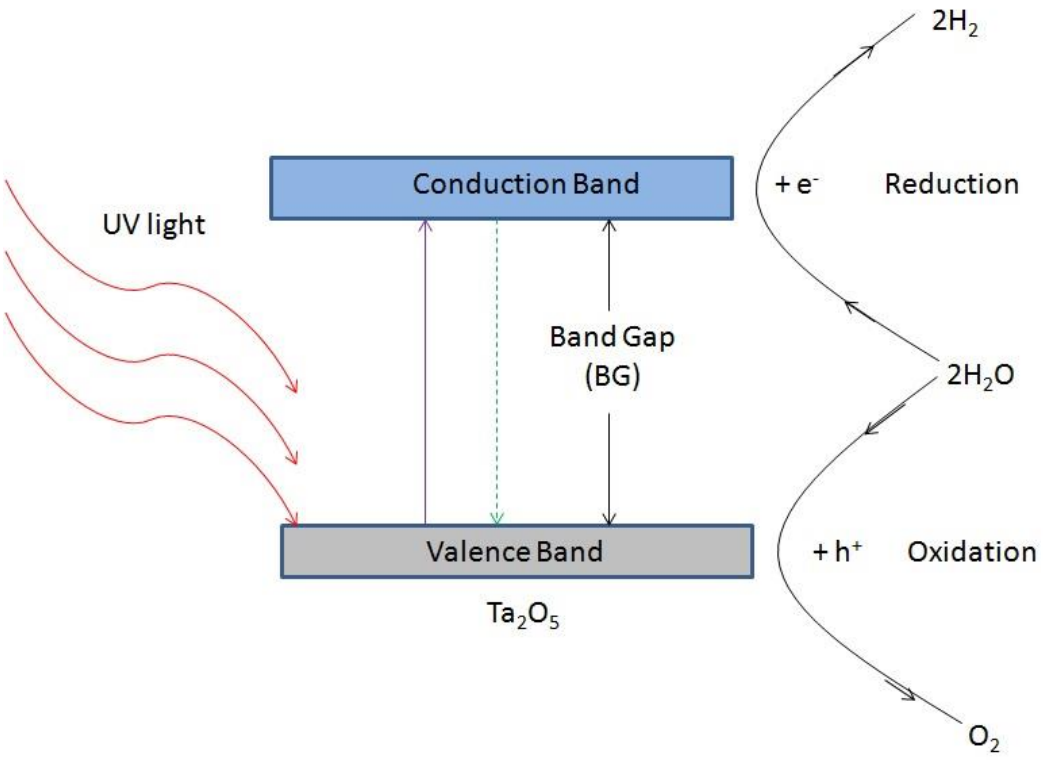

Figure 1.13: Diagram depicting the photocatalytic process of water degradation using Ta_2O_5

Tantalum oxide has been investigated for its potential applications as a photocatalyst. Domen *et al*.[170] initially reported the effectiveness of mesoporous tantalum oxide as a photocatalyst in the UV region of the spectrum for the purposes of producing H_2 and O_2 from water (Figure 1.13).[171] Once loaded with a NiO catalyst the high surface area materials were found to increase the photoactivity of tantalum oxide and were more effective catalysts than those materials made using other methods. This improved performance was attributed to the higher NiO loading achieved in the high surface area porous host.[171] In addition, the ability for tantalum materials to undergo calcinations without complete loss of pore structure increases performance as the walls are able to become more crystalline due to the higher thermal stability of the tantalum materials.

1.6.3 Alkali Reduced Nb Ti and Ta oxides

The electron acceptor properties mesoporous oxides were investigated using alkali reduction reactions.[172] The insertion of the electrons into the structure could not be carried out until the formation of the mesostructure, as these air sensitive reagents Na naphthalene would affect the formation of the mesostructure during synthesis. The Na naphthalene was successfully able to

reduce Nb^{5+} to Nb^{4+} whilst retaining its mesostructure. This procedure was repeated with Ti and Ta materials giving stability ratings of Ta>Nb>>Ti.[9] The band gap for materials is usually between 3.3-4 eV with a gap of 2.1 eV between the impurity band and the conduction band (Figure 1.14).

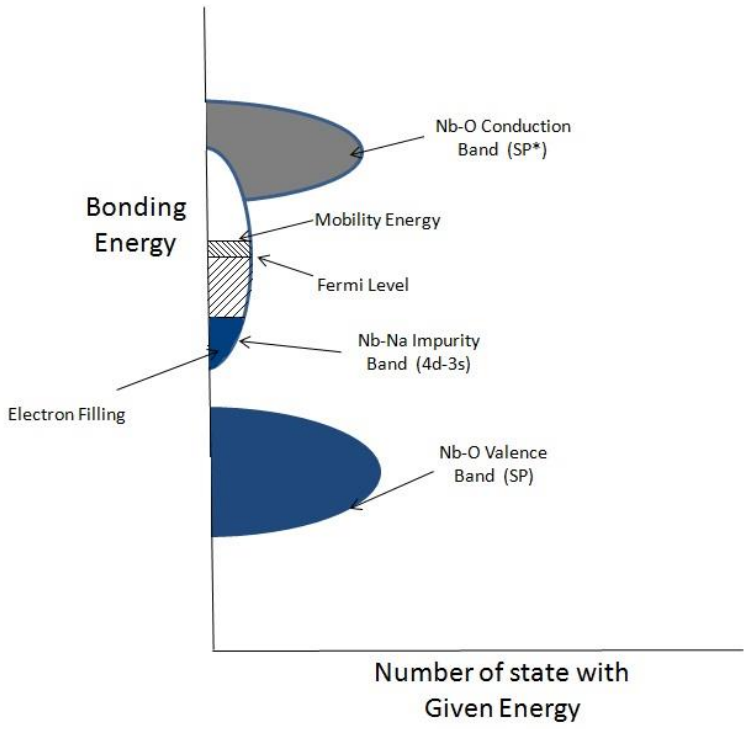

Figure 1.14: Energy level diagram of electronic structure of high surface area amorphous oxides

The ability of these material to maintain their mesostructure during reduction was attributed to the flexibility of their amorphous nature, which can better accommodate the changes that accompany reduction,[169] compared to rigid crystalline materials which usually lose their porosity upon reduction. The Nb and Ta materials are insulating with the Ti material showing to be a low conducting semiconductor. This is attributed to Anderson's localisation [9] which is caused by the absence of diffusion in a disordered medium leading to the localisation of electrons. It was proposed that the Ti material undergoes a transition to a more continuous electronic state that allows it to act as a semiconductor.

1.6.4 Superparamagnetic Cobaltocene Composites

When mesoporous Nb oxide reacted with certain concentrations of cobaltocene (Figure 1.15)

(>1:2 ratio of Co:Nb) the results produced a noticeable effect on the magnetic properties of the material, switching from paramagnetic to super paramagnetic[173] whereas the bulk Nb_2O_5 does not react with the cobaltocene. This super paramagnetic behaviour is usually only seen in nano sized granules, and was attributed to the broad distribution of D bands present in the amorphous walls. This broad distribution of D bands enables the reaction with the cobaltocene, not typically possible with crystalline materials with a narrower band structure. This superparamagnetic behaviour was not observed in other reduced mesoporous oxides therefore the property was attributed to the presence of the cobaltocene. Changes to pore size of the host material made little difference to the properties however other metals did not absorb as much cobaltocene and failed to show super paramagnetic properties.

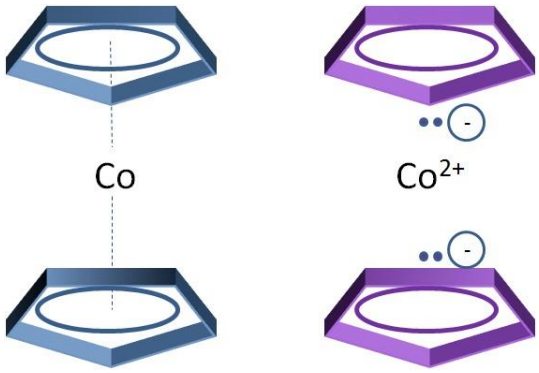

Figure 1.15: Neutral and Cationic Cobaltocene structures

1.6.5 Oganometallic Molecular Wires (Benzene$_2$Cr)

Research progressed to the use of organometallic molecular wires to create a conducting pathway throughout the pores of the material.[10,174] This was achieved by synthesising composites of mesoporous oxides with a number of early transition metal complexes. When these were reacted with mesoporous Nb oxide the composites were able to maintain their porosity, with both the neutral and cationic forms present within the walls of the structure, producing conductivities up to 10^{-5} $S.cm^{-2}$.[10] This is a result of the hole produced by the reduction of the molecular wire behaving as the charge carrier enabling electron transport down the chain by a hopping mechanism. It is necessary for both forms to be present for the molecular wires to be conducting with the cationic forms acting as a charge carrier. However having only cationic forms present reduces performance due to electrostatic repulsion and pure uncharged bis(benzene) chromium, as seen in Figure 1.16, is insulating as there are no charge carriers.

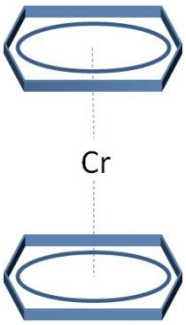

Figure 1.16: Structure of bis (benzene) chromium

In this investigation the doping levels were significantly lower at less than 0.01 equivalents compared to the 0.5 seen in cobaltocene composites. The disadvantage to this approach is the air sensitivity of the molecular wires because when left in air the compounds become insulating.

1.6.6 1D Alkali Fulleride Wires

Building on the success achieved using Na naphthalene, composites were made using alkali fullerides to make conducting nanowires and explore the effect of 1D intercalation on superconductive and metallic states of the fullerides. This produced high conducting composites of mesoporous Nb oxides with KC60 nanowires within the pores.[11,175] The oxidation state of the fulleride is essential to the electron conducting properties of the nanowires. When reacting the fullerides with the transition metal oxides alone, the oxidation state of the fulleride was 0.5 and produced conductivities as high as 10^{-3} S.cm^{-2}.[176] The effect of oxidation state was further investigated by increasing reduction using Na naphthalene. These results showed two conductivity maxima at oxidations states of 2.6 and 4.1 with peak conductivity at 10^{-1} Scm^{-2}.[177] Changes made to pore size and choice of transition metal had little effect on performance. However EPR studies showed a much higher number of states present near the Fermi level, typically seen for materials approaching metallic behaviour.

The next section will discuss aspects surrounding electron conductivity focusing on how it works and a variety of methods used to improve it.

1.7 Electron Conductivity

Electron conductivity is an essential characteristic of battery materials and determines the rate at which electrons can be transported throughout the material.

1.7.1 Band Theory

Band theory is the best means to explain electron conductivity in solid materials with the electronic structure of the materials split into different bands determined by the bonding orbitals used within the material. The arrangements of these bands and the degree to which the electrons fill them are essential and determine the electron conductivity of the material. Electrons can only exist within these orbitals which combine together to make up energy bands. Depending upon the structural arrangements and degree of crystallinity, the orbitals exist at a variety of different energy levels and arrangements. According to Hund's rules the electrons must distribute throughout the orbitals from the lowest energy upwards until they are filled as much as possible with minimal repulsion between electrons. This distribution of electrons in the bands determines the properties of the material. The distribution of these orbitals determines the order in which they are filled.

The outermost orbitals with electrons furthest from the nucleus of the atoms affect the properties of the material, and are split into two different bands.

(1) **The valance band:** The band that contains electrons within the highest occupied molecular orbital's (HOMO) of the materials. These are typically the orbitals containing the electrons involved in bonding.

(2) **The conduction band:** The band that contains the lowest unoccupied molecular orbital's (LUMO), the orbitals situated above and closest to the valance band.

In order for electrons to be transported throughout the material an electron must be able to be promoted from the valance band to the conduction band, examples of orbital fillings for different types of materials are shown in Figure 1.17. Materials that possess a completely filled or empty band are non-conducting (insulators (a)). These materials require energy to move the electron from the HOMU to the LUMO, presenting an energy barrier which prevents electron

transport through the material. When a material possesses bands that are partially filled, it is easy to promote an electron from the HOMO to the LUMO. Such materials possess metallic conductivity (b) as there is little or no energy barrier required to make the transition.

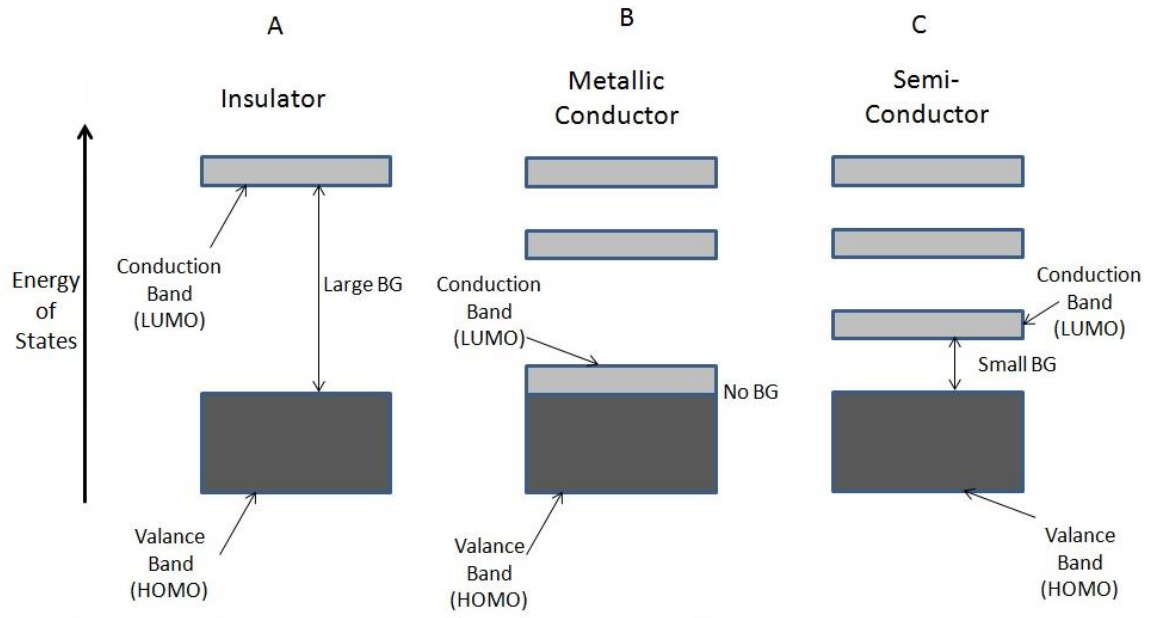

Figure 1.17: Demonstration of differnt band filling in materials that are (a) insulators, (b) metallic and (c) semiconductors

When a band is filled completely but the conduction band is only slightly higher in energy, it possesses a small band gap. Thermal or photoexcitation produces improvements in conductivity as the required energy is externally supplied. These types of materials and referred to as semiconductors (c).[178]

1.7.2 Methods of Improving Conductivity

It is possible to improve the electron conductivity of materials by doping them with other elements or compounds within the materials which will raise the HOMO or lower the LUMO, thus reducing the band gap and enabling the transport of electrons throughout the structure.

The dopants used to improve the conductivity of such materials can be separated into electron donor dopant (N-doping) or electron acceptor dopants (P-doping).

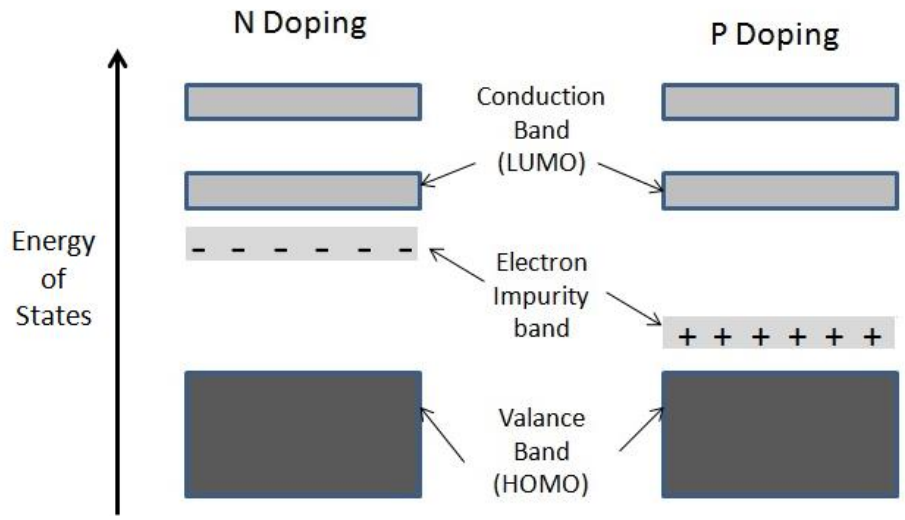

Figure 1.18: Molecular orbital band structure for N-type and P-type doped semiconductors

P-Doping, referred to as acceptor doped semiconductors, is the process of doping a material with an electron deficient species. For example doping silicon based semiconductor with boron or a metal oxide with nitrogen. This type of doping produces a material with less valence electrons than the initial semiconductor. This creates electron holes above the valance band (Figure 1.18) which produces a series of shifts in electrons from neighbouring atoms to fill the holes enabling movement of charge thought the structure. The presence of such holes acting as charge carriers.[179]

N-Doping, referred to as donor doping, is the exact opposite, this process is where the host material being doped with an electron rich species contains more valance electrons than the initial semiconductor, for example doping Si with phosphorous. In this type of doping, the presence of more valance electrons leads to weakly bonded electrons situated just below the conduction band (Figure 1.18). This allows the charges to migrate more easily through the material with these extra valance electrons acting as charge carriers.[179]

Another doping approach to produce improved conductivity is to use dopants which are of the same group but possess larger molecular orbitals, for example doping oxides with atoms of sulfur or selenium. The reasoning for this strategy is that the presence of larger orbitals will increase the orbital overlap. The atomic radius of atoms increases going down the group, producing orbitals with a greater overlap and are situated at higher energies. This increase in overlap between neighbouring orbitals leads to either a reduction in the band gap (Figure 1.19)

between the conduction band and the valance or it can eventually lead to overlap between the two bands,[180] leading to a partially filled band and metallic conductivity.

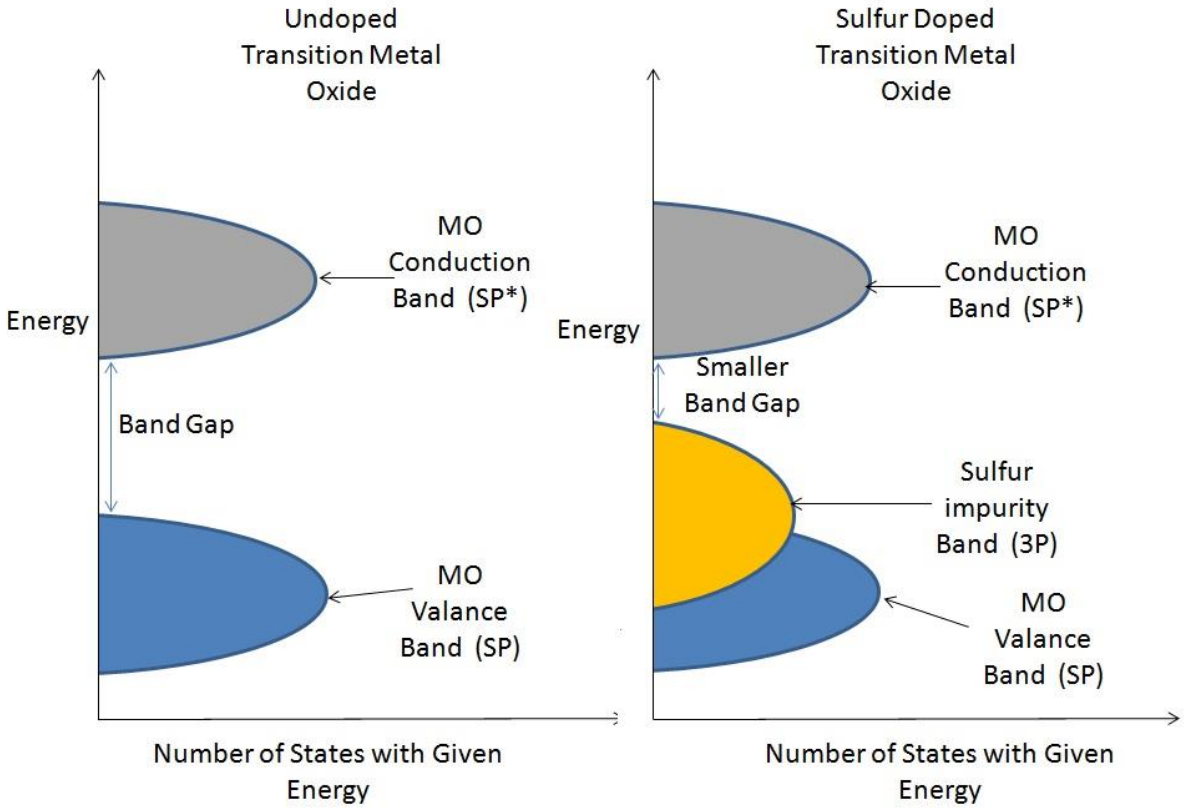

Figure 1.19: Electronic structure energy level diagram of undoped and doped transition metal oxides

The final approach to doping is to make a complex or composite material where the host material is either coated or impregnated with an electron conducting material such as carbon black, electron conducting polymers[181] or molecular wires.[10] These materials provide a conduction pathway into and throughout the host material which passively improves the conductivity as opposed to the active methods discussed previously.

1.8 Electron Conjugated Polymers.

1.8.1 General Background

Electron conducting polymers have existed for a number of years and are commonly used to improve the conductivity of materials. When first investigated, these organic polymers were found to be insulating so were not initially used as electron conductive additives.[182] Over time it was discovered that by doping the polymers during synthesis, they become highly conducting due to the loosely bound charges located along the polymers chain acting as charge carriers.

When these loosely bound charge carriers are coupled with a long chain of conjugated bonds, this enables fast and easy charge transport. The properties of these materials were not investigated in great depth until the 1970's. There was a difficulty synthesising the polymers due largely to the insolubility in both organic and aqueous solvents, making solution based synthesis procedures very difficult to develop. It is for this reason that in more recent studies, branched versions of the polymers are now used in order to encourage solubility in solvents for ease of processing. Due to the combination of high conductivity, mechanical stability and environmentally friendly nature of the polymers they remain useful and are still regularly used in research.[183] Common applications for conducting polymers include capacitor electrodes, battery membrane separators, protection against corrosion and electromagnetic interference imaging.[184,185] There are a number of different methods of synthesising conducting polymers with the two main techniques including chemical oxidation using an oxidant[186] and electrochemical polymerisation by sweeping the voltage of an electrode in a solution of monomer within a set potential window.[187] This initiates a polymerisation reaction of the monomer to form a polymer with dopants incorporated from the electrolyte. The electrochemical polymerisation synthesis route consistently produced higher conducting polymers than the chemical oxidation route. The route utilising a chemical oxidant leads to an easier and simpler synthesis procedure.

1.8.2 Polythiophene

1.8.2.1 Background

Polythiophene is an electron conducting polymer made up of monomer units that are a heterocyclic five membered conjugated ring containing a sulfur atom as can be seen in Figure 1.20.

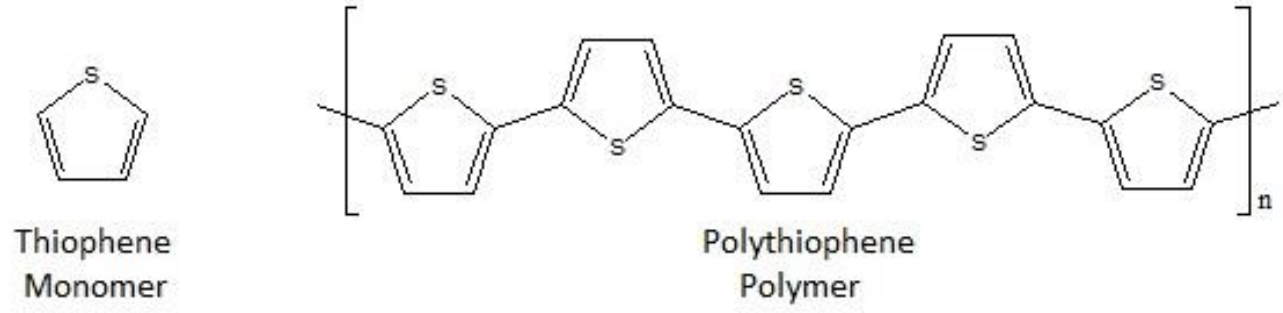

Figure 1.20: Units of thiophene and polythiophene

Despite being highly conjugated, the polymer chain is not conducting under standard conditions therefore it requires doping to become conducting. This is achieved in a similar way to that of a P/ N doped semiconductor, by adding or removing electrons to the structure creating charge carriers.

These polymers require significantly higher levels of doping than in typical semiconductors to become conducting. For example, typical semiconductors are doped at ≤1%, whereas polythiophene or other similar polymers must be doped at levels of 20-40% to reach their maximum conductivity.[188]

In the synthesis of polythiophene, the monomer is oxidised either electrochemically or chemically removing an electron from the structure which produces a cationic radical electron deficient species. This leads to the formation of a polymer and the incorporation of counter ions to balance the charges created during the synthesis, this type of doping is similar to that of a P-doped semiconductor. A variety of different doping ions have been used, typically those of the halogens such as Br^-, I^- and Cl^- have produced some of the best conductivities. The dopants are not always highly stable with the counter ions present on the polymer backbone evaporating off of the structure slowly over time causing the polymer to become more insulating.

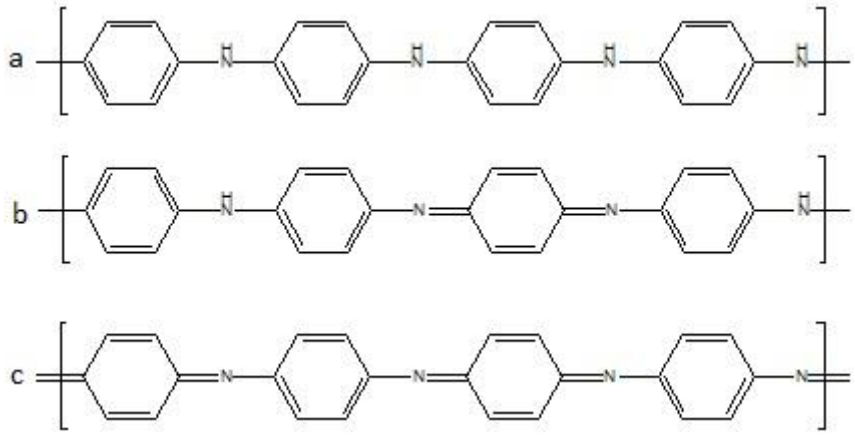

Figure 1.21: Different forms of Polyaniline (a) leucoemeraldine, (b) emeraldine and (c) pernigraniline

Polythiophene and its sister compounds such as polypyrrole are popular because of their ease of synthesis compared to other conducting polymers such as polyaniline. Polyaniline can exist in one of the three possible states depending upon the extent of oxidation within the polymer chains (Figure 1.21). Leucoemeraldine (fully reduced form), emeraldine (half oxidised half

reduced) and pernigraniline (fully oxidised) with only the emeraldine form having conducting properties. [189] Polythiophene and its sister compounds only produce one form of polymer which is always conducting when successfully doped. They are more popular because the synthesis procedure is more simplistic.

1.8.2.2 Synthesis

There are two different ways of synthesising depending upon the form which the polymer is required. Firstly, electrochemical polymerisation forms highly conducting forms of the polymer present as a film that forms on the surface of the anode.[190] Secondly, the polymer can be synthesised chemically using an oxidising agent to produce a powder.[191]

There is a difficulty when carrying out synthesis because the thiophene is very insoluble in both aqueous and organic solvents with it only truly being soluble in solutions of arsenic tri and pentafluorides.[192] This has resulted in research that uses branched forms of thiophene or thiophene monomers containing functional groups to help solubility in a variety of solvents.[193]

In the electrochemical synthesis procedure, a film is formed on the surface of the anode as the potential of the cell causes the monomers to become oxidised at the surface. This oxidation causes the incorporation of counter ions from the electrolyte to balance out the charges caused by the oxidation of the polymer. The key factors that influence the synthesis of conducting polymers is this procedure are:

(1) Solvent used

(2) Current density during synthesis

(3) Choice of electrolyte and counter ions present

(4) Presence of water in the electrolyte

(5) Monomer concentration

(6) Temperature

The functional groups present on the monomer affects the potential which the thiophene units will become oxidised at the anode. The presence of electron donors on the monomer lowers the potential needed to oxidise the monomer where electron acceptor groups will increase the oxidation potential. The standard thiophene monomer will usually oxidise at a value of around 1.5 V vs a saturated calomel electrode (SCE).[194]

The chemical synthesis of thiophene was first deliberately synthesised in the early 1990's using 2,5 dibromothiophene with a nickel based catalyst.[195,196] This produced high molecular weight polythiophenes with good conducting properties. To be successful, the synthesis needed to be carried out under very strict conditions using low temperatures with no trace of water. Methods were developed using a less expensive oxidant ($FeCl_3$) in organic solvents such as chloroform and carbon tetrachloride.[197,198] This synthesis required less strict conditions to be successful therefore simplifying the procedure, this is the most common chemical method used to make polythiophene based materials. The use of $FeCl_3$ as an oxidising agent has one disadvantage, upon completion of the polymerisation reaction there is some retention of the oxidising agent within the material, therefore there is a slight contamination of the sample in addition to extra weight being added.[199]

During the developments of the synthesis it was discovered that to achieve polymers with the best conductivity, initially lower ratios of catalyst to monomer concentration must be used. This helps the regioselectivity of the polymerisation process along with allowing the polymerisation process to take place at a slower rate.[200] Lower reaction temperatures produce longer polymer chains with higher conductivity in place of shorter chain lower conducting polymer made using higher temperatures.[201]

Polythiophene has a number of applications within research, however none have been commercialised. The most popular application is for the use in electronic devices due to its beneficial electron conducting properties. The applications can be split into two categories,

(1) Static applications: The intrinsic properties of the material are used such as additives to improve electron conductivity of materials.[202]

(2) Dynamic applications: The application of an external stimulus such as applying a potential to change the optical properties of the material.[203]

1.8.3. Polypyrrole

1.8.3.1 Background

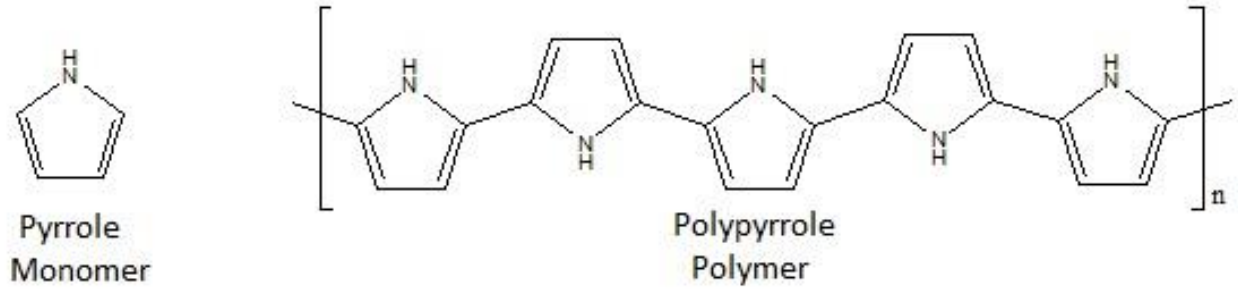

Figure 1.22: Units of pyrrole and polypyrrole

Polypyrrole is conjugated hetrocyclic five membered ring, similar to polythiophene, with the exception that instead of sulfur it contains a nitrogen atom (Figure 1.22).

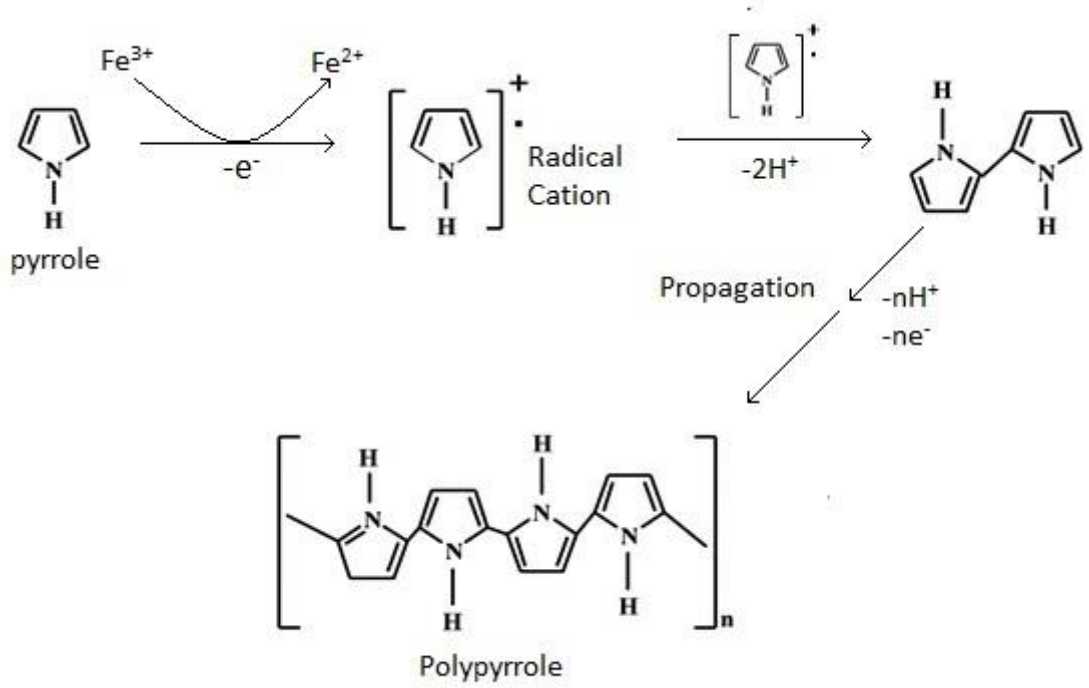

Scheme 1.2: Mechanism for the synthesis of polypyrrole.[204]

The mechanism for the synthesis of polypyrrole is the same used to synthesise polythiophene, with the initial monomer being oxidised to form a radical cation, before combining with other radical cations to become reduced over time this forms a long chain polymer. The mechanism for the chemical synthesis method using the iron based catalyst $FeCl_3$ can be seen in Scheme 1.2.

Polypyrrole is one of the most highly represented electron conducting polymers in current research due to the fact that it is

(1) One of the easiest polymers to synthesise and is able to be synthesised in the presence of water unlike that of polythiophene.[205]

(2) It is one of the most stable electron conducting polymers whilst still possessing high electron conductivities.[206]

The undoped form of polypyrrole appears yellow in colour. Depending upon the thickness of the polymer and as the amount of doping increases it becomes dark blue or black in colour as it begins to absorb more light. This indicates that there are changes to the optical properties of the material.

The best solvents used when carrying out chemical based synthesis method is either that of methanol or water with the oxidant $FeCl_3$.[207] As with thiophene based polymers, the polymer is formed when doped with counter ions. In chemical synthesis methods these are provided by the oxidant and in electrochemical methods these are provided by the electrolyte. The method used to make the polymer again depends on what form of polymer is required, either electrochemical producing films or chemical methods producing powders. The best oxidant to monomer ratio for pyrrole materials is stated to be 2.25 and 2.33 which produces maximum conductivity.[208]

Polypyrrole unlike its sister compounds is able to be synthesised directly using UV light due to its optical properties. However polymers such as polythiophene have been able to be synthesised using photosensitisors such as iodinium salts.[209] Pyrrole is able to by photopolymerised with the aid of enzyme based catalysts.[210] This synthetic route can be used

to create composites other than films without the need for an external oxidising agent preventing the issues caused by the retention of $FeCl_3$ post-polymer synthesis.

As with most electron conducting polymers, many of its applications involve uses in electronic devices or as an electron conducting additive in the form of composite materials. Due to its optical properties polypyrrole is commonly used in optical devices such as solar cells,[211] in addition to these, there have been other applications investigated in modern research such as a catalytic support for a fuel cell,[212,213] gas sensors,[214–217] and even a support for drug delivery systems,[13,218] demonstrating the potential polypyrrole shows in more than just electronic devices.

1.8.4 Polarons

The previous section discussed band theory on electron conductivity which can be used demonstrate how electron conducting polymers possess high electron conductivity.

The charge transport is carried out with the use of polarons and bipolarons. Polarons are radical cations distributed over a number of monomer units acting as charge carriers and bipolarons are diradical dications. The degree of doping within the polymer determines both how many polarons are present and whether they are present as polarons or bipolarons. In a similar way to that of electrons in a P-doped semiconductor, the delocalised charges enables electrons to move down the conjugated chain of the polymer and the formation of each polaron is balanced by respective counter ions such as I^- and Cl^-.[182,207]

Once the polymer has been synthesised the backbone begins to undergo oxidative doping. The oxidation of the polymer chain leads to the extraction of an electron producing a radical cation. This forms localised states within the gap between the conduction band and the valance band in the electronic structure (polypyrrole 0.5 eV from band edges).[207,219] Further doping leads to further removal of electrons forming bipolarons. The bipolarons electronic states are located further from the band edge than polarons (0.75 eV polypyrrole) but are closer to each other, reducing the band gaps and increasing the number of charge carriers and therefore improving electron conductivity. As doping continues, bands of bipolarons form which eventually mix to produce partially filled bands and enabling metallic conductivity.

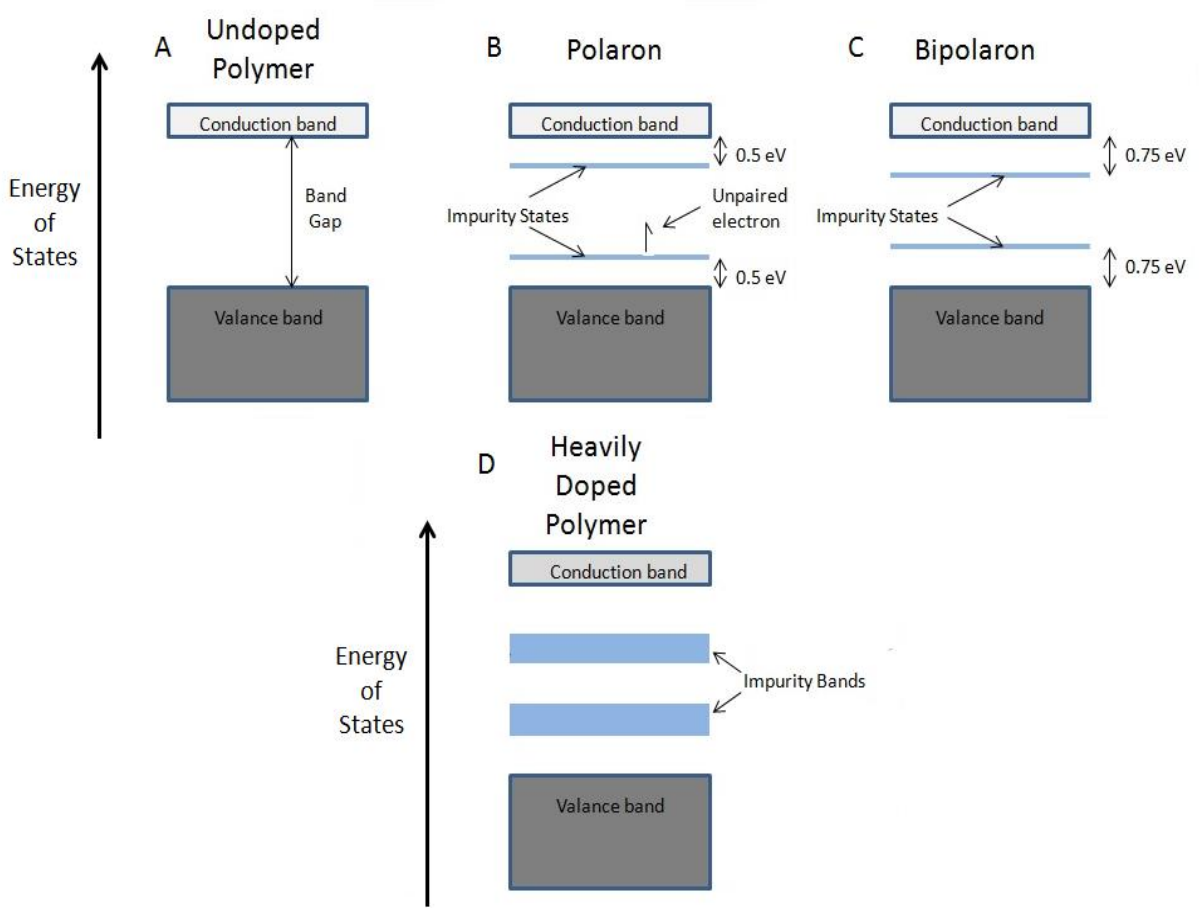

Figure 1.23: Electric struture bands for undopped electron conducting polymers, polarons, bipolarons and highly dopped electron conducting polmyers[219]

During the synthesis, the polymers become oxidised with an electron being removed from the structure. An example includes polythiophene and polypyrrole having an electron removed from the five membered carbon ring, forming a radical cation($C^{+\cdot}$).[207] The formation of the polaron leads to a change in the band structure of the material, this new radical forms a new states present within the band gap of the standard undoped polymer reducing the band gap (Figure 1.23). In pyrrole, the polaron states are situated 0.5 eV above and below the valance and conduction bands respectively. With increased doping and the formation of bipolarons these bands become closer in energy than those of polarons (pyrrole 0.75 eV from respective bands). With continuous increase in doping levels this leads to the formation of two new bands states above and below the standard bands of the polymer. This production of partially filled bands leads to metallic conductivity and explains their use as electron conducting additives.

1.9. Key Findings the Thesis

Chapter two shows the first assessment of high surface area mesoporous TiO_2 as a Li^+ battery electrode. In addition, it was the first attempt to create a composite of these materials using electron conducting polymers via a vapour diffusion method followed by oxidation using a chemical oxidising agent. The synthesis of an electron conducting composite using this vapour diffusion technique proved successful after confirmation by NMR and IR spectroscopy. The characterisation demonstrated partial retention of the high surface area and mesoporous nature of the initial hosts. The oxides were assessed using electrochemical methods to investigate their reversibility, Li^+ storage capacity, conductivity and the effect of different discharge rates on these properties. The composite materials were found to significantly improve in electron conductivity but at the cost of Li^+ storage capacity. This was attributed to the reduction in Li^+ transport through blocking of pores with excess polymer. The initial host material possessed the superior storage capacity however failed to retain much of its capacity over the course of 50 cycles.

In Chapter three the focus was on variation in synthesis conditions to observe the effects on the properties of the material in order to maximise electrochemical performance and retention of surface area within the material. The choice of polymer was changed from polythiophene to polypyrrole to simplify the synthesis procedure, with a variety of polymer loadings and using hosts of different pore sizes to investigate the effects of changing parameters. The results showed that Li^+ storage performance and conductivity increases up to a certain content of polymer (5%). However excess content did not produce significant improvement and reduced Li^+ storage performance by increasing the weight of the material and greatly reducing the surface area with only negligible increase in conductivity. This Chapter also assesses the effects of surface area on the initial capacity of the material and the pore sizes on the capacity retention. However the capacity retention was still not sufficient enough to be an effective battery material.

Chapter four investigates the use of a new strategy of using UV induced synthesis of a conducting composite of polypyrrole and mesoporous Ti and Ta oxides. The effects on the properties of the material were observed, The Li^+ storage performance increased and improvements were made to the long term stability through a direct reaction between the metal oxide host and that of the conducting polymer. The synthesis was successfully achieved and

confirmed by a full characterisation of the materials. This method produced significantly higher retention of surface area then the chemical based methods and produced similar improvements in conductivity to those seen using the chemical methods. The Li^+ storage capacity increased slightly higher than those achieved via chemical doping however capacity retention and conductivity were not significantly improved compared to that of the previous methods.

Chapter five investigates the use of sulfur donor agents to synthesis a reduced band gap semiconductors in the form of transition metal oxysulfides using a variety of temperatures and reagent quantities. This was achieved using the reagent HMDST with sulfur incorporation confirmed through materials characterisation. The conductivity was found to increase with reagent quantity and increasing temperature. However this produces a significant decrease in the surface area, and beyond the peak temperature the conductivity deteriorates. The increase in polymer content decreased the Li^+ storage capacity of the materials. The best performing materials were those produced using large amounts of reagent at lower reaction temperatures, this enabled reasonable Li^+ capacity values with high capacity retention, improvements on those achieved through conduction polymer doping methods. This synthesis strategy requires further work to improve it understanding and to optimise performance.

Chapter six investigates the use of non-stoichiometric vanadium hydride gels in application as a low weight energy storage material. After being characterised to confirm the synthesis of a mixed valency hydride gel, the materials were found to be amorphous in nature with a low surface area. The Li^+ storage capacity of the materials was found to be similar to that of bulk oxide equivalents; however the capacity retention was not sufficient for it to be a suitable Li battery electrode material. Finally it possessed an ability to be improved with development of the synthesis procedure.

Chapter 2 : TiO_2 – Thiophene Composites Using a Chemical Synthesis in Organic Solvents

2.1: Introduction

One method for the improving conductivity of a porous materials is the use of oxidatively robust electron conducting polymers confined within the pore structure.[155] Bein *et al.* synthesised polyaniline nanowires in the pores of mesoporous silica [221] using vapour diffusion of aniline into the pores followed by polymerisation *in situ* using a Copper catalyst. This improved the bulk conductivity of the MCM-41 by almost twenty fold.[221] While this method offers an attractive alternative to the air sensitive dopants used previously by our group, the use of different conducting polymers may be preferred because polyaniline exists in numerous oxidation states, of which only one form (emeraldine salt) is conducting.

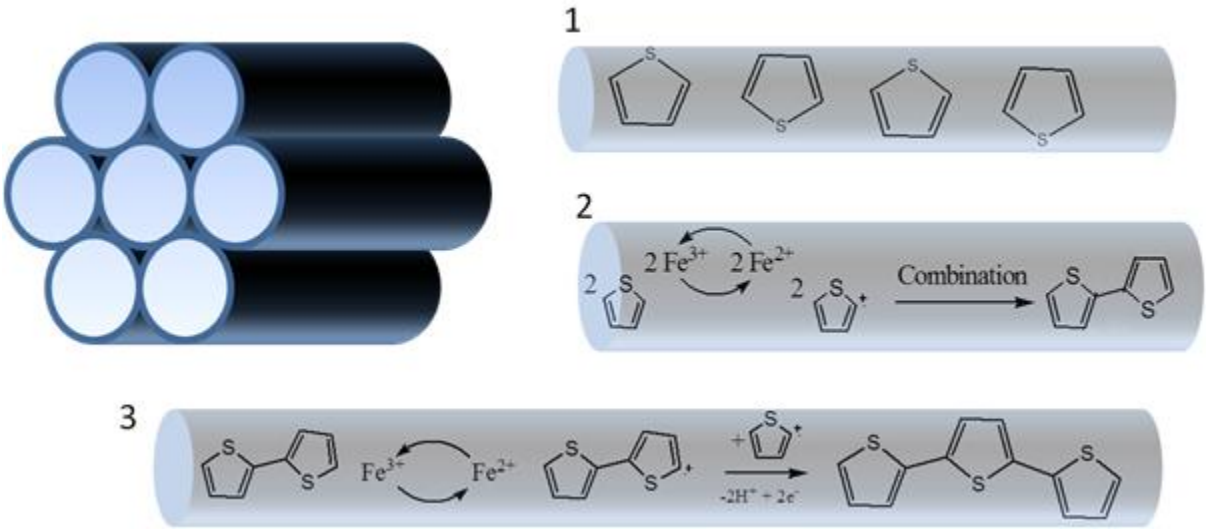

Scheme 2.1: (1) Thiophene monomer vapour loading into the pours by diffusion; (2) the initial polymerisation of monomers to dimers using $FeCl_3$ (3); the propagation of polymerisation in the pores to form longer chains of the conducting polymer.

Presented herein is a synthesis of mesoporous titanium oxide with conducting polythiophene nanowires in the pores, and the subsequent characterisation and electrochemical evaluations compared to pristine mesoporous titania. The synthetic method is summarised in Scheme 2.1 and uses the chemical oxidant $FeCl_3$ to polymerise the vapour-loaded thiophene monomers [222] and forms a conducting polymer inside the pores of the oxide host, whilst still maintaining a high surface area with respect to titanias made by other synthetic routes.[31,222]

2.2: Experimental

2.2.1 Synthesis Procedures and Research Methods

Mesoporous TiO_2 (m-TiO_2)

m-TiO_2 was prepared according to the published procedure using ligand assisted templating. Thus, a 3:1 mixture of titanium isopropoxide (90 g) and dodecylamine (18 g) was treated with water (600 mL) to form a white gel and this was left to stand for 24 hours. To this mixture three drops of 12 M HCl were added, and the resultant solution was stirred and left to stand for an additional 24 hours before being transferred to an oven at 40 °C. After 48 hours the temperature was increased to 60 °C and the sample was aged for another 48 hours. This was repeated at 80 °C, after which the solid was collected by filtration and placed into a dry sealed sample tube and returned to the oven at 100 °C for an additional 48 hours. The ageing process was completed at 120 °C for 48 hours and 140 °C for 48 hours, respectively. Removal of the organic template was accomplished by treatment of the material with *p*-toluenesulfonic acid (pTSA) (18 g) in methanol (600 mL) followed by stirring for 24 hours. Following filtration, the material was further treated with pTSA (23.4 g) and again stirred with methanol (600 mL) for 24 hours. This process was completed with three subsequent filtrations and washings with methanol with no further portions of pTSA.

Trimethylsilylchloride (TMS-Cl) Treatment of Mesoporous m-TiO_2 (m-TiO_2-TMS)

m-TiO_2 was treated with TMS-Cl as described in previous publications [9] to cap any hydroxyl groups to prevent them from interfering with the electrochemistry by reacting with Li^+. The mesoporous oxide was heated under vacuum at 200 °C overnight and then stirred with excess TMS-Cl in diethyl ether (50 mL) for 12 hours. Once completed the solid was filtered and washed with ether (4 x 50 mL) to remove residual TMS-Cl. This was then vacuum dried for 2 hours to remove the remaining solvent.

Composite Synthesis Procedure:

Polythiophene Composite (Sample TC1)

Polythiophene composites of m-TiO_2 were prepared by first loading m-TiO_2-TMS (ca. 300 mg) with thiophene monomer by vapour diffusion into the powder within a sealed container. This

was left for 24 hours to ensure that the pores were saturated with vapour to maximise thiophene uptake. The sample was then weighed to determine the thiophene content by difference. $FeCl_3$ with 4.0 equivalents respect to thiophene was then added to dichloromethane (5 mL) and this suspension stirred until a homogenous solution was achieved. To this solution the m-TiO_2-TMS loaded with thiophene was then added with stirring. This solution was then sealed and left to stir for 24 hours to complete the polymerisation. The resulting solid was then collected by filtration and washed (3 x160 mL) with dichloromethane, each time with stirring for 24 hours, to remove residual oxidant. After the washing stage the product was dried under vacuum for 3 hours to remove any remaining dichloromethane.

Polythiophene Composite (Sample TC2)

The sample TC2 was prepared by the same procedure as stated above however it was subjected to extra washing steps after the above procedure was completed. Thus, the sample was washed for an additional 72 hours in 150 mL of methanol to remove any remaining traces of residual oxidant. Once filtered the sample was washed with 0.2M HCl for 24 hours and then dried at room temperature under vacuum for 3 hours.

2.2.2 Characterisation Techniques:

Brunauer Emmett Teller (BET) surface area and pore size measurements were derived from nitrogen adsorption/desorption data collected on a Micromeritics ASAP 2020. FTIR spectroscopy was conducted on a Perkin Elmer FT-IR Spectrometer Spectrum RX1 using oven dried KBr discs and data treated on Spectrum 5.1 software. XRD was performed on Bruker D8 DAVINCI diffractometer with Cu Kα radiation (40 kV, 30 mA) source. The step size was 0.025°. The diffraction patterns were recorded in the 2θ range 1.0°–100° and the total counting time was 3 hours. TGA and DTA were carried out on a STA 449C analyser from Netzsch under a flow of dried air at 10.00 °C/min up to 650 °C. Argon was used to protect the balance section. HRSTEM was performed in a HD-2700 dedicated scanning transmission electron microscope (STEM) from Hitachi, with a cold field emitter equipped with a CEOS Cs corrector and operated at 200 kV. The powder samples were simply dry deposited onto a Cu grid covered with a carbon film (Quantifoil) having periodical holes with diameter of 1.2 micron. Observation was made in three different modes: bright field (BF), high angle annular dark field (HAADF) and secondary electron (SE).

2.2.3 Sold State MAS NMR

The ^{13}C cross polarisation, magic-angle-spinning nuclear magnetic resonance (CPMAS NMR) data of TC1, TC2 and polythiophene systems were acquired at ambient temperatures (~20 °C) using a Bruker DSX-400 spectrometer (B_0 = 9.4 T) operating at ^{1}H and ^{13}C Lamor frequencies of 398.8 and 100.3 MHz, respectively. These ^{13}C CPMAS data were acquired using a Bruker 4 mm double channel HX probe which achieved rotational frequencies of 10 kHz. The $^{1}H/^{13}C$ CPMAS NMR were performed with an initial ^{1}H $\pi/2$ pulse of 2.5 μ seconds duration, a $^{1}H/^{13}C$ Hartmann-Hahn contact period of 1 m second and a recycle delay of 3 seconds. TPPM decoupling with a 15° phase change between π pulses of 5 μ seconds duration was applied during acquisition. All ^{13}C chemical shifts were referenced against the primary standard of TMS via a secondary solid standard of alanine.

Corresponding ^{1}H single pulse MAS NMR data and ^{13}C spin echo MAS NMR data from the TC1, TC2 and polythiophene systems were acquired at ambient temperatures (~20 °C) using a Varian InfinityPlus-300 spectrometer (B_0 = 7.05 T) operating at ^{1}H and ^{13}C Larmor frequencies of 300.09 MHz and 75.46 MHz respectively. Both the ^{1}H MAS NMR and ^{13}C spin echo MAS NMR data were acquired using a Bruker 4 mm double channel HX probe which enabled rotational frequencies of 10 kHz to be implemented. The single pulse ^{1}H MAS NMR measurements used a ^{1}H $\pi/2$ excitation pulse of 3 μs and a recycle delay of 3 seconds. The ^{13}C spin echo MAS experiment used $\pi/2$ and π pulses of 2.5 and 5 μ seconds, respectively, a recycle delay was 3 seconds and TPPM decoupling with a 15° phase change between π pulses of 7 μ seconds was applied during acquisition. The ^{1}H and ^{13}C chemical shifts were referenced against the primary standard of TMS via a secondary solid standard of adamantane.

^{1}H and ^{13}C MAS NMR data for the thiophene monomer were acquired at ambient temperatures (~20 °C) using a Bruker AvanceIII-500 spectrometer (B_0 = 11.7 T) operating at the ^{1}H and ^{13}C Lamor frequencies of 500.1 and 125.8 MHz respectively. The ^{1}H NMR MAS spectrum was acquired using a Bruker 4 mm triple channel HXY probe in double channel mode. The ^{1}H data was obtained using a single pulse experiment which used a $\pi/2$ excitation pulse of 2.5μ seconds, a MAS frequency of 3 kHz and a recycle delay of 3 seconds. The corresponding ^{13}C data was obtained using the same singe pulse experiment but with a $\pi/2$ excitation pulse of 5 μ seconds duration and a recycle delay of 3 seconds. All ^{1}H and ^{13}C chemical shifts were referenced against the primary standard of TMS via a secondary solid standard of alanine.

2.2.4 Electrochemical Analysis

All electrochemical analysis was performed with a Princeton Applied Research VersaSTAT. Electrochemical performance of the synthesised electrode materials as a Li^+ battery electrode was assessed using a two electrode set up. The working electrodes (cathode) consisted of 80% active material, 10% super conducting carbon black, and 10% polyvinylidenefluoride (PVDF) by weight. The electrode paste was made by grinding the active material and carbon black to ensure a good mixture of the powders. The powders were then stirred with PVDF and *n*-methyl-2-pyrrolidinone (NMP) solvent until a homogenous paste was formed. The paste was spread onto copper foil (current collector) and the electrode was dried by first heating to 80 °C to bake off any excess NMP solvent before increasing the temperature to 120 °C overnight to allow the electrode material to bind with the current collector, followed by punching out a 15 mm electrode disk. The metal lithium disks used as the counter electrodes (anode) was also punched into a 15 mm disk. The electrolyte used in this investigation was 1.0 M $LiPF_6$ dissolved in ethylene carbonate (EC) and diethyl carbonate (DEC) solutions at a ratio of 1:1 by volume. All cells were constructed within an argon filled glove box to ensure minimal exposure to oxygen

CV measurements were carried out at a variety of sweep rates 0.5, 1, 2 and 5 mVs^{-1}. The potential windows used in all experiments were that of 1–3.4 V vs Li/Li^+ reference electrode. The initial potential of the scan was determined by the open circuit potential the cell (typically 2.3-2.6 V vs Li/Li^+) with the initial scan direction being directed in the reduction direction towards a lower potential limit (1 V vs Li/Li^+) with cycles being completed once the final reduction sweep reaches the starting potential of the cycling process.

Galvanostatic charge discharge analysis measurements were carried out a current density of 0.2 $mA.cm^{-2}$ and between the potential window of 1–3.4 V vs Li/Li^+ reference electrode. Weights of each electrode were taken prior to cell assembly to determine cathode mass and then used to calculate capacity relative to mAh/g according to the mass of the electrode.

2.2.5 Electrochemical Impedance Spectroscopy

Electron conductivity measurements were carried out using a two electrodes set-up. Silver wire of length 5 cm was used as the working and counter electrodes, these were attached to each

pellet via a silver two part conductive adhesive. Each pellet was made from a 300 mg of sample ground and formed into pellets using a 25 tonne manual hydraulic press. The flat sides of this pellet were coated using a silver two part conductive adhesive. Potentiostatic impedance spectra were recorded using a DC Bias of 0 V as the working and counter electrodes are the same electrochemical potential, measurements were taken between the frequency range of 10^6 and 10 Hz with amplitude of 100 mV using the VersaStudio software. For analysis the data was exported to ZView. The electronic conductivity of each pellet was determined using Equation (2.1) which has been derived from Equations (2.1.1) and (2.1.2).

Equation 2.1 $$\sigma = \frac{L}{RA}$$

Equation 2.1.1 $$\sigma = \frac{1}{\rho}$$

Equation 2.1.2 $$\rho = \frac{RA}{L}$$

σ is the conductivity (mS.cm^{-1}), L is the distance between the two wires (cm), A is the area covered by the silver adhesive in (cm^2) and R is the initial resistance (Ω) measured where the plot intercepts the x-axis on the Nyquist plot.

2.3: Results and Discussion:

2.3.1 Characterisation

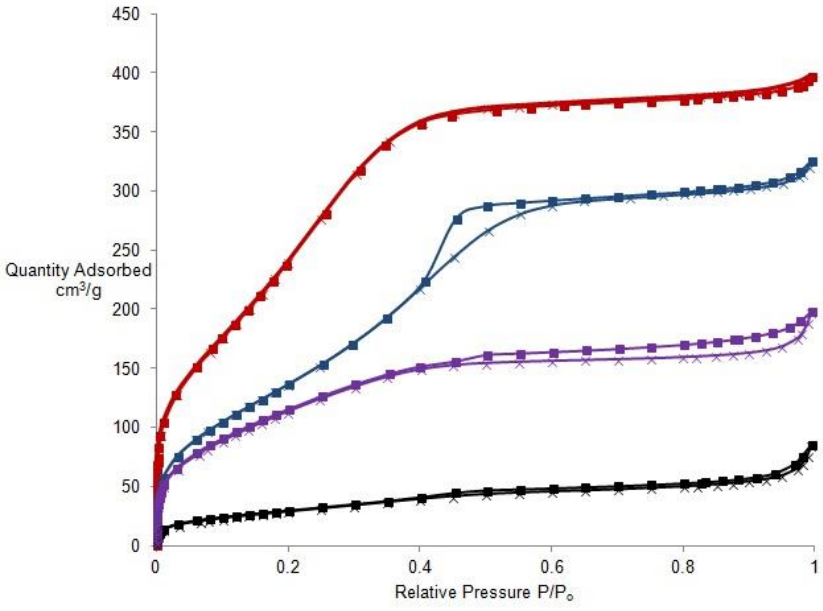

Figure 2.1: Nitrogen adsorption (crosses) and desorption (squares) for m-TiO_2 (red), m-TiO_2-TMS (blue), composite TC1 (black) and composite TC2 (purple).

Material	**BET Surface Area/ m^2/g**	**BJH Pore Volume / cm^3/g**
m-TiO_2	949	0.406
m-TiO_2 TMS	700	0.223
TC1	182	0.038
TC2	438	0.136

Table 2.1: Surface area and pore volume of m-TiO_2 and respective polythiophene composites.

The Brunauer Emmett Teller (BET) surface area data for the as-synthesised materials is reported in Table 2.1 while the nitrogen adsorption-desorption isotherms of all materials are shown in Figure 2.1. In all cases the samples are on the cusp between type I and IV isotherms, as expected for these materials with a ca. 20 Å pore size, confirming retention of the pore structure after polymer incorporation. m-TiO_2 possesses a surface area of 949 m^2/g, which decreases to 700 m^2/g when treated with TMS-Cl. Sample TC1 has a surface area of 182 m^2/g, while an additional wash in methanol followed by HCl (TC2) leads to a material with a surface area of 438 m^2/g, the increase in surface area possibly due to removal of residual iron salts and thiophene from the structure. There is a decrease in pore volume from 0.406 cm^3/g to 0.223 cm^3/g upon treatment with TMS-Cl and the final composites have pore volumes of 0.038 cm^3/g and 0.136 cm^3/g for samples TC1 and TC2, respectively. All pore volumes were calculated using desorption cumulative pore volume plots up to a maximum 40 Å pore size. The loss of surface area and pore volume upon thiophene impregnation indicates that the pores have been filled with thiophene polymer.

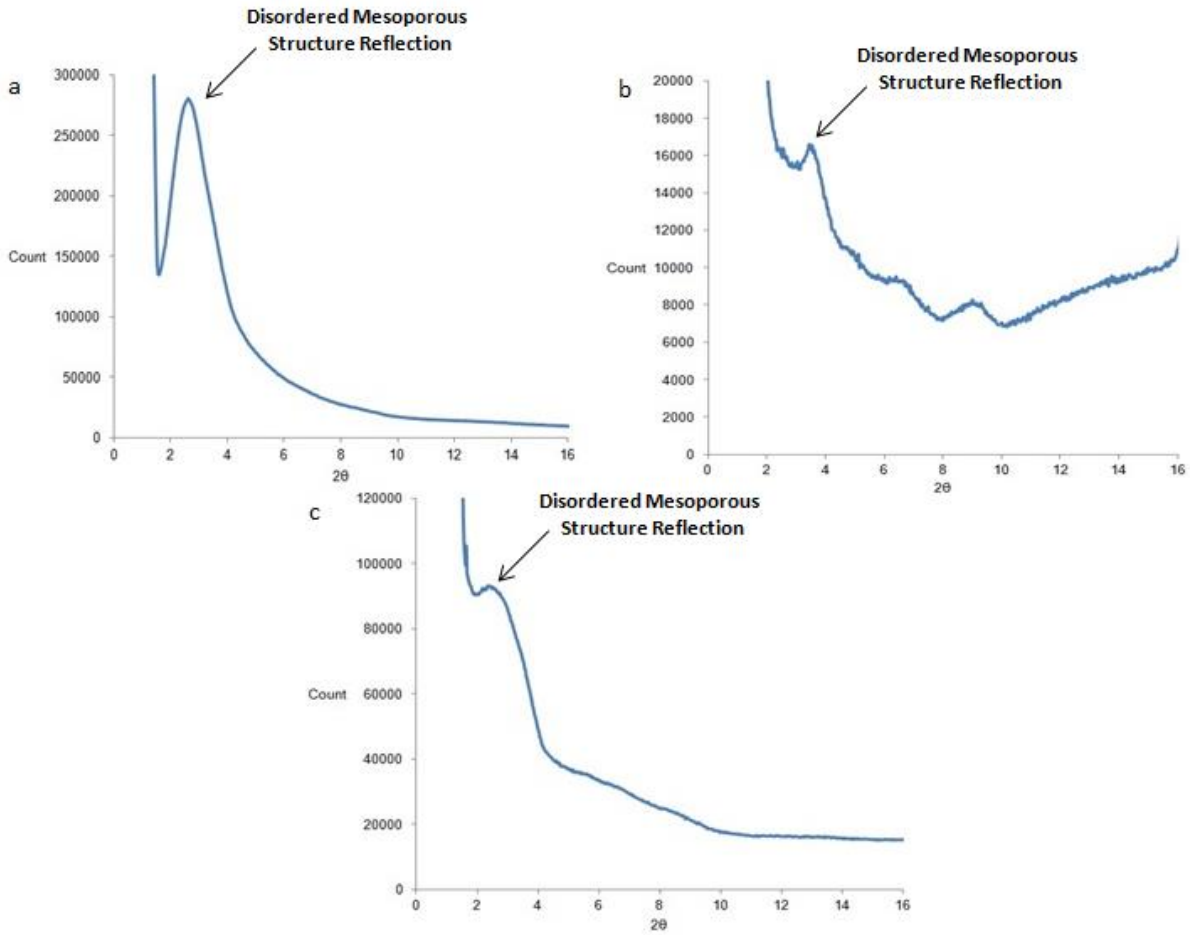

Figure 2.2: Powder X-ray diffraction pattern for (a) m-TiO_2, (b) TC1 and (c) TC2

Low angles of the powder X-ray Diffraction (PXRD) patterns for as synthesised m-TiO_2 and composites TC1 and TC2 are shown in Figure 2.2. Composite TC1 shows a very weak reflection around approximately 3° 2θ that is indicative of a disordered mesoporous structure and is typically observed for amine templated mesoporous oxides. These reflection confirms that the mesostructure of the material has been retained upon polymer incorporation.[7] In addition there are two broad reflections that are likely due to residual iron salts from residual oxidant because they disappear after further washing with TC2.

The hydrocarbon content was probed using thermogravimetric analysis (TGA) and differential thermal analysis (DTA), and the data shown in Figure 2.3. The TGA plot shows weight loss of 12% and 6% up to 200 °C for composites TC1 and TC2, respectively, which is attributed to water loss. At 500 °C there is a total weight loss of 48% and 16% for TC1 and TC2, respectively, for combustion of the polymer giving values of 36% and 10% polymer within the structure of composites TC1 and TC2 respectively. These are confirmed by the overlaying

DTA data, which show endothermic peaks up to 200 °C and exothermic peaks up to the optimum temperature of 650 °C. TC2 continues to lose weight up to 650 °C, possibly because the iron salts, which could act as a catalyst, are removed. These results are consistent with washing out of residual thiophene and/or polymer upon washing TC1 with methanol to give TC2.

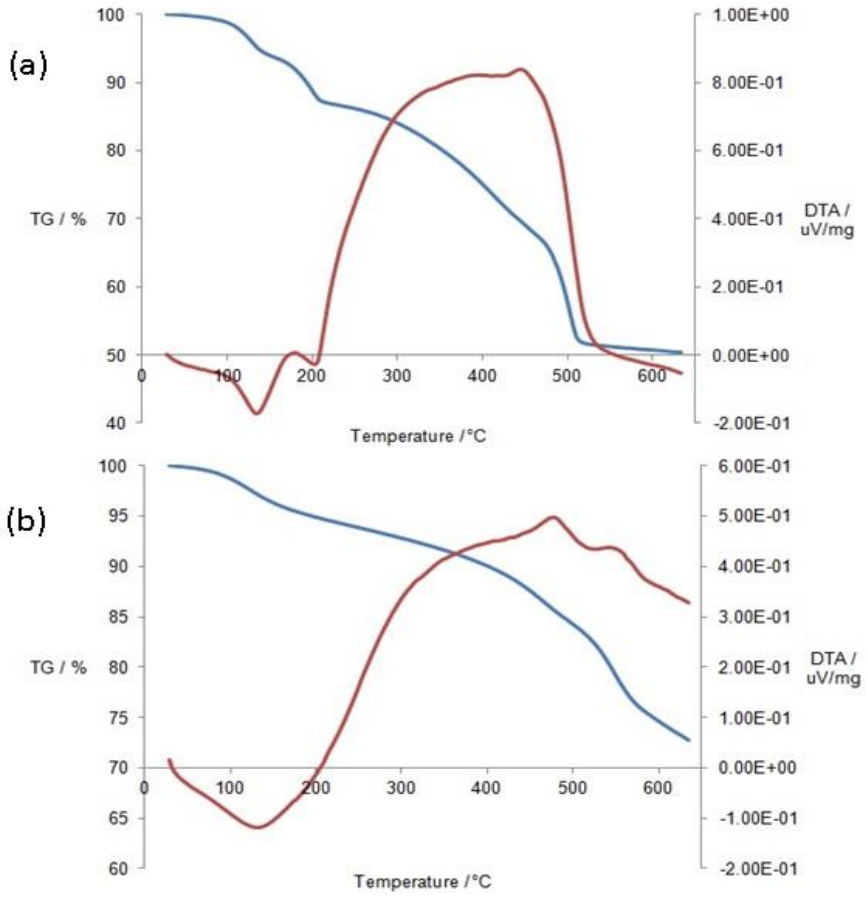

Figure 2.3: Thermogravimetric analysis (blue) and differential thermal analysis (red) plots for (a) TC1 and (b) TC2

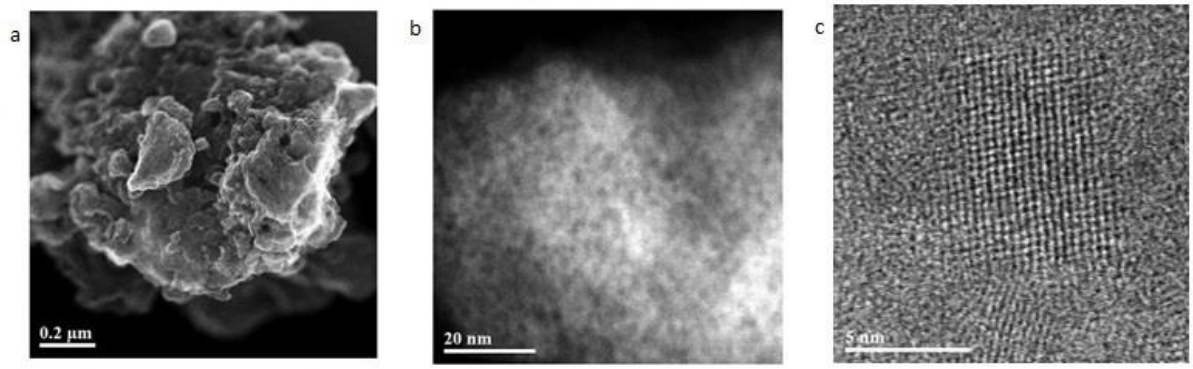

Figure 2.4: STEM Images of thiophene composite TC1 at (a) SE low magnification (80 kx), (b) HAADF higher magnification (1.3 Mx), and (c) BF highest magnification (7 Mx)

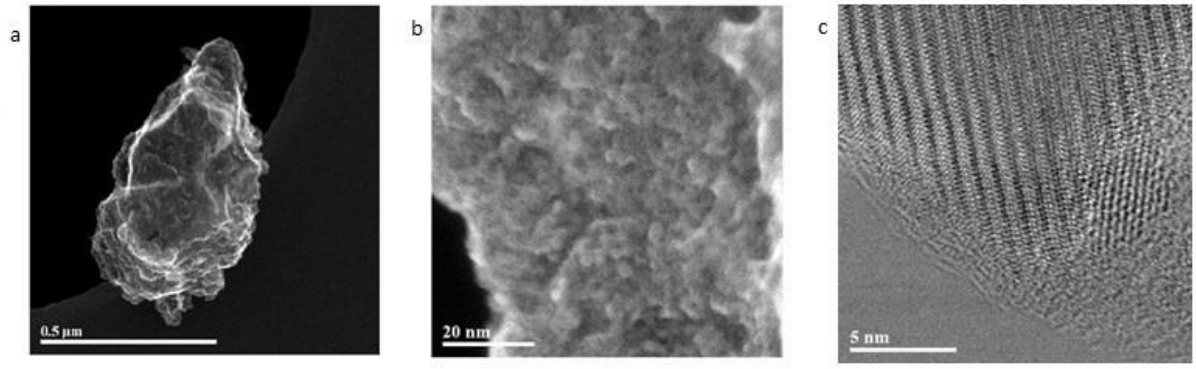

Figure 2.5: STEM Images of thiophene composite TC1 at (a) SE low magnification (100 kx), (b) SE higher magnification (1.3 Mx) and (c) BF highest magnification (6 Mx)

To further confirm the pore structure and lattice of the as synthesised materials scanning transmission electron microscopy (STEM) was performed. Using three levels of magnifications we are able to make a number of observations. The lowest magnification images of 200-500 nm, seen in Figures 2.4a and 2.5a, show that both composite powders exist as large clusters of smaller grains as have been seen previously with our materials.[223] The higher magnification seen in Figures 2.4b and 2.5b shows images at 20 nm allow us to observe that the mesoporous structure of the materials is retained with the incorporation of polymer content, which is in agreement with nitrogen adsorption data. The fact that there only a single phase present in these images confirms the incorporation of the polymer into the structure as opposed to two distinct phases or merely coating the material with polymer, which would have resulted in a dramatic loss of porosity.[224] The highest magnification images at 5nm in Figures 2.4c and 2.5c, allow us to observe the lattice structure. Here, the images show that the general structure remains predominantly amorphous, despite some crystalline structure being observed, in particular Figure 2.4c, which may represent either crystallisation within the walls of the TiO_2 pore walls, or traces of iron crystals from the oxidant used during the polymer synthesis.

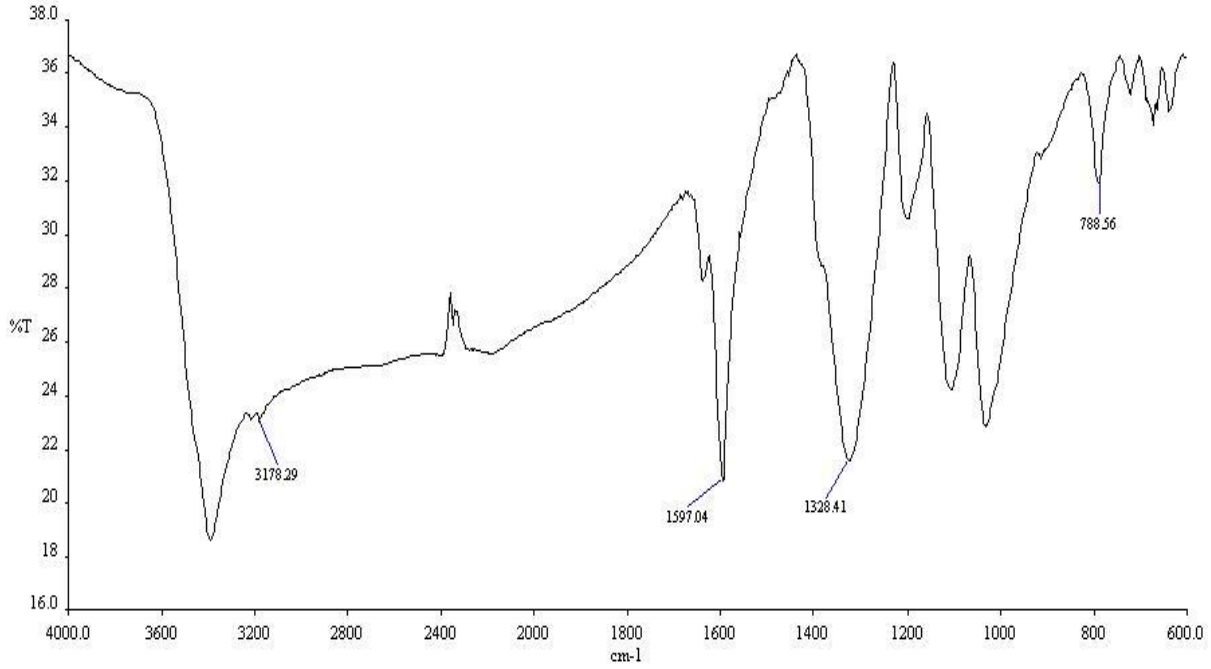

Figure 2.6: IR spectrum of composite TC1

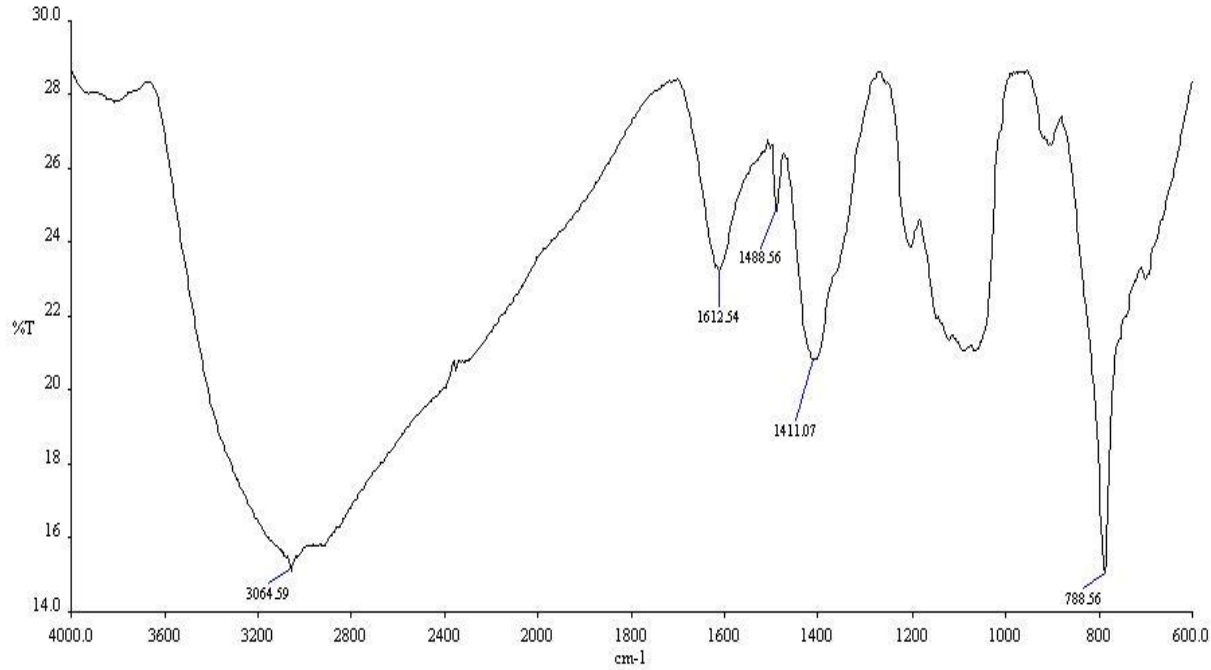

Figure 2.7: IR spectrum of composite TC2

The infrared (IR) spectra of the as-synthesised materials are shown in the appendices Figures 8.1 to 8.4 with the IR spectra for composite materials shown in Figure 2.6 and 2.7 for TC1 and TC2 respectively. The spectra of starting material, thiophene, and the final product, polythiophene, were recorded in Figures 8.1 and 8.2. Thiophene compounds are expected to show key diagnostic stretches at 3100 cm^{-1} (aromatic C-H stretches), 2900 cm^{-1} (aliphatic

C-H stretches), 1600 cm^{-1} (aromatic C=C stretches), 1400 cm^{-1} (C-C stretching vibrations)[225] and finally stretches at 800 cm^{-1} and 780 cm^{-1} (C–H aromatic bending vibrations).[226–228] These features are observed as expected in the thiophene and polythiophene spectra, with the polythiophene stretches situated at lower wavenumbers than those of the thiophene monomer due to increases in the degree of conjugation.[226] However, the presence of water in m-TiO_2 treated with TMS-Cl produces peaks at 3200 cm^{-1} and 1600 cm^{-1} and the subsequent treatment of this material with TMS-Cl produces new bands at 2900 cm^{-1} and 820 cm^{-1}. These IR features associated with the oxide substrate are thus expected to obscure the diagnostic bands for thiophene. In spite of this the spectrum of the m-TiO_2TMS loaded with thiophene vapour shows a significant increase in the size of the C-H stretch at 2900 cm^{-1} as well as the appearance of a small band at 1400 cm^{-1}, confirming the presence of thiophene in the sample. In the polymer composites TC1 and TC2 there are stretches at 1330 cm^{-1} and 1400 cm^{-1}, respectively. These bands confirm the incorporation of polythiophene in the sample because they were not present in the host material and are observed in the spectra of thiophene and polythiophene representing a C-C stretching vibration.

2.3.2. NMR Studies

Because only limited information on the nature of the thiophene species in the pores can be extracted from the IR, NMR studies were conducted. The ^{1}H and ^{13}C NMR spectra of the thiophene monomer in Figure 2.8.(a) and (b) shows resonances at ^{1}H δ: 6.36, 6.48 ppm and ^{13}C δ: 125.6, 127.5 ppm which are consistent with literature values.[227] The corresponding ^{1}H MAS NMR spectrum of polythiophene in Figure 2.9(c) contains numerous broad and overlapping resonances due to strong dipolar and paramagnetic interactions caused be the presence of residual iron oxidant. Previous ^{1}H solution NMR studies of polythiophene have reported two resonances 6.9 and 7.2 ppm;[228] in contrast, due to strong anisotropic dipolar and paramagnetic interactions in the solid state only a single broad resonance is observed at ~7 ppm is observed in this study which can be assigned to polythiophene. Additional upfield resonances at significantly lower chemical shifts (i.e. ^{1}H δ: ~0.5 - 1.0 ppm) are assigned to hydrogenated (reduced) thiophene moieties[228] which have been shown to form during polymerisation of the thiophene monomer.[229,230]

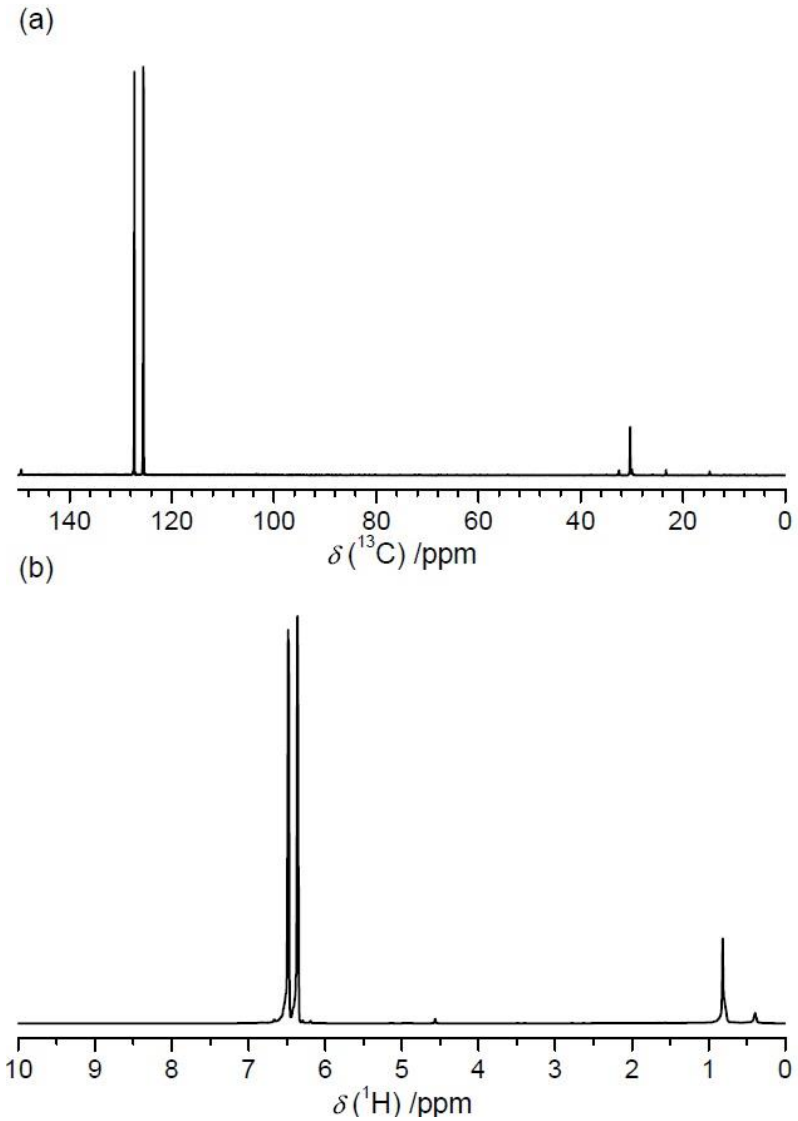

Figure 2.8: ^{1}H and ^{13}C one pulse MAS NMR data of thiophene monomer acquired at 11.7 T (ν_0 = 500.1 MHz and 125.8 MHz for ^{1}H and ^{13}C, respectively) using a Bruker 4 mm HXY probe spinning at 3 kHz.

The ^{13}C CPMAS and spin echo MAS NMR data from polythiophene (see Figure 2.10(c)) is consistent with these observations. The most intense resonances at ^{13}C δ: 125.7 and 135.7 ppm are consistent with polythiophene[227], while the additional broad resonances in the ^{13}C δ: 10-70 ppm range are consistent with the expected chemical shifts of the hydrogenated (reduced) thiophene moieties. From Figure 2.10(c) the resonances in the ^{13}C δ: 10-70 ppm range are more prominent and well resolved as the CPMAS experiment in comparison to those represented in the spin echo MAS experiment, however the CPMAS data will not be quantitative. This is due to the enhanced $^{1}H/^{13}C$ dipolar contact in regions where reduced electron motion will be manifest, and the spin echo MAS experimental data will thus be a quantitative measure of the carbon speciation.

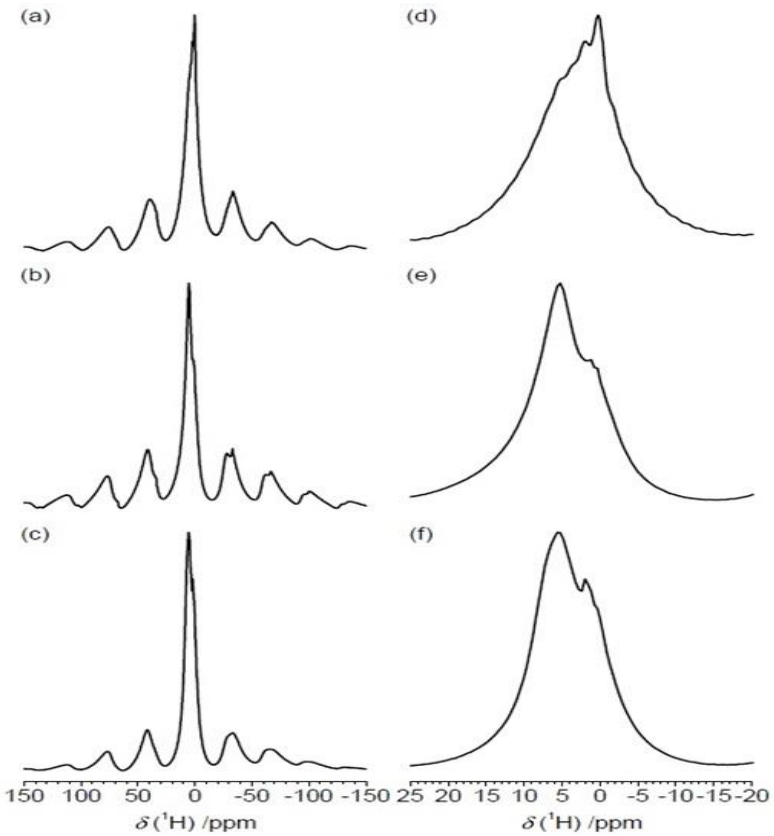

Figure 2.9: ^{1}H one pulse MAS NMR data of (a) & (d) TC1, (b) & (e) TC2, and (c) & (f) polythiophene, acquired at 7.05 T (ν_0 = 300.09 MHz) using a Bruker 4 mm HX probe spinning at 10 kHz.

From Figures 2.9(b)/(e) and 2.10(b) representing the ^{1}H single pulse MAS and ^{13}C CPMAS data from the polythiophene/m-TiO_2 system (TC2), it can be observed that the polythiophene component within this organic/inorganic composite is very similar to that of the original pure polythiophene. The main resonances at ^{13}C δ: ~125 and ~135 ppm are preserved and the signals in the ^{13}C δ: 10-70 ppm region are still evident although less intense, probably due to the reduced formation of hydrogenated (reduced) thiophene moieties on the m-TiO_2 surface in comparison to pure polythiophene. In addition, the ^{1}H MAS NMR data of Figures 2.9(b)/(e) and (c)/(f) are also very similar, suggesting that the hydrogen speciation in the supported and unsupported systems remains stable.

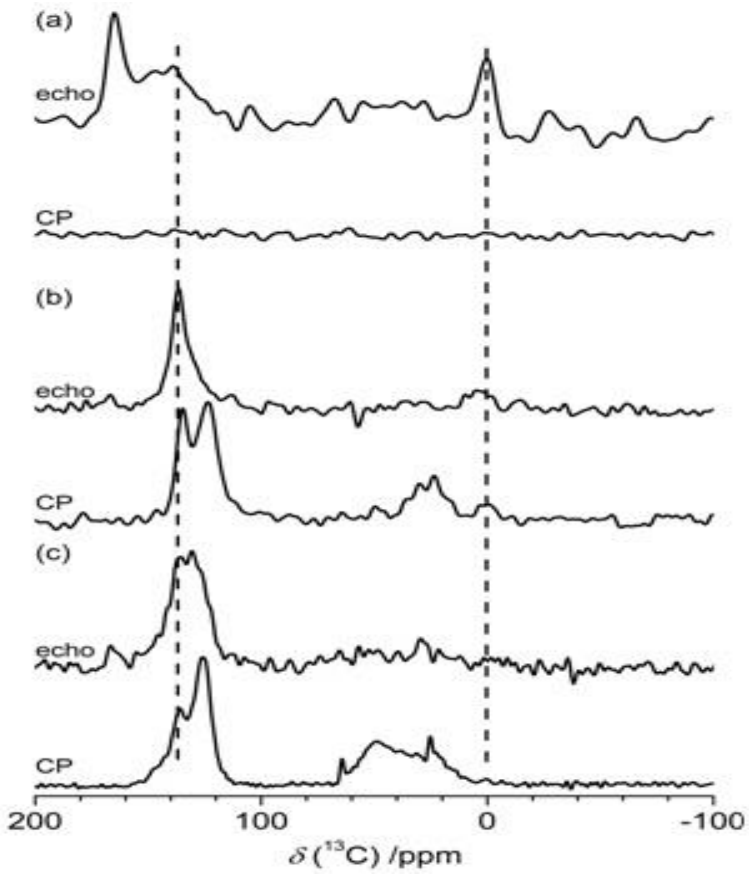

Figure 2.10: ^{13}C CPMAS and spin echo MAS NMR data of (a) TC1 (b) TC2 and (c) polythiophene, acquired at 9.40 T (ν0 = at 100.3 MHz) using a Bruker 4 mm HX probe spinning at 10 kHz.

However, the ^{1}H single pulse MAS and ^{13}C CPMAS data of another preparation of polythiophene/m-TiO_2 system (TC1) shown in Figures 2.9(a)/(d) and 2.10(a) differ markedly from both polythiophene and TC2 data. It was not possible to record a ^{13}C CPMAS spectrum of TC1 and therefore only a direct polarisation spin echo MAS spectrum was acquired. This ^{13}C data contains resonances that exhibit chemical shifts which are consistent with the other thiophene-based systems, however additional resonances at ^{13}C δ: ~165 and ~0 ppm are also observed suggesting that additional aliphatics (hindered methyl groups) and carboxyl functionalities are also present, possibly from thiophene reduction. The inability to record ^{13}C CPMAS data suggests that the paramagnetic character and electron motion within this system are enhanced, and the distribution of ^{1}H chemical shifts (and hence H speciation) has been altered from the original thiophene composition to favour a greater aliphatic presence at ^{1}H δ: ~0 ppm.

2.3. Electrochemical Analysis

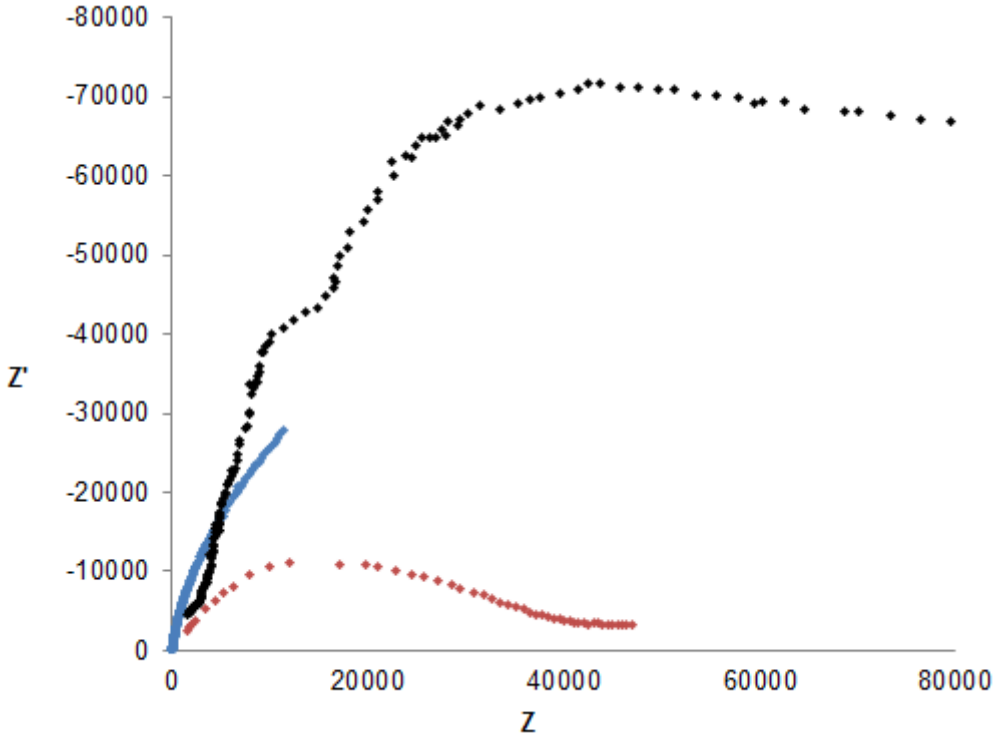

Figure 2.11: Nyquist plot showing the potentiostatic impedance of, (black) $mTiO_2$, (blue) $mTiO_2$-Polythiophene Composite TC1, (red) $mTiO_2$- Polythiophene Composite TC2 taken using a two electrode setup with an applied DC bias of 0 V between the frequency range of 10^6 and 10 Hz

Each material was studied by potentiostatic impedance recorded at standard atmospheric conditions between the frequency range of 10^6 and 10 Hz using a two electrode setup with an applied DC bias of 0 V with the results displayed in Figure 2.11.

Though traditionally when carrying out conductivity measurements a frequency region of 100 kHz to 0.01 kHz is used to assess the material. As these materials are being assessed as pellets, the main interest is that of the high frequency intercept as there is no Li^+ diffusion between the 2 electrodes. This high frequency region provides the value of the resistance of the pellet. For this reason a higher frequency was used in order to obtain the most accurate x axis intercept available. Measurements have been undertaken previously using frequencies up to 1 MHz [231,232] for electrochemical impedance spectroscopy demonstrating that it is an acceptable limit for use in these measurements. However due to the nature of these measurements it is important to take into account the influence of contact resistance. This is the resistance to current flow caused by the surface conditions present at the contact.[233] This is important as the contact

resistance between the active material and that of the silver conducting resin used as the electrode could affect the readings that are recorded for the conductivity of the material. Pristine m-TiO_2 has the largest intercept and hence the lowest conductivity (3.56 x 10^{-2} $mS.cm^{-1}$). The composite washed with dichloromethane only (TC1) showed a significant improvement in conductivity (5.79 $mS.cm^{-1}$), while the sample with the extra methanol and acid wash (TC2) showed reduced conductivity compared to the first composite (0.231 $mS.cm^{-1}$) but still almost an order of magnitude higher than m-TiO_2. These improvements in conductivity are one order of magnitude higher than the improvements in conductivity observed in doping MCM-41with polyaniline nanowires (1.6 x 10^{-3} $S.cm^{-2}$)[221] using a similar doping method and suggest that our strategy is effective. Looking at these values of conductivity, all of the values produced have been situated between those reported previously for these amorphous mesoporous TiO_2 (1 x 10^{-3} $mS.cm^{-1}$)[9] and those reported previously for polythiophene using chemically based synthesis procedures (0.4-2 $S.cm^{-1}$)[234] is possible to therefore to conclude that the effects of contact resistance on these measurements has not significantly influenced the conductivity results.

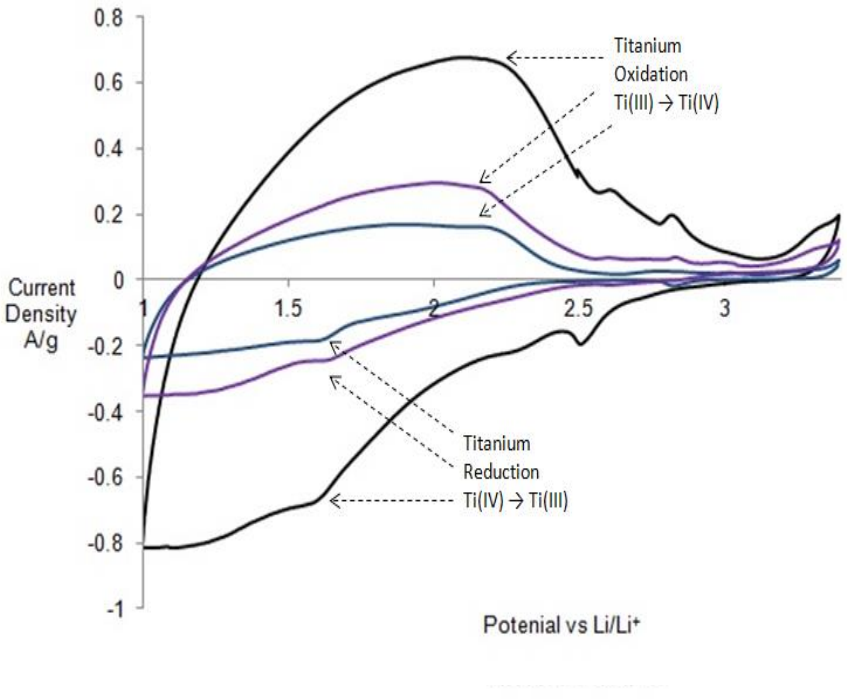

Figure 2.12: Cyclic Voltammetry over a potential range of 1-3.4 V vs Li/Li^+ standard electrode potential at various sweep rates of m-TiO_2TMS (black) 2 mVs^{-1}, (purple) 1 mVs^{-1}, (blue) 0.5 mVs^{-1}

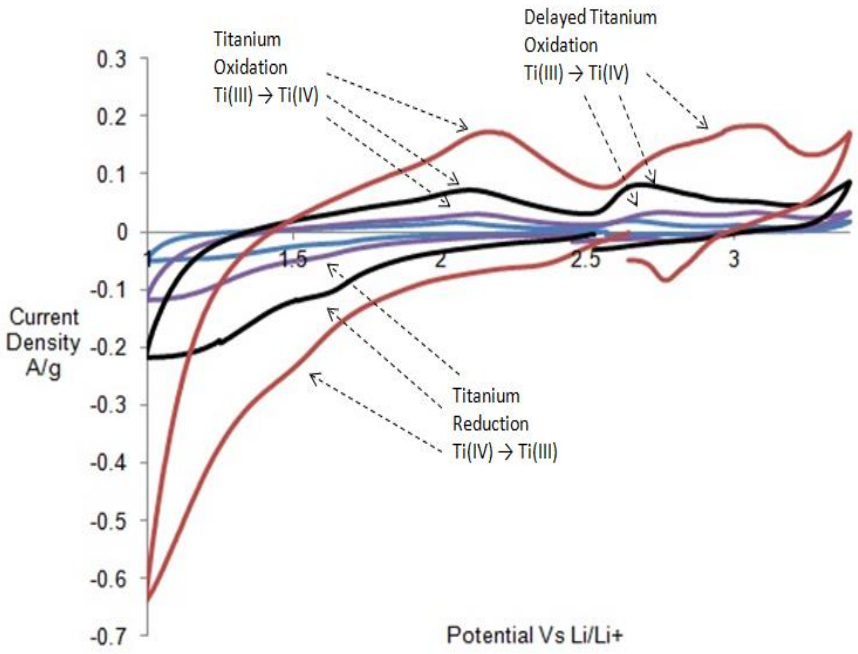

Figure 2.13: Cyclic Voltammetry over a potential range of 1-3.4 V vs Li/Li^+ standard electrode potential at various sweep rates of composite TC2 (red) 5 mVs^{-1}, (black) 2 mVs^{-1}, (purple) 1 mVs^{-1}, (blue) 0.5 mVs^{-1}

Each synthesised material underwent electrochemical analysis to evaluate performances as a lithium battery cathode material. Cyclic voltammetry was carried out on materials at various scan rates and can be seen in Figures 2.12 and 2.13. The results show that the m-TiO_2 material appears to increase in current proportional to the sweep rate indicating a 1st order response to an increase in sweep rate indicative of a surface limited process typically seen for capacitive materials.[31] The cyclic voltammogram of TiO_2TMS at 0.5 mVs^{-1}, seen expanded in Figure 2.14, displays broad peaks for both reduction and oxidation between 2.4-1 V, which is typical behaviour for amorphous materials caused by mixed energy levels of the amorphous pore walls.[27] Sample TC2 showed similar behaviour to the m-TiO_2 however it is possible to observe the reduction and oxidation peaks more clearly as can be seen in Figure 2.15. Reduction peaks were observed at 2.8, 1.65 and 1.25 V and oxidation peaks at 2.1 2.65 and 3.05 V, respectively. However, the current produced by the composite TC2 was lower than for the m-TiO_2TMS starting material. So despite the improved conductivity, it appears the Li^+ charge storage potential of the material has decreased.

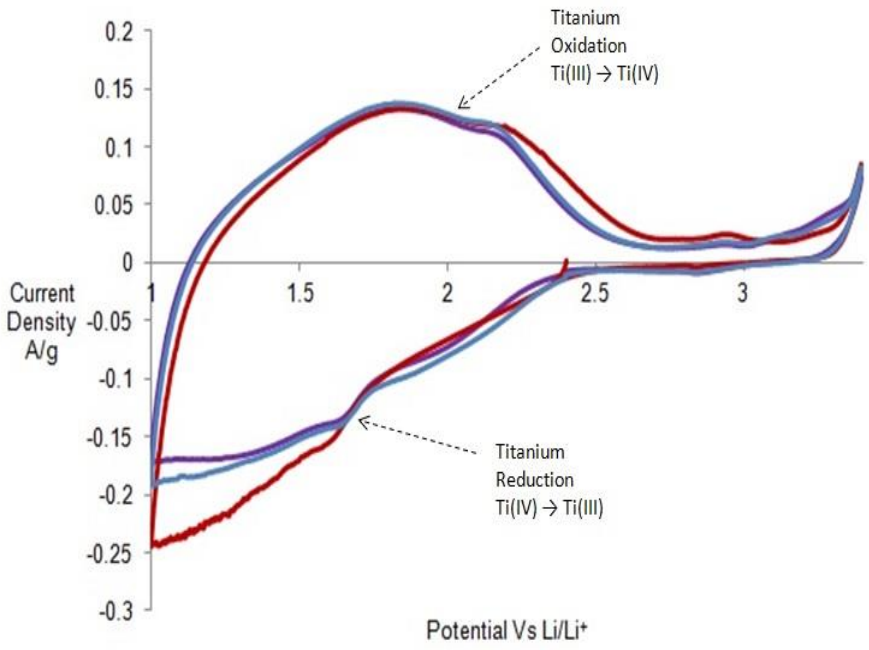

Figure 2.14: Cyclic voltammetry over a potential range of 1-3.4 V vs Li/Li^+ standard electrode potential m-TiO_2 heated and treated with TMS-Cl at a sweep rate of 0.5 mVs^1 (red) cycle 1, (blue) cycle 2, (purple) cycle 3

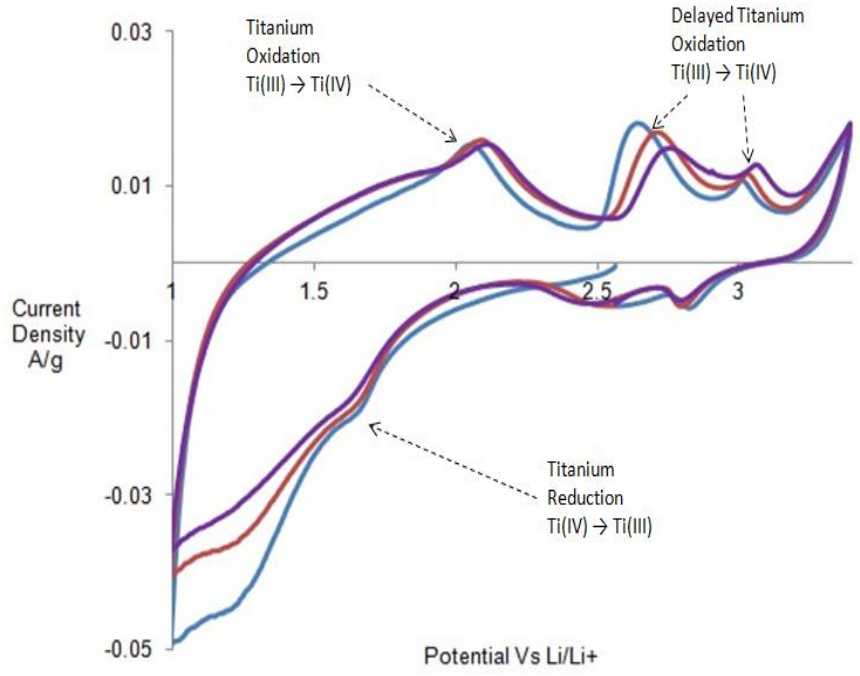

Figure 2.15: Cyclic voltammetry over a potential range of 1-3.4 V vs Li/Li^+ standard electrode potential of composite TC2 for the first 3 cycles, blue (1), red (2) and purple (3)

Galvanostatic charge discharge analysis of the synthesised materials was carried out using a discharge rate of 0.2 $mA.cm^{-2}$. The m-TiO_2, displayed in Figure 2.16, showed a peak capacity

of 301 mAh/g which dropped to 75 mAh/g after 50 cycles, whereas sample TC2 (Figure 2.17) showed a peak capacity of 50 mAh/g and a capacity of 7 mAh/g after 50 cycles. This data correlates with the cyclic voltammetry data in suggesting that the m-TiO_2TMS has the superior lithium storage performance despite having lower conductivity than the composite TC2, composite TC2 is therefore not suitable as an effective lithium battery cathode material. This observation is similar to results seen previously with the fulleride composites of Ta oxide,[235] where despite improvements to the conductivity of the material, the overall lithium transport was reduced. The reason for this could be due to the polythiophene hindering Li^+ transport and blocking access to titanium centres within the pores, thus hindering redox reactions deep within the structure that were otherwise expected to lead to pseudocapacitive sites.

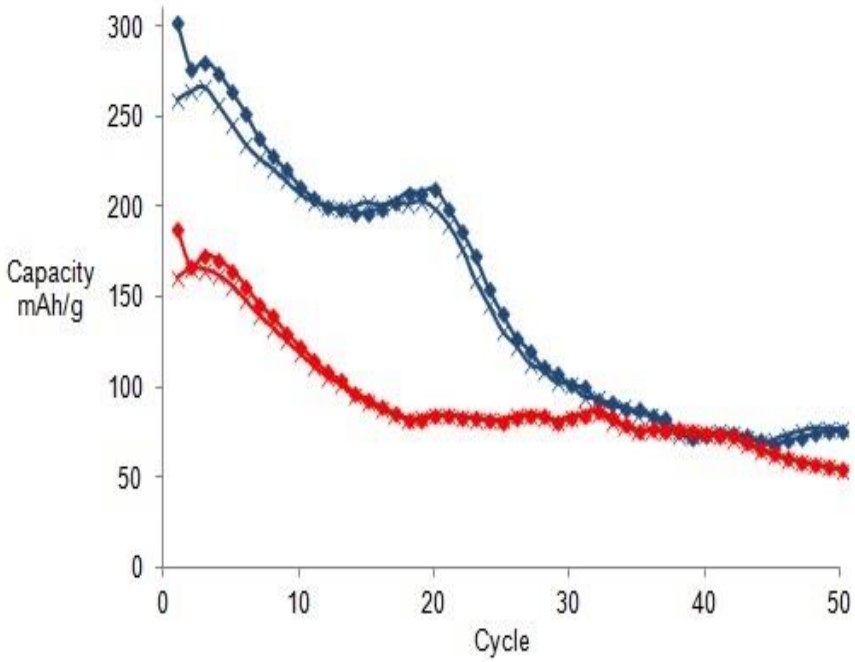

Figure 2.16: 50 Cycles charge (squares) discharge (crosses) capacity data for m-TiO_2 at (red) 1 mA.cm^{-2} and (blue) 0.2 mA.cm^{-2}

The performance of the m-TiO_2 TMS was also assessed at a higher discharge rate of 1 mA.cm^{-2} (Figure 2.16), showing a peak capacity of 187 mAh/g and a final capacity of 54 mAh/g after 50 cycles. A decrease in capacity is expected with increasing discharge current, however the m-TiO_2 still produces a superior performance, at a higher discharge rate, to that of the thiophene composite TC2 at a lower discharge rate. Thus, m-TiO_2TMS shows typical broad redox behaviour as expected for an amorphous material, and despite a high initial capacity, the performance decreases upon recycling to 54 and 75 mAh/g after 50 cycles at high and low discharge rates respectively.

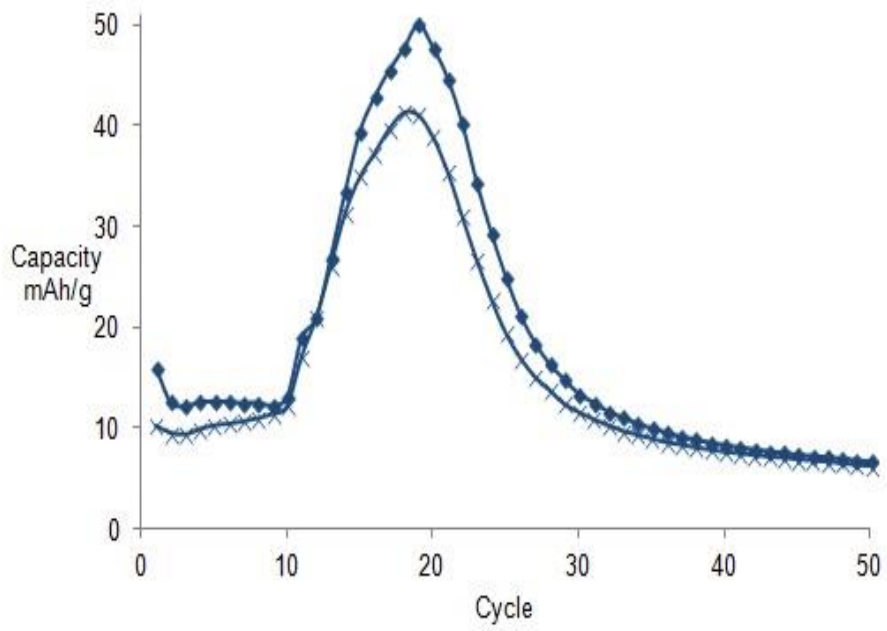

Figure 2.17: 50 Cycles charge (squares) discharge (crosses) capacity data for TC2 at 0.2mA.cm^{-2}

2.4 Conclusions:

In conclusion, high surface area (ca. 1000 m^2/g) electroactive mesoporous titanium oxide was successfully impregnated with air-stable conducting polythiophene nanowires in an attempt to exploit the high fraction of internal redox sites for pseudocapacitive charge storage in these otherwise insulating materials. The incorporation of polymer improved the conductivity of the material by up to two orders of magnitude, producing a material with superior conductivity to those similarly created polyaniline-impregnated MCM-41 materials. However the lithium storage capacity of the material dropped possibly due to Li^+ diffusion problems through the material. Further investigations using materials with larger pores and/or different polymers and polymer loading levels may yet lead to improved electrochemical performance using this approach of synthesising conducting polymer transition metal oxide composites.

Chapter 3 : TiO_2 – Pyrrole Composites Using a Chemical Synthesis in Aqueous Solvents and Various Synthesis Conditions

3.1 Introduction

After the attempt to synthesise polythiophene in the pores of mesoporous Ti oxide (m-TiO_2). The incorporation of the polymer resulted in improved conductivity from 3.56 x 10^{-2} $mS.cm^{-1}$ to 5.79 $mS.cm^{-1}$.[236] Despite improvements in conductivity, the Li^+ transport was negatively affected by the incorporation of the conducting polymer leading to disappointing battery performance. For this reason we hoped that further investigations using different polymers and synthesis procedure could produce better results.

Presented herein are the synthesis and subsequent characterisation and electrochemical evaluation of m-TiO_2 with conducting polypyrrole nanowires within the pores, with a comprehensive investigation into the effects of different loading levels of polymer and variation in pore sizes, on the electrochemical performance of the material. The synthesis procedure uses the chemical oxidant $Fe(NO_3)_3$ [237] to polymerise the vapour-loaded pyrrole monomers to form a conducting polymer inside the pores of the oxide host, whilst still maintaining a high surface area. The oxidant $Fe(NO_3)_3$ was used instead of previously employed $FeCl_3$ [236] because of its higher solubility in water, ensuring easier removal of residual oxidant from the structure after the polymerisation step. The best material shows improved electrochemical performance over that of the pristine m-TiO_2 and significantly improved results as compared to our initial investigations using polythiophene.

3.2 Experimental

3.2.1 Synthesis Procedure

Polypyrrole composites of C12 m-TiO_2 were prepared by first loading C12 m-TiO_2 (ca. 300 mg) with pyrrole monomer. This was left for the necessary period to ensure that the pores were loaded with the correct amount of vapour to synthesis a composite of designated pyrrole content, 5, 10, 15 and 30 weight % pyrrole vapour identified as samples PC(5), PC(10), PC(15) and PC(30), respectively. The material was then weighed to determine the accurate pyrrole

content by the increase in weight. $Fe(NO_3)_3$, 2.4 equivalents with respect to pyrrole content, was then added to deionised water (20 mL) and stirred until the salt was dissolved and a homogenous solution was obtained. To this solution the pyrrole loaded C12 m-TiO_2 was then added with stirring. This solution was then sealed and left to stir for 24 hours to complete the polymerisation. The resulting precipitate was then collected by filtration and washed 3 times with 50 mL of deionised water, each time with stirring for 1 hour, to remove residual oxidant present in the material. After the washing stage the product was dried under vacuum for 2 hours to remove any remaining water from the sample.

The composites with different pore sizes were synthesised using the same procedure as that of the materials above, with the exception of the C12 m-TiO_2 materials, the synthesis was carried out using different amine templates, hexylamine (C_6 template) and octadecylamine (C_{18} template) to yield host materials with smaller and larger pore sizes, respectively. These samples were further treated using 5% polymer loading, and were identified as samples C6PC (C_6 template composite) and C18PC (C_{18} template composite).

3.2.2 Characterisation

Brunauer Emmett Teller (BET) surface area and pore size measurements were derived from nitrogen adsorption/desorption data collected on a Micromeritics ASAP 2020. Infrared (IR) spectroscopy was conducted on a Perkin Elmer FT-IR Spectrometer Spectrum RX1 using oven dried KBr discs and data treated on Spectrum 5.1 software. X-ray diffraction (XRD) was performed on Bruker D8 DAVINCI diffractometer with Cu K_a radiation (40 kV, 30 mA) source. The step size was 0.025°. The diffraction patterns were recorded in the 2θ range 1.0 - 100° and the total counting time was 3 hours. The thermogravimetric analysis (TGA) and differential thermal analysis (DTA) was carried out on a STA 449C analyser from Netzsch under a flow of dried air at 10.00 °C/min up to 700 °C. Argon was used to protect the balance section. High Resolution Scanning Transmission Electron Microscopy (HRSTEM) was performed in a HD-2700 dedicated Scanning Transmission Electron Microscope (STEM) from Hitachi, with a cold field emitter equipped with a CEOS Cs corrector and operated at 200 kV. The powder samples were simply dry deposited onto a Cu grid covered with a carbon film (Quantifoil) having periodical holes with diameter of 1.2 micron. Observation was made in three different modes: bright field (BF), high angle annular dark field (HAADF) and secondary electron (SE).

3.2.3 Solid State NMR

The ^{13}C cross polarisation, magic-angle-spinning nuclear magnetic resonance (CPMAS NMR) data from the TC1, TC2 and polythiophene samples were acquired at ambient temperatures (~20 °C) using a Bruker DSX-400 spectrometer (B_0 = 9.4 T) operating at ^{1}H and ^{13}C Lamor frequencies of 398.8 and 100.3 MHz, respectively. These ^{13}C CPMAS data were acquired using a Bruker 4 mm double channel HX probe which achieved rotational frequencies of 10 kHz. The $^{1}H/^{13}C$ CPMAS NMR were performed with an initial ^{1}H $\pi/2$ pulse of 2.5 μ seconds duration, a $^{1}H/^{13}C$ Hartmann-Hahn contact period of 1 ms and a recycle delay of 3 s. TPPM decoupling with a 15° phase change between π pulses of 5 μ seconds duration was applied during acquisition. All ^{13}C chemical shifts were referenced against the primary standard of TMS via a secondary solid standard of alanine.

Corresponding ^{1}H single pulse MAS NMR data and ^{13}C spin echo MAS NMR data from the TC1, TC2 and polythiophene samples were acquired at ambient temperatures (~20 °C) using a Varian InfinityPlus-300 spectrometer (B_0 = 7.05 T) operating at ^{1}H and ^{13}C Larmor frequencies of 300.09 MHz and 75.46 MHz, respectively. Both the ^{1}H MAS NMR and ^{13}C spin echo MAS NMR data were acquired using a Bruker 4 mm double channel HX probe which enabled rotational frequencies of 10 kHz to be implemented. The single pulse ^{1}H MAS NMR measurements used a ^{1}H $\pi/2$ excitation pulse of 3 μ seconds and a recycle delay of 3 seconds. The ^{13}C spin echo MAS experiment used $\pi/2$ and π pulses of 2.5 and 5 μ seconds, respectively, a recycle delay was 3 seconds and TPPM decoupling with a 15° phase change between π pulses of 7 μ seconds was applied during acquisition. The ^{1}H and ^{13}C chemical shifts were referenced against the primary standard of TMS via a secondary solid standard of adamantane.

^{1}H and ^{13}C MAS NMR data from the thiophene monomer were acquired at ambient temperatures (~20 °C) using a Bruker AvanceIII-500 spectrometer (B_0 = 11.7 T) operating at the ^{1}H and ^{13}C Lamor frequencies of 500.1 and 125.8 MHz respectively. The ^{1}H NMR MAS spectrum was acquired using a Bruker 4 mm triple channel HXY probe in double channel mode. The ^{1}H data was obtained using a single pulse experiment which used a $\pi/2$ excitation pulse of 2.5μ seconds, a MAS frequency of 3 kHz and a recycle delay of 3 seconds. The corresponding ^{13}C data was obtained using the same singe pulse experiment but with a $\pi/2$ excitation pulse of 5 μ seconds duration and a recycle delay of 3 seconds. All ^{1}H and ^{13}C

chemical shifts were referenced against the primary standard of TMS via a secondary solid standard of alanine.

3.2.4 Electrochemical Analysis

All electrochemical analysis was performed with a Princeton Applied Research VersaSTAT. Electrochemical performance of the synthesised electrode materials as a Li^+ battery electrode was assessed using a two electrode set up. Working electrodes consisted of 80% active material, 10% super conducting carbon black, and 10% polyvinylidenefluoride (PVDF) by weight. The electrode paste was made by grinding the active material and carbon black to ensure a good mixture of the powders. The powders were then stirred with PVDF and *n*-methyl-2-pyrrolidinone (NMP) solvent until a homogenous paste was formed. The paste was spread onto a copper foil (current collector). The electrode was dried by first heating to 80 °C to bake off any excess NMP solvent before increasing the temperature to 120 °C overnight to allow the electrode material to bind with the current collector. Once completed, the electrodes were punched using a Hohsen electrode punch to produce uniform sized discs of 15 mm. The respective counter electrode is lithium metal foil and was also punched into a 15 mm disk. The electrolyte used in this investigation is 1.0 M $LiPF_6$ dissolved in ethylene carbonate (EC) and diethyl carbonate (DEC) solutions at a ratio of 1:1 by volume. All electrochemical cells were constructed within an argon filled glove box to ensure minimal exposure to oxygen. Cyclic voltammetry measurements were carried out at a variety of sweep rates 0.5, 1, 2 and 5 mVs^{-1} and the potential windows used in all experiments were that of 1-3.4 V vs Li/Li^+ reference electrode. The initial potential of the scan was determined by the open circuit potential the cell (typically 2.3-2.6 V vs Li/Li^+) with the initial scan direction being directed in the reduction direction towards a lower potential limit (1 V vs Li/Li^+) with cycles being completed once the final reduction sweep reaches the starting potential of the cycling process.

Galvanostatic charge discharge measurements were carried out a current density of 1 $mA.cm^{-2}$ and between a potential window of 1-3.4 V vs Li/Li^+ reference electrode. Weights of each electrode were taken prior to cell assembly to determine cathode mass and then used to calculate capacity relative to mAh/g according to the mass of the electrode. All measurements were carried out at room temperature using a Hohsen HS flat cell.

3.2.5 Electrical Impedance Spectroscopy

Electron conductivity measurements were carried out using a two electrodes set-up. Silver wire of length 5 cm was used as the working and counter electrodes and these were attached to each pellet via a silver two part conductive adhesive. Each pellet was made from a 300 mg of sample ground and formed into pellets using a 25 tonne manual hydraulic press. The flat sides of this pellet were coated using a silver two part conductive adhesive. Potentiostatic impedance spectra were recorded using a DC Bias of 0 V as the working and counter electrodes are the same electrochemical potential, measurements were taken between the frequency range of 10^6 and 10 Hz with amplitude of 100 mV using the VersaStudio software. For analysis the data was exported to ZView. The electronic conductivity of each pellet was determined using Equation 3.1, which was derived from Equations 3.1.1 and 3.1.2.

Equation 3.1 $$\sigma = \frac{L}{RA}$$

Equation 3.1.1 $$\sigma = \frac{1}{\rho}$$

Equation 3.1.2 $$\rho = \frac{RA}{L}$$

σ is the conductivity ($mS.cm^{-1}$), L is the distance between the two wires (cm), A is the area covered by the silver adhesive in (cm^2) and R is the initial resistance (Ω) measured where the plot intercepts the x-axis on the Nyquist plot.

3.3 Results and Discussion:

3.3.1 Characterisation

The Brunauer Emmett Teller (BET) surface area data for all synthesised materials is displayed in table 3.1. The nitrogen adsorption-desorption isotherms for dodecylamine templated C12 m-TiO_2 and the polypyrrole composites containing various loading levels of polymer are shown in Figure 3.1. All isotherms are on the cusp between type I and IV, in agreement with previous work on amine-templated mesoporous transition metal oxides [238,239] confirming retention of the mesostructure after polymerisation within the pore structure. The pristine C12 m-TiO_2 sample possesses a BET surface area of 876 m^2/g, which decreases with polymer incorporation to 427, 257, 219 and 145 m^2/g at initial vapour loading levels of 5% PC(5), 10% PC(10), 15% PC(15) and 30% PC(30), respectively. Samples PC(5) and PC(10) still possess a higher surface

area than the nanoparticles synthesised by Wang *et al*, which possess a surface area of only 220 m^2/g,[31] even after the incorporation of polypyrrole. The pore volume decreases with increasing polymer content inside the host from 0.241 cm^3/g to 0.158, 0.081, 0.059 and 0.032 cm^3/g for samples PC(5), PC(10), PC(15) and PC(30) respectively. All pore volumes were calculated using the desorption cumulative pore volumes data plots up to a maximum pore size of 40 Å, beyond which the only pores are due to textural porosity. The loss of surface area and pore volume upon pyrrole impregnation is consistent with the pores having been filled with polymer. In addition, the increasing levels of vapour loading in the pores results in an increase in polymer content.

Material	BET surface area/ m^2/g	BJH Pore volume / cm^3/g
C12 m-TiO_2	876	0.241
C6 m-TiO_2	693	0.199
C18 m-TiO_2	539	0.156
PC(5)	427	0.158
PC(10)	257	0.081
PC(15)	219	0.059
PC(30)	145	0.032
C6PC	402	0.122
C18PC	172	0.118

Table 3.1: Surface area and pore volume of m-TiO_2 and respective polythiophene composites.

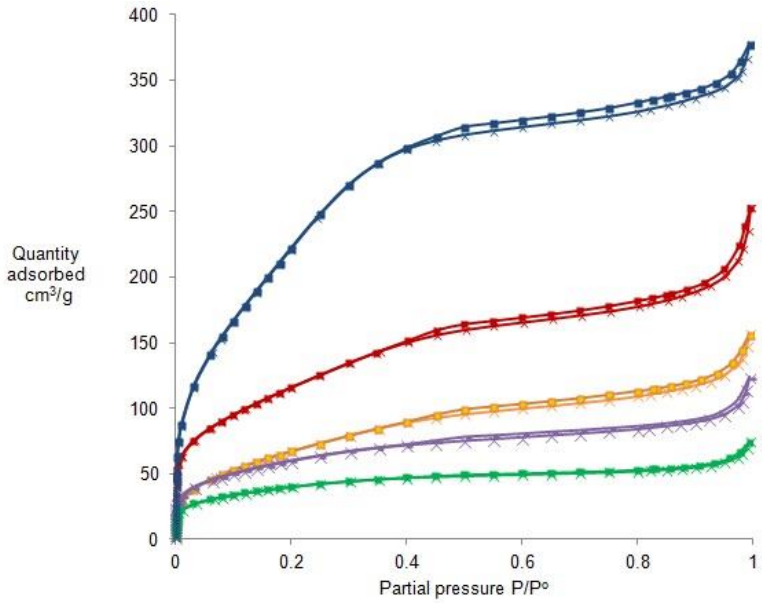

Figure 3.1: Nitrogen adsorption (crosses) and desorption (squares) for m-TiO_2 (blue) composite PC(5) (red), PC(10) (orange), PC(15) (purple) and PC(30) (green)

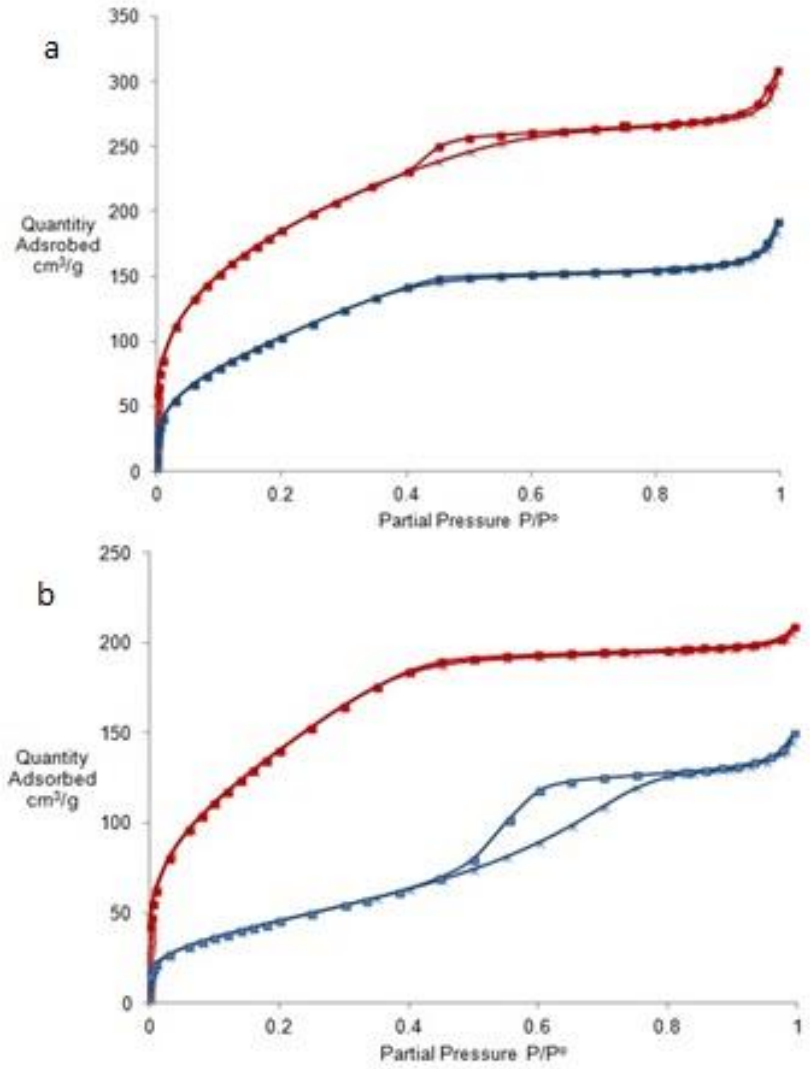

Figure 3.2: Nitrogen adsorption (crosses) and desorption (squares) isotherms for (a) C6 m-TiO_2 (red) and C6PC (blue) (b) C18 m-TiO_2 (red) and C18PC (blue)

The isotherms of materials synthesised using different pore sizes are shown in Figure 3.2 for the C6 and C18 templated m- TiO_2 and their respective composites C6PC and C18PC. Both materials were made containing the 5% vapour loading as previously carried out with composite PC(5). The surface area for both materials drops upon the incorporation of polymer, from 693 m^2/g to 402 m^2/g and 539 m^2/g to 172 m^2/g for samples C6PC and C18PC respectively. The pore volume drops from 0.199 cm^3/g to 0.122 cm^3/g for sample C6PC and from 0.156 cm^3/g to 0.118 cm^3/g for sample C18PC. Both composites therefore show a decrease in pore volume and surface area, indicating successful incorporation of the polymer within the mesostructure.

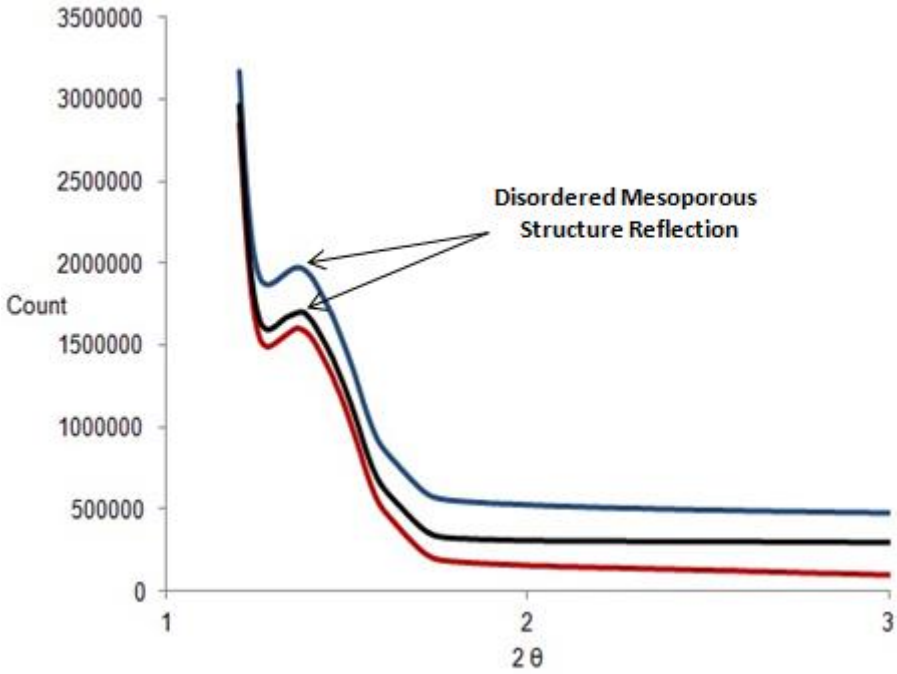

Figure 3.3: Powder X-ray diffraction pattern for samples C6PC (red), PC(5) (black) and C18PC (blue)

The powder X-ray diffraction (PXRD) patterns for composites of different pore sizes C6PC, PC(5) and C18PC are shown in Figures 3.3, while the data for as synthesised C12 m-TiO_2 has been published previously.[7] Figure 3.3 shows a reflection for all composites at approximately 1-3° 2θ typical for mesoporous structures and has been observed previously for amine templated mesoporous oxides.[7,236] This data confirms that the mesostructure of the material was retained upon incorporation of the polypyrrole within the pores. Figure 8.5 focuses on the higher reflection angles up to 100° 2θ. These show all typical reflections expected for anatase materials,[240] indicating that post-polymer incorporation the walls of the structure begin to crystallise.

Thermogravimetric analysis (TGA) and differential thermal analysis (DTA) were used to investigate the hydrocarbon content of the composite materials synthesised using various pore sizes. The data is shown in Figure 3.4. The TGA plot for all samples show weight losses of 8, 9 and 6% for samples C6PC, PC(5) and C18PC, respectively, in the region of 25-200 °C. Weight losses in this initial region are associated with water loss.[236] This is confirmed by the overlaying DTA data which shows an endothermic peak up to 200 °C in all samples.

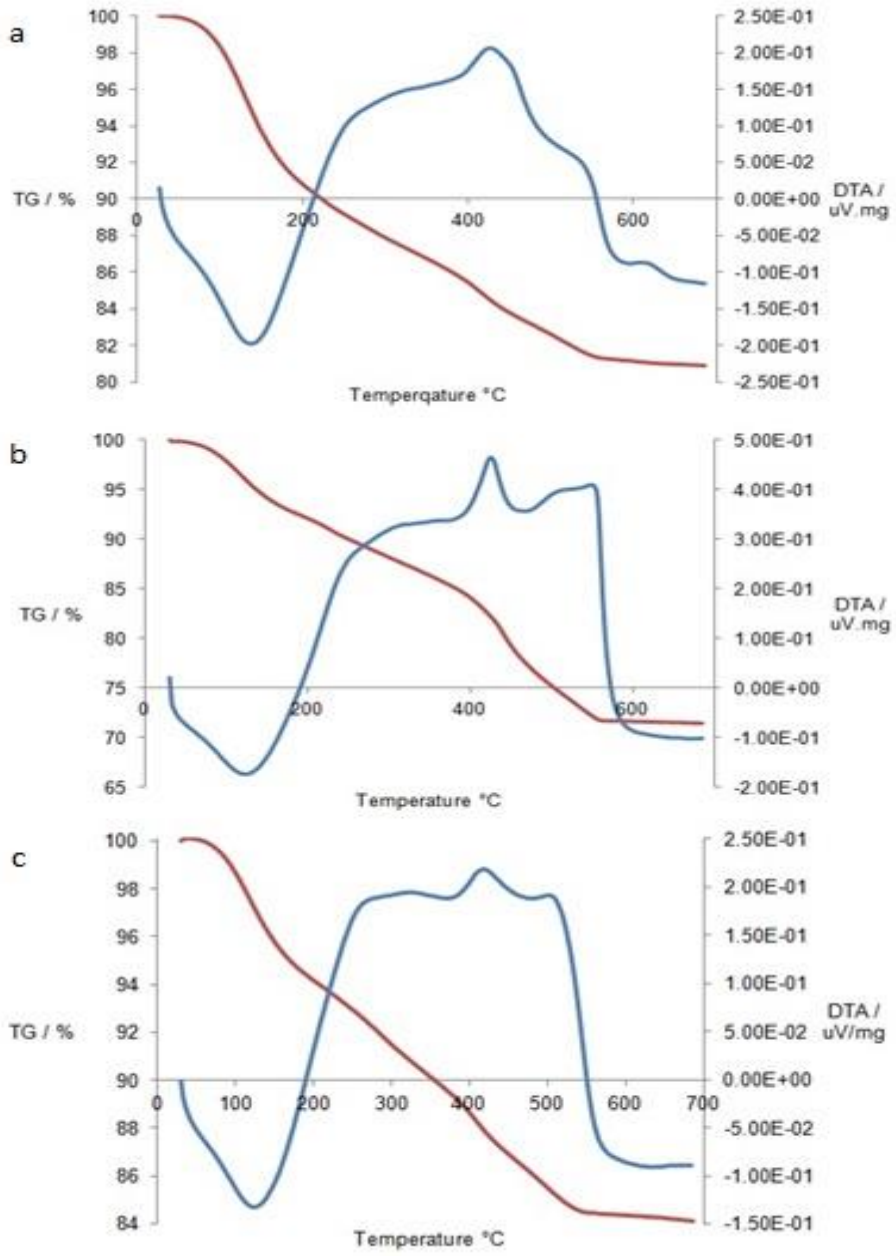

Figure 3.4: Thermogravimetric analysis (blue) and differential thermal analysis (red) plots of (a) PC(5), (b) C6PC and (c)C18PC

The higher temperature regions of the TGA plot (200-600 °C) display total weight loss values of 28%, 19% and 16% for samples C6PC, PC(5) and C18PC, respectively. When subtracting the values of initial water loss from the total weight loss, the organic content of the composites can be derived as 20%, 10% and 10%, respectively, for C6PC, PC(5) and C18PC. This is again corroborated by the overlaying DTA traces which show an exothermic peak for all composites in the temperature range 200-600 °C. This data demonstrates that despite loading all composites to the same initial weight of vapour, the larger pore sized materials retained less

polymer. This is most likely due to the larger pores allowing loss of pyrrole during the polymerisation process due to leaching from the pores, whereas the pore windows of C6PC becomes quickly blocked during the polymerisation process, leading to higher polymer content due to better pyrrole retention during the polymer synthesis procedure.

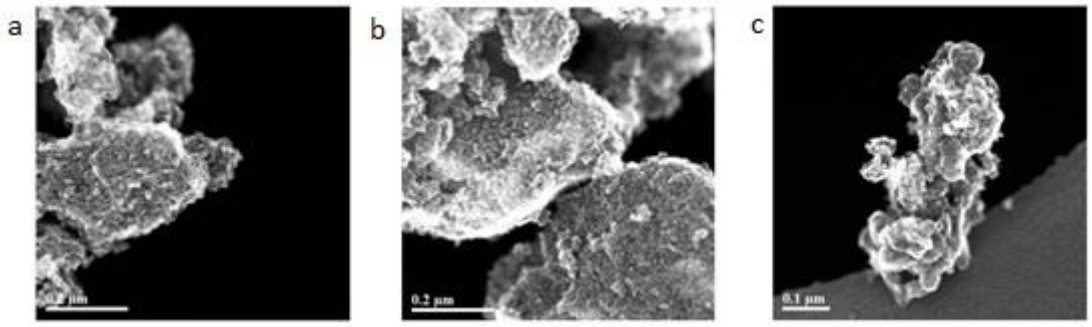

Figure 3.5: SEM SE Images of pyrrole composite (a) C6PC (130 kx), (b) PC (130 kX) (5) and (c) C18PC (150 kx) at low magnifications

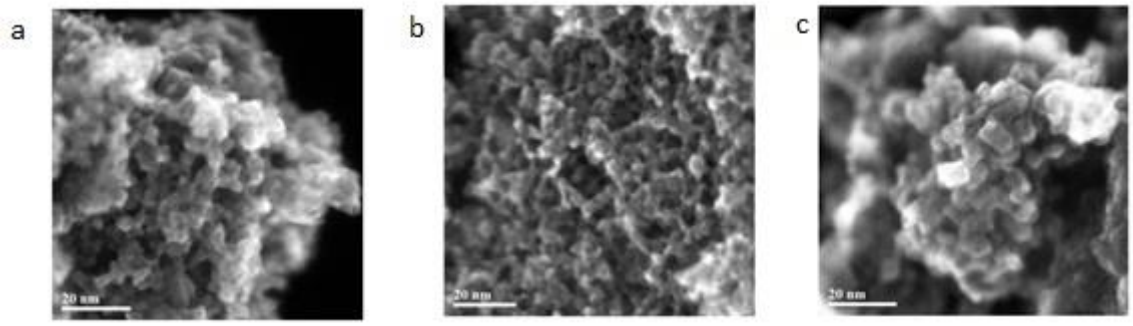

Figure 3.6: SEM SE Images of pyrrole composite (a) C6PC (1.1 Mx), (b) PC(5) (1.0 Mx) and (c) C18PC (1.1 Mx) at higher magnifications (~1MX),

To confirm the nature of the lattice, pore structure and powder morphology of the synthesised composites, scanning transmission electron microscopy (STEM) was performed. The lowest magnification of ~ 130 kX reveals the powder morphology of the samples, shown in Figure 3.5. These images display what appear to be clusters composed of smaller grains. This is expected based on what has been observed previously in related materials.[223,236] At a higher magnification of ~ 1 MX, the images shown in Figure 3.6 illustrate the worm like pore structure of the materials. This confirms that the mesostructure of the host material remains present after polymer incorporation. These images importantly demonstrate that the materials largely exist primarily as a single composite phase, confirming that the organic phase has been impregnated within the pore structure and not simply just coating the external surface. The STEM images also show small amounts of crystallised carbon on the external surface, most likely due to

leaching of monomer and or/polymer from the pores during the synthesis. Coating of the particles as opposed to impregnation would be visible as two distinct phases in the STEM and also lead to a dramatic loss in surface area of the mesoporous composites due to clogging of the pore windows. These images are thus consistent with the nitrogen adsorption data, and support the retention of the majority of the polymer within mesoporous structure.

Highest magnification images, shown in Figure 3.7, enable us to observe the lattice structure of the materials. These images establish that the structure remains mostly amorphous despite the appearance of some small areas of crystallisation within the pore walls of the m-TiO_2, with small traces of nanocrystalline carbon also present. The main crystalline phase is likely anatase based on the XRD of these materials and previous research demonstrating that the walls of amine-templated mesoporous titanium oxide loses structure by crystallising in the anatase form.[238] However the crystalline regions may also be due in part to residual iron crystals from the iron oxidant used in the polymerisation process.

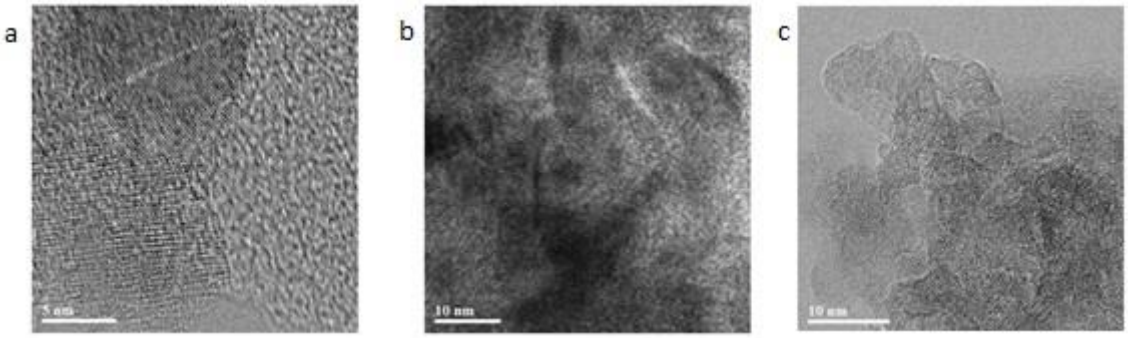

Figure 3.7: TEM BF images of pyrrole composite (a) C6PC (3 Mx), (b) PC(5) (2 Mx) and (c) C18PC (2.5 Mx) at highest magnifications

The infrared (IR) spectra of the as-synthesised materials are shown in Figures 3.8 to 3.12 with the fully characterised material shown in Figure 3.13 to 3.15. The spectra of pure pyrrole and polypyrrole are shown in Figures 8.6 and 8.7. These display key diagnostic bands at 3100 cm^{-1} (aromatic C-H stretches), 1500-1600 cm^{-1} (aromatic C=C stretches), 1300-1400 cm^{-1} (C-C stretching vibrations), 800 cm^{-1} and 730 cm^{-1} (C–H aromatic bending vibrations).[241,242] These stretches are observed in both the pyrrole and polypyrrole spectra. The polypyrrole stretches are situated at lower wavenumbers than those of the pyrrole monomer due to the increases in conjugation. In the C12 m-TiO_2 spectrum, residual water in the sample produces stretches at 3200 cm^{-1}, 1650-1600 cm^{-1} and a small stretch at 820 cm^{-1}.

Therefore the polypyrrole bands expected in these regions for the composites will be obscured by water stretches and thus cannot be used to confirm the presence of polymer in the composites.

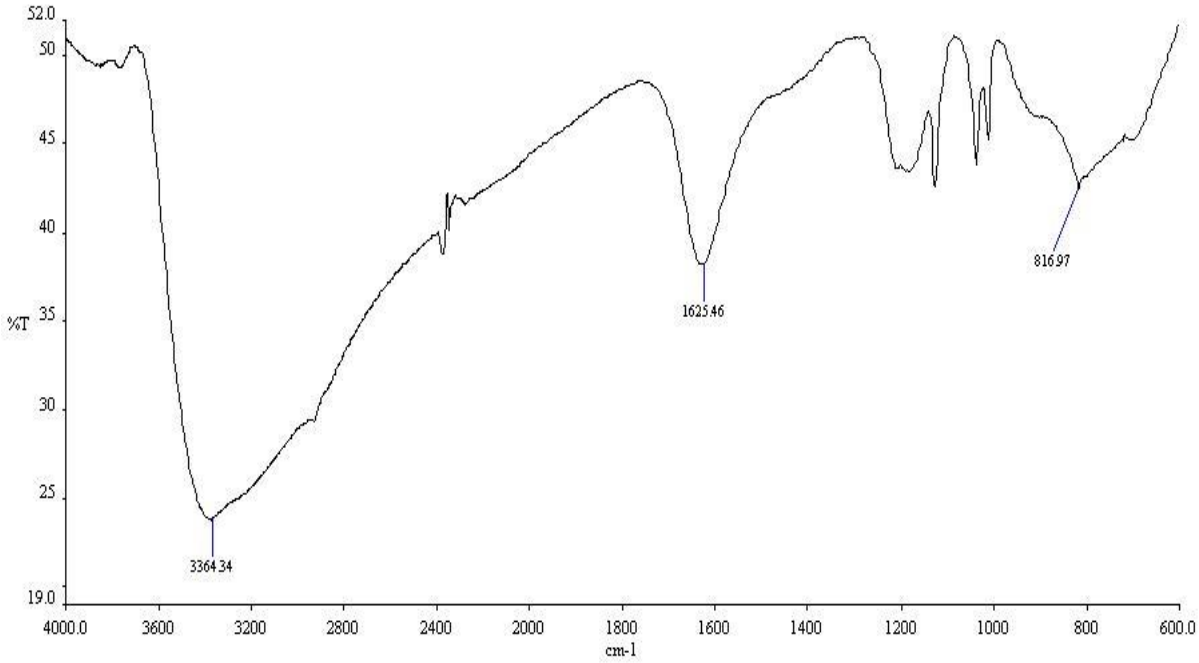

Figure 3.8: IR spectrum of C12 m-TiO_2

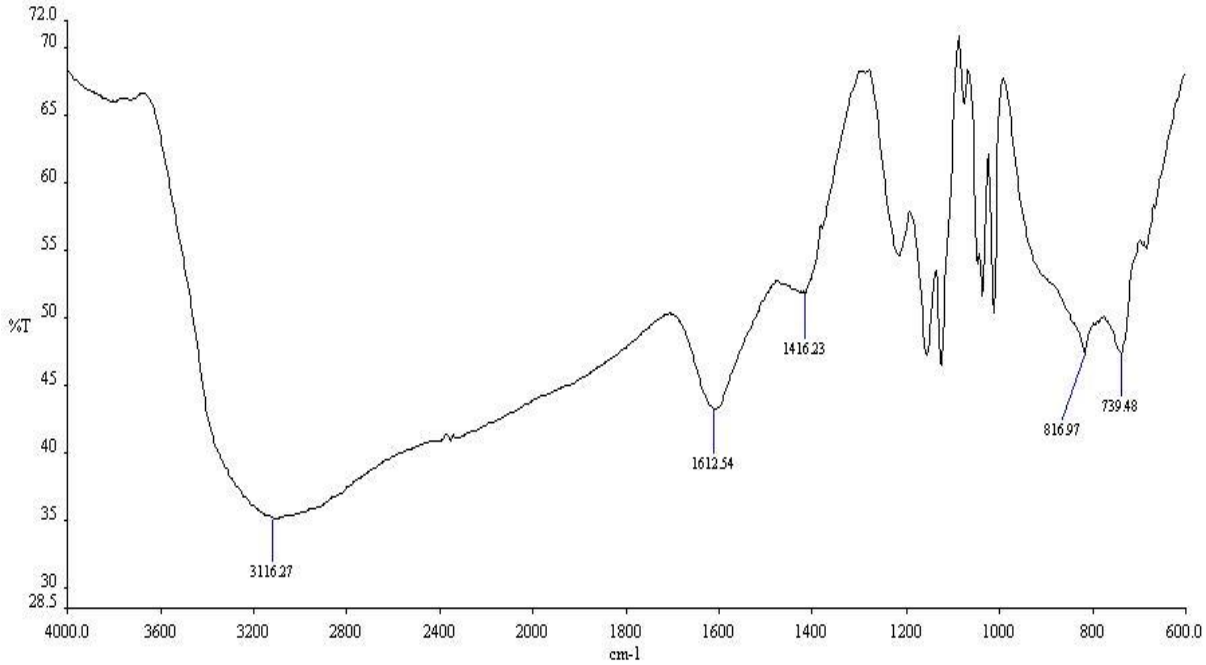

Figure 3.9: IR spectrum of C12 m-TiO_2 loaded with pyrrole vapour

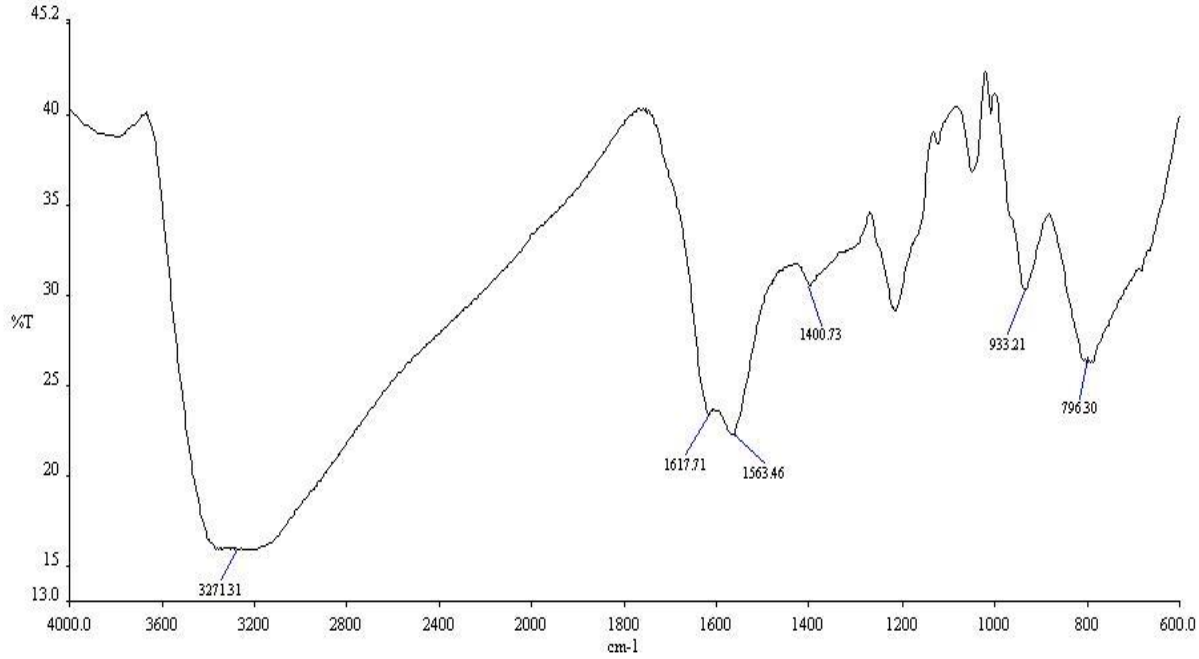

Figure 3.10: IR spectrum of composite PC (10)

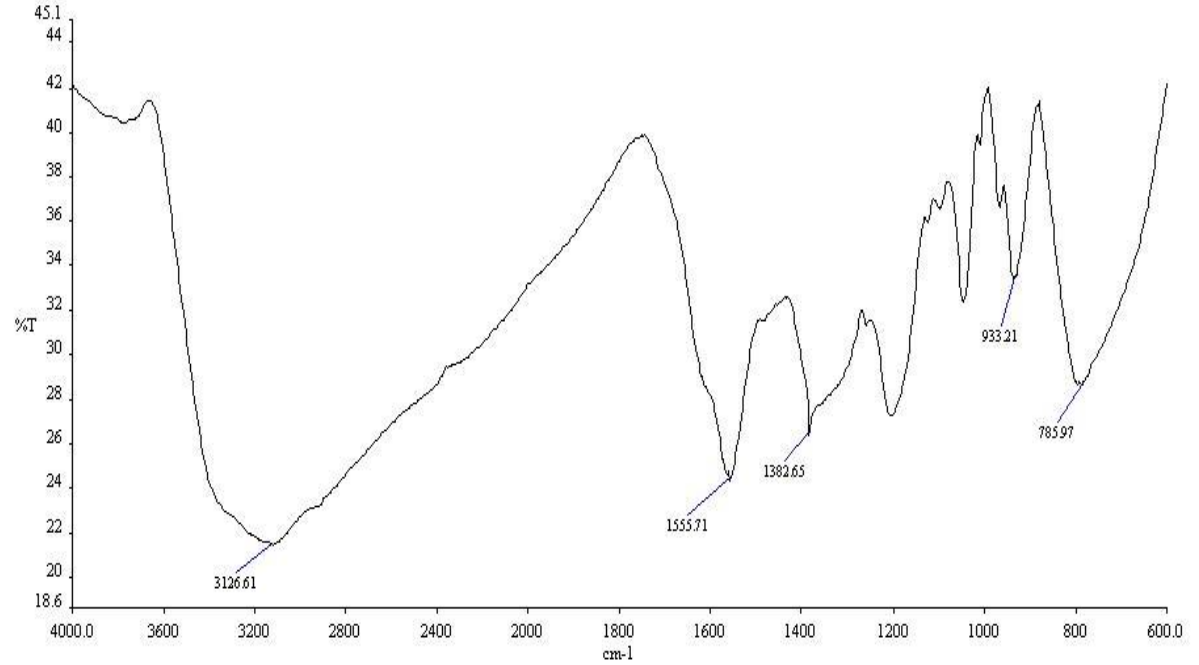

Figure 3.11: IR spectrum of composite PC (15)

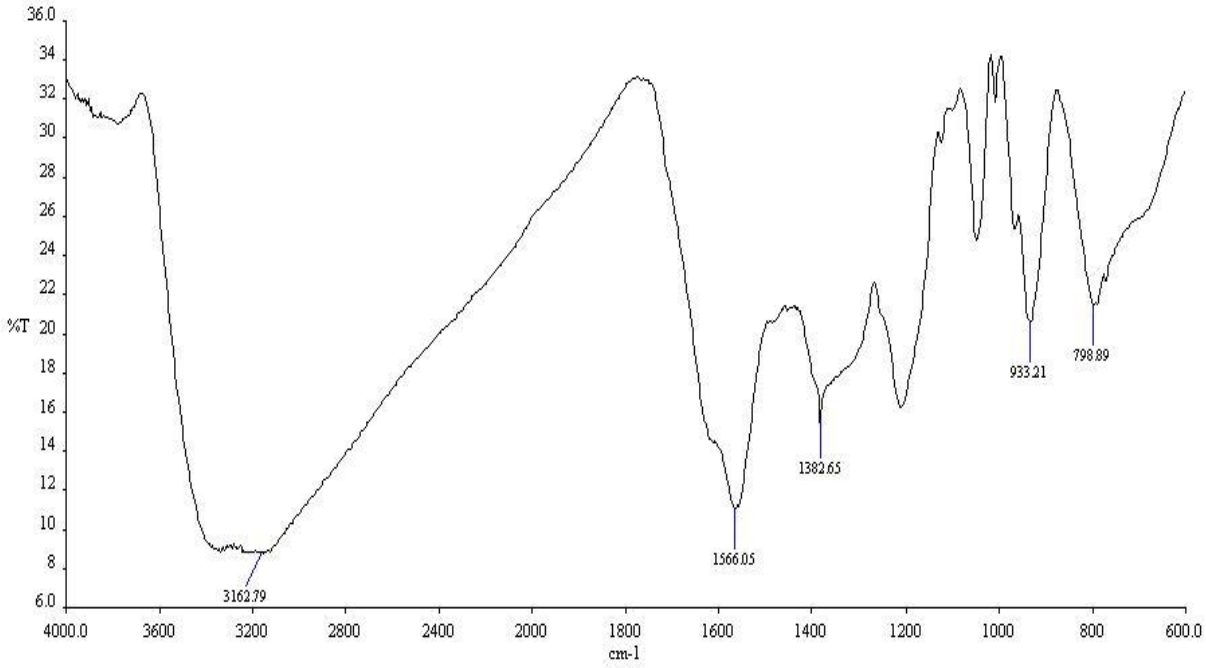

Figure 3.12: IR spectrum of composite PC (30)

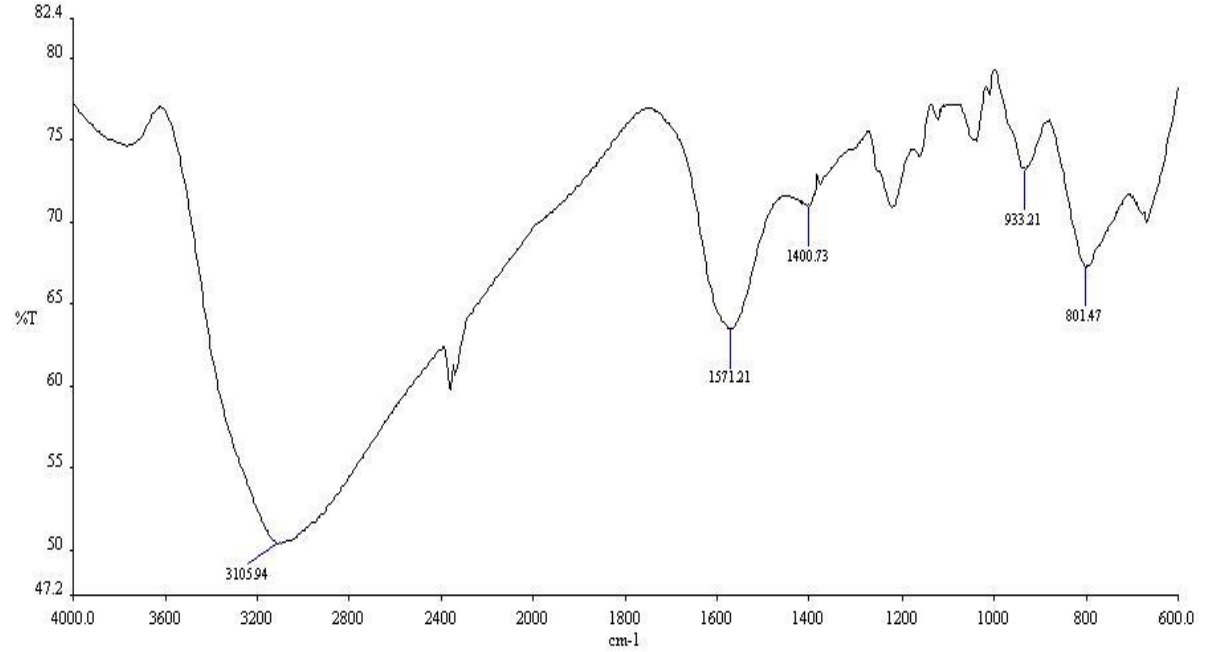

Figure 3.13: IR spectrum of composite PC(5)

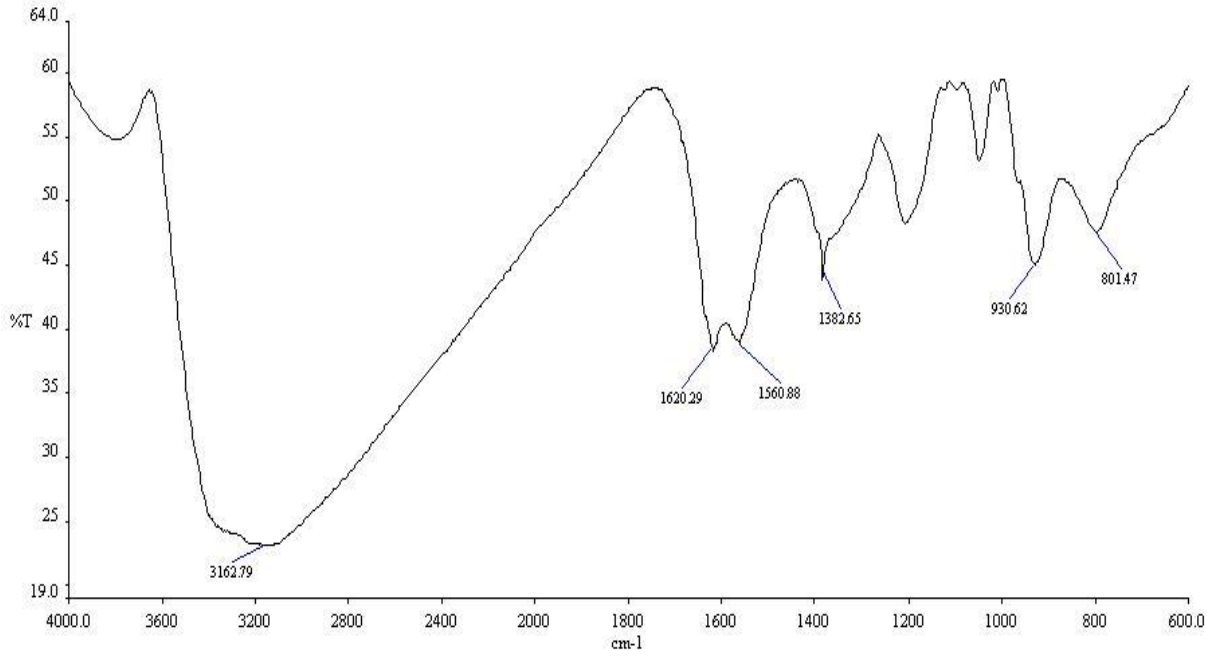

Figure 3.14: IR spectrum of composite C6PC

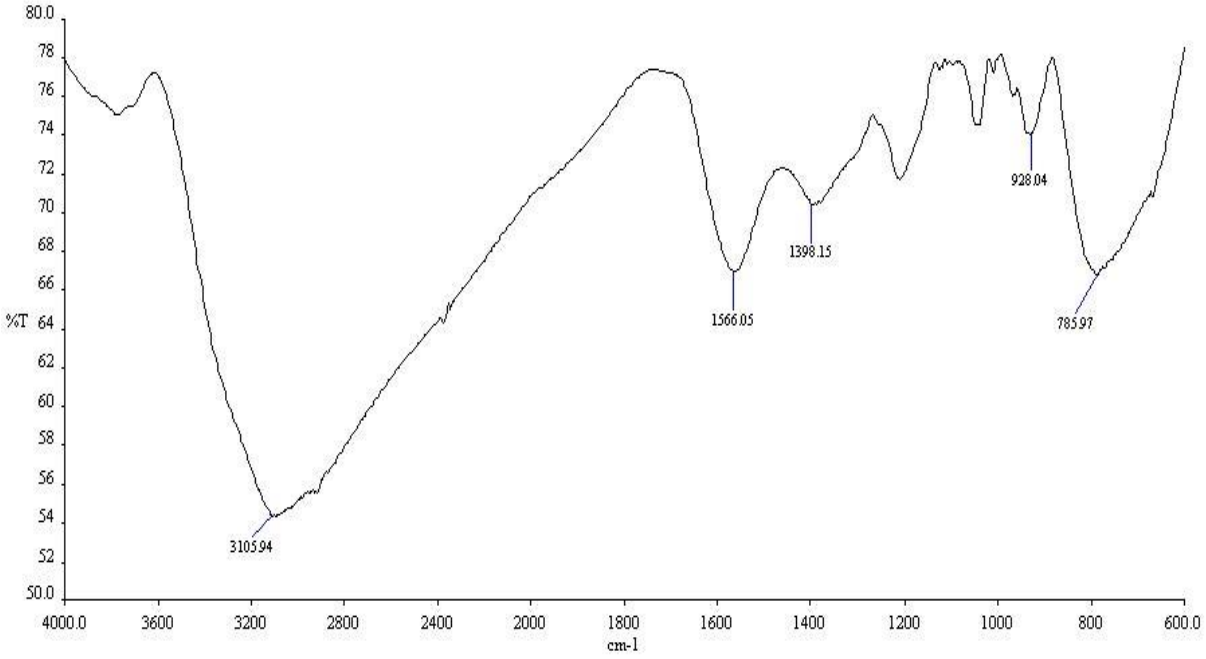

Figure 3.15: IR spectrum of composite C18PC

However, the spectra of all C12 m-TiO_2 samples loaded with pyrrole vapour showed small stretches at 1416 cm^{-1} and 730 cm^{-1} also observed in the pyrrole spectra, indicating that the monomer was successfully loaded into these samples. In all polymer composites there are also bands situated at 1550-1570 cm^{-1} representing a C=C stretching vibration, 1350-1400 cm^{-1} representing a C-C stretching vibration, 930 cm^{-1} representing a C-H out of plane vibration and

finally the stretch at 780-790 cm^{-1} representing the C-H wagging vibration. These confirm the incorporation of polypyrrole in the samples as these stretches are not present in the host material, but are observed in the spectrum of pure polypyrrole.

3.3.2 Solid State NMR

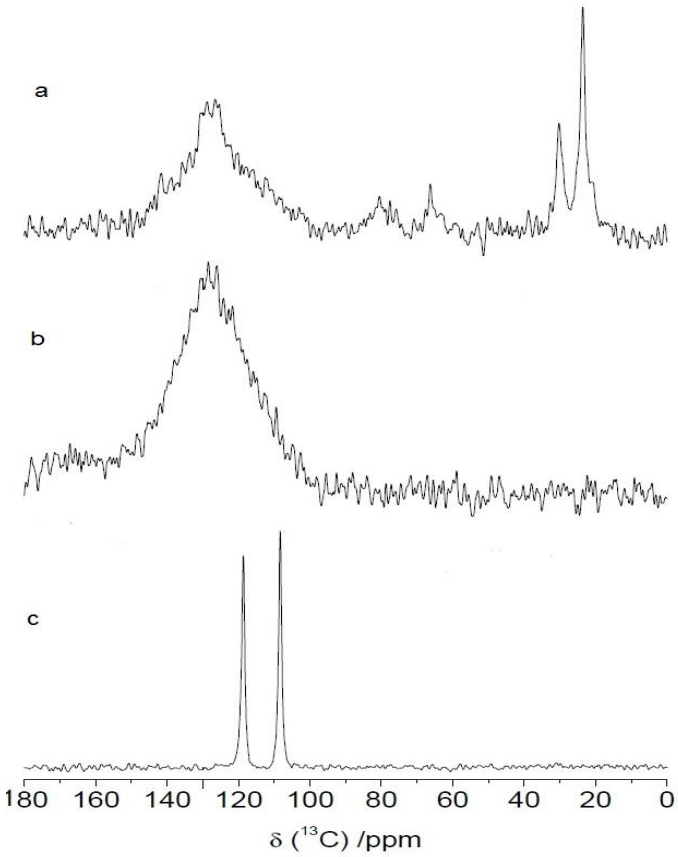

Figure 3.16: ^{13}C CPMAS NMR data of (a) m-TiO_2 polypyrrole composite, (b) polypyrrole and (c) pyrrole acquired at 7.05 T ($\nu 0$ = at 75.45 MHz) using a Bruker 4 mm HX probe spinning at 10 kHz.

The ^{13}C NMR spectrum (Figure 3.16(c)) of the liquid pyrrole monomer exhibits two resonances at δ 107 and 118 ppm, which are in agreement with literature values.[243] However, the corresponding ^{13}C CPMAS NMR spectrum of the solid polypyrrole (Figure 3.16(b)) shows that only a single broad resonance at δ ~130 ppm is observed; this broadening is greater than expected for conventional ^{1}H-^{13}C dipolar coupled induced broadening, and is indicative of additional paramagnetic broadening emanating from the presence of delocalised electrons within the polypyrrole ring and adjoining chain structure. When the pyrrole monomer is polymerised inside the TiO_2 metal oxide framework (Figure 3.16(a)) a similar broad resonance attributed to polypyrrole is detected at δ ~130 ppm, with additional (narrower) resonances

observed in the carbohydrate and aliphatic regions. Low intensity resonances at δ 80 and 65 ppm and high intensity aliphatic resonances δ 23 and 30 ppm are consistent with the partial and complete hydrogenation of pyrrole ring.

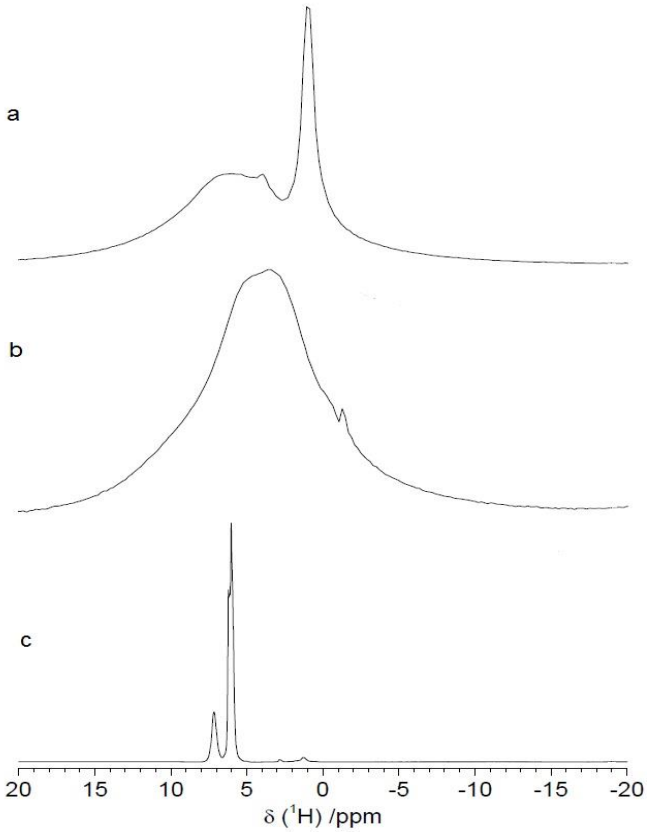

Figure 3.17: ^{1}H one pulse MAS NMR data of (a) m-TiO_2 polypyrrole composite, (b) polypyrrole and (c) pyrrole monomer , acquired at 7.05 T (ν0 = 300.09 MHz) using a Bruker 4 mm HX probe spinning at 10 kHz.

The ^{1}H spin-echo MAS NMR data of the pyrrole monomer (Figure 3.17(c)) exhibits resonances at δ 6.0 and 7.2 ppm which are consistent with the expected ^{1}H chemical shifts of aromatic pyrrole protons.[244] The corresponding ^{1}H spin-echo MAS NMR spectrum of the solid polypyrrole shows a single broad peak centred at δ ~4 ppm which possesses characteristics of both the ^{1}H-^{13}C dipolar and paramagnetic interactions (Figure 3.17(b)). In contrast, the ^{1}H data measured from the polypyrrole/metal oxide composite system in Figure 3.17(a) shows that this broad resonance appears shifted downfield to δ ~6 ppm with this chemical shift change being ascribed to interaction of the pyrrole rings with the electronegative metal oxide surface thus causing the observed deshielding. An additional narrower resonance at δ ~0.8 ppm has become very prominent and this feature is assigned to the aliphatic proton species that are directly associated with the corresponding aliphatic carbon species depicted in Figure 3.17(a).

3.3.3 Electrochemical Analysis:

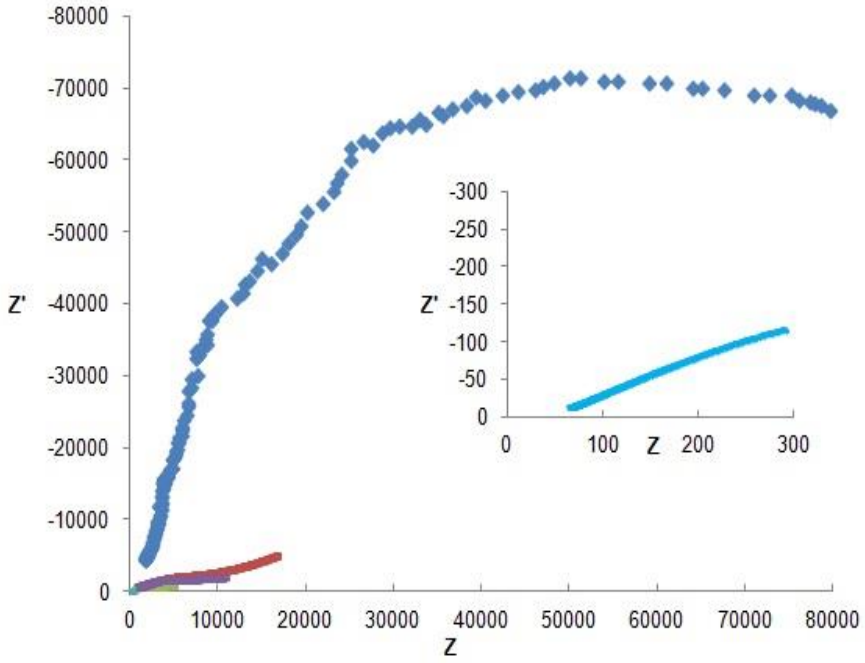

Figure 3.18: EIS Nyquist Plots for C12 m-TiO_2 (blue) PC(5) (red), PC(10) (green), PC(15) (purple) and PC(30) (cyan/ Inset) taken using a two electrode setup with an applied DC bias of 0V between the frequency range of 10^6 and 10 Hz .

As described in the experimental section, powder samples of all materials were pressed into individual disk cells. The potentiostatic impedance for each material was recorded between the frequency range of 10^6 and 10 Hz using a two electrode setup with an applied DC bias of 0 V at standard atmospheric conditions. the results are displayed in the Nyquist plot (Figure 3.18), due to the difficulty in comparing the relative performances in this plot the bode plots for the material is also used shown in Figure 3.19. The inset of the Nyquist plot shows the zoomed spectrum of sample PC(30), which is not clearly visible in the main spectra. This data was used to determine how the amount of polymer present within the pores of the material affects the conductivity. As was the case in Chapter 2, because these materials are being assessed as pellets, the main interest is that of the x axis intercept situated at high frequency region of the impedance spectrum as there is no Li^+ diffusion taking place. this high frequency region provides the value of the resistance for the pellet. For this reason a higher frequency was used in order to obtain the most accurate x axis intercept using frequencies up to 1 MHz that have been shown used in published work demonstrating that it is an acceptable limit for use in these measurements.[231,232] However as mentioned in Chapter 2 it is also important to take into account the influence of contact resistance as the resistance between the active material and

that of the silver conducting resin used as the electrode could affect the readings that are recorded for the conductivity of the material.

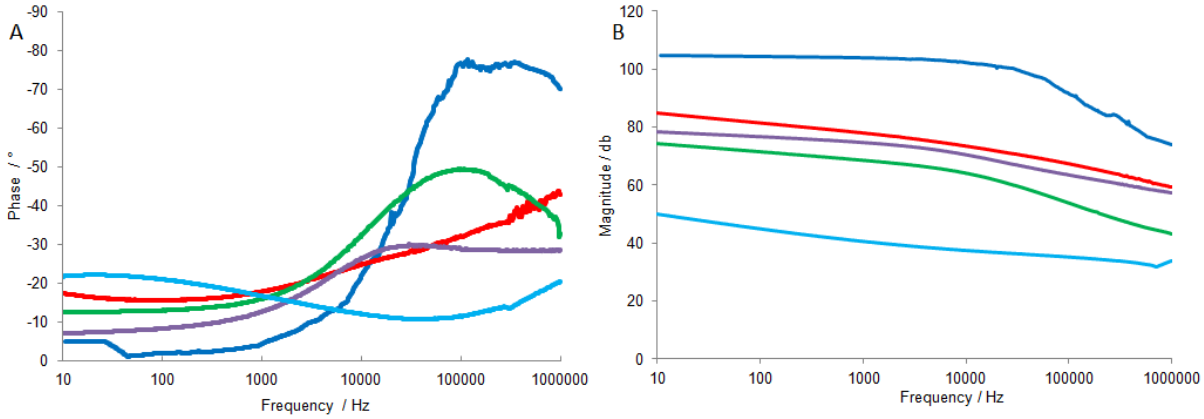

Figure 3.19: EIS Bode Plots depicting (a) phase response and (b) magnitude response for C12 m-TiO_2 (blue) PC(5) (red), PC(10) (green), PC(15) (purple) and PC(30) (cyan/ Inset) taken using a two electrode setup with an applied DC bias of 0V between the frequency range of 10^6 and 10 Hz .

The pristine C12 m-TiO_2 has the largest x axis intercept and hence the lowest conductivity (3.84×10^{-2} mS.cm^{-1}). The composite PC(5) showed a noticeable improvement in conductivity (1.04 mS.cm^{-1}), with increased polymer loading however it is clear that the conductivity did not increase significantly with larger amounts of pyrrole loaded into the structure. Samples PC(10), PC(15) and PC(30) showed similar levels of conductivity 9.96×10^{-1} mS.cm^{-1}, 9.89×10^{-1} mS.cm^{-1} and 2.17 mS.cm^{-1} respectively. The best result shown by sample PC(30) was double the conductivity of sample PC(5) but in the same order of magnitude, despite the significantly higher polymer content. These results are similar to those reported in our previous work where C12 m-TiO_2 saturated with thiophene and then polymerised produced conductivities higher than those of the pristine material (5.79 mS.cm^{-1}).[236] Remarkably, this data demonstrates that the material does not need to be saturated with polymer to reach the peak conductivity level, and that increased loading makes little difference. Thus, further increasing the polymer content increases the weight without producing a noticeable improvement to the conductivity, which decreases the gravimetric energy storage capacity of the material.

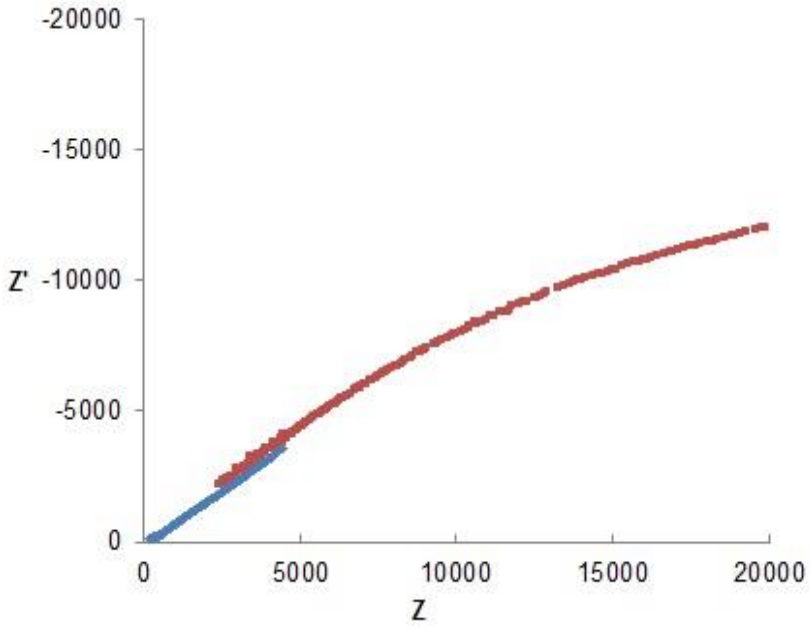

Figure 3.20: EIS Nyquist plots for samples C6PC (blue) and C18PC (red) taken using a two electrode setup with an applied DC bias of 0 V

Conductivity data were also recorded for samples of different pore sizes. Samples C6PC and C18PC were assessed using a two electrode setup with an applied DC bias of 0 V, The Nyquist plots are shown in Figure 3.20 and their respective bode plots can be seen in Figure 3.21. These materials showed similar conductivity values to those of the other composites, producing values of 1.70 $mS.cm^{-1}$ and 1.81 $mS.cm^{-1}$ for samples C6PC and C18PC, respectively.

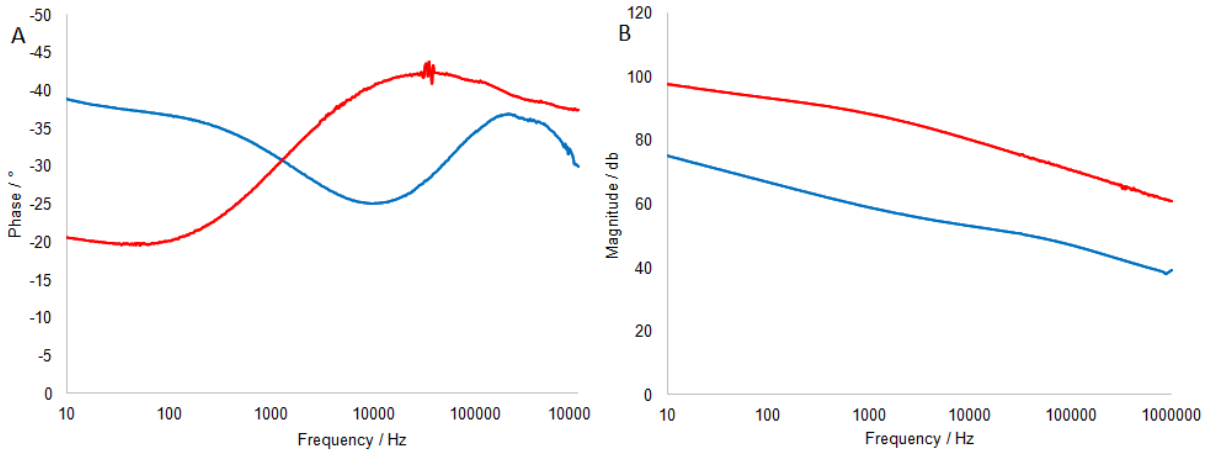

Figure 3.21: EIS Bode plots depicting (a) phase response and (b) magnitude response for samples C6PC (blue) and C18PC (red) taken using a two electrode setup with an applied DC bias of 0 V

Cyclic voltammetry of all materials was carried out using a variety of sweep rates ranging from 0.5 – 5 mVs^{-1}, allowing us to observe the electrochemical characteristics of the material at a variety of different power outputs. Figure 3.21 demonstrates the CV comparisons of all materials at 0.5 mVs^{-1}. The comparison at this slow scan rate presents the clearest picture of the electrochemical nature of the material. The C12 m-TiO_2 shows a higher current output than all of the composites with the exception of sample PC(5), the trend displaying that with increased polymer content the current produced becomes smaller. This is because there is little gain in conductivity to accompany the increase in weight, resulting in a decrease in current produced per gram of material. These results explain why in previous work on polythiophene doped mesoporous titanium oxide, the composites saturated with polythiophene produced inferior CV data compared to the host material.[236] The CV comparison at a high scan rate of 5 mVs^{-1} (Figure 8.8) again shows the same trend. Composite materials show a decrease in performance relative to composite PC(5), however a more resolved oxidation peak situated at 2.2 V is present in all composites whereas the C12 m- TiO_2 shows a single broad peak from 1-2.8 V.

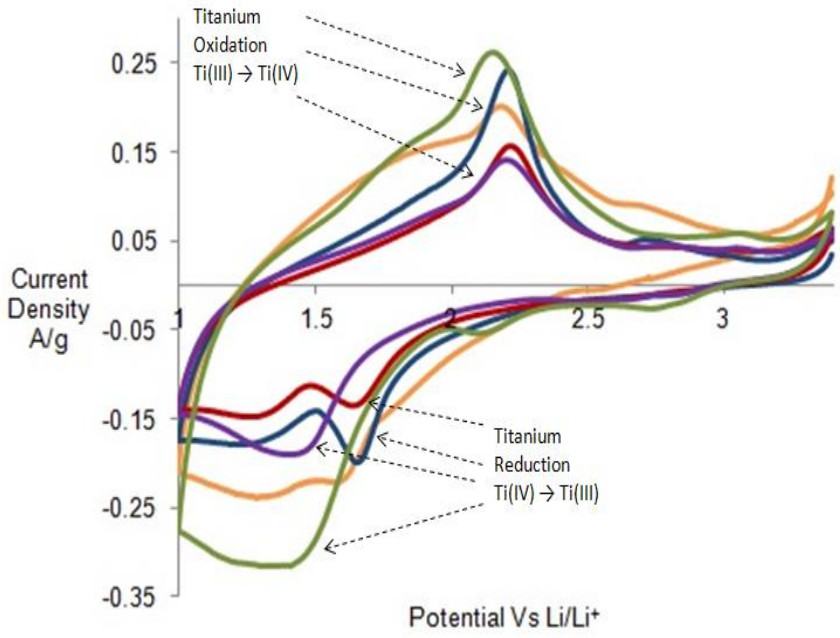

Figure 3.22: Cyclic voltammetry over a potential range of 1-3.4 V vs Li/Li^+ standard electrode potential at a sweep rates of 0.5 mVs^{-1} of samples C12 m-TiO_2 (orange), PC(5) (green), PC(10) (blue), PC(15) (red) and PC(30) (purple)

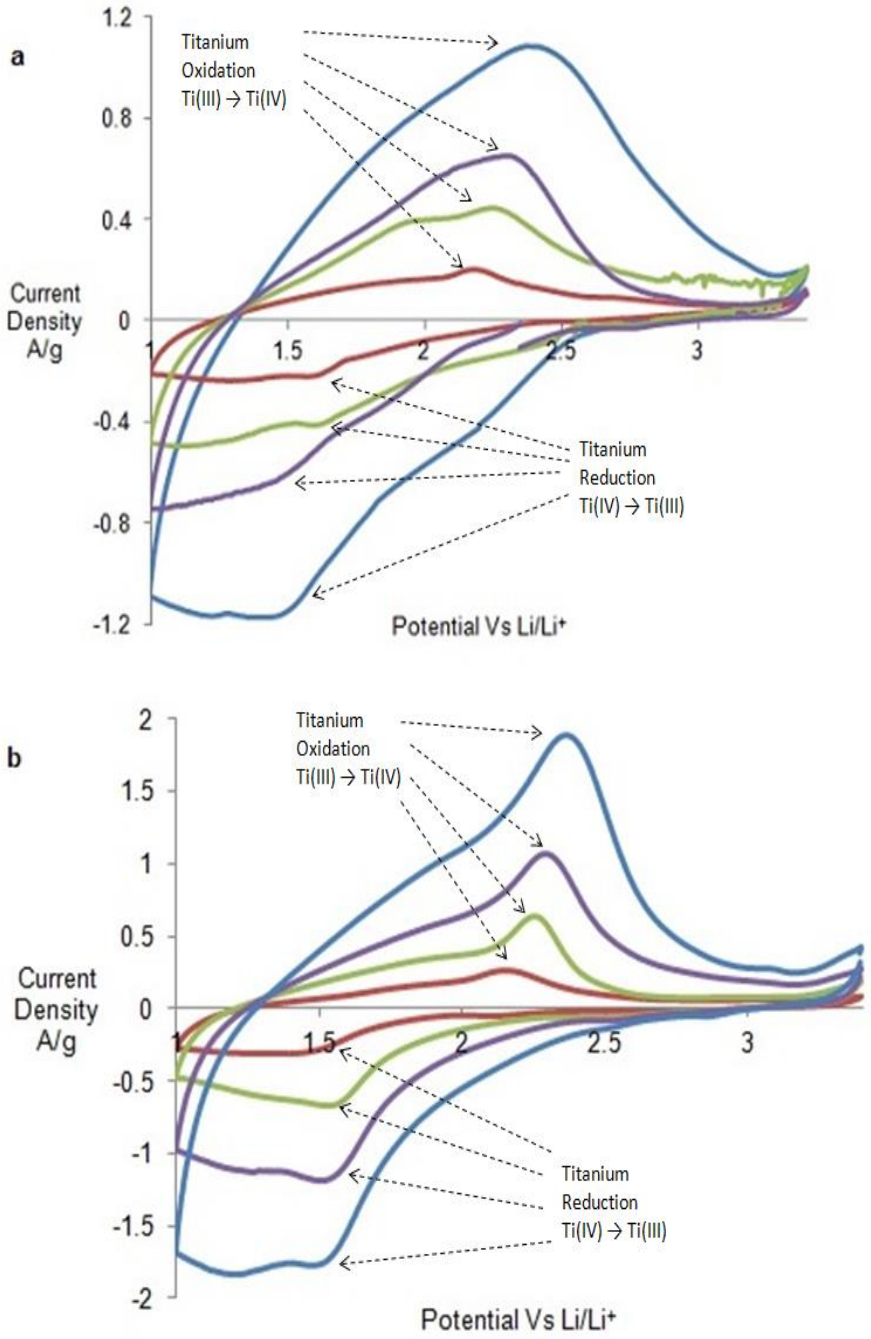

Figure 3.23: Cyclic voltammetry over a potential range of 1-3.4 V vs Li/Li^+ standard electrode potential at various sweep rates of (a) m-TiO_2 and (b) PC(5) (blue) 5 mVs^{-1} (purple) 2 mVs^{-1}, (green) 1 mVs^{-1}, (red) 0.5 mVs^{-1}

This indicates that the composites show a more redox active character when compared to that of the pristine C12 m-TiO_2. When we compare C12 m-TiO_2 and sample PC(5) (Figure 3.23) we are able to observe that with an increase in sweep rate, the composite maintains its redox nature and the peaks remain resolved despite some broadening, whereas the C12 m-TiO_2 peaks remain broad throughout. This is presumably due to the improvements in conductivity allowing

faster insertion and extraction of Li^+ into the internal titanium sites. Both materials appear to produce increases in current proportional to sweep rate, indicative of a surface limited process typically seen for capacitive materials rather than the traditional diffusion limited processes typical for intercalation materials.[31] All other C12 composite materials multiple scan rate CV data is displayed in Figures 8.9 to 8.11. One noticeable trend in the CV data shows that as polymer content increases to 10%, redox nature becomes more pronounced. In composites PC(15) and (30) the peaks become less pronounced and more broad once again, which is likely due to the high level of polymer preventing the Li^+ from being transported to large number of titanium sites, similar results can be seen with samples of different pore sizes. All composites produced superior results when compared to those studied previously using polythiophene.[236] The composites C6PC and C18PC show with the incorporation of polymer, the improved conductivity results in improved redox behaviour relative to the host.

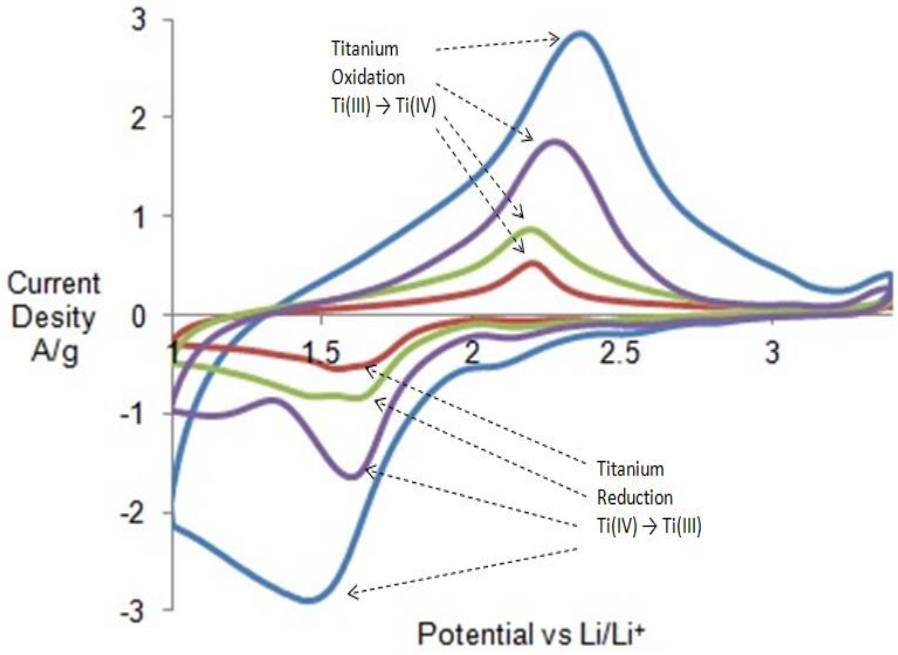

Figure 3.24: Cyclic voltammetry over a potential range of 1-3.4 V vs Li/Li^+ standard electrode potential at various sweep rates of C18PC (blue) 5 mVs^{-1} (purple) 2 mVs^{-1}, (green) 1 mVs^{-1}, (red) 0.5 mVs^{-1}

The composite C18PC shown in Figure 3.24 shows the most resolved redox character of all the samples tested. This is manifested as both more resolved redox peaks in the place of broad capacitive peaks in the host species (Figures 8.12 to 8.14), and an increase in the amount of current produced upon cycling, indicating an increase in both capacity and performance.

The capacity of the material was assessed by carrying out galvanostatic charge discharge analysis. Using cycling measurements over the course of 50 cycles, we are able to assess its capabilities as a secondary lithium battery cathode material. These were carried out at a current density of 1 $mA.cm^{-2}$. The results of the polypyrrole composite materials were compared to the performance of their respective m-TiO_2 hosts, in order to gauge the relative performance each material.

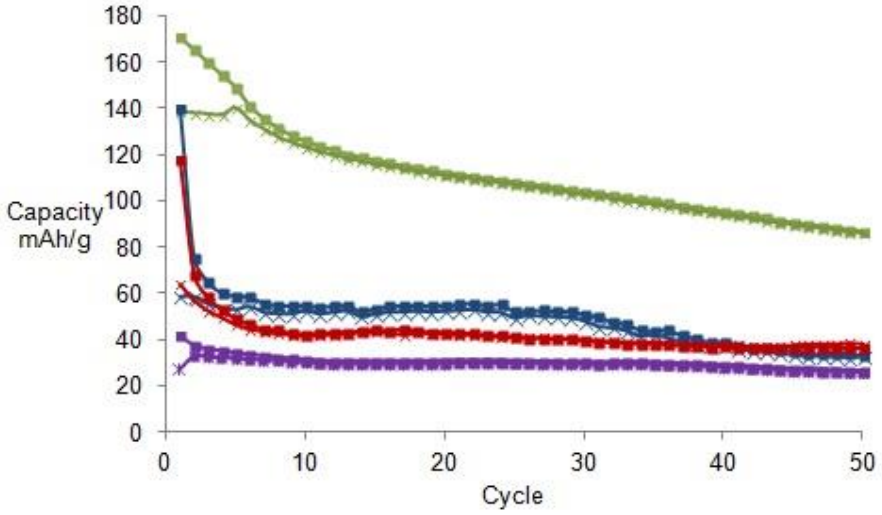

Figure 3.25: 50 Cycles charge (crosses) discharge (squares) capacity data for polypyrrole composites PC(5) (green), PC(10) (blue), PC(15) (red) and PC(30) (purple)

It is apparent from Figure 3.25 that as the polymer content in the structure is increased it produces a noticeable effect on electrochemical performance. The polypyrrole composite materials show initial capacities of 170, 138, 115 and 42 mAh/g, which drop to 86, 33, 36 and 26 mAh/g after cycling, for composites PC(5), (10), (15) and (30), respectively. This was compared to the pristine C12 m-TiO_2 (Figure 8.15), which possesses an initial capacity of 139 mAh/g, which drops to 39 mAh/g after cycling. The cycle life data correlates well with the cyclic voltammetry showing that with an increase in polymer content beyond 5 wt%, the capacity is reduced. In addition the cycling performance of the material decreases. By doping C12 m-TiO_2 with a small amount of polypyrrole within the pores (5 wt%), the performance improves by increasing the initial capacity, and maintaining this capacity over the course of 50 cycles (86 mAh/g), more than double that of the C12 m-TiO_2 (39 mAh/g). Further increasing the polymer content leads to a sudden drop in performance. The initial capacity decreases, and with repeated cycling the capacity falls off dramatically so that after 3 cycles the capacities are reduced to 62, 58 and 38 mAh/g for polypyrrole composites PC(10), PC(15) and PC(30), respectively. This suggests that increasing polymer content within the pores reduces the Li^+

transport capabilities, causing the capacity to decrease as it becomes no longer able to transport Li^+ in and out of the pores. In addition to blocking the pores, the increase in weight with higher polymer content also reduces the amount of lithium stored per gram of material. This explains the results from our previous work on polythiophene nanowires in C12 mTiO_2, where saturation of the host with thiophene vapour prior to polymerisation leads to improved conductivity with a significant decrease in its lithium storage capacity. This effect was attributed to the blockage of the pores post polymer synthesis, because increasing polymer content causes the pore volume to decrease.

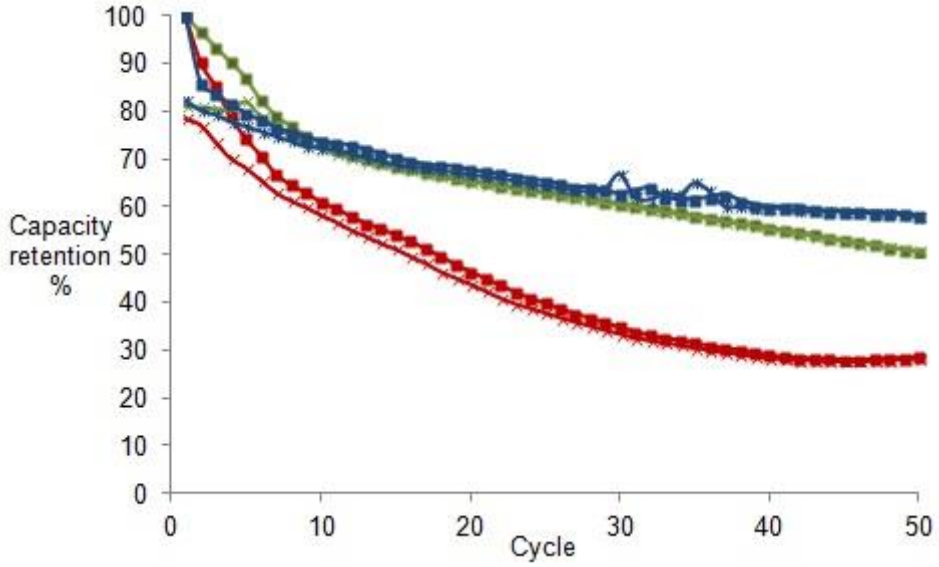

Figure 3.26: 50 Cycles charge (cross) discharge (square) capacity retention of polypyrrole composites C6PC (red), PC(5) (green) and C18PC (blue)

To investigate this hypothesis in this system we investigated the performance of the 5% polypyrrole composites with C12 m-TiO_2 with both smaller and larger pore sizes. Figure 3.26 shows the comparative capacity retention performance of the 5% composites of C6, C12 and C18 templated m-TiO_2. Capacity data for C6PC, C18PC and their respective host materials can be seen in Figure 3.27. The main trend with the pristine materials is that with a decrease in pore size there is little effect on the initial capacity of the material. However, with inclusion of polymer, the initial capacity increases from 100, 138 and 98 mAh/g to 144, 178 and 146 mAh/g for sample C6PC, PC5 and C18PC, respectively. The main difference in initial capacity is most likely due to different surface areas of the host m-TiO_2 materials.

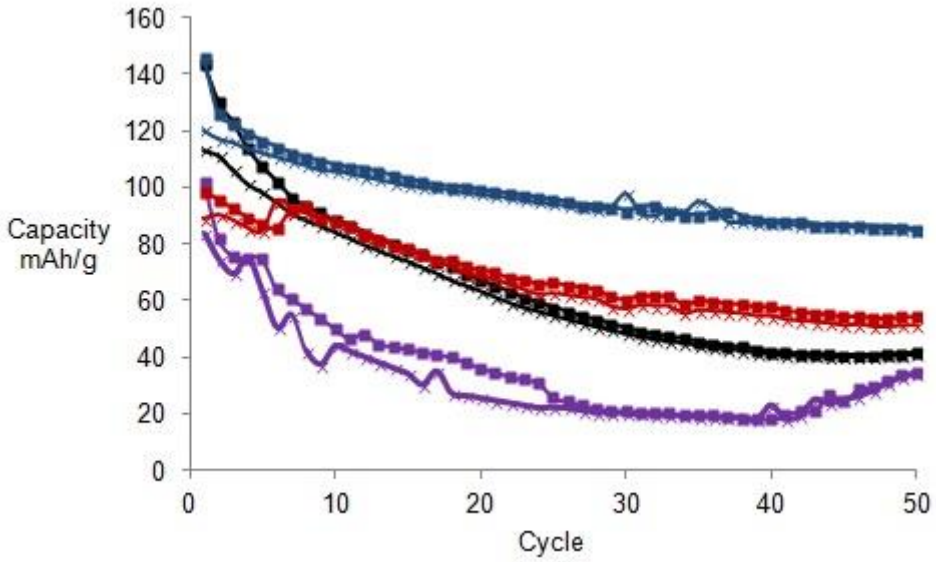

Figure 3.27: 50 Cycles charge (crosses) discharge (squares) capacity data for C6 TiO_2 (red), C6PC (blue) C18 TiO_2 (red) and C18PC (blue) at 1 $mA.cm^{-2}$

It does however produce a notable effect on the cycling performance of the material. After cycling it is observed that the material possessing the largest pores C18PC retains the highest proportion of its initial capacity after cycling at 85 mAh/g (58%), sample PC(5), made with C12 m-TiO_2, retained a capacity of 86 mAh/g, (50.7%) and sample C6PC produced the lowest capacity at 41 mAh/g (28.6%). This trend supports the hypothesis that the smaller pores effect the recyclability of the composite material, when the pores are increased in size there is more room for the ions to diffuse through. This facilitates the insertion-deinsertion process. The reduction in initial capacity of the material therefore is most likely due to the increase in weight of the material brought by incorporation of larger quantities of polymer within the structure, and capacity retention is affected by both the conductivity and pore width of the material.

3.4 Conclusions

By exploring a variety of synthesis parameters, it was possible to determine the best conditions for the successful synthesis of a conducting composite of high surface area amine-templated mesoporous titanium oxides. The incorporation of polymer improved the conductivity of the material, but impregnating the host with excess polymer has little effect on further improving conductivity. By using only 5 wt% polymer loading the conductivity peaks at nearly two orders of magnitude higher than the pristine sample, with retention of high surface area ($427m^2/g$). Sample PC(5) produces the best performance showing the highest initial capacity of 178

mAh/g. The incorporation of the polymer also allowed for improved capacity retention (50% compared to 28% from the host material) over the course of 50 cycles.

The impact of pore size and surface area on the performance on these materials was also determined. Using mesoporous titanium oxides synthesised using C6 and C18 templates, it was determined that over the course of cycling, the C18 materials retained the highest proportion of their initial capacity at 58%. C6 templated materials, despite increasing initial capacity with polymer inclusion, only managed to retain 28% of its initial capacity after cycling. The differences in initial capacity can be linked to that of the surface area of the material, as the mesoporous titanium oxides hosts with the higher surface area possessed the highest initial capacity. Therefore the best performing materials for electrochemical applications are those combining larger pore sizes with high surface area impregnated with only a small amount (5%) of polymer.

Chapter 4 : TiO_2 and Ta_2O_5 – Pyrrole Composites Using a Photochemical Synthesis Procedure

4.1 Introduction

Previously composites of polypyrrole and TiO_2 nanoparticles have been made using UV light in the place of chemical oxidants such as $FeCl_3$.[245–247] The optical excitation of TiO_2 induces the formation of an excited state, reacting with pyrrole to form a radical cation, which then reacts with other cation radicals to form polymer on the surface of the TiO_2. This approach is advantageous over catalyst-based methods because it produces greater interfacial bonding between the two phases, and improves charge migration throughout the structure, while the chemical oxidation route only produces a deposited coating of polymer on top of the oxide.[245] This synthesis technique also reduces the risk of pore blockage by an externally adsorbed oxidant. While the extension of this approach to mesoporous TiO_2 seems obvious, previous work by Domen *et al.* also demonstrated that mesoporous tantalum oxide performs well as a photocatalyst with a bandgap of 3.9-4 eV.[27,28] Thus, this material is also a promising candidate for UV-initiated polymerisation of pyrrole, however, at present very little research has been carried out on the synthesis of polypyrrole composites of large bandgap semiconductor such as Ta_2O_5.[249]

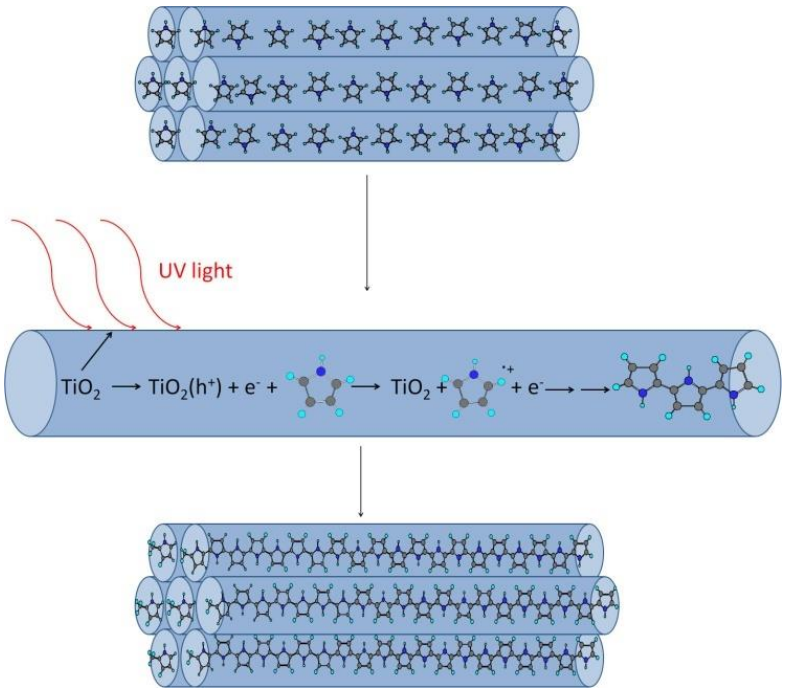

Scheme 4.1: UV synthesis strategy to produce polypyrrole nanowires within the pores of mesoporous TiO_2.

In this work we continue our exploratory studies of improving the electron conductivity of high surface area mesoporous transition metal oxides employed as cathodes in Li^+ battery cells, building on the previous success achieved with polypyrrole nanowires in Chapter 3.[250] The current investigation utilises a superior UV synthesis technique in the place of the previous solution based chemical oxidant synthesis. During the investigation the best materials are fully characterised to observe the effect of this different synthesis on the structure and performance of the materials. The mechanism is outlined in Scheme 4.1. The first step uses the previous method of monomer vapour diffusion loading into the host. This is followed by direct illumination to initiate cation radical formation followed swiftly by polymerisation without the need of any solvent or additional oxidant. During illumination the polymerisation undergoes propagation until the reaction has been completed. This alternative approach of synthesis to improve the interface between the two phases results in the overall simplification of the synthesis procedure by removing the need for a chemical oxidant. It also reduces the effect of leaching of polymer during the polymerisation step as there is no solvent present that can wash out polymer during this process.

4.2 Experimental Section

4.2.1 Synthesis

All chemicals were purchased from either Sigma Aldrich or Alfa Aesar and used without further purification.

Mesoporous TiO_2 (m-TiO_2) and Ta_2O_5 (m-Ta_2O_5)

m-TiO_2 and m-Ta_2O_5 were prepared according to the experimental procedure described previously in section 2.2.1.[250] The only differences in procedure was the use of a tantalum precursor (tantalum(V) ethoxide) for tantalum based composites and the ligand assisted templating was carried out with octadecylamine in the place of dodecylamine.

Transition Metal Oxide-Polypyrrole Composites

Polypyrrole composites of C18 m-TiO_2 were prepared by first loading the host (ca. 400 mg) with pyrrole monomer by vapour diffusion in a sealed container for ½ hour, 1 hour, or 2 hours at 298 °K. The resulting samples were identified as TiC(0.5) TiC(1) and TiC(2), respectively.

The same procedure was used to prepare the Ta_2O_5 composite, however only at the loading time (1 h) that produced the best electrochemical results for Ti. This was identified as sample TaC. The materials were weighed before and after loading to determine increase in weight before transferring them to a stoppered quartz flask. The powders were stirred overnight under 160 W UV illumination at an irradiation distance of 8 cm to complete the polymerisation process. The resulting powders were then washed with 200 mL deionised water for 6 h and filtered, and this process repeated twice to remove residual monomer that might still be present within the material. After the washing stage was complete the product was dried under vacuum for 2 hours at 200 °C to remove any remaining water from the sample.

4.2.2 Characterisation

Brunauer Emmett Teller (BET) surface area and pore size measurements were derived from nitrogen adsorption/desorption isotherms collected on a Micromeritics ASAP 2020. Infrared (IR) spectra were recorded on a Perkin Elmer FT-IR Spectrometer Spectrum RX1 using oven dried KBr discs and data treated on Spectrum 5.1 software. X-ray diffraction (XRD) was performed on Bruker D8 DAVINCI diffractometer with Cu Kα radiation (40 kV, 30 mA) source. The step size was 0.025°. The diffraction patterns were recorded in the 2θ range 1.0 - 100° and the total counting time was 3 hours. The thermogravimetric analysis (TGA) and differential thermal analysis (DTA) was performed on a STA 449C analyser from Netzsch under a flow of dried air at 10.00 °C/min up to 650 °C. Argon was used to protect the balance section. High Resolution Scanning Transmission Electron Microscopy (HRSTEM) was performed in a HD-2700 dedicated Scanning Transmission Electron Microscope (STEM) from Hitachi, with a cold field emitter equipped with a CEOS Cs corrector and operated at 200 kV. The powder samples were simply dry deposited onto a Cu grid covered with a carbon film (Quantifoil) having periodical holes with diameter of 1.2 microns. Observation was made in three different modes: bright field (BF), high angle annular dark field (HAADF) and secondary electron (SE).

4.2.3 Solid State NMR

The ^{13}C cross polarisation, magic-angle-spinning nuclear magnetic resonance (CPMAS NMR) and ^{1}H spin echo MAS NMR data from the TiC(1) and TaC systems were acquired at ambient temperatures (~20 °C) using a Varian InfinityPlus-300 spectrometer (B_0 = 7.05 T) operating at

^{1}H and ^{13}C Larmor frequencies of 300.09 MHz and 75.46 MHz respectively. The ^{13}C CPMAS and ^{1}H spin echo data were acquired using a Bruker 4 mm double channel HX probe which achieved rotational frequencies of 10 kHz. The $^{1}H/^{13}C$ CPMAS NMR were performed with an initial ^{1}H $\pi/2$ pulse of 2.5 μ seconds duration, a $^{1}H/^{13}C$ Hartmann-Hahn contact period of 1 ms and a recycle delay of 3 seconds. TPPM decoupling with a 15° phase change between π pulses of 5 μs duration was applied during acquisition. The 1H spin echo MAS NMR were performed with an initial $\pi/2$ pulse of 2.5 μ seconds duration and a π pulse of 5 μ seconds while the refocus time was 100 μ seconds and a recycle delay of 3 seconds. All ^{1}H and ^{13}C chemical shifts were referenced against the primary standard of TMS via a secondary solid standard of alanine.

4.2.4 Electrochemical Analysis

All electrochemical analysis was performed with a Princeton Applied Research VersaSTAT. Electrochemical performance of the synthesised electrode materials as a Li^{+} battery electrode was assessed using a two electrode set up. The working electrodes (cathode) consisted of 80% active material, 10% super conducting carbon black, and 10% polyvinylidenefluoride (PVDF) by weight. The electrode paste was made by grinding the active material and carbon black to ensure a good mixture of the powders. The powders were then stirred with PVDF and *n*-methyl-2-pyrrolidinone (NMP) solvent until a homogenous paste was formed. The paste was spread onto copper foil (current collector) and the electrode was dried by first heating to 80 °C to bake off any excess NMP solvent before increasing the temperature to 120 °C overnight to allow the electrode material to bind with the current collector, followed by punching out a 15 mm electrode disk. The metal lithium disks were used as the counter electrodes and were also punched into a 15 mm disk. The electrolyte used in this investigation was 1.0 M $LiPF_6$ dissolved in ethylene carbonate (EC) and diethyl carbonate (DEC) solutions at a ratio of 1:1 by volume. All cells were constructed within an argon filled glove box to ensure minimal exposure to oxygen.

Cyclic voltammetry measurements were carried out at a variety of sweep rates 0.5, 1, 2 and 5 mVs^{-1} and the potential windows used in all Titanium based experiments were 1-3.4 V vs Li/Li^{+} reference electrode. Tantalum based experiments carried out within a reduced potential window of 1-3 V vs Li/Li^{+} reference electrode. The initial potential of the scan was determined by the open circuit potential the cell (typically 2.3-2.6 V vs Li/Li^{+}) with the initial scan direction being directed in the reduction direction towards a lower potential limit (1 V vs Li/Li^{+}) with

cycles being completed once the final reduction sweep reaches the starting potential of the cycling process.

Galvanostatic charge discharge measurements were carried out with a current density of 1 $mA.cm^{-2}$ between the potential window of 1-3.4 V vs a Li/Li^+ reference electrode. Weights of each electrode were taken prior to cell assembly to determine cathode mass and then used to calculate capacity relative to mAh/g according to the mass of the electrode.

4.2.5 Electrochemical Impedance Spectroscopy

Electrochemical AC impendence spectra (EIS) were obtained using the same two electrode Li^+ battery cell set up using the active material as the active electrode and a lithium metal foil as the counter electrode. Measurements were applied using a sine wave with amplitude of 5 mV over the frequency range from 100 KHz to 0.01 Hz. Measurements were carried out prior to the initial discharge of the cell, using a biased potential equivalent to that of the open circuit potential of the cell, this was necessary in order to remove the influence of polarisation on the values of conductivity that are produced.

4.3 Result and Discussion

Initial FTIR analysis was used to confirm the successful incorporation of polymer and this was followed by complete electrochemical analysis to determine the best performing materials. These were then subject to further characterisation by nitrogen adsorption, XRD, TGA, NMR and STEM to confirm structure and explore possible structure-property relationships.

4.3.1 Characterisation:

The nitrogen adsorption studies were conducted on starting materials m-TiO_2 and m-Ta_2O_5 as well as their respective composites TiC(1) and TaC. The isotherms for the titanium and tantalum materials are shown in Figure 4.1. Both materials display isotherms on the cusp of type I or type IV, as expected for materials possessing a pore size of between 20-30 Å.[7] Pristine m-TiO_2 possesses a Brunauer Emmett Teller (BET) surface area of 798 m^2/g, which decreases to 691 m^2/g for composite TiC(1). This drop in surface area on polymer incorporation is significantly lower (13.4% decrease) than that observed using the chemical oxidant synthesis

procedure used previously (51.2% decrease).[250] Similar results are observed with the tantalum materials, with the surface area of m-Ta_2O_5 dropping from 256 m^2/g to 222 m^2/g for composite TaC upon polymer incorporation. This small loss of surface area upon completion of vapour loading and UV treatment suggests the pores have been filled with polymer and the composites have retained the mesostructure of the host materials. Furthermore, this higher relative retention of surface area post impregnation may leave more free space within the pores, which could ease Li^+ transport, shown to be a limiting factor in previous work.[236,250]

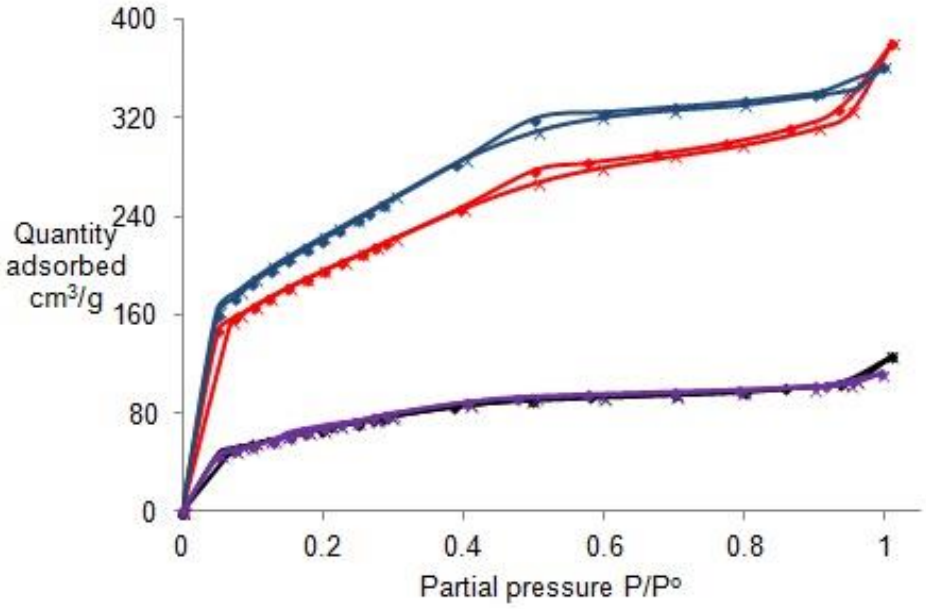

Figure 4.1: Nitrogen adsorption (crosses) and desorption (squares) for m-TiO_2 (blue) composite TiC(1) (red), m-Ta_2O_5 (purple), composite TaC (black)

The low-angle region of the powder X-ray diffraction (PXRD) patterns of composite materials TiC(1) and TaC are shown in Figure 4.2. The broad reflection at 2-3° 2θ related to the mesostructure repeat distance is clearly visible in composite TaC, but less so in TiC(1).[251] While some loss of mesoscopic order may have occurred in the latter material, the presence of this reflection in both composites confirms that the mesoporosity of the materials has largely been retained upon incorporation of the polymer, supporting the nitrogen adsorption data. The high angle XRD patterns for composite TiC(1) and TaC are shown in Figures 8.16 and 8.17, respectively, and clearly show reflections for anatase in TiC(1) with no additional reflections for TaC, confirming the amorphous nature of the walls of this material. The appearance of anatase in the walls of TiC(1) upon UV treatment supports the reduction in the intensity of the

reflection associated with the mesostructure observed in Figure 4.2, as loss of ordered porosity normally accompanies crystallisation of the walls.

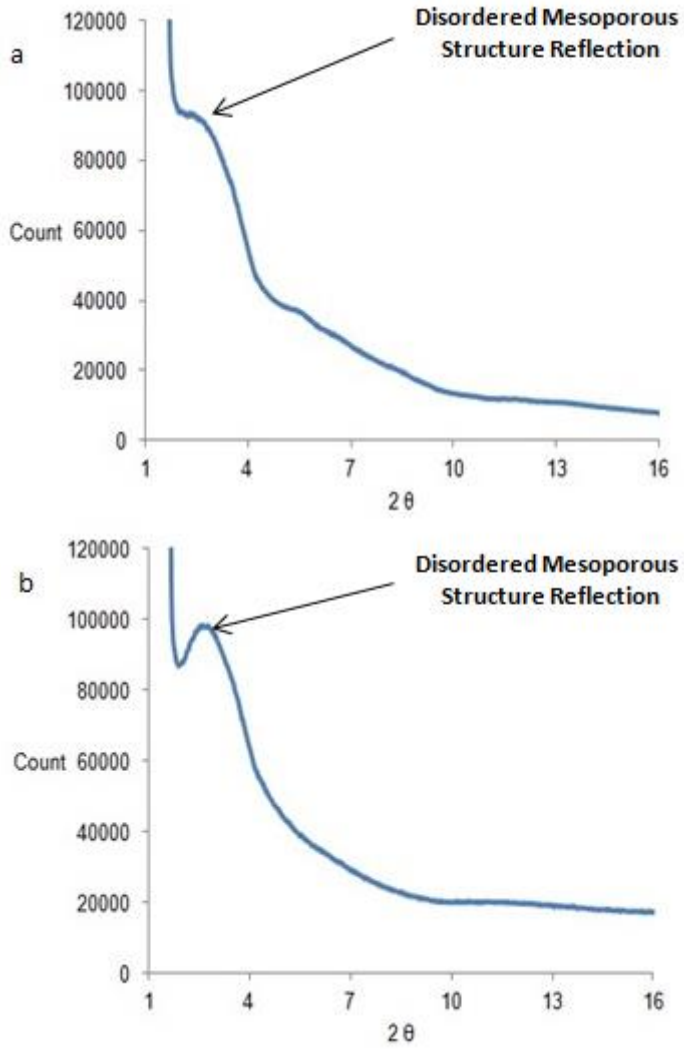

Figure 4.2: PXRD pattern at low angles for samples (a)TiC 1 and (b) TaC

The TGA/DTA data for composites TiC(1) and TaC is shown in Figure 4.3. From previous work on polymer doped mesoporous transition metal oxides we would expect to observe an initial weight loss up to 200 °C corresponding to an endothermic peak in the DTA related to solvent loss.[236,250] However, in both TiC(1) and TaC there is only a small exothermic peak observed from 20-150 °C, which could be due to the release of any residual organic monomer likely that of the amine template, trapped within the pores of the structure. This produces a small exothermic peak, as the smaller organics are desorbed.

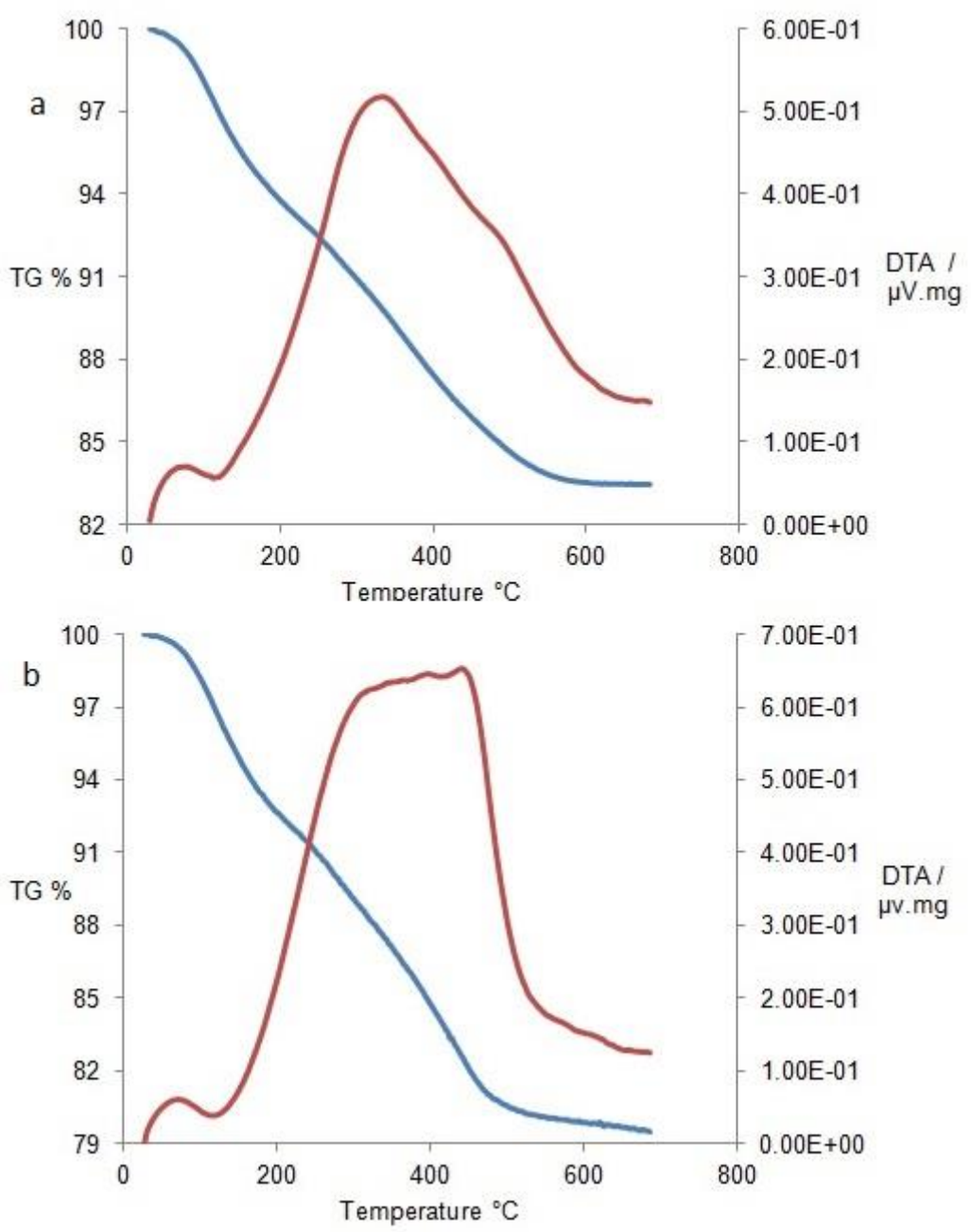

Figure 4.3: Thermogravimetric analysis (blue) and differential thermal analysis (red) plots of (a) TiC 1 and (b) TaC

In this initial region both composites lost approximately 3 wt%. The second region of the plot from 150-600 °C corresponds to the combustion of the longer polymer chains within the structure, and displays a much larger exothermic peak, as expected from our previous work on related systems. Composite TiC(1) lost 13 wt% in this region with sample TaC losing 17 wt%. The greater incorporation of polymer in TaC, in spite of its lower surface area relative to the Ti composites suggests a more efficient polymerisation process in the Ta system. Comparison

of the TGA results for TiC(1) to the chemical oxidant method, which produces a Ti composite containing only 10 wt% carbon with greater loss of surface area relative to the parent material,[250] underline the superiority of the UV method.

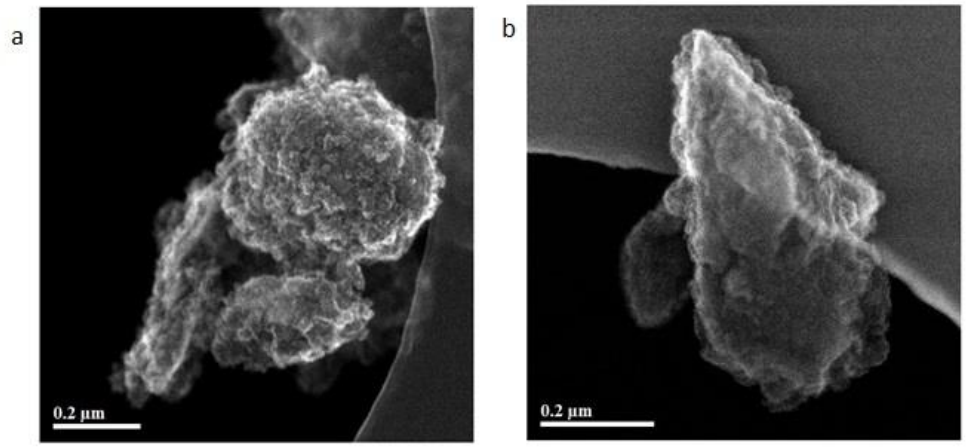

Figure 4.4: SEM SE images of pyrrole composites (a) TiC(1) (100 kx) and (b) TaC (130 kx)at low magnification

To further explore the pore structure and powder morphology, scanning transmission electron microscopy (STEM) was carried out on composites TiC(1) and TaC at three different levels magnification. Figure 4.4 shows the powder morphology of the composites as the images reveal clusters of grains without any clear structural motif. This is similar to what has been observed in previous work and is expected for amine-templated mesoporous oxides.[236]

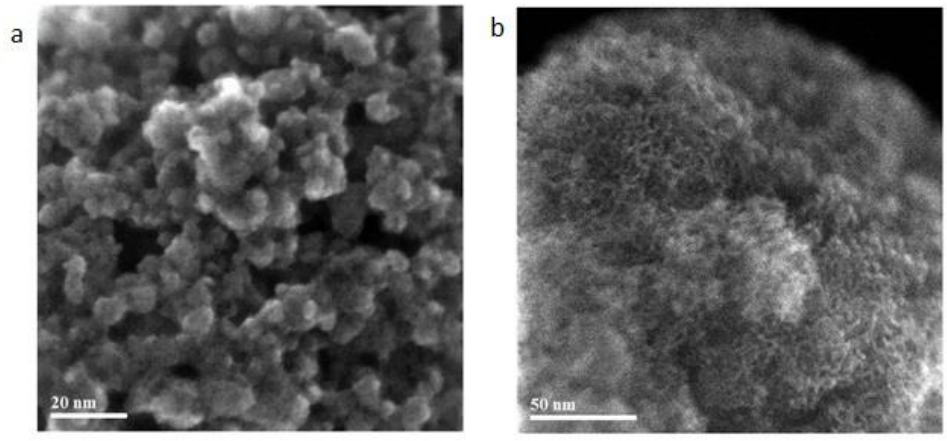

Figure 4.5: SE images of pyrrole composites (a) TiC(1) (900 kx) and (b) TaC (500 kx) at intermediate magnification

When viewed at a higher magnification it is possible to discern the amorphous pore structure of both materials, which is fully visible throughout the image for composite TiC(1) and

discernible towards the lower half of the image for composite TaC, as shown in Figures 4.5(a) and b, respectively. Holes and dark patches demonstrate the gaps produced by the presence of pores within the structure. The presence of pore structure in these images after incorporation of the polymer further confirms the retention of the mesostructure.

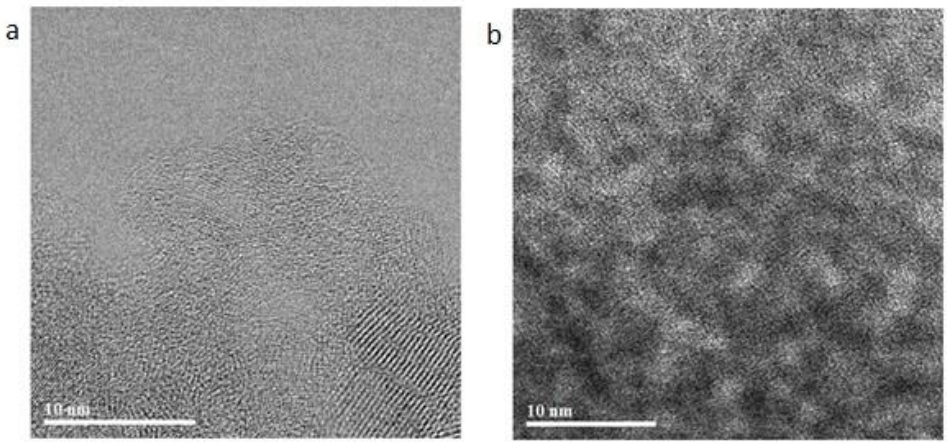

Figure 4.6: TEM BF images of pyrrole composites (a) TiC(1) (3.5 Mx)and (b) TaC (3.0 Mx) at highest magnification

The highest magnification images shown in Figure 4.6, enable us to observe any crystal lattice structure, if present, in the materials. The titanium composite in Figure 4.6(a) remains predominantly amorphous with small crystalline regions scattered throughout, consistent with the appearance of anatase in the XRD. The images of TaC from Figure 4.6(b) show predominantly amorphous regions with little if any traces of crystalline lattice structure. These observations are in agreement with the XRD data shown in Figure 4.2 and are typical of amine templated mesoporous oxides in general.[163]

FTIR studies were carried out on all materials and the results shown in Figures 4.7 and 4.8 with remaining spectra shown in Figure 4.9 to and 4.10 along with spectra from pyrrole and polypyrrole (Figures 8.6 and 8.7 respectively) to assist in assigning bands in the composite samples. Figures 4.7 and 4.8 shows typical spectra for fully characterised materials TiC(1) and TaC respectively. The pyrrole and polypyrrole spectra display four characteristic peaks located at 3100 cm^{-1} (aromatic C-H stretch), 1500-1600 cm^{-1} (aromatic C=C stretch), 1300-1400 cm^{-1} (C-C stretching vibration) and 800 cm^{-1} (C-H aromatic bending vibrations).[241,252] These stretches are observed in both the spectra of the monomer and polymer, however the stretches for the polymer are situated at lower wavenumbers than those of the respective monomer due to an increase in the conjugation. Since the spectra of pristine m-TiO_2 and Ta_2O_5 both show

strong residual water stretches at 3200 cm^{-1} and 1600-1650 cm^{-1}, in addition to a weaker stretch situated at 800-820 cm^{-1}, polypyrrole stretches expected in these regions will be obscured, and therefore only the stretches situated at 1400 and 730 cm^{-1} can only be used to confirm the presence of polymer within the structure.[250] In all composites there is a C-C stretching vibration from 1417-1400 cm^{-1}, indicating an increase in conjugation due to polymerisation. Furthermore, when comparing the respective Ti composites prepared at different vapour-loading times, as monomer loading increases this stretch at 1417-1400 cm^{-1} gains intensity and definition as more polymer is incorporated into the structure. In addition to this increase in intensity, the stretch at 1400-1402 cm^{-1} in the monomer moves to lower wavenumbers, indicating an increase in conjugation and successful polymerisation by the UV reaction with mesoporous hosts.

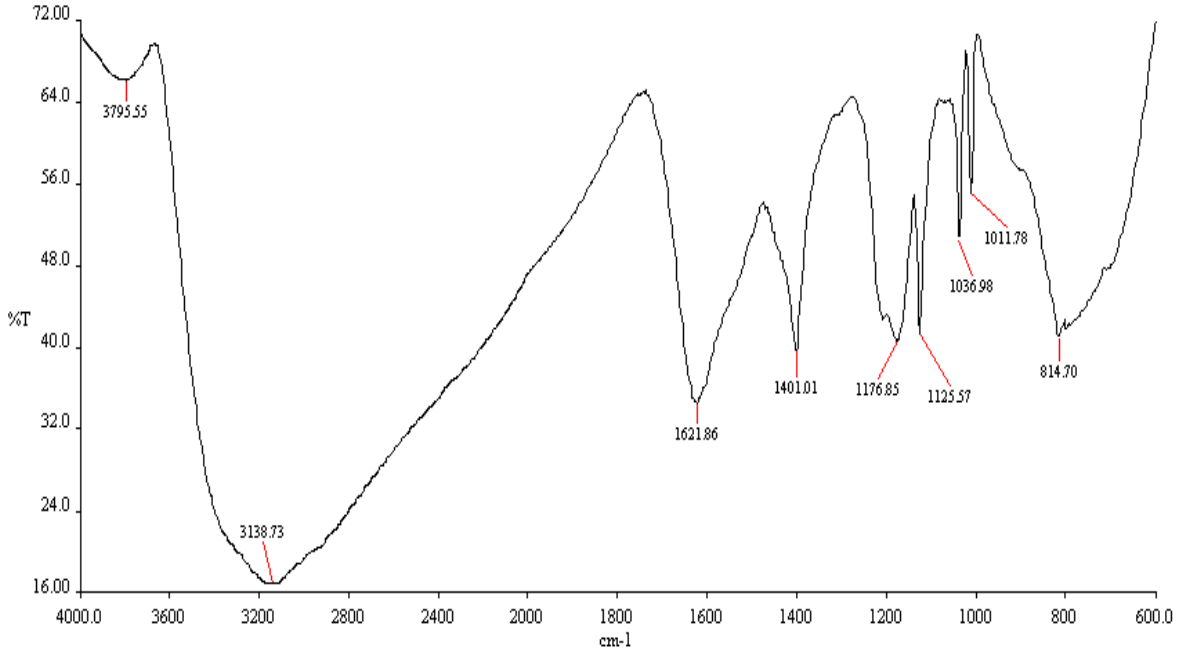

Figure 4.7: IR spectrum of composite TiC 1

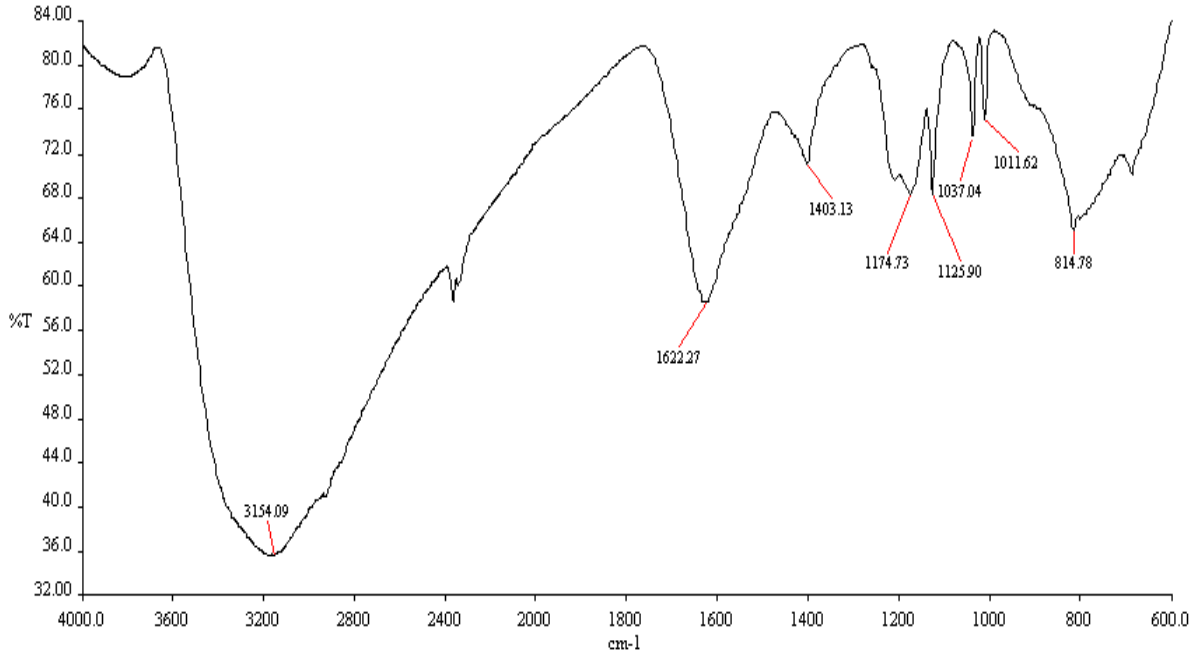

Figure 4.8: IR spectrum of composite TaC

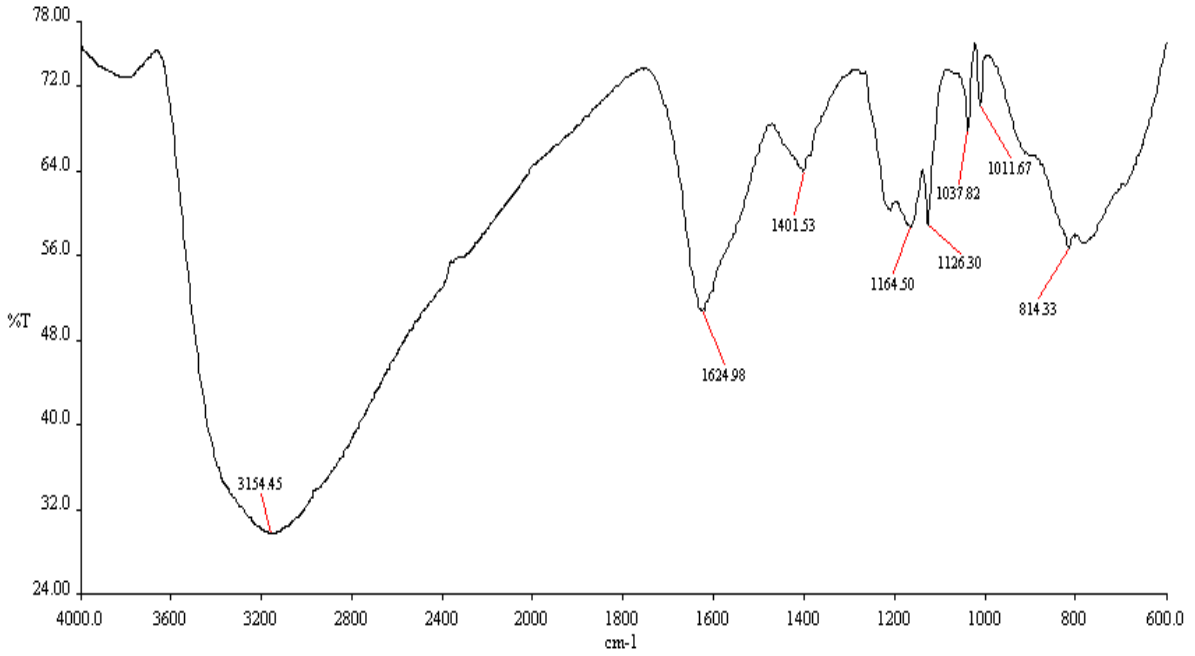

Figure 4.9: IR spectrum of composite TiC 0.5

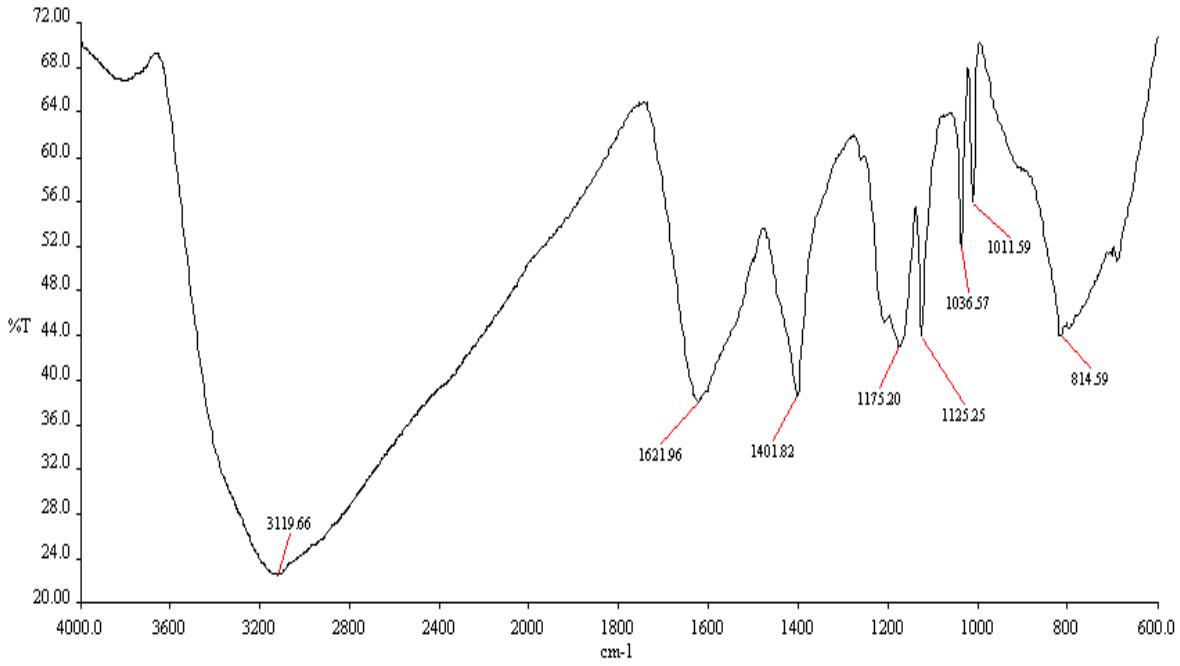

Figure 4.10: IR spectrum of composite TiC 2

As only limited information on the nature of the pyrrole species in the pores can be extracted from these FTIR spectra, NMR studies were conducted on the composites.

4.3.2 Solid State NMR

The ^{13}C spectra of polypyrrole and pyrrole synthesised using the chemical oxidant method is shown in Figure 4.11. Pyrrole displays resonances at 108 and 118 ppm, compared to the polypyrrole, which shows a single broad resonance at 130 ppm. Figure 4.12(b) shows aromatic ^{13}C resonances at δ 140.8, 126.6 and 128.9 ppm. The gap between 140.8 ppm and 126.6, 128.0 ppm is roughly consistent with the expected gap between alpha and beta carbon in polypyrrole, (~125 and ~105 ppm in literature).[253,254] Thus, these resonances confirm the successful polymerisation by the UV reaction. However, the chemical shift values of polypyrrole in TiC(1) are significantly higher than their pure counter parts due to the environment in the pores. Additionally, there is a very broad resonance under these narrow resonances which could be the narrower resonances broadened by proximity to a paramagnetic centre (the conduction protons). The resonances at 19.4 and 30.0 ppm are consistent with the chemical shift of reduced pyrrole.

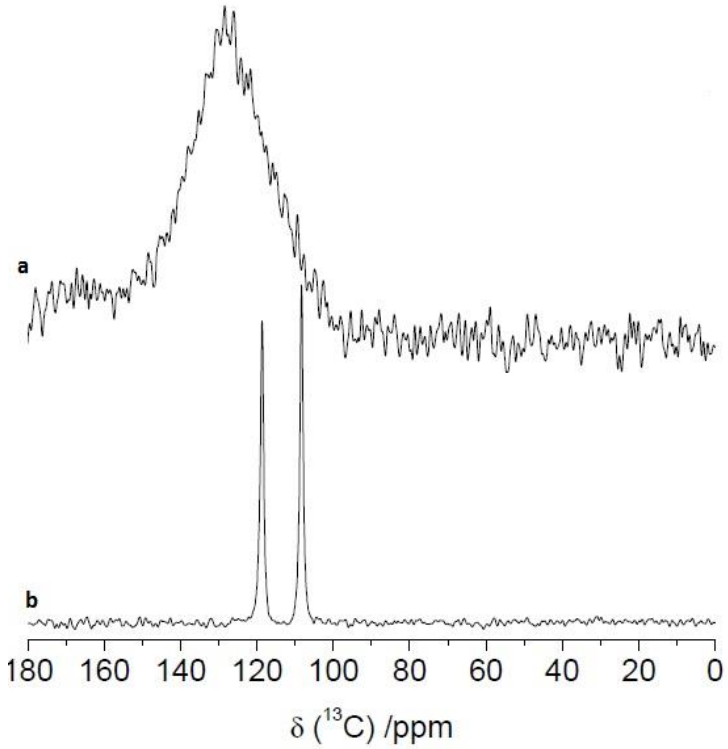

Figure 4.11: ^{13}C CPMAS NMR data of (a) polypyrrole and (b) pyrrole acquired at 7.05 T ($\nu 0$ = at 75.45 MHz) using a Bruker 4 mm HX probe spinning at 10 kHz.

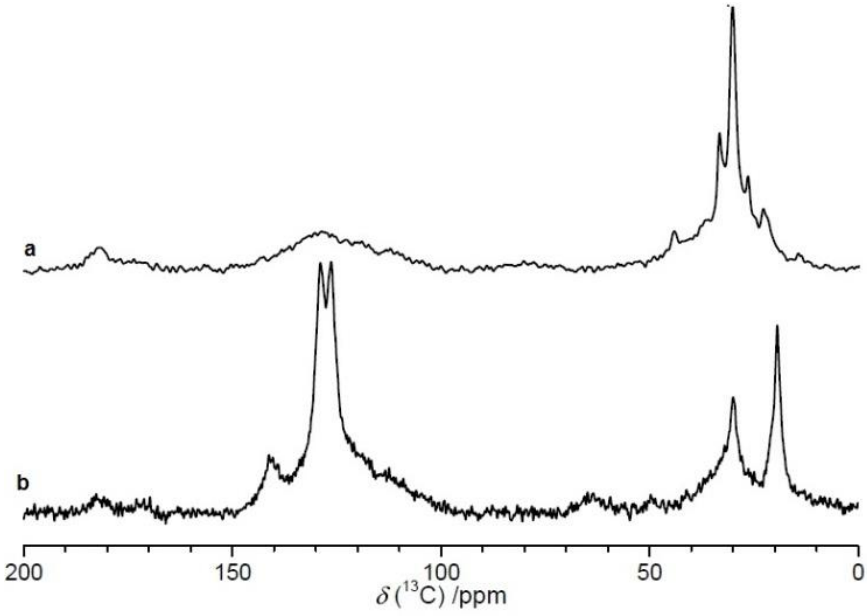

Figure 4.12: ^{13}C CPMAS NMR data of (a) composite TaC, (b) composite TiC(1) acquired at 7.05 T ($\nu 0$ = at 75.45 MHz) using a Bruker 4 mm HX probe spinning at 10 kHz

The ^{1}H spectrum of pyrrole and polypyrrole is provided in Figure 4.13. Pyrrole protons show resonances at 6 and 7.2 ppm while the solid polypyrrole has a single broad resonance centred

around 4 ppm due to paramagnetic interactions. composite TiC(1) seen in Figure 4.14(b) shows broad resonances at δ 6.9 and 7.7 ppm which are consistent with aromatic and/or hydrogen bonded protons similar to those seen in previous work, but less so than one would be expected if there were broadened by paramagnetism. However, there are also aliphatic proton resonances at δ 1.4, 2.0 and 3.4 ppm, which are not expected in the spectrum of polypyrrole. These have previously been assigned to reduced pyrrole. This is in agreement with the ^{13}C spectra of TiO_2 polypyrrole. The ^{13}C spectrum of TaC shown in Figure 4.12(a) is significantly different than that of TiC(1). First, there is a very broad and consequently weak resonance at δ ~130 ppm which is the aromatic ^{13}C resonance. However, there are no narrow resonances like those in the TiC(1) spectrum. This suggests that in TaC these environments are broadened by proximity to a paramagnetic centre (the conduction protons). There are several narrow resonances between δ 20 and 40 ppm, which are again assigned to reduced pyrrole. However, these resonances are not broadened because they are further away from the conduction protons. The TaC ^1H spectrum, displayed in Figure 4.14(a), shows a resonance at δ 5.5 ppm consistent with aromatic protons. There are also two resonances at δ 0.4 and 0.9 ppm which could be consistent with reduced polypyrrole though they are at significantly lower chemical shift than they appear in the TiC(1) spectrum.

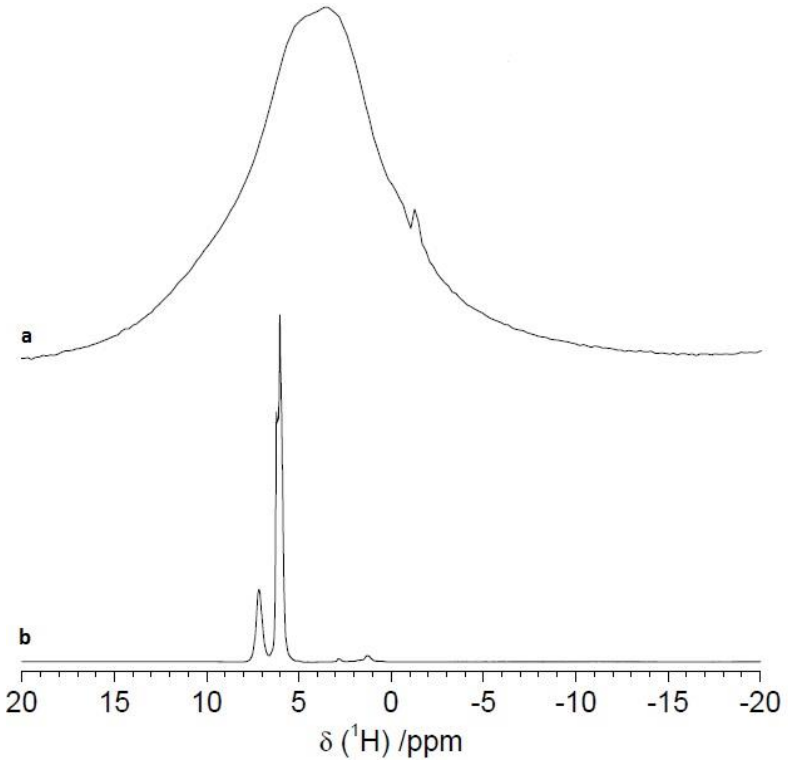

Figure 4.13: ^1H one pulse MAS NMR data of (a)polypyrrole and (b) pyrrole monomer , acquired at 7.05 T ($\nu 0$ = 300.09 MHz) using a Bruker 4 mm HX probe spinning at 10 kHz.

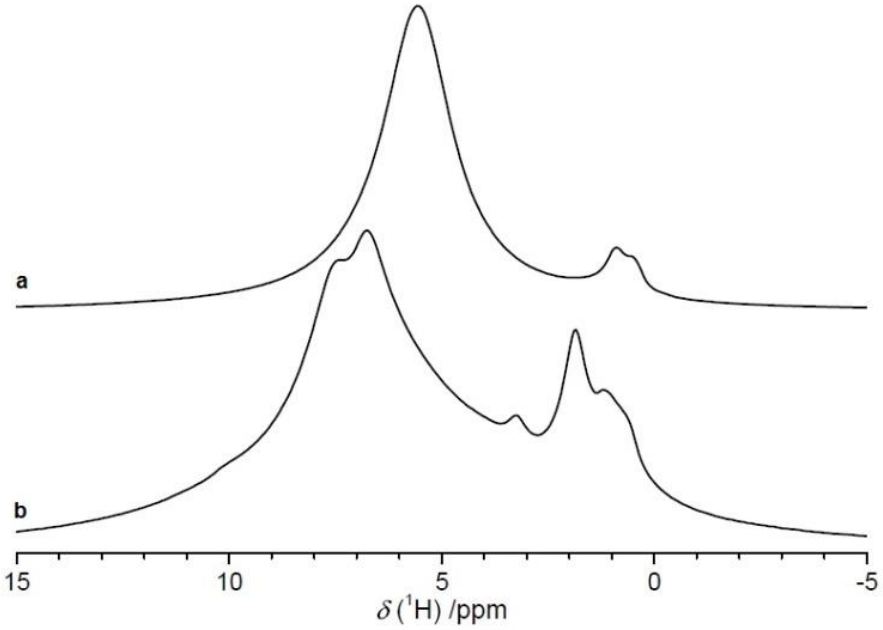

Figure 4.14:[1]H one pulse MAS NMR data of (a) composite TaC, (b) composite TiC(1) acquired at 7.05 T (ν0 = 300.09 MHz) using a Bruker 4 mm HX probe spinning at 10 kHz.

4.3.3 Electrochemical Analysis:

In order to study the effect of polymer incorporation on the conductivity of the materials, electrochemical impedance spectroscopy (EIS) experiments were carried out on all materials. The impedance measurements were all carried out using a two electrodes setup prior to the initial discharge, using a biased potential equivalent to that of the open circuit potential of the cell over the frequency range from 100 KHz to 0.01 Hz, all open circuit potential values are listed in the Figure caption. By examining a Nyquist plot it is possible to discern three separate regions. First, there is the high frequency segment, which contains the lowest x-axis intercept and corresponds to the resistance of the electrolyte within the cell (R_{el}). As frequency decreases this is followed by a partial semicircle, from which a higher intercept, known as the charge transfer resistance (R_{ct}) can be obtained by modelling. This is finally followed by a linear section at low frequencies corresponding to the lithium diffusion process (W). Because the diffusion rate within the electrolyte solution is always significantly higher than that of the solid-state electrode, the R_{ct} is considered the rate-determining step in this measurement. Figure 4.15 shows the Nyquist plots for m-TiO_2 and all its respective composites prepared at different loading levels. with all values for R_{ct} and R_{el} provided in Table 4.1. The composite materials possess R_{ct} values of 50.84, 25.46 and 55.01 Ω for TiC(0.5), (1) and (2), respectively, which

are all significantly smaller than the value of 102.66 Ω measured for the m-TiO_2 host. This decrease in R_{ct} indicates that polymer incorporation into the host has produced a significant improvement in the conductivity, and that the amount of polymer present in the initial loading stage directly affects the resistivity of the final material. Figure 8.18 shows the Nyquist plots for mesoporous tantalum oxide and its composite TaC. The R_{ct} has also decreased from 341.57 Ω in the host materials to 145.54 Ω in TaC. Once again, these results confirm that incorporation of polypyrrole within the pores of the material leads to improved conductivity, however the Ta materials are generally more resistive than their Ti analogues.

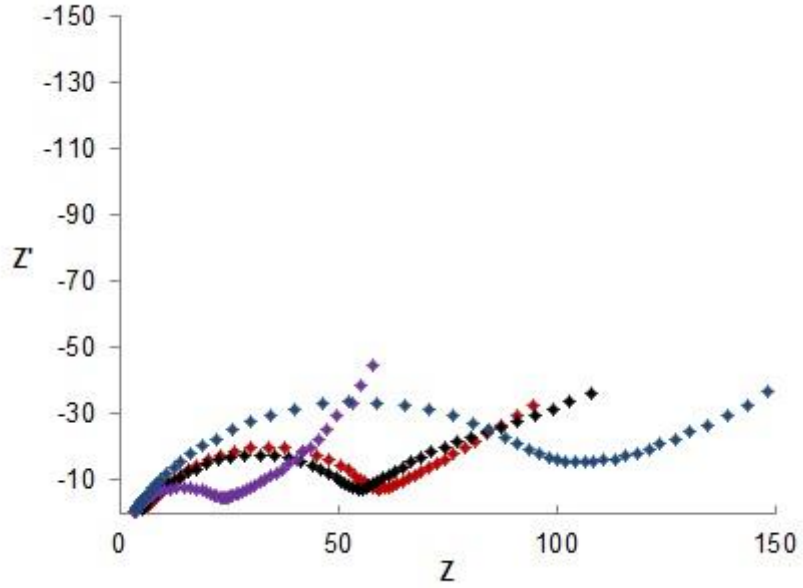

Figure 4.15: Nyquist Plot over the frequency range from 100 KHz to 0.01 Hz using a two electrode setup, using biased potentials equivalent to the open circuit potential of the cell, m-TiO_2 at 2.275 V vs Li/Li^+ (blue), TiC(0.5) at 2.255 V vs Li/Li^+ (black), TiC(1) at 2.290 V vs Li/Li^+ (purple) and TiC(2) at 2.215 V vs Li/Li^+ (red)

Sample	**R_{el}**	**R_{ct}**	**Actual R_{ct} (R_{ct}-R_{el})**
m-TiO_2	3.16	105.81	102.65
TiC 0.5	4.50	55.34	50.84
TiC 1	3.36	28.82	25.46
TiC 2	5.00	60.01	55.01
Ta_2O_5	4.56	346.13	341.57
TaC 1	2.27	147.81	145.54

Table 4.1: EIS data for M-TiO_2, m-Ta_2O_5 and all respective composite materials

The low frequency region of the Nyquist plot, referred to as the Warburg impedance, is used to calculate the Li^+ diffusion coefficient using Equation 4.1.[255]

Equation 4.1 $$D = (R^2T^2)/(2A^2n^4F^4C^2\sigma^2)$$

Where T is the absolute temperature (298 ºK), R is the noble gas constant (8.314 MPa cm^3 mol^{-1} K^{-1}), n is the number of electrons involved in the redox reaction, A is the contact area of the electrode (π x 0.75^2 (cm^2)), F is Faraday constant (96485 C mol^{-1}), C is the concentration of Li^+ in the electrolyte (1 mol cm^{-3}), D is the lithium diffusion coefficient (cm^2 s^{-1}), and σ is the Warburg factor (Ω $s^{-1/2}$).

The lithium diffusion coefficient allows us to compare diffusion charge transport properties of the respective materials. However to calculate the diffusion coefficient we must first calculate the Warburg factor, this can be calculated according to Equation 4.2.[256,257]

Equation 4.2 $$Zre = Rct + R1 + \sigma\omega^{-1/2}$$

Where ω is the frequency and Z_{re} is the real impedance. The relationship between real impedance and frequency is used to plot a straight line in which the gradient will provide the value of the Warburg factor (σ). The plots for σ are provided in Figure 4.16 and 4.17 for the Ti and Ta materials, respectively.

The values of σ demonstrate the differences of Li^+ diffusion coefficient, as concentrations are identical in all materials, with all measurements taking place prior to initial discharge. Mesoporous TiO_2 produced a σ value of 32.05 Ω $s^{-1/2}$ with the composite materials TiC(0.5), TiC(1) and TiC(2) producing σ values of 22.67, 14.62, 23.57 Ω $s^{-1/2}$ respectively. By inserting these values into Equation 4.1 it is possible to calculate values of Li^+ diffusion coefficient for all the materials. Mesoporous TiO_2 was calculated at 1.1 x 10^{-17} cm^2 s^{-1} changing to 2.21 x 10^{-17}, 5.3 x 10^{-17} and 2.04 x 10^{-17} cm^2 s^{-1} for composite materials TiC(0.5), TiC(1) and TiC(2) respectively. This produces respective ratios of (4.80):(2.0):(1.85):(1) for TiC(1), TiC(0.5), TiC(2) and TiO_2, respectively. These ratios demonstrate the material with the best Li diffusion capabilities is TiC(1) as it has a diffusion coefficient nearly five times higher than the starting material. These values are of a similar magnitude to those seen for other reported TiO_2 materials

($1x10^{-15}$ – $1x10^{-17}$ cm^2 s^{-1})[31,92,258] These results show close agreement to the results obtained from impedance analysis with the order of performance being TiC(1)>TiC(0.5)>TiC(2)>TiO_2.This confirms that with increased polymer content up to 10 wt%, the performance increases before deteriorating due to reduced lithium transport properties and increased weight.

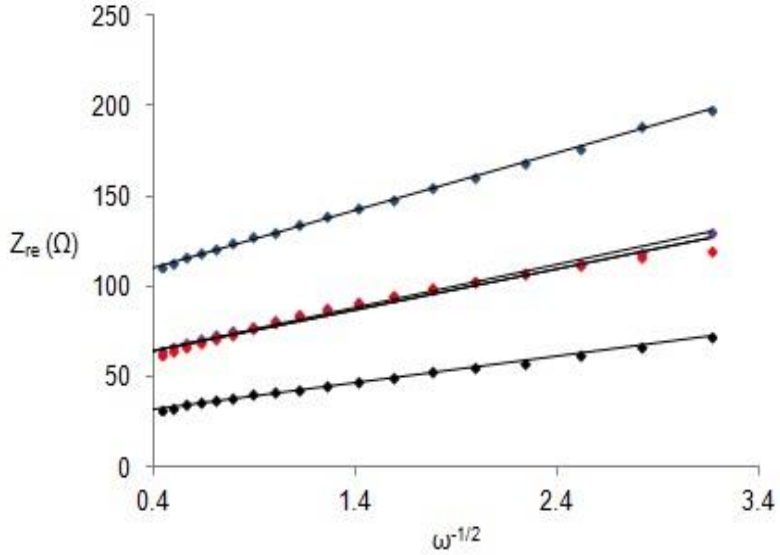

Figure 4.16: Plot real impedance vs reciprocal square root of frequency for titanium materials TiO_2 (blue), TiC(0.5) (red), TiC(1) (black) and TiC(2) (purple)

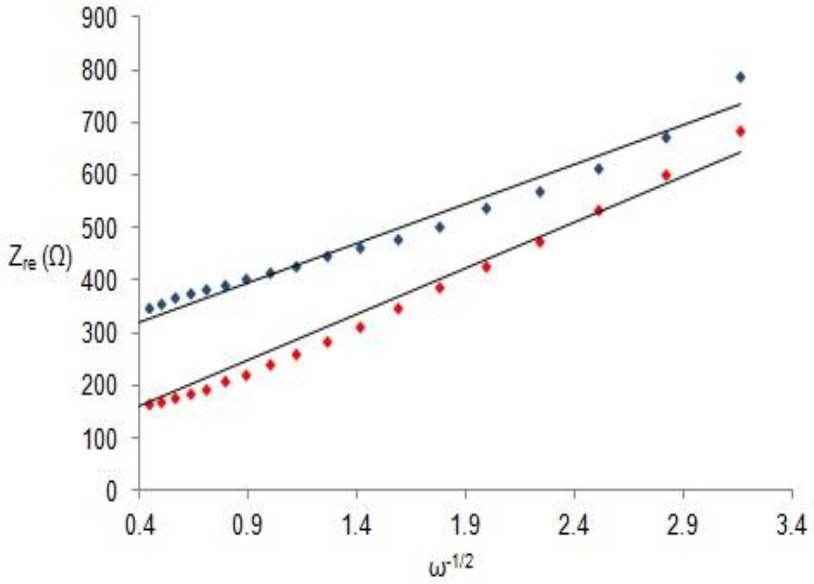

Figure 4.17: Plot of real impedance vs reciprocal square root of frequency for tantalum materials Ta_2O_5 (blue), TaC (red)

The results for the Ta materials produced a σ value of 149.6 to 148.2 Ω $s^{-1/2}$ for m-Ta_2O_5 and TaC respectively. By inserting these values into Equation 4.1 it is possible to calculate values of Li^+ diffusion coefficient. Mesoporous. Ta_2O_5 was calculated at 5.07 x 10^{-19} cm^2 s^{-1} and Composite TaC produced a value of 5.16 x 10^{-19} cm^2 s^{-1}. These results demonstrate that there is little change to the diffusion coefficient with polymer incorporation, these diffusion coefficients are both sufficiently lower (~100 x) than those of the analogous Ti materials.

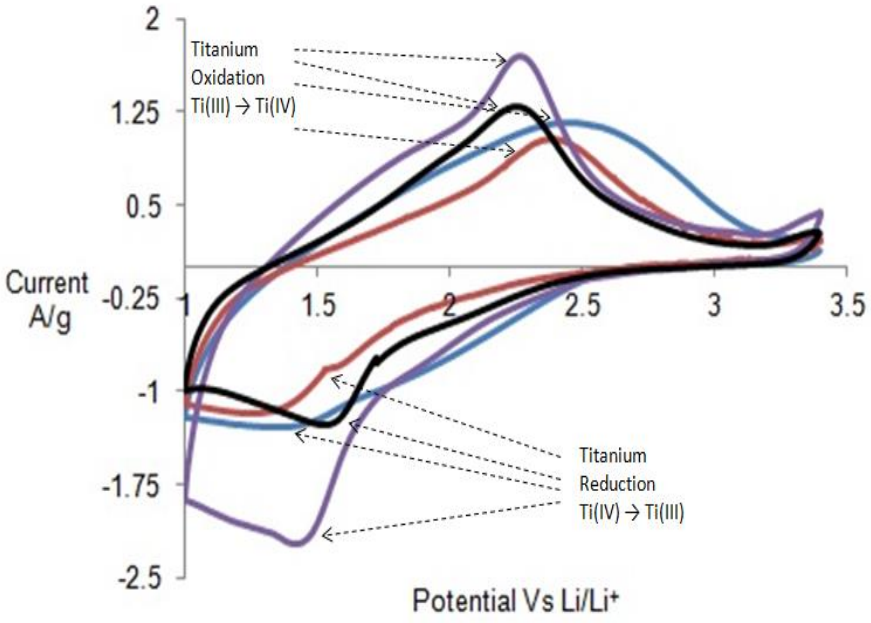

Figure 4.18: Cyclic voltammetry over a potential range of 1-3.4 V vs Li/Li^+ standard electrode potential at sweep rates of 5 mVs^{-1} of samples C12 m-TiO_2 (blue), TiC(0.5) (black), TiC(1) (purple), TiC(2) (red)

Cyclic voltammetry was carried out at a variety of cycle rates on all samples in order to explore the electrochemical behaviour of the materials. Looking first at the Ti series, the difference between materials is most salient in the cyclic voltammograms (CV's) recorded at the highest scan rate of 5 mVs^{-1} (Figure 4.18). The first observation is that charge transfer in the composites has become more redox like, as demonstrated by the narrowing of the reduction and oxidation peaks when compared to m-TiO_2.

The mesoporous oxide host shows broad peaks situated at 1.35 and 2.45 V, for reduction and oxidation, respectively. Whereas the composite materials TiC(0.5), (1) and (2) show reduction peaks at 1.55, 1.45 and 1.35 V and oxidation peaks at 2.2 and 2.35 V, respectively. The oxidation peak has shifted down in potential compared to the host material and the reduction peak, with exception of TiC(2), has increased in potential, demonstrating that all composites

possess smaller differences in charge separation compared to the host material, in part similar to our previous work.[250] This indicates an increase in conductivity, corroborating the results of the Nyquist plots and demonstrating that incorporation of the largest (TiC(2)) quantities of polymer produces a smaller current response than the host material, whereas the lowest (TiC(0.5)) and medium loading levels (TiC(1)) produces a larger current response. Thus, at lower loading levels the electrochemical performance improves due to optimal gains in conductivity with minimal addition of weight to the material. At the lowest loading level the performance only increases slightly. This may be because this loading level is lower than any used in previous studies and that using very small amounts of polymer leads to limited pore penetration of the polymer and any gain in performance due to improved conductivity is offset by pore blockage.

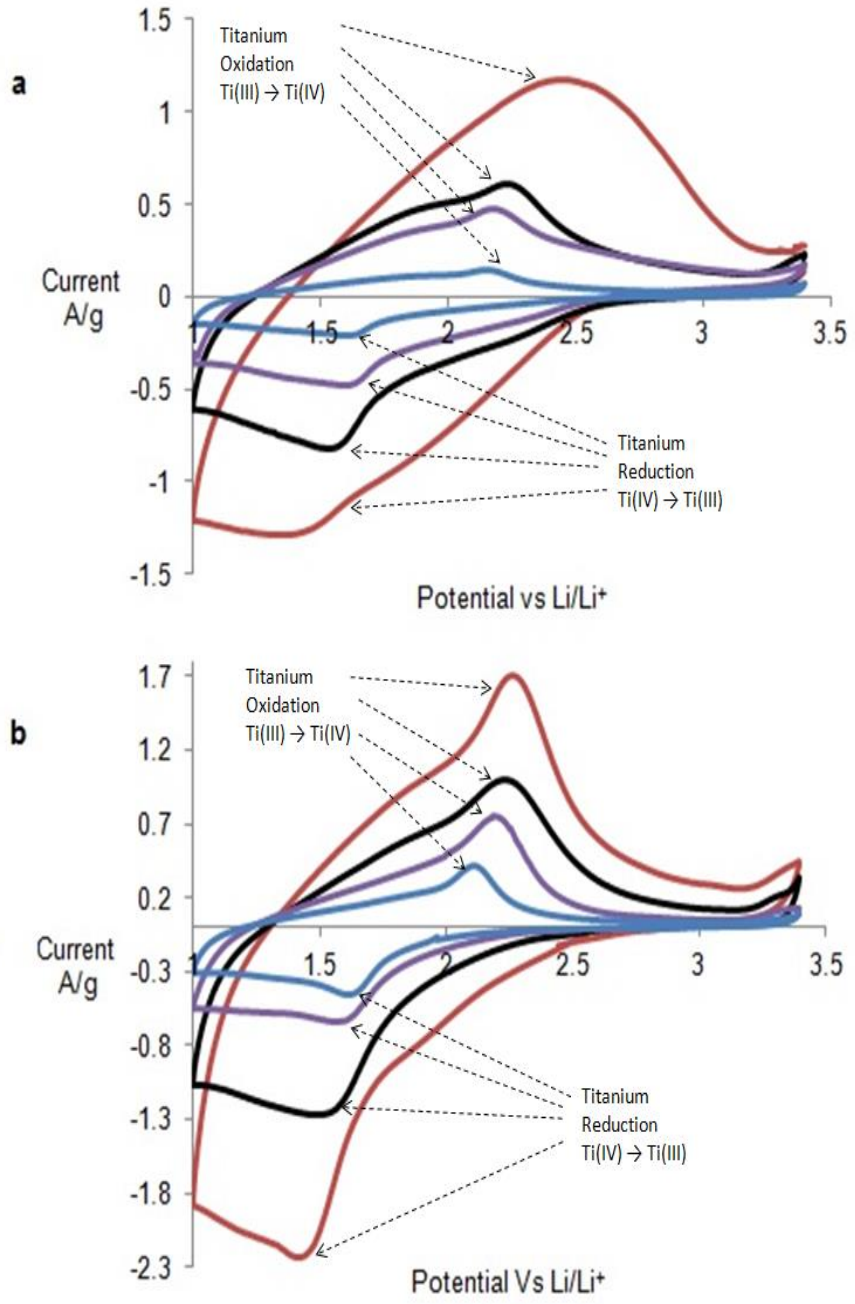

Figure 4.19: Cyclic voltammetry over a potential range of 1-3.4 V vs Li/Li^+ standard electrode potential at various sweep rates of (a) m-TiO_2 and (b) TiC(1) at 0.5 mVs^{-1} (blue), 1mVs^{-1} (purple), 2 mVs^{-1} (black), 5 mVs^{-1} (red)

Figure 4.19 shows the CV of multiple scan rates of m-TiO_2 and its best performing composite TiC(1). In these data it is possible to see the differences in performance between the host and composite over a variety of cycle rates. As sweep rates are increased the composite retains its peak shapes better than that of the host material, which shows significant broadening. The current response for both materials increases in close proportion to the sweep rate used, which

is typical for a capacitive type response. The CV's for all other samples are shown in Figures 8.19 and 8.20, while the CV's of mesoporous Ta oxide and its respective composites are displayed in Figures 8.21 and 8.22. The results of the Ta series demonstrate that the incorporation of polymer into the structure has produced very little change in the electrochemical nature of the material. Despite an increase in the current produced on the initial cycle there is very little difference between the features of the CV of each material. This indicates that Li^+ insertion in this system still remains irreversible, as in the host material, despite the incorporation of polymer to improve the conductivity.

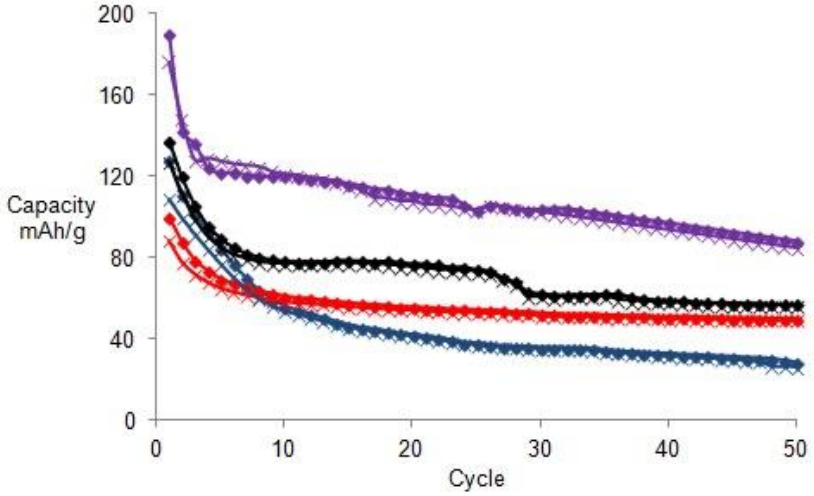

Figure 4.20: 50 Cycles charge (crosses) discharge (squares) capacity data for m-TiO_2 (blue), TiC(0.5) (black), TiC(1) (purple), TiC(2) (red)

The capacity for all materials was measured using galvanostatic charge discharge analysis over the course of 50 cycles to determine peak capacities and explore cycle stability. All assessments were carried out at a discharge current density of 1 $mA.cm^{-2}$. Looking at the results shown in Figure 4.20, the incorporation of the polymer into the structure has significantly affected the cycling performance of the materials. The composites of m-TiO_2 possess initial capacities of 137, 190 and 100 mAh/g, which then drop after 50 cycles to 57, 88 and 49 mAh/g for composites TiC(0.5), (1) and (2), respectively. These compare to m-TiO_2, which produced an initial capacity of 128 mAh/g, which drops to 28 mAh/g after cycling. The scaled and unscaled capacity data of oxidant synthesised polypyrrole is provided in Figure 8.23. To demonstrate that the improvements in performance are not merely caused by the inclusion of polymer alone. Tests were carried out on synthesised polypyrrole in the absence of transition metal oxides and assessed at the equivalent amounts expected for doping levels of 5-15 wt%. These produced a

peak capacity of <9 mAh/g, and thus demonstrate the superior electrochemical properties are not simply the inclusion of polymer.

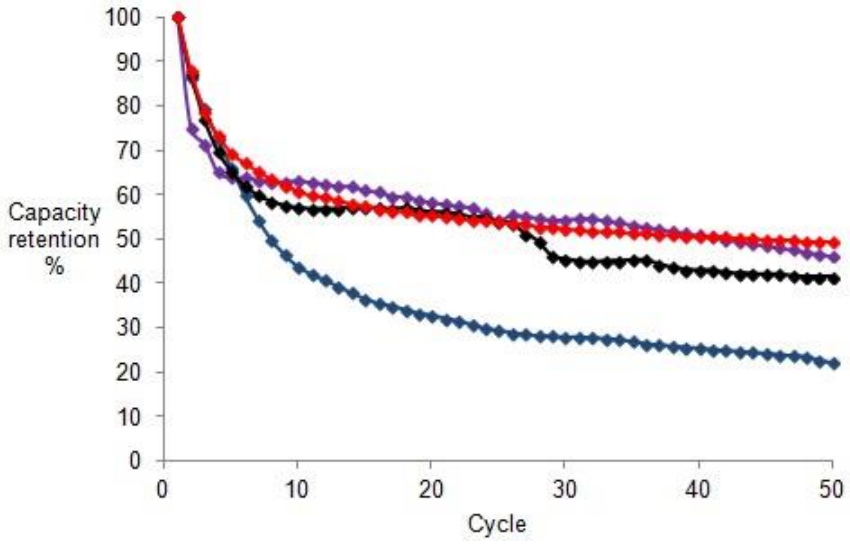

Figure 4.21: Discharge capacity retention % data for m-TiO_2 (blue), TiC(0.5) (black), TiC(1) (purple), TiC(2) (red)

Moreover, by comparing the percentage of capacity retention throughout cycling, Figure 4.21 shows that despite the decrease in initial capacity for composite TiC(2), all three materials possess significantly improved capacity retention compared to m-TiO_2. Thus, with the smallest loading level of polymer the capacity increases only slightly with respect to the pristine material. This is likely due to the increase in weight of the material coupled with only a moderate enhancement in conductivity by the low-loaded polymer, possibly because of discontinuities in the charge carrier pathways. In addition to this small increase in capacity, the overall capacity retention increases due to the marginally improved conductivity of the material, allowing for easier charge transport. When the pore loading time increases to one hour in TiC(1), it produces both increases in initial capacity and improvements in capacity retention. This is likely due to a bridging of the discontinuous charge carrier pathways by increasing the polymer distribution and conjugation length, hence allowing greater electron flow into the inner channels. However, in TiC(2), excess polymer from two hours loading causes the performance to decrease, lowering the initial capacity due to the increase in weight, but still producing good capacity retention. This final observation is similar to conclusions from our previous work with chemical oxidation of thiophene and pyrrole,[236,250] where excessive loading improved conductivity but inhibited Li^+ transport.

These results demonstrate that while this more direct and elegant method of incorporation of conducting nanowires in the pores leads to improvements over the results using chemical oxidant routes, which achieved capacities of 170 mAh/g dropping to 86 mAh/g after cycling,[250] the 190 mAh/g performance does not surpass that of some of the best performing TiO_2 materials from the literature, which can reach 237 mAh/g or more.[259] The reasons for this are likely related to the lower conductivity of TiC(2) versus TiC(1), which could be due to shorter chain polymers formed in TiC(2) with respect to TiC(1). The reason for this is higher concentration of monomer coupled with the limited capability of the UV light to penetrate completely through the bulk material limits, as reported previously in UV polymerisation work using narrow porous hosts.[245] This would allow for only a certain efficiency of polymerisation within the pores, thus leaving discontinuities in the charge carrier pathways, which would inhibit charge transport. This ultimately limits the advantages of the additional organic content as further addition of polymer only adds excess weight while lowering conductivity and decreasing capacity performance.

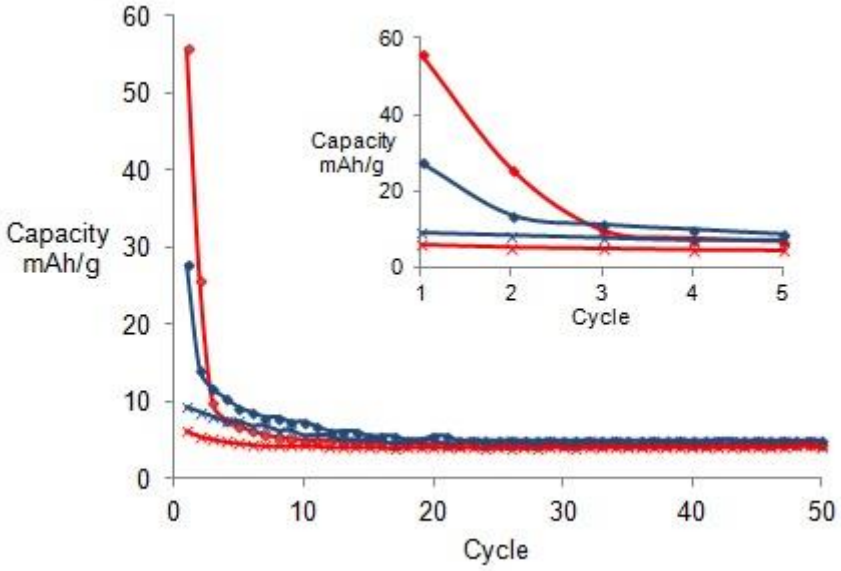

Figure 4.23: 50 Cycles charge (crosses) discharge (squares) capacity data for m-Ta_2O_5 (blue), TaC (red)

The capacity data for TaC is displayed in Figure 4.23 with capacity retention data show in Figure 8.24. As with the titanium composite TiC(1) incorporation of the polymer within the structure improves the initial capacity from 27 mAh/g for the m-Ta_2O_5 to 55 mAh/g for TaC. This, however, is followed by a rapid decrease in capacity, so that after the first three cycles the capacities have dropped to 11 and 10 mAh/g, for m-Ta_2O_5 and TaC, respectively, before levelling off at final capacities of 4.9 and 4.5 mAh/g after cycling. The reason for this rapid

drop in capacity is likely due to the irreversible nature of the Li^+ intercalation into the material. Because the Li^+ cannot be removed from the structure, there is little space in subsequent cycles to insert fresh Li^+. The composite TaC also shows inferior capacity retention when compared to m-Ta_2O_5 as the improved initial capacity of the composite material is followed by a rapid decline as the final capacity approaches that of m-Ta_2O_5.

4.4 Conclusions

Using UV initiated polymerisation of vapour-loaded pyrrole in mesoporous Ti and Ta oxides at a variety of different loading levels, it was possible to overcome the insulating nature of these high surface area porous oxides and exploit redox sites on the inner walls of the mesostructure. The post-polymerisation retention of surface area for these materials was much higher than observed in previous chemical-based polymerisation methods, with only a 13.4% decrease in surface area compared to 51.2% when using a catalyst.[250] Electrochemical studies established that inclusion improves the conductivity of both the Ti and Ta materials up to loading times of one hour, however loading for longer periods produces a drop in conductivity and capacity due to increase in weight with no benefits to performance. The best composite TiC(1) showed superior Li^+ capacity to the pristine host (190 vs 128 mAh/g), dropping to 88 mAh/h after cycling, and significantly higher than results achieved using chemical oxidation (170 mAh/g dropping to 86 mAh/g after cycling). The tantalum materials showed a large increase in their initial capacity (27 - 55 mAh/g), however due to the irreversible nature of the process, the performance tapered off for both materials to yield similar final capacity values (≈ 5 mAh/g).

Thus, the improvements in conductivity coupled with superior retention of post-polymerisation surface area and porosity suggests that UV-initiated polymerisation of pyrrole is a promising synthesis strategy that can be used to improve the performance of a wide range of insulating porous oxides without adversely affecting the structure. Since the majority of battery materials are inherently insulating and require carbon coating before implementation, this method may provide a convenient and inexpensive alternative to pyrolysis and graphene-based methods of improving charge transport.

Chapter 5 : Sulphide Treatment of Mesoporous TiO_2 with HMDST to Improve Conductivity of the Host Species

5.1 Introduction

Initial Li^+ batteries developed in the 1970's and 1980's were made using the layered transition metal chalcogen (TiS_2),[260–262] which possesses metallic levels of conductivity due to the Ti-S band overlap.[180] This removes the need for conducting additives such as carbon, which reduce the volumetric and gravimetric energy densities. Because of this the introduction of air-stable sulfur impurities into mesoporous titanium oxides could significantly improve their conductivity without inhibiting diffusion through the pores. Mesoporous chalcogenides have previously been made directly,[263–268] but in the present case S doping at the inner surface on a mesoporous Ti oxide by O-S exchange to give a Ti oxysulfide may give the advantages of the lower weight of oxides coupled with the higher conductivities of sulfides (Scheme 5.1). Sulfur doped TiO_2 materials are usually synthesised using compounds such as thiourea [269,270] and H_2S [271] and are annealed to temperatures exceeding 600 °C to produce crystalline materials.

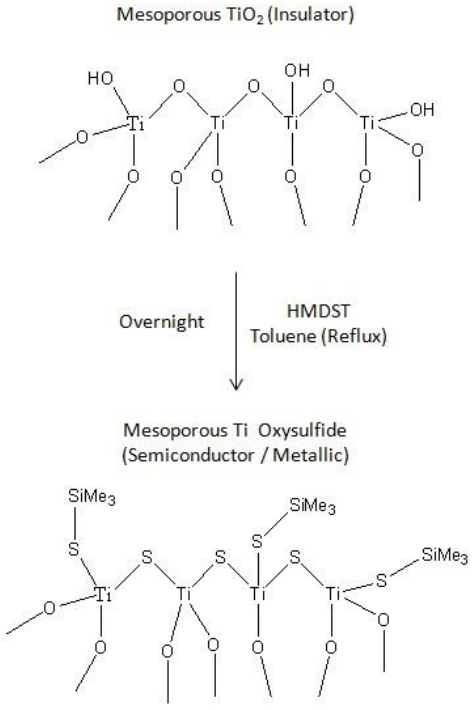

Scheme 5.1: Schematic of electronic structure of transition metal oxides and oxysulfides

In this work we continue improving the electron conductivity of mesoporous oxides by utilising a sulfur doping procedure. However the high annealing temperatures normally used are not possible because the thermal stability of the mesoporous oxides only allow temperatures of < 300 °C. Low temperature procedures are thus explored using hexamethyldisilathiane (HMDST) [272,273] as a sulfur donor in a mild reflux reaction are used to maximise the reaction without the loss of mesostructure. The sulfur in the HMDST exchanges with the oxygen at the surface of the pore walls leading to the formation of a Ti-S bond at the expense of the more stable Si-O bond to form Hexamethyldisiloxane. The incorporation of the sulfur improves the conductivity of the material compared to that of the pure oxide. This reduces the energy barrier to transport electrons throughout the material. During this investigation we evaluated the use of different dopant quantities and heat treatments at various temperatures to determine how this affects the structure and electrochemical properties of the resulting materials.

5.2 Experimental:

5.2.1. Synthesis

All chemicals were purchased from either Sigma Aldrich or Alfa Aesar without further purification.

Mesoporous TiO_2 (m-TiO_2)

m-TiO_2 was prepared according to the experimental procedure described previously in Chapter 2 section 2.2.1.[250] The only differences in procedure was the ligand assisted templating was carried out with octadecylamine in the place of dodecylamine.[236,250,274]

Transition Metal Oxysulfide Composites

All synthesis procedures were undertaken either within a glove box or under vacuum in order to minimise exposure to oxygen. Transition metal oxysulfide composites of C18 templated mesoporous TiO_2 were prepared by taking 400 mg of mesoporous oxide and placing it in 40 mL of toluene, this was then placed into a reflux set up and followed by the addition of HMDST via syringe. Once the addition of HMDST was complete the sample was heated steadily (20 ºC every 5 minute) until under reflux (120-130 ºC), this was left overnight under a slow nitrogen

flow to complete the reaction and prevent any build up of pressure of backflow. Upon completion of the reaction, the mixture is cooled down to room temperature, and the condenser replaced with a glass stopper under fast nitrogen flow. Volatiles were removed *in vacuo* removing all of the solvent and as much reagent as possible, once completed the solid is heated under vacuum at a designated temperature for four hours. The solid is then washed in 50 mL of toluene for one hour before being filtered and is twice to remove residual sulfur reagent that may be present within the material. All washing procedure takes place within an argon filled glove box. After the washing stage was complete the product was dried *in vacuo* for 2 hours at 200 °C to remove any remaining solvent from the sample.

In this investigation the amount of HMDST used during the reaction was varied, using 1.6 (1.5 mL), 2.8 (2.5 mL) and 4 (3.5 mL) equivalent's with respect to m-TiO_2 at a fixed temperature of 150 °C. This was then followed by the use of different heating treatments, using temperatures of 100, 150 and 200 °C using the quantity of reagent that produced the composite with the best electron conductivity.

5.2.2 Characterisation

Brunauer Emmett Teller (BET) surface area and pore size measurements were derived from nitrogen adsorption/desorption isotherms collected on a Micromeritics ASAP 2020. Infrared (IR) spectra were recorded on a Perkin Elmer FT-IR Spectrometer Spectrum RX1 using oven dried KBr discs and data treated on Spectrum 5.1 software. X-ray diffraction (XRD) was performed on Bruker D8 DAVINCI diffractometer with Cu Kα radiation (40 kV, 30 mA) source. The step size was 0.025°. The diffraction patterns were recorded in the 2θ range 1.0 - 100° and the total counting time was 3 hours. The thermogravimetric analysis (TGA) and differential thermal analysis (DTA) was performed on a STA 449C analyser from Netzsch under a flow of dried air at 10.00 °C/min up to 650 °C. Argon was used to protect the balance section. High Resolution Scanning Transmission Electron Microscopy (HRSTEM) was performed in a HD-2700 dedicated Scanning Transmission Electron Microscope (STEM) from Hitachi, with a cold field emitter equipped with a CEOS Cs corrector and operated at 200 kV. The powder samples were simply dry deposited onto a Cu grid covered with a carbon film (Quantifoil) having periodical holes with diameter of 1.2 microns. Observation was made in

three different modes: bright field (BF), high angle annular dark field (HAADF) and secondary electron (SE).

5.2.3 Electrochemical Analysis

All electrochemical analysis was performed with a Princeton Applied Research VersaSTAT using a cell constructed within an argon filled glove box to ensure minimal exposure to oxygen. Electrochemical performance of the synthesised electrode materials as a Li^+ battery electrode was assessed using a two electrode set up. Working electrodes (cathode) consisted of 80% active material, 10% super conducting carbon black, and 10% polyvinylidenefluoride (PVDF) by weight. The electrode paste was made by grinding the active material and carbon black to ensure a good mixture of the powders. The powders were then stirred with PVDF and *n*-methyl-2-pyrrolidinone (NMP) solvent until a homogenous paste was formed. The paste was spread onto copper foil (current collector) and the electrode was dried by first heating to 80 °C to bake off any excess NMP solvent before increasing the temperature to 120 °C overnight to allow the electrode material to bind with the current collector, followed by punching out a 15 mm electrode disk. Metal lithium disks were used as the counter electrodes were also punched into a 15 mm disk. The electrolyte used in this investigation was 1.0 M $LiPF_6$ dissolved in ethylene carbonate (EC) and diethyl carbonate (DEC) solutions at a ratio of 1:1 by volume with a lithium disk used as the anode. Cyclic voltammetry measurements were carried out at a variety of sweep rates 0.5, 1, 2 and 5 mVs^{-1} and the potential windows used in all experiments was cycled between 1 and 3 V vs. Li/Li^+ reference electrode. The initial potential of the scan was determined by the open circuit potential the cell (typically 2.3-2.6 V vs Li/Li^+) with the initial scan direction being directed in the reduction direction towards a lower potential limit (1 V vs Li/Li^+) with cycles being completed once the final reduction sweep reaches the starting potential of the cycling process.

Galvanostatic charge discharge measurements were carried out with a current density of 1 $mA.cm^{-2}$ between the potential window of 1-3 V vs. a Li/Li^+ reference electrode. Each electrode was weighed prior to cell assembly to determine cathode mass and then used to calculate capacity relative to mAh/g according to the mass of the electrode.

5.2.4 Electrochemical Impedance Spectroscopy

Electrochemical AC impendence spectra were obtained using the same two electrode Li^+ battery cell set up using the active material as the active electrode and a lithium metal foil as the counter electrode. Measurements were applied using a sine wave with amplitude of 5 mV over the frequency range from 100 KHz to 0.01 Hz. Measurements were carried out prior to the initial discharge of the cell, using a biased potential equivalent to that of the open circuit potential of the cell, this was necessary in order to remove the influence of polarisation on the values of conductivity that are produced.

5.3. Results and Discussion:

5.3.1. Characterisation

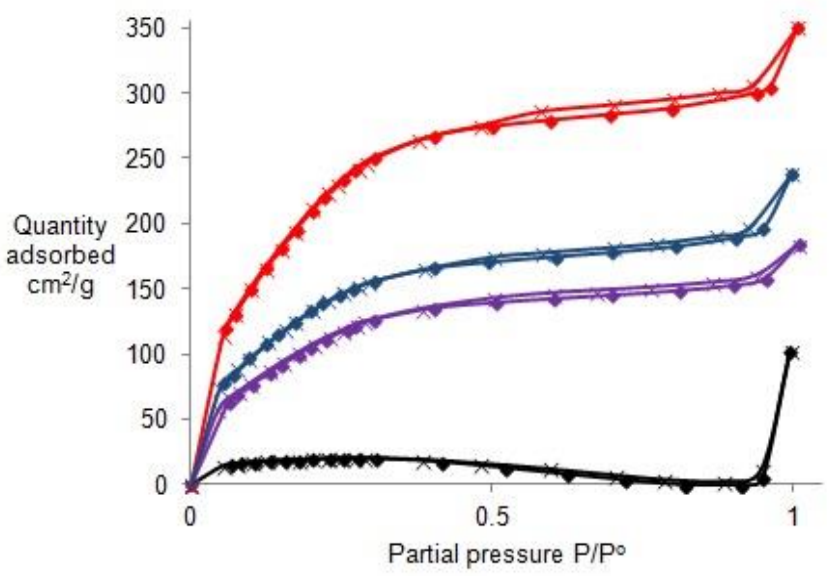

Figure 5.1: Nitrogen adsorption (crosses) and desorption (squares) for m-TiO_2 (red), composites made using 1.5 mL (blue), 2.5 mL (purple), 3.5 mL (black) of HMDST at temperatures of 150 °C

Nitrogen adsorption studies were carried out on all composites to determine the effect of synthesis conditions on the surface area and pore structure of the materials. The isotherms of pristine m-TiO_2 and the composite materials synthesised using various amounts of HMDST at 150 °C are shown in Figure 5.1 with all Brunauer-Emmett-Teller (BET) surface area results displayed in Table 5.1. As expected m-TiO_2 and the composite materials synthesised using 1.5 and 2.5 mL of HMDST display isotherms between type I and type IV, typical for amine-templated mesoporous materials with pores sized between 18-25 Å. However, the composite

made with 3.5 mL of HMDST at 150 °C resembles more closely a type II isotherm for a non-porous material, suggesting a much lower surface area for this material. Indeed, the parent m-TiO_2 possessed a BET surface area of 862 m^2/g, which decreased to 527, 429, and 66 m^2/g, respectively, for composites made using 1.5, 2.5, and 3.5 mL of HMDST. This trend demonstrates that the mesoporous structure is maintained on treatment with lower levels of HMDST, but as the amount of HMDST increases, the surface area is significantly reduced, possibly because of mesostructure collapse or because of significant increase in weight and/or filling of the pores with organic residue.

Material	**BET surface area/ m^2/g**
C18 m-TiO_2	862
1.5 mL of HMDST at 150 °C	527
2.5 mL of HMDST at 150 °C	429
3.5 mL of HMDST at 150 °C	66
3.5 mL of HMDST at 100 °C	660
3.5 mL of HMDST at 200 °C	41

Table 5.1: Surface area of m-TiO_2 and respective oxysulfide composites.

The nitrogen adsorption isotherms for samples synthesised at 100 °C, 150 °C, and 200 °C with 3.5 mL of HMDST can be seen in Figure 8.25. The isotherm of the material synthesised at the lowest temperature of 100 °C is between type I and IV, suggesting retention of pore structure with only small to moderate loss of surface area, while the samples synthesised at 150 and 200 °C possess isotherms that resemble more closely type II, This shape is suggestive of a large loss of surface area due to pore blockage or collapse, as it is typically observed for low surface area and non-porous materials.[250] Following this predicted trend, the BET surface areas of the composite materials drop from 660 m^2/g to 66 and 41 m^2/g on increase of synthesis temperature from 100 °C to 150 and 200 °C, respectively. So in summary, the composites generally retain their pore structure and surface area under milder synthesis conditions and lower HMDST levels, and the loss of surface area and pore structure at the higher synthesis temperatures or loading levels appears to be due to a combination of temperature effects and possible presence of residual HMDST or its decomposition products in the pore channels.

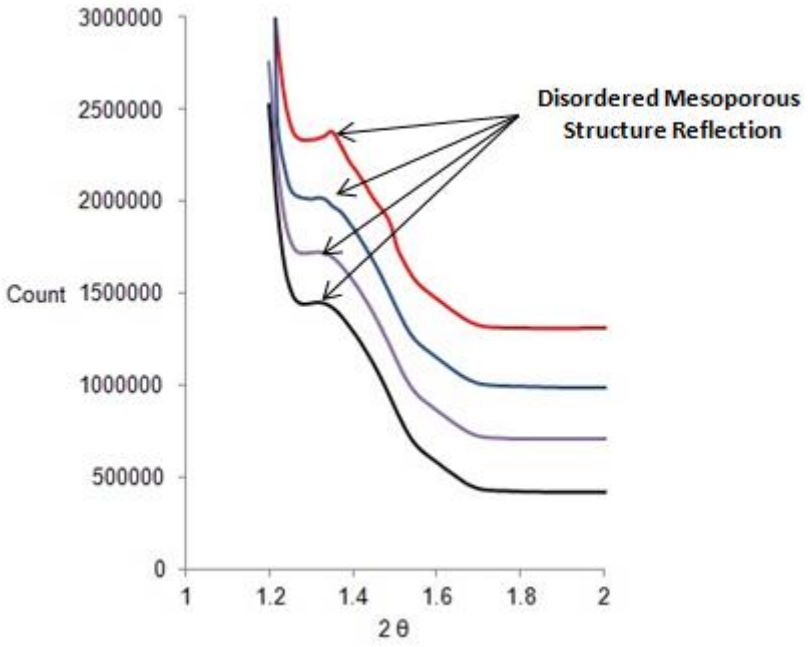

Figure 5.2: X-ray powder diffraction pattern at low angles for pristine m-TiO_2 (red) and composites made using 1.5 mL (blue), 2.5 mL (purple), 3.5 mL (black) of HMDST at 150 °C

In order to fully assess the degree or post-synthesis retention of mesoscopic order, low-angle powder X-ray diffraction (PXRD) experiments were conducted. The results for composites synthesised using different quantities of HMDST at 150 °C are shown in Figure 5.2, while the patterns for materials synthesised at different heating treatment temperatures are shown in Figure 8.26 For all materials synthesised at 150 °C there is a broad reflection at approximately 1-2° 2θ. This reflection at similar intensity is also observed in pristine m-TiO_2 and is diagnostic of a wormhole pore structure as demonstrated in previous work.[164,250] The patterns for materials synthesised with different heating temperatures (Figure 8.26) also display this reflection, however there is a slight decrease in the reflection intensity relative to the pristine sample indicating some degree of structure loss. This data confirms that the mesostructure is largely retained upon completion of the synthesis, and that pore filling and increase in weight are likely the cause behind the significantly lower surface areas derived from the nitrogen adsorption data.

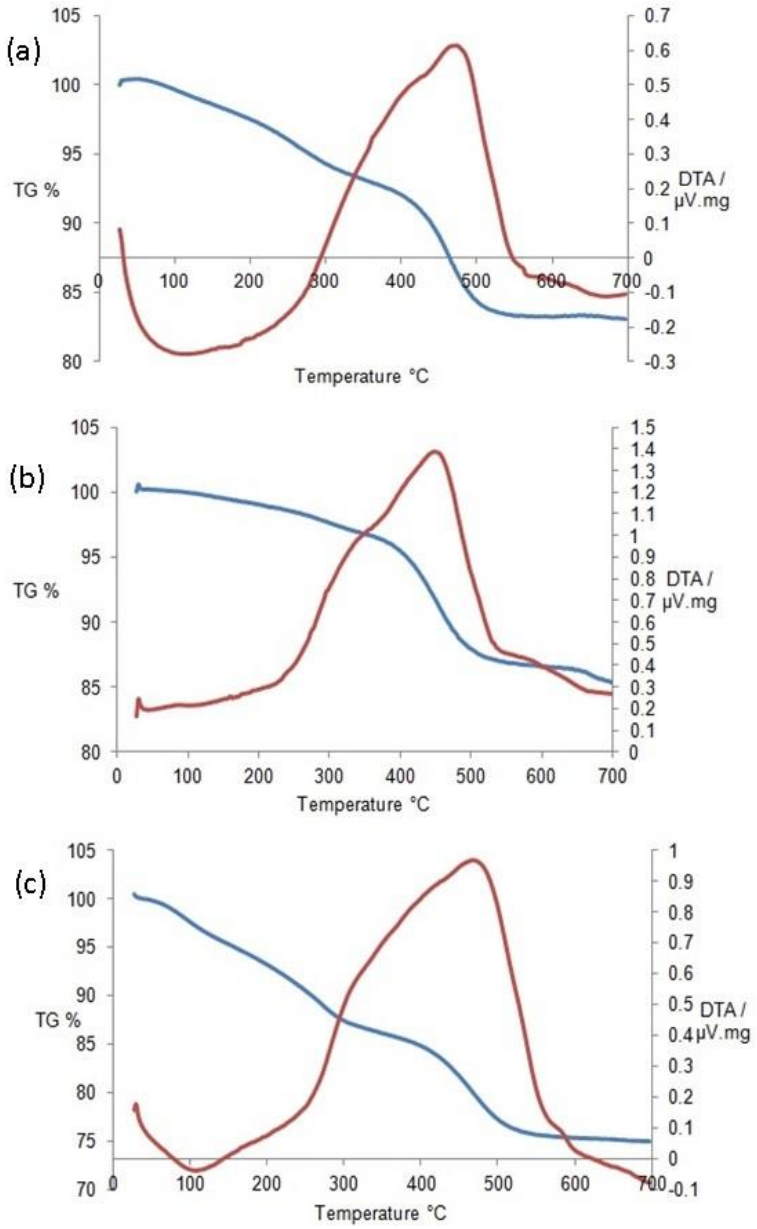

Figure 5.3: Thermogravimetric analysis (blue) and differential thermal analysis (red) plots for the composite made with (a) 1.5 mL (b) 2.5 mL and (c) 3.5 mL of HMDST 150 °C

In order to probe the amount of residual organic matter in the pores of the materials suggested by the XRD and nitrogen adsorption data, the TGA/DTA data for composite materials made using various amounts of HMDST are shown in Figure 5.3. Looking at the TGA and DTA plots for samples made using various amounts of HMDST. The sample synthesised at 150 °C using 1.5 mL of HMDST produces an endothermic peak up to 300 °C. The sample made from 3.5 mL produces a small endothermic peak up to 200 °C. However the sample synthesised using 2.5 mL failed to produce an endothermic peak, instead producing a line with no significant changes at exothermic values up to 250 °C. Mesoporous transition metal oxides

typically show an initial endothermic weight loss up to 200 °C caused by the loss of residual solvents present within the sample. After a temperature of 250 °C is reached, all materials show a sharp increase towards positive values in the DTA plot typically indicating the start of the exothermic process in these samples.[250,274] The weight loss between 0-250 °C can be used to determine the losses of residual solvent within the samples. These losses were 9, 2 and 10 wt% for samples made using 1.5 2.5 and 3.5 mL of HMDST, respectively. The second region of the plot between 250-700 °C corresponds to the combustion of the organic content within the main sample producing a large exothermic peak as seen in our previous work.[236] Composites synthesis using 1.5, 2.5 and 3.5 mL of HMDST lost 8, 13 and 15 wt% respectively. These results indicate that with increased amounts of HMDST the residual organic content of the material increases as expected from the higher concentration of Ti-S-Ti or Ti-S-Si$(CH_3)_3$ groups present on the surface after reaction.

The data for composites synthesised using a variety of different heating treatments (Figure 8.27, 5.3(b) and 8.28) shows an endothermic region between 0-250 °C which produces losses of 6, 10 and 9 wt% before going on to lose a further 13, 15, 17 wt% in the exothermic region for samples synthesised using 3.5 mL of HMDST at 100, 150 and 200 °C respectively. These data show that higher loading levels of reagent results in increased organic content in all samples, and that higher heating temperatures also leads to more organic incorporation, further corroborating the results from the nitrogen adsorption and XRD, suggesting that loss of surface area results from pore filling of the materials due to incomplete reaction of the HMDST to produce some surface Ti-S-Si$(CH_3)_3$ groups in addition, possibly, to the desired Ti-S-Ti linkages needed for enhanced conductivity.

FTIR studies were carried out on all materials with spectra shown in Figures 8.29 to 8.36, additionally the spectrum for the reagent HMDST (Figure 8.29) is added to assist in assigning bands in the composite samples. In the spectrum for neat HMDST there are a number of diagnostic peaks situated at 2950-2800 cm^{-1} (aliphatic C-H stretch), 1250 and 800-850 cm^{-1} (Si-CH_3 stretches).[275][276] The spectrum of the mesoporous oxide host shows strong residual water stretches at 3200 cm^{-1} and 1600-1650 cm^{-1}, in addition to a weaker stretch situated at 800-820 cm^{-1}. As expected, these stretches are also observed in the spectrum of the sample in which HMDST has been mixed with the host material before heating, all diagnostic stretches

still clearly visible with the strongest indicator being the stretches at 2800-2950 cm^{-1}, as there are no stretches in these regions for the host material.

In the first set of synthesised samples, with increasing HMDST content, the size of the aliphatic C-H aliphatic stretch at 2850-3000 cm^{-1} increases with increasing HMDST loading, but is in every case smaller than in the spectrum of the material before heating. This is further evidence that despite multiple washings and heating treatments *in vacuo* there is still a significant amount of organic content within the material, most likely due to Ti-S-Si$(CH_3)_3$ groups within the structure, in place of the desired Ti-S-Ti bonds. The second group of samples shows that with increased heat treatment temperature, the signal intensity increase further, likely due to the increase in the number of Ti-O centers reacting with the reagent. Once again, this suggests that loss of surface area in the samples loaded at 3.5 mL and 200 °C is due to pore blockage by incompletely converted Ti-S-SiC$(CH_3)_3$ moieties and that steric constraints between these groups and proximal Ti-OH groups prevent further reaction.

XPS was carried out on composite samples to determine the number and oxidation states of the sulfur species present after the doping procedure. Baseline corrected XPS spectra for materials made using different amounts of HMDST at a temperature of 150 °C are displayed in Figure 5.4 with samples synthesised using 3.5 mL and different temperatures in Figure 5.5. In the sulfur 2p3/2 region appears within the region of 165 – 174 eV, typically indicative of S^{4+} and S^{6+} species such as sulfates and sulfonates (SO_4^{2-} and RSO_3^-). These emissions demonstrate the successful incorporation of sulfur into the material after completion of the synthesis, however they do not provide any evidence for the S^{2-} state (162 eV) expected for TiS_2.[277] These species are similar to the those observed in sulfur doped TiO_2 materials made using thiourea (169.5 eV).[278,279] These S^{4+} and S^{6+} species are unexpected as all syntheses carried out in the absence of oxygen, suggesting that the samples may have been oxidised during XPS analysis. Precise assignment of surface species is thus difficult, however it is still possible to identify the presence of two distinct sulfur species within the spectra. Peak fitting shows the presence of a single emission in the sample made using 1.5 mL at 169.0 eV. Since this loading level is associated with the lowest amount of residual hydrocarbon, this emission likely originates from the reaction of HMDST with adjacent surface OH groups to produce Ti-S-Ti species, which later become oxidised. As the amount of HMDST increased to 2.5 mL and 3.5 mL a new emission is visible within the fitted spectra at 170.3 eV, indicative of a S^{4+} or S^{6+} species.[280]

Since these higher loading levels are associated with higher levels of residual hydrocarbon, it is likely that this new emission is related to surface sulfur species with trimethylsilyl groups unable to undergo a second reaction step with neighbouring Ti-OH groups. The most likely reason is the limited concentration of OH groups present on the material's surface leading to incomplete reaction with higher loading levels of HMDST. This limiting reagent effect of surface hydroxyl species has been demonstrated in previous studies with dangling benzyl titanium fragments on mesoporous silica.[281]

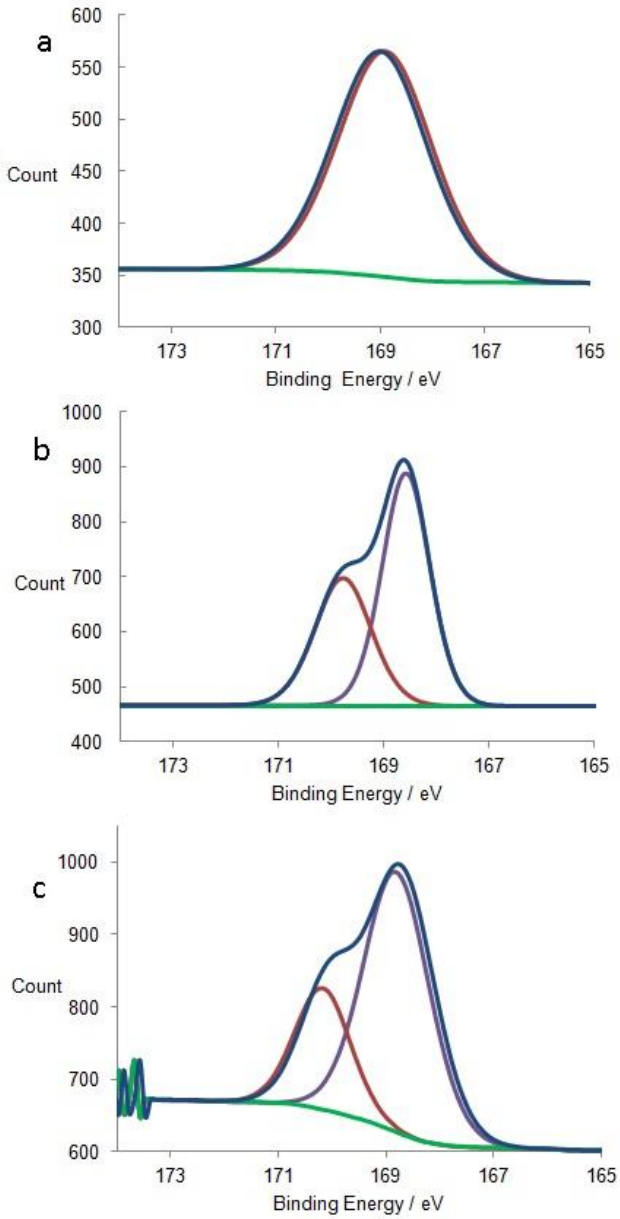

Figure 5.4: Peak fitting of sulfur 2p3/2 region of XPS of composites synthesised using 1.5 mL (a), 2.5 mL (b) and 3.5 mL (c) of HMDST at temperatures of 150 °C

The XPS of the materials synthesised using 3.5 mL of HMDST at 100 °C, 150 °C and 200 °C are shown in Figure 5.5. All samples exhibit emissions at 168.9 and 170.4 eV in relatively similar ratios, again establishing the presence of S^{6+} and S^{4+} states within each material. The presence of two sulfur species at high dopant concentrations are again consistent with incomplete reaction at the surface caused by oversaturation of the surface OH groups with HMDST leading to residual TMS groups attached to sulfur on the surface. Once the Ti-S-Ti and Ti-S-Si$(CH_3)_3$ groups are formed they later become oxidised during XPS analysis to form the two higher oxidation state species.

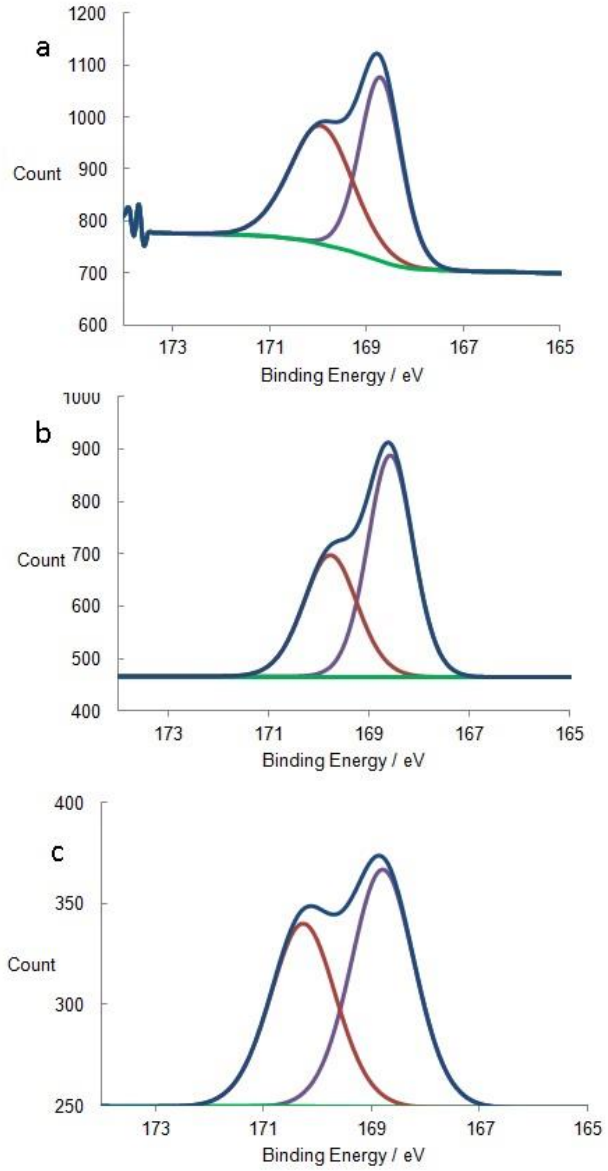

Figure 5.5: Peak fitting of sulfur 2p3/2 region of XPS of composites synthesised at (a) 100 °C, (b) 150 °C (c) 200 °C with 3.5 mL of HMDST

To further explore the morphology and pore structure of the composites, scanning and transmission electron microscopy (STEM) was carried out on all materials. Figure 5.6 shows SEM images taken at low magnification demonstrating the powder morphology of the composites in the form of large grain like clusters. Similar images are typically obtained for amine template materials and can also be seen in the starting material (Figure 5.6(f)).[236]

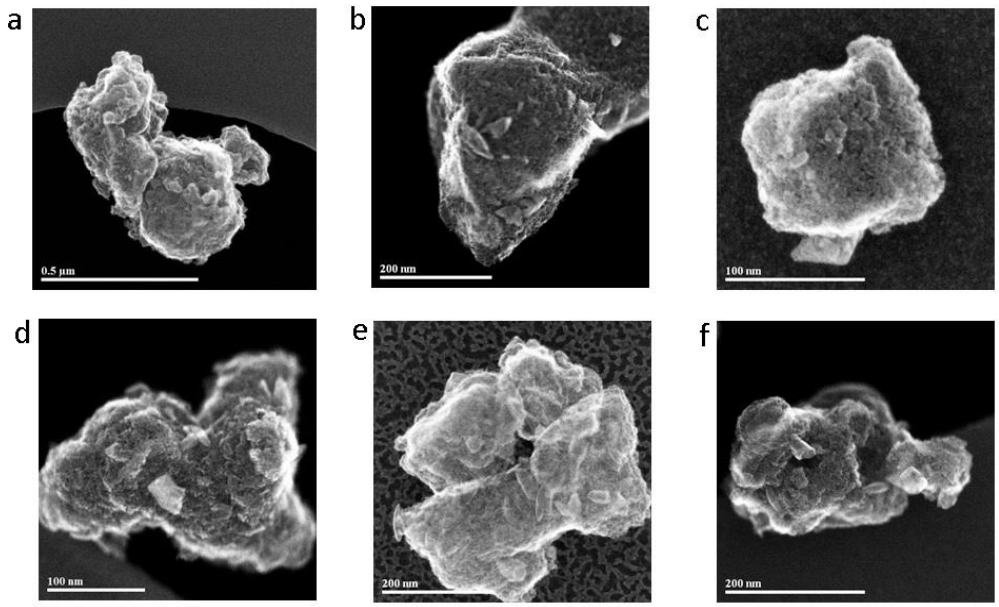

Figure 5.6: SEM SE images of composite made using (a) 1.5 mL(100 kx) , (b) 2.5 mL (200 kx), (c) 3.5 mL (500 kx) of HMDST at 150 °C, composites synthesised at (d)100 °C (500 kx), (e)200 °C with 3.5 mL (200 kx).of HMDST and the starting material (f) m-TiO_2 (250 kx) at low magnification

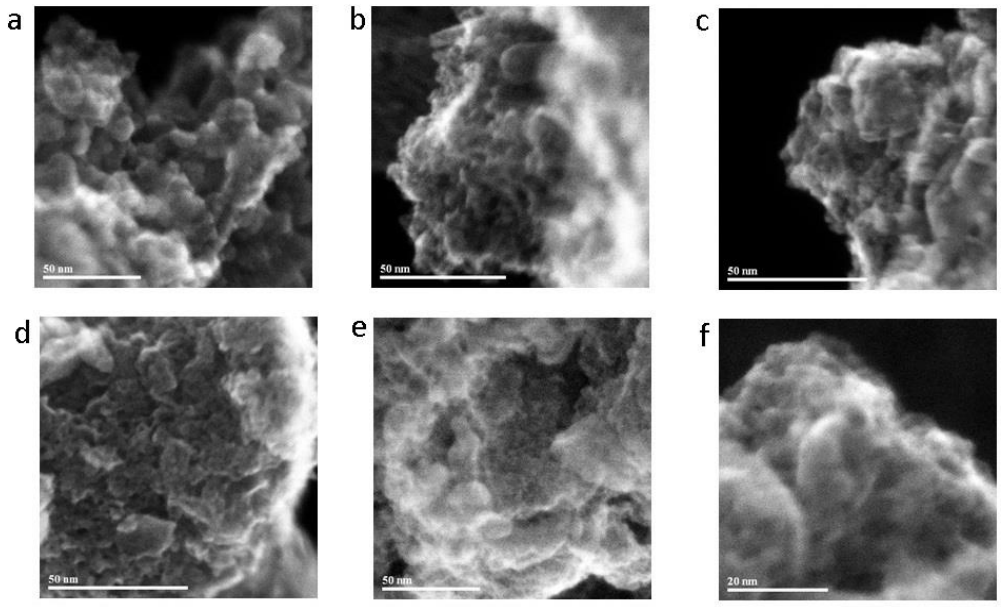

Figure 5.7: SEM SE images of composite made using (a) 1.5 mL (700 kx), (b) 2.5 mL (900 kx), (c) 3.5 mL (1 Mx) of HMDST at 150 °C, composites synthesised at (d)100 °C (1 Mx), (e) 200 °C (700 kx) with 3.5 mL of HMDST and the starting material (f) m-TiO_2 (1.8 Mx) at intermediate magnification

When the magnification is increased (Figure 5.7) the SEM images allows us to observe that the ca. 2 nm amorphous pore structure of the materials remains present after completion of the synthesis procedure. The confirmation of pore structure retention after doping corroborates with the BET and XRD data. This supports the conclusion that the decrease in surface area comes from an increase in surface sulfur species concentration within the pores rather than pore collapse caused by the synthesis procedure.

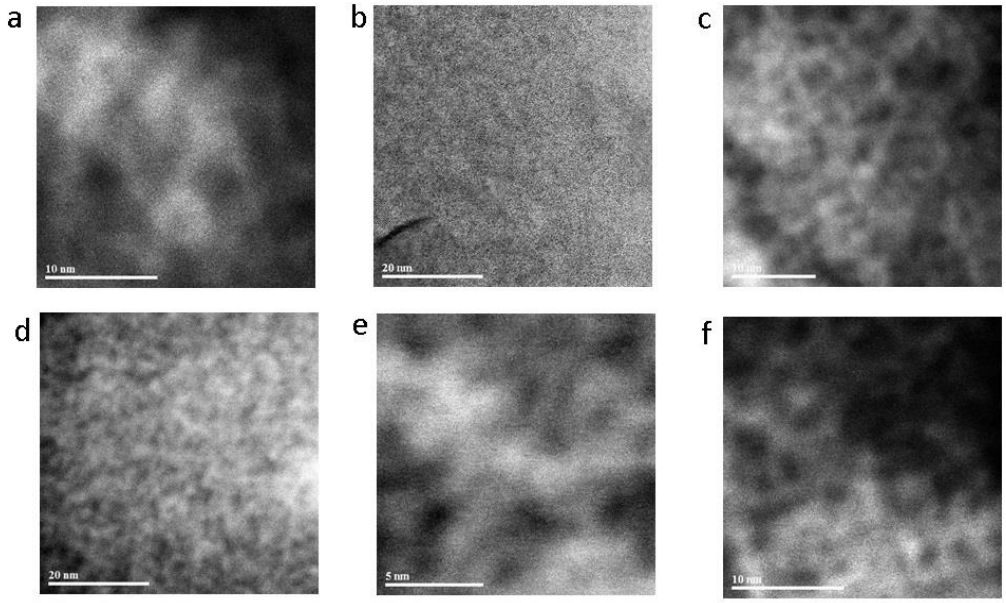

Figure 5.8: TEM HAADF images of composite made using (a) 1.5 mL (4 Mx), (b) 2.5 mL (1.8 Mx), (c) 3.5 mL (3 Mx) of HMDST at 150 °C, composites synthesised at (d) 100 °C (1.8 Mx), (e) 200 °C (7 Mx) with 3.5 mL of HMDST and the starting material (f) m-TiO_2 (4 Mx) at highest magnification

The highest magnification TEM images shown in Figure 5.8 allow us to observe the pore structure more closely and determine the extent of crystallinity of the composites. All samples demonstrate that the materials remain predominantly amorphous with a disordered wormhole pore structure. These observations are in close agreement with what has been reported previously for this class of materials.[274]

5.3.2. Electrochemical Analysis

In order to study the effects of the sulfur doping on the conductivity of the materials, electrochemical impedance spectroscopy (EIS) experiments were carried out on all materials. All impedance measurements were all carried out over the frequency range from 100 KHz to 0.01 Hz using a two electrodes setup prior to the initial discharge, using a biased potential

equivalent to that of the open circuit potential of the cell, all open circuit potential values are listed in the figure captions. The Nyquist plots of materials can be split into three different sections. First, the high frequency region to the far left of the plot which is used to determine the electrolyte resistance of the cell (R_{el}), this is obtained from the x axis intercept. As the frequency decreases the plot forms a partial semicircle, which is used to calculate the charge transfer resistance (R_{ct}) by determining the second x axis intercept, the value of the electrolyte resistance is then subtracted from this value. The lowest frequencies to the far right of the plot forms a linear section which is used to assess the Li^+ diffusion process also known as the Warburg impedance (W). The value to compare the conductivity in solid state electrodes is that of R_{ct}. Using modelling software it is possible to calculate the values for these different properties which are used to compare the materials. The Nyquist plots for pristine m- TiO_2 and composites made using different quantities of HMDST are shown in Figure 5.9. The R_{ct} values of composite materials using 1.5, 2.5 and 3.5 mL at 150 °C were 77, 80 and 25 Ω, respectively. All samples produced significantly smaller R_{ct} values than that of the starting material m-TiO_2 (189 Ω). The decrease in the size of R_{ct} indicates that the reaction with HMDST has produced a noticeable improvement in conductivity with the largest quantity (3.5 mL) producing the biggest improvement, thus indicating that using more dopant leads to the largest improvement in conductivity.

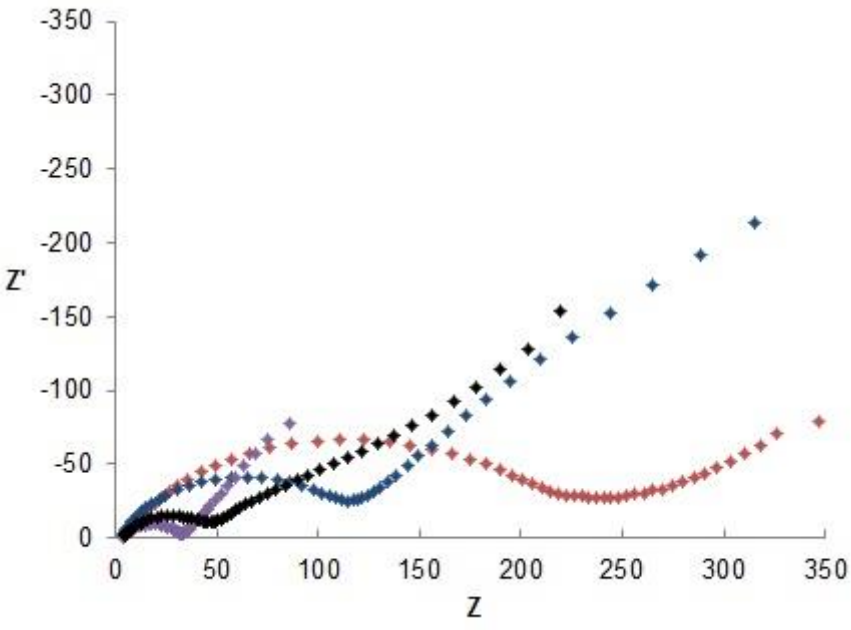

Figure 5.9: Nyquist Plot over the frequency range from 100 KHz to 0.01 Hz using a two electrode setup, using biased potentials equivalent to the open circuit potential of the cell, m-TiO_2 at 2.309 V vs Li/Li^+ (red), composites made using 1.5 mL at 2.428 V vs Li/Li^+ (blue), 2.5 mL at 2.405 V vs Li/Li^+ (purple), 3.5 mL at 2.394 V vs Li/Li^+(black) of HMDST at temperatures of 150 °C

The Nyquist plots for samples synthesised at different temperatures are shown in Figure 8.37. Samples made using 3.5 mL of HMDST at 100, 150 and 200 °C produced values of 103, 25 and 33 Ω, respectively. These results show that as temperature is increased to 150 °C the conductivity improves. Further increases in temperature to 200 °C produced a slight drop in conductivity but this value was still significantly higher than that of the host material. Since conductivity is most likely due to increased Ti-S-Ti moieties on the surface it appears from the data that the higher synthesis temperature forces reaction with extra HMDST. However, by crowding the surface these additional Ti-S-Si$(CH_3)_3$ groups are unable to be converted to Ti-S-Ti bridges and have an adverse effect on diffusion and conductivity.

Using the Warburg impedance at the low frequency region of the Nyquist plot, it is possible to assess the effects of sulfur doping on the Li^+ diffusion properties of the material by comparing the Li^+ diffusion coefficients, which can be calculated using Equation 5.1

Equation 5.1 $$D = (R^2T^2) / 2A^2n^4F^4C^2\sigma^2$$

Where D is the lithium diffusion coefficient($cm^2\ s^{-1}$), R is the gas constant (8.314 MPa $cm^3\ mol^{-1}\ K^{-1}$), T is the absolute temperature (298 ºK), A is the contact area of the electrode (π x 0.75^2 (cm^2)), n is the number of electrons involved in the redox reaction, F is Faradays constant (96485 C mol^{-1}), C is the concentration of Li^+ in the electrolyte (1 mol cm^{-3}) and σ is the Warburg factor(Ω $s^{-1/2}$).

Warburg factor is calculated by using Equation 5.2 using the low frequency region of the Nyquist plot.

Equation 5.2 $$Z_{re} = R_{ct} + R_1 + \sigma\omega^{-½}$$

Where ω is the frequency and Z_{re} is the real impedance. This relationship between the frequency and the real impedance of the material can be used in a straight line equation, from which the gradient of the line provides the value for the Warburg factor.

The plots for Warburg factor can be seen in Figures 5.10 and 5.11. The differences in gradient (σ) represent differences in the diffusion coefficient values. As these cathode materials have

no Li^+ present prior to initial discharge the diffusion coefficients are directly proportional to the change in the Warburg factor. Looking first at composites made using different amounts of HMDST, the σ values for mesoporous TiO_2 was calculated at 38.04 **Ω** $s^{-1/2}$ which became 26.36, 31.98 and 16.7 **Ω** $s^{-1/2}$ for composites made using 1.5, 2.5 and 3.5 mL of HMDST respectively. Then using these values in Equation 5.2 this provides the Li^+ diffusion coefficients of 7.83 x 10^{-18} cm^2 s^{-1} for mesoporous TiO_2 changing to 1.63 x 10^{-17}, 1.11 x 10^{-17} and 4.06 x 10^{-17} cm^2 s^{-1} for composites made using 1.5, 2.5 and 3.5 mL of HMDST respectively. This produces respective ratios of (1.0):(2.08):(1.42):(5.19) for m-TiO_2, 1.5, 2.5 and 3.5 mL of HMDST, respectively. The ratios show that the Li^+ diffusion capability of the materials being 3.5>1.5>2.5>m-TiO_2 similar to the results seen for R_{ct} analysis. The best material possesses a diffusion coefficient >5 times that of the starting material. These values are a similar in magnitude to the results that were seen in Chapter 2, and are slightly lower than those seen for previously reported TiO_2 materials (1x10^{-15} – 1x10^{-17} cm^2 s^{-1}).[31,92,258]

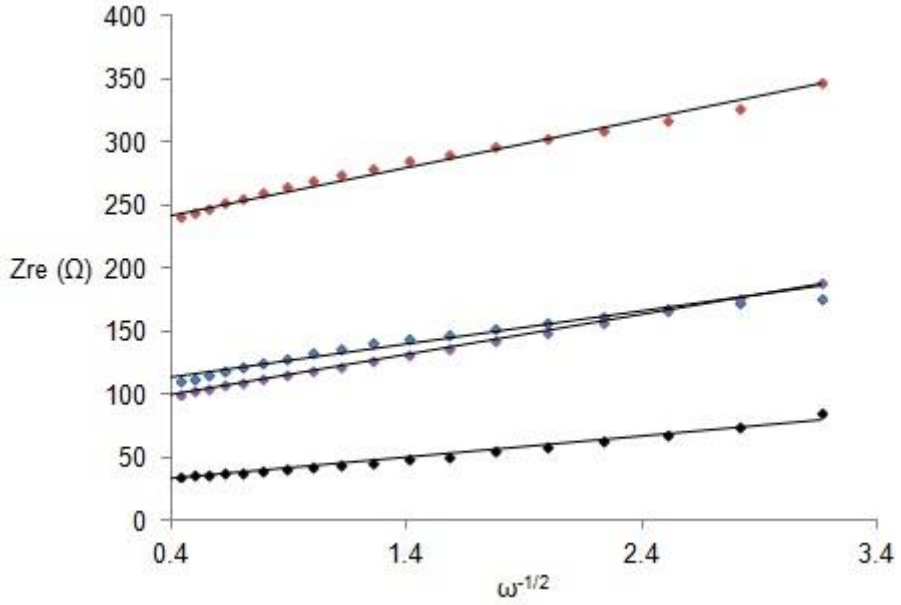

Figure 5.10: Plot of real impedance vs reciprocal square root of frequency for pristine m-TiO_2 (red), and composites made using 1.5 mL (blue), 2.5 mL (purple), 3.5 mL (black) of HMDST at 150 °C

When progressing on to the investigation of different heating treatment temperatures the Warburg factors were calculated to produces values of 34.11, 16.70 and 54.59 **Ω** $s^{-1/2}$ for composites made at 100, 150 and 200 °C respectively. Then using these values in Equation 5.2 this provides the Li^+ diffusion coefficients of 9.74 x 10^{-18}, 4.06 x 10^{-17} and 3.80 x 10^{-18} cm^2 s^{-1} for composites mate at 100, 150 and 200 °C respectively. This produces respective ratios of

(1.0):(1.48):(5.19):(0.49) for m-TiO_2, 100, 150 and 200 °C, respectively. As temperature increases to 150 °C the diffusion coefficient improves. However when heating to 200 °C the diffusion coefficient drops significantly to half of that of the initial host material, and 1 order of magnitude lower than that of the best material. These results show that despite improving conductivity, the diffusion capabilities of the material decrease at temperatures above 150 °C. This is consistent with the pore blockage caused by excess surface Ti-S-$(CH_3)_3$ groups.

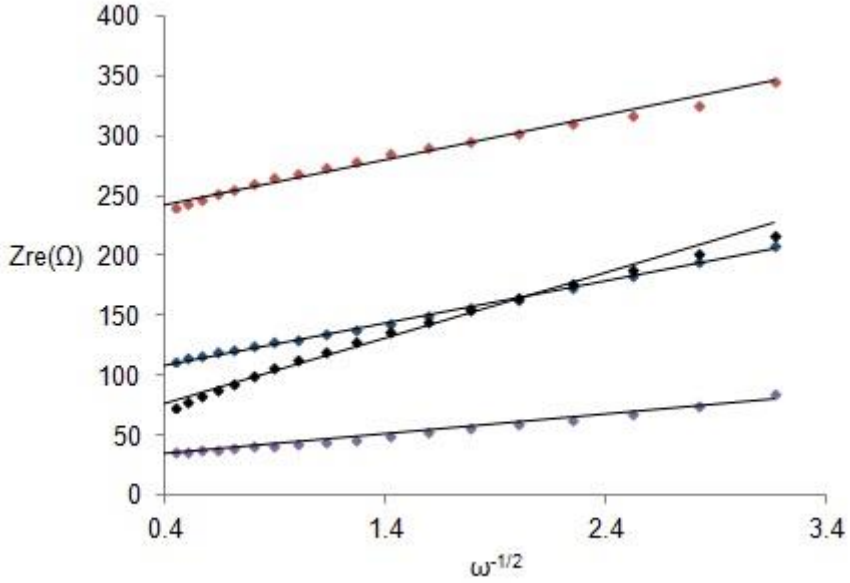

Figure 5.11: Plot of real impedance vs reciprocal square root of frequency for pristine m-TiO_2 (red), and composites synthesised at 100 °C (blue), 150 °C (purple) and 200 °C (black) with 3.5 mL of HMDST

Cyclic voltammetry was carried out on all samples at a variety of different cycle rates between 0.5 to 5 mVs^{-1} to assess the electrochemical nature of the materials when undergoing redox reactions between Ti^{4+}/Ti^{3+} states according to the reaction shown in Equation 5.3.

Equation 5.3

$$TiO_2 + xLi^+ + xe^- \underset{\text{Oxidation}}{\overset{\text{Reduction}}{\rightleftharpoons}} Li_xTiO_2$$

Ti^{4+} $\qquad$ Ti^{3+}

Looking at the effects of the amount of HMDST used, the best comparison between materials is most clearly demonstrated at the highest scan rate of 5 mVs^{-1} (Figure 5.12). The materials show increases in current proportional to the sweep rate used, which is indicative of a capacitive response. All materials show very broad oxidation and reduction peaks across a wide potential window, a phenomenon commonly observed in amorphous materials. With the exception of the sample synthesised using 1.5 mL of HMDST, which shows a slight peak shape at around

1.6 V, all the materials show no clearly resolved peaks on the reduction scan. The oxidation scan displays a decrease in current at higher potential to produces a very broad peak shape. As the amount of HMDST used increases, the centre of oxidation peaks shifts towards a lower potential, which reduces the charge separation between the reduction and oxidation processes. This results in a reduction in the overpotential, a change indicative of improved charge transfer kinetics.[282] However, the composite made using 3.5 mL of HMDST does not shift to a lower potential, but instead shows a more redox active peak shape than the other composites. Cyclic voltammetry measurements of this material at a variety of different scan rates are shown in Figure 5.13 (other samples are presented in Figure 8.38 to 8.40).). These data indicate an improvement in conductivity due to the improved charge transport of the materials and corroborates with the EIS data analysis, which shows that as the amount of HMDST increases the current response decreases. This is caused by increase in weight of material and filling of the pores reducing the current produced per gram of active material and indicates a likely drop in capacity. The data thus demonstrates that excess heat and HMDST cause pore blockage and reduction in performance due to build up of Ti-S-$(CH_3)_3$ groups on the surface at the expense of Ti-S-Ti moieties to observe a similar trend.

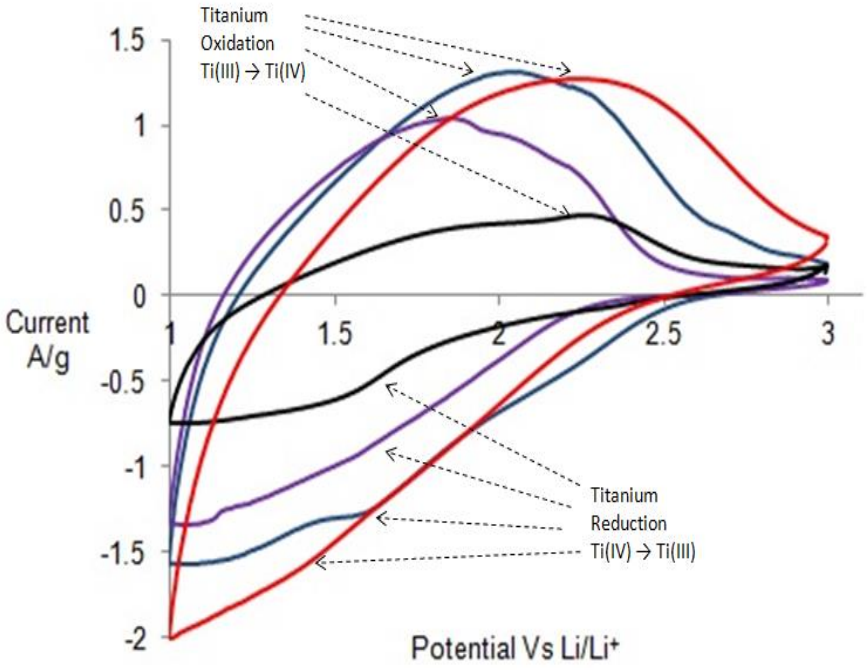

Figure 5.12: Cyclic voltammetry over a potential range of 1-3.4 V vs Li/Li^+ standard electrode potential at 5 mVs^{-1} for m-TiO_2 (red), composites made using 1.5 mL (blue), 2.5 mL (purple), 3.5 mL (black) of HMDST at temperatures of 150 °C

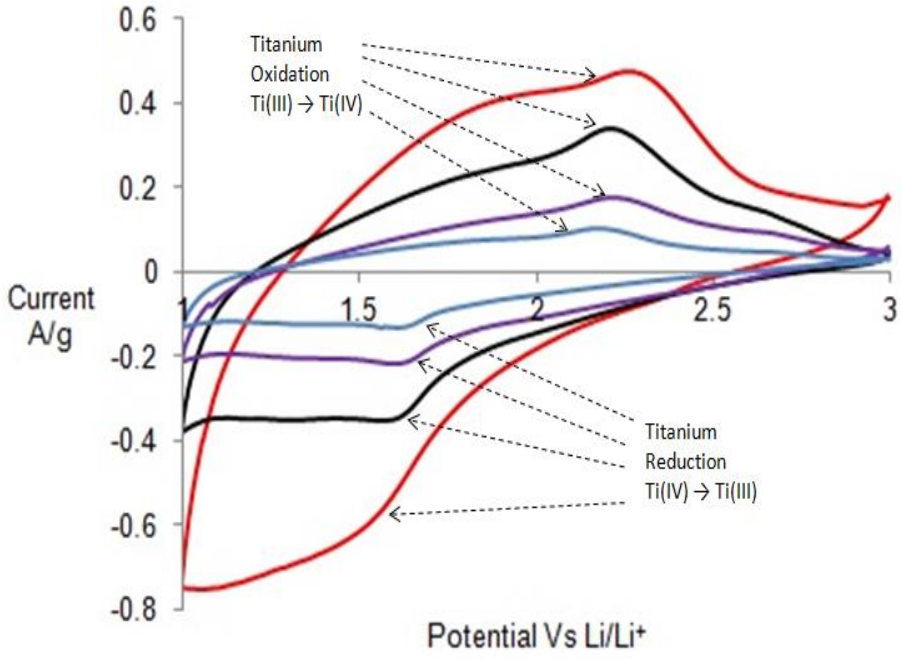

Figure 5.13: Cyclic voltammetry over a potential range of 1-3.4 V vs Li/Li^+ standard electrode potential at various sweep rates of composite made using 1.5 mL of HMDST at 150 °C at 0.5 mVs^{-1} (blue), 1mVs^{-1} (purple), 2 mVs^{-1} (black) and 5 mVs^{-1} (red)

Initially the shape of the voltammogram becomes slightly more resolved using temperatures of 100 °C before becoming more resolved for samples made above 150 °C. The most resolved peak being that of the composite made at 150 °C with 3.5mL of HMDST. As the heat treatment temperature is increased, the size of the current produced decreases significantly for the sample made using temperatures >100 °C. These results agree with the BET data which showed significant decrease in surface area at temperatures >100 °C, indicating that this dramatic decrease in active surface area is the reason for this drop in the quantity of current produced. The cyclic voltammetry of other composites is presented in Figure 8.41 and 8.42

Chronopotentiometry (charge discharge analysis) was carried out to assess the respective capacitates of each composite material in addition to the stability of the material over a period of 50 charge cycles. All assessments were carried out at a current density of 1 $mA.cm^{-2}$ and the data for the composite materials synthesised using different quantities of HMDST is shown in Figure 5.14. Composites synthesised at 150 °C using 1.5, 2.5 and 3.5 mL of HMDST possessed initial capacities of 111, 96 and 59 mAh/g which decreased over the course of 50 cycles to values of 60, 64 and 48 mAh/g, respectively. These results are compared to m-TiO_2, which has an initial capacity of 137 mAh/g and drops to 45 mAh/g after cycling. These results

demonstrate that although the conductivity of the composites is higher than that of the starting material, the initial capacities decrease, with the largest decreases observed with the use of higher amounts of HMDST. This is likely due to the increase in the weight and loss of surface area caused by increased hydrocarbon content and pore blockage, as confirmed by nitrogen adsorption and TGA analysis. It is also noticeable that over the course of 50 cycles, as the amount of HMDST used increases, the cycle stability of the material also increases, with capacity retentions of 54, 62 and 81% for composites synthesised using 1.5 2.5 and 3.5 mL, respectively, compared to 33% for the starting material (Figure 8.43) This is the result of the improved conductivity and slight improvement to Li^+ diffusion coefficients demonstrated in the EIS analysis.

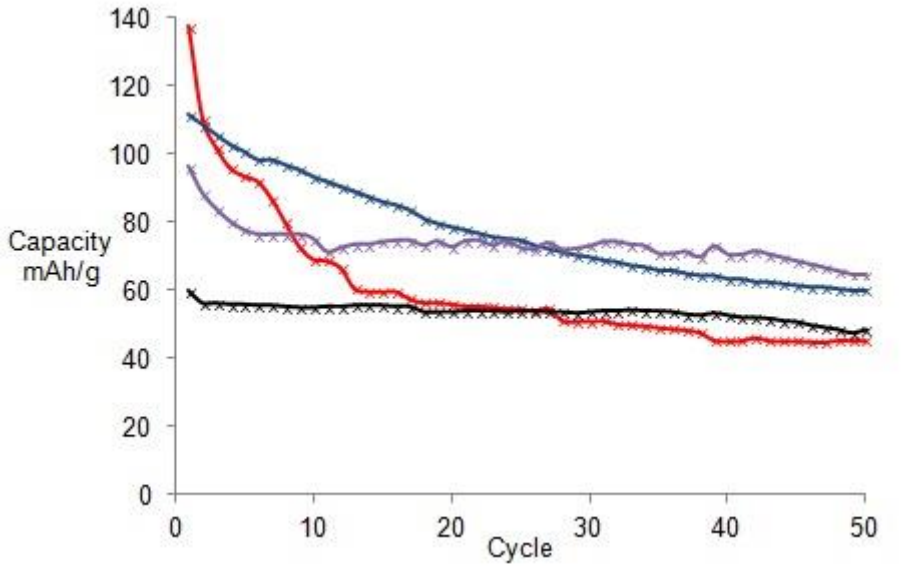

Figure 5.14: 50 Cycles discharge capacity data for m-TiO_2 (red), composites made using 1.5 mL (blue), 2.5 mL (purple) and 3.5 mL (black) of HMDST at temperatures of 150 °C

The cycle data for materials synthesised using 3.5 mL of HMDST at different heating temperatures is shown in Figure 5.15. The initial capacities are 101, 60 and 42 mAh/g, decreasing to 77, 48 and 30 mAh/g for composites made at 100, 150 and 200 °C, respectively. These results indicate that with the same amount of reagent, the performance is influenced by the heating treatment temperature. All materials possessed lower initial capacities than the starting material, and by increasing the temperature leads to a larger decrease in the initial capacity. This is in close agreement to the surface area data which demonstrates that loss of surface area leads to a decrease in capacity performance of the material. All materials possess good capacity retention as can be seen in Figure 5.16. The final capacity retention values are

76, 81 and 72% for composites made at 100, 150 and 200 °C, respectively. This compares to 35% for the pristine material, demonstrating that S-doping dramatically improves the cycling retention of the materials, which show only a small decrease in performance after an initial drop over the first three cycles.

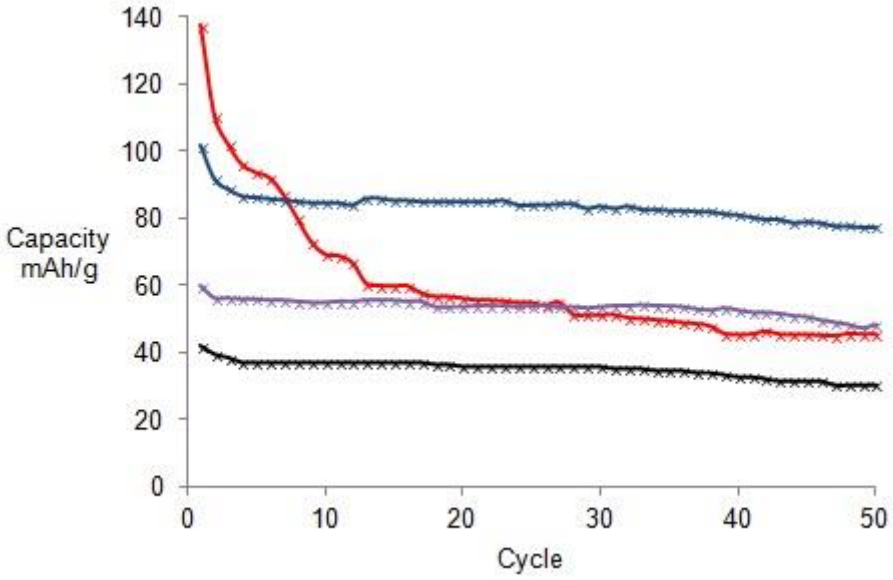

Figure 5.15: 50 Cycles discharge capacity data for m-TiO_2 (red), composites made using 100 °C (blue), 150 °C (purple) and 200 °C (black) with 3.5 mL of HMDST

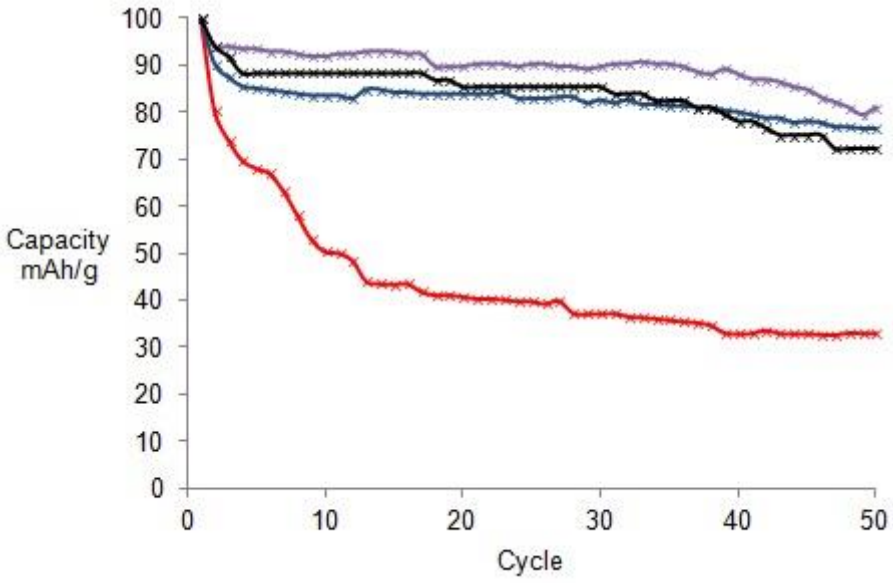

Figure 5.16: 50 Cycles discharge capacity retention data for m- TiO_2 (red), composites made using 100 °C (blue), 150 °C (purple) and 200 °C (black) with 3.5 mL of HMDST

5.4. Conclusions:

By exploring the use of HMDST under a number of various synthesis conditions, we successfully synthesised high surface area titanium oxysulfides to improve electron conductivity without the loss of mesostructure and porosity. While incomplete reaction to surface S-Ti-S moieties hindered ultimate performance by leaving diffusion-obstructing organic residue anchored to the surface, the conductivity of the materials improved significantly with the use of larger amounts of HMDST up to 3.5 mL demonstrated from the reduction of R_{ct} from 189 to 25 Ω. Increasing synthesis temperature up to a peak of 150 °C improves the conductivity before dropping off at 200 °C. Despite improvements to conductivity, the materials lose surface area with increased amounts of HMDST reagent due to anchored Ti-S-$(CH)_3$ groups, dropping from 660 – 66 m^2/g. This loss in surface area lead to the loss of Li^+ storage capabilities with initial capacities dropping from 137 to 48 mAh/g from 0 – 3.5 mL of HMDST, in addition to reduction in capacity for higher heating temperatures. Composite materials showed improved capacity retention over the course of 50 cycles. With the best battery material proving to be the composite made with 3.5 mL of HMDST at 100 °C, retaining most of the hosts initial capacity at 111 mAh/g while also possessing the highest final capacity of 77 mAh/g. While further improvements in synthesis may lead to even better performance pay-offs by increasing the concentration of surface Ti-S-Ti units while minimising pore blockage by organic residues, the current protocol appears to be a useful strategy in improving cycle life and retaining peak performance in amine-templated mesoporous transition metal oxides, which have up to now shown disappointing electrochemical performance due to low conductivity and loss of activity on cycling.

Chapter 6 : Vanadium Hydride Gels for Use in Energy Storage

6.1 Introduction

Homoleptic hydrides of the first row transition metals[283] represent a new frontier in energy storage because of their low molecular weight, electrochemical flexibility, a feature that can be exploited in energy storage. The transition metal dihydrides, MH_2 (M= Cr,[284] Mn,[285] Fe,[286] Co, and Ni[287]) and trihydride of the form MH_3 (M= Ti[288]) have been observed as molecular species using matrix isolation techniques at cryogenic temperatures but have previously never been isolated in bulk form. Because of the low cost (ca. 15-20 USD/kg) and importance in battery materials, the development of general synthetic routes into vanadium hydrides would represent an important advance. Metallic vanadium reacts with hydrogen at room temperature and atmospheric pressure to give non stoichiometric monohydrides up to $VH_{0.9}$. Higher hydrides of vanadium ($VH_{\sim 1.6}$) were prepared by Maeland *et al* using electrolytic techniques.[289] Later the dihydride, VH_2 was formed by reaction of vanadium with 6.9 bar hydrogen at 450 °C but this was found to be unstable at room temperature.[290] From the standpoint of electrochemical energy storage the synthesis of higher oxidation state vanadium hydrides is important because of the greater electron per mole capacities than the lower oxidation state species, however to the best of our knowledge a higher hydride such as a VH_4 species has never previously been isolated or characterised.

Previous research into battery materials has shown that transition metal compounds perform well as cathode materials for Li^+ batteries. This is particularly true for light weight high oxidation state vanadium materials as shown by the relative performance of V_2O_5.[291,292] The lower oxidation state vanadium materials such as VO_2 and V_2O_3 have also shown potential with initial capacities of >150 mAh/g.[293–295] Related vanadium hydride materials could have significant potential as a lithium battery cathode material as they would possess a number of vanadium centers in the V(IV) or V(III) oxidation states, providing the capacity for lithium insertion, and because the hydride ligands are considerably lighter than the oxygen present in traditional vanadium oxides, affording higher electron per gram energy storage numbers. Fabricating these materials in a nanocrystalline form would be of added benefit because of the potential for pseudocapacitance,[27] which uses a similar mechanism to that of traditional bulk phase materials, however the vast majority of the redox centers are situated near the surface.

This significantly improves the charge transfer kinetics due to more facile redox reactions and shorter diffusion path lengths allowing the easier release of ions.[27,31] This is highly desirable as it allows the material to possess the high energy densities seen in bulk insertion materials, but in addition possesses a higher power density due to the materials ability to release charge faster than with bulk materials.

6.2 Experimental

General

All chemicals were purchased from Sigma-Aldrich and used without further purification. Manipulations were performed in an argon glove box or on a nitrogen Schlenk line. Reactions with hydrogen were carried out in the solid state using a stainless steel PARR hydrogenation vessel. Grade 6 hydrogen purchased from Air Liquide was used for synthesis and isotherms.

6.2.1. Syntheses

Preparation of Tetraphenyl Vanadium(IV)

By analogy to Wilkinson's synthesis of tetrakis(trimethylsilylmethyl) vanadium from VCl_4 and the alkyl lithium,[296] phenyllithium (50 mmol, 25 mL of a 2.0M solution in dibutylether) was stirred at room temperature. To this (2.03 mL, 12.5 mmol) of VCl_4 was added drop wise via a syringe. The reaction mixture turned dark brown in color, increased in temperature and bubbled vigorously. The reaction continued stirring for fifteen minutes until it had stopped bubbling and had cooled back to room temperature. The reaction was filtered to give a dark brown precipitate and brown filtrate. Because of the well-documented thermal instability of homoleptic alkyl complexes of vanadium,[297] the tetraphenyl vanadium (IV) complex was not isolated, but used immediately in the next synthesis protocol described below.

Preparation of Vanadium Hydride Gel

The filtrate was immediately transferred to the PARR pressure vessel and was stirred under an inert atmosphere of argon for 48 hours at 100 °C. The reaction was filtered to give a black precipitate. The precipitate was dried *in vacuo* for four hours at 100 °C to afford a fine black powder (V(IV)-100) (728 mg). The black powder was hydrogenated in the PARR vessel at a

pressure of 70 bar H_2 for 48 hours at 25 °C. The material was then dried *in vacuo* for 4 hours at 100 °C and allowed to cool to room temperature to give a black powder (V(IV)-25C-H_2) (109.3 mg).

6.2.2. Characterisation

Infrared spectroscopy was conducted on a Perkin Elmer Spectrum RX1 using KBr. Prior to analysis the IR grade KBr was oven dried overnight at 120°C to remove residual water. A blank sample of KBr was ground in an oven-dried pestle and mortar in the glovebox and then compressed in air to form a disc. A background was taken of the blank KBr disc. Approximately 5 mg of sample was ground with 200 mg KBr in the glovebox and then compressed in air quickly to form a disc. The spectrum of KBr was subtracted from the IR of the sample. Nitrogen adsorption and desorption data were collected at -196 °C on a Micromeritics ASAP 2020. A fluid (xylene) displacement method was used 25 °C to measure the density of the material. The PXRD spectrum was taken using a Bruker Discover diffractometer with a Vantec 500 2D detector using Co Kα radiation. The X-ray beam was limited using a 0.2 mm collimator. The X-ray spectrum was taken using a Bruker DaVinci diffractometer with Cu Kα radiation. The XPS analysis was performed using a PHI-5500 spectrometer using monochromated Al Kα radiation. The positions of the peaks were referenced to surface C-C or C-H bound at 284.8 eV. The powder was placed on the XPS holder inside an Ar glove box and transferred under Ar to the XPS intro chamber without any exposure to air. For insulating materials, an electron-flooding gun was used to compensate the surface charges. The different chemical contributions for each spectrum were obtained using CasaXPS. The thermogravimetric analysis (TGA) and differential thermal analysis (DTA) were carried out in a STA 449C analyser from Netzsch under a flow of dried air at 10.00 °C/min up to 650 °C. Argon was also used to protect the balance section.

6.2.3. Electrochemistry

All electrochemical analysis was performed with a Princeton Applied Research VersaSTAT using a cell constructed within an argon filled glove box to ensure minimal exposure to oxygen. Electrochemical performance of the synthesised electrode materials as a Li^+ battery electrode was assessed using a two electrode set up. Working electrodes of V(IV)-25C-H_2 and VO_2 consisted of 80% active material, 10% super conducting carbon black, and 10%

polyvinylidenefluoride (PVDF) by weight. The electrode paste was made by grinding the active material with carbon black to ensure a good mixture of the powders. The powders were then stirred with PVDF and *n*-methyl-2-pyrrolidinone (NMP) solvent until a homogenous paste was formed. The paste was spread onto copper foil (current collector). The electrode was dried by first heating to 80 °C to bake off any excess NMP solvent before increasing the temperature to 120 °C overnight to allow the electrode material to bind with the current collector. Once completed, the electrodes were punched using a Hohsen electrode punch to produce uniform sized discs of 15 mm. The respective counter electrode of lithium metal foil was also punched into a 15 mm disk. The electrolyte used in this investigation is 1.0 M $LiPF_6$ dissolved in ethylene carbonate (EC) and diethyl carbonate (DEC) solutions at a ratio of 1:1 by volume.

The cell potential window used for these tests was between 1-3.2 V vs. Li/Li^+. The cyclic voltammetry measurements were carried out at scan rates of 0.5, 1, 2 and 5 mVs^{-1}. The initial potential of the scan was determined by the open circuit potential the cell (typically 2.5-2.55 V vs Li/Li^+) with the initial scan direction being directed in the reduction direction towards a lower potential limit (1 V vs Li/Li^+) with cycles being completed once the final reduction sweep reaches the starting potential of the cycling process. Galvanostatic charge discharge data was recorded at a current density of 1 $mA.cm^{-2}$. All measurements were carried out at room temperature using a Hohsen HS flat cell.

6.2.4 Electrochemical Impedance Spectroscopy

Electrochemical AC impedance spectra were obtained using the same two electrode Li^+ battery cell set up using the active material as the active electrode and a lithium metal foil as the counter electrode. Measurements were applied using a sine wave with amplitude of 5 mV over the frequency range from 100 KHz to 0.01 Hz. Measurements were carried out prior to the initial discharge of the cell, using a biased potential equivalent to that of the open circuit potential of the cell, this was necessary in order to remove the influence of polarisation on the values of conductivity that are produced.

6.3 Results and Discussion

6.3.1Materials Characterisation

In this Chapter the synthesis of a multivalent vanadium hydride gel and its properties as an energy storage material. To prepare the non-stoichiometric vanadium hydride gel, VCl_4 was reacted with phenyllithium in dibutyl ether and the subsequent mixture was filtered to give a black solution. The solution was placed immediately in a stainless steel pressure vessel and the reaction was stirred at 100 °C for 48 hours. The reaction was filtered to give a black precipitate which was dried *in vacuo* at 100 °C for four hours to afford a black air moisture sensitive solid (V(IV)-100). The summery of the proposed reaction mechanism is shown in Scheme 6.1, we presume that during heat treatment the vanadium alkyl precursor polymerises via a bimolecular C-H activation process with loss of benzene to form a metal containing polymer with bridging phenyl groups. An alternate decomposition route would involve some combination of disproportionation and bond homolysis to form two equivalents of biphenyl and V metal. However the IR evidence discussed below shows hydrocarbon in the polymer, supporting our assignment as an organometallic polymer. The material V(IV)-100 was then treated with hydrogen at 70 bar for 48 hours at 25 °C to give sample V(IV)-25C-H_2. In this step, it is proposed that the bridging phenyl ligands are replaced with bridging hydrides via hydrogeneolysis to form a polymeric vanadium(IV) hydride material. Physical characterisation and hydrogen storage measurements have been carried out on each sample.

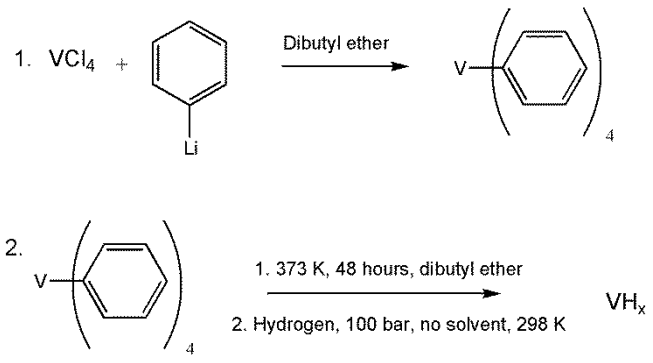

Scheme 6.1: Proposed mechanism for the synthesis of vanadium(IV) hydride

Infra-red spectroscopy was used to determine the reduction in hydrocarbon content of each material by looking at the intensity of the C-H stretch in the 2900–2960 cm^{-1} region. The infra-red spectra of V(IV)-100 and V(IV)-25C-H_2 are shown in Figure 6.1. For V(IV)-100 there are C-H stretches at 2958, 2919 cm^{-1} and 2868 cm^{-1}. The intensity of the C-H stretches decrease slightly after room temperature hydrogenation at 70 bar as the hydrocarbon ligands are replaced

by hydrides during hydrogeneolysis. Typically transition metal-hydride bonds come in the region of 1900±300 cm^{-1}. However they can be weak in intensity and appear lower in the case of bridging.[298] There is a stretch in this region at 1633 cm^{-1} for V(IV)-25C-H_2 with a shoulder at 1575 cm^{-1}. In KBr, water displays bands at 3300 and 1647 cm^{-1}, therefore the V-H stretch in the spectrum of V(IV)-25C-H_2 at 1575-1633 cm^{-1} is possibly obscured by an O-H stretch from water absorbed by the KBr disc during the transfer from the glove box to IR apparatus.

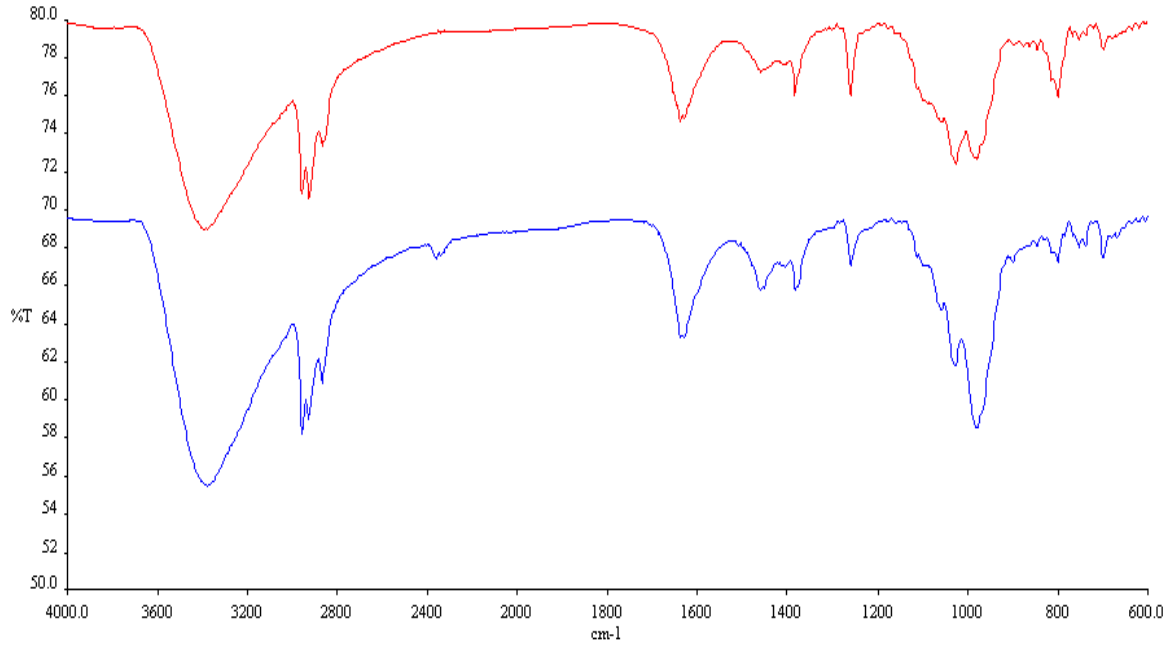

Figure 6.1 Infrared spectra of V(IV)-100 (blue) and V(IV)-25C-H_2 (red)

Nitrogen adsorption-desorption isotherms of V(IV)-100 and V(IV)-25C-H_2 are shown in Figures 8.45 and 8.46 respectively. The surface area of VH-100 is 0.6 m^2/g. After hydrogenating this material in the solid state at 150 °C the surface area of VH-150 increases to 2.2 m^2/g. The increase in surface area could be due to loss of hydrocarbon from the material new pathways in the material. In both materials the nitrogen adsorptions can be described as type II in nature. There is no significant increase in slope between 0 and 0.1 P/P_0 indicating that there is no microporosity in both materials. The low surface area and lack or porosity differs from those of the CrH_3 [299] and TiH_3 [300] materials synthesised previously using similar strategies, these possess significant microporosity and surface areas from 300-500 m^2/g, suggesting a more closely packed structure.

The PXRD pattern is shown in Figure 8.47. Apart from a low angle reflection suggestive of some mesoscopic order, there are some small reflections in the 25 – 35 ° region that correspond to the glass capillaries. The majority of the diffraction does not give rise to reflections meaning that the sample is largely amorphous. This is not surprising as the vanadium region of the XPS discussed below shows that there are multiple species of vanadium in different oxidation states present in the material. Thermogravimetric analysis (TGA) was carried out on V(IV)-100 and V(IV)-25C-H_2 to determine the percentage of hydrocarbon remaining in each material after thermal precipitation and hydrgoeneolysis.

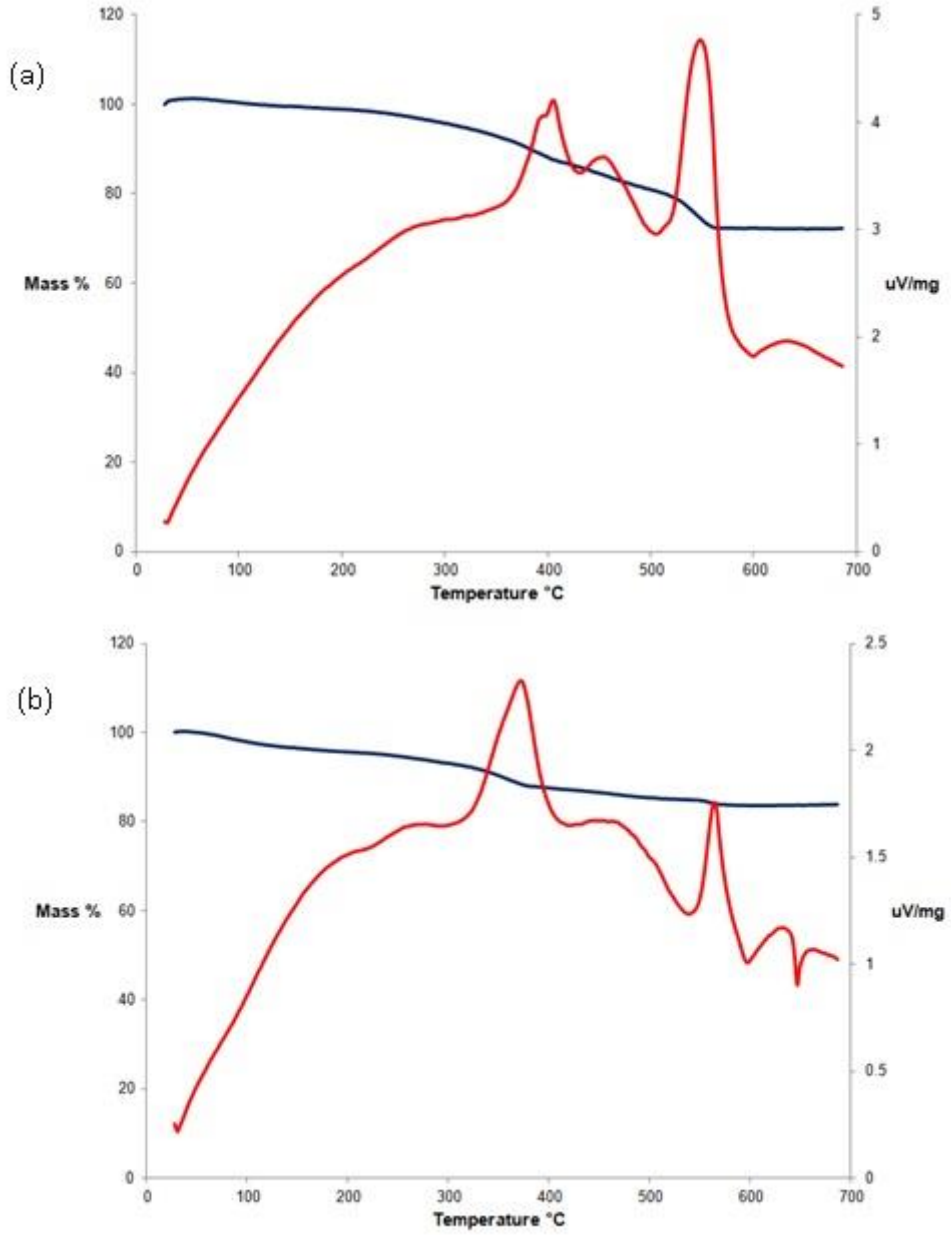

Figure 6.2: TGA (red) and DTA (blue) curves of (a) V(IV)-100 and (b) V(IV)-25C-H_2

The TGA and DTA curves of V(IV)-100 and V(IV)-25C-H_2 are shown in Figure 6.2. For V(IV)-100, as the temperature increases from room temperature to 563 °C the mass of the sample decreases by 27.5%, due to the combustion of remaining phenyl ligands in the material. This is also observed in the DTA curve where there is a broad peak centered at 548 °C. After 563 °C the percentage mass of the material then stabilises. After solid state hydrogenation, the TGA plot of V(IV)-25C-H_2 shows that as the temperature of the sample increases from 0-572 °C the mass of the sample decreases until it reaches a plateau. The loss of sample decreases more rapidly between 0-376 °C where an exotherm is observed in the DTA plot centered at 371 °C. The mass of the sample decreases less rapidly between 376-572 °C, where an exotherm is seen in the DTA plot centered at 564 °C. The plateau between 572-685 °C is where the mass of the sample stabilises with 83.7% of the original sample mass remaining. This demonstrates that solid-state hydrogenation indeed leads to the expected reduction in the amount of hydrocarbon left in the material. As the final material is still 16.3% hydrocarbon by weight, possibly solid-state hydrogenation for longer periods or at higher temperatures and pressures may be able to fully remove all the phenyl ligands and replace them with hydrides by hydrogeneolysis. While the exact composition of the final material cannot be determined precisely by elemental analysis to determine the exact molecular formula of to make V(IV)-25C-H_2 due to the formation of vanadium carbide on combustion. This data in combination with the synthetic pathway used is consistent with the formulation of the material as a vanadium alkyl hydride gel with a formula $VH_{x-y}(C_6H_5)_y$.

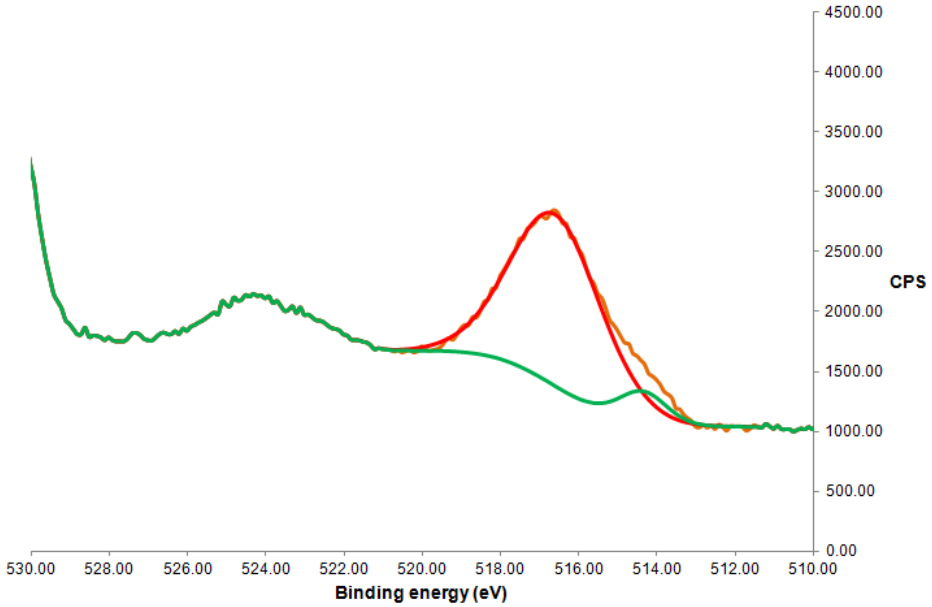

Figure 6.3: Peak fitting of vanadium 2p3/2 region of XPS of V(IV)-100

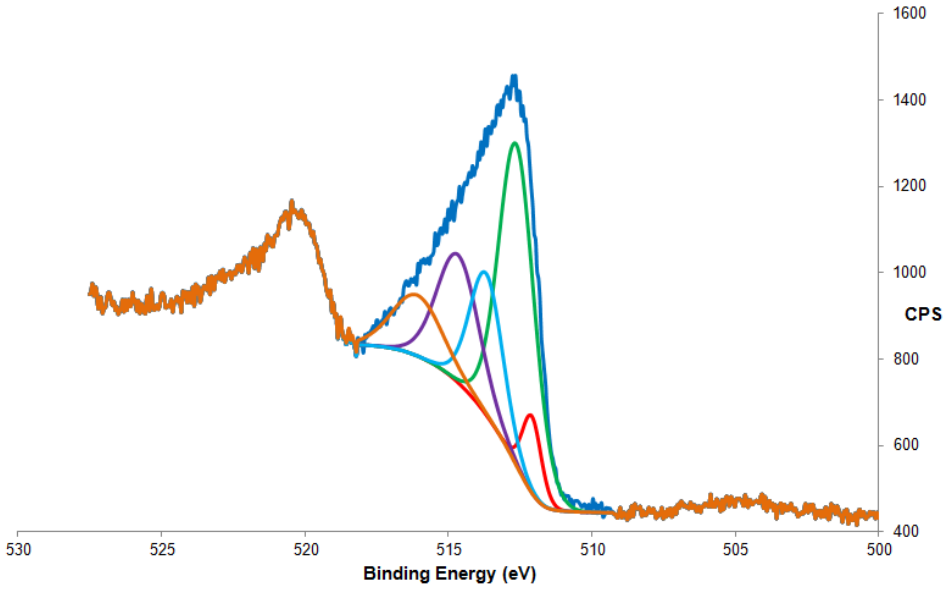

Figure 6.4: Peak fitting of vanadium 2p3/2 region of XPS of V(IV)-25C-H_2

XPS was carried out to determine the oxidation state of the vanadium in both materials as shown for V(IV)-100 and V(IV)-25C-H_2 in Figures 6.3 and 6.4 respectively. The base line corrected XPS are shown in Figures 8.48 and 8.49. In the vanadium 2p/3 region of V(IV)-100 there is a broad emission centred around 517 eV. Peak fitting of this emission demonstrates that there are multiple oxidation states of vanadium present in the material. A vanadium (V) species is present at 516.9 eV. The emission for a V(V) is close to the emission of V(V) at 515 eV for V_2O_5.[301] The emission at 515.3 eV can be attributed to a V(III) species as it is close to the emission seen for VCl_3 at 515 eV.[302] After hydrogenation of V(IV)-100 to give V(IV)-25C-H_2 there is broad emission around 512 – 516 eV as shown in Figures 6.3 and 6.4. Peak fitting of this emission demonstrates that there are multiple oxidation states of vanadium present in the material. A vanadium (IV) species is now present in the material after treatment with hydrogen as shown by the emission at 516.1 eV, which is likely caused by reduction during hydrogenation. The emission for a V(IV) is close to the emission of V(IV) at 516.3 eV for V_2O_4.[303] The emission at 515.3 eV and 514.3 are very similar in intensity and can be attributed to a V(III) species as they are both close to the emission seen for V_2O_3 at 515.7.[303] This suggests that there could be two different V(III) species with slightly different environments which gives rise to the two emissions that are close together and of similar in intensity. The emission with the largest intensity is at 513.8 eV and can be attributed to a V(II) species as it is close to the emission at 513.9 eV seen for VS. This emission most likely originates from reduction by hydrogen of some of the V(III) species in V(IV)-100 to a V(II).

The emission at 512.2 eV can be attributed to V(0)[304] produced by some combination of hydrogen reduction and subsequent reduction.

6.3.2 Electrochemical Assessment

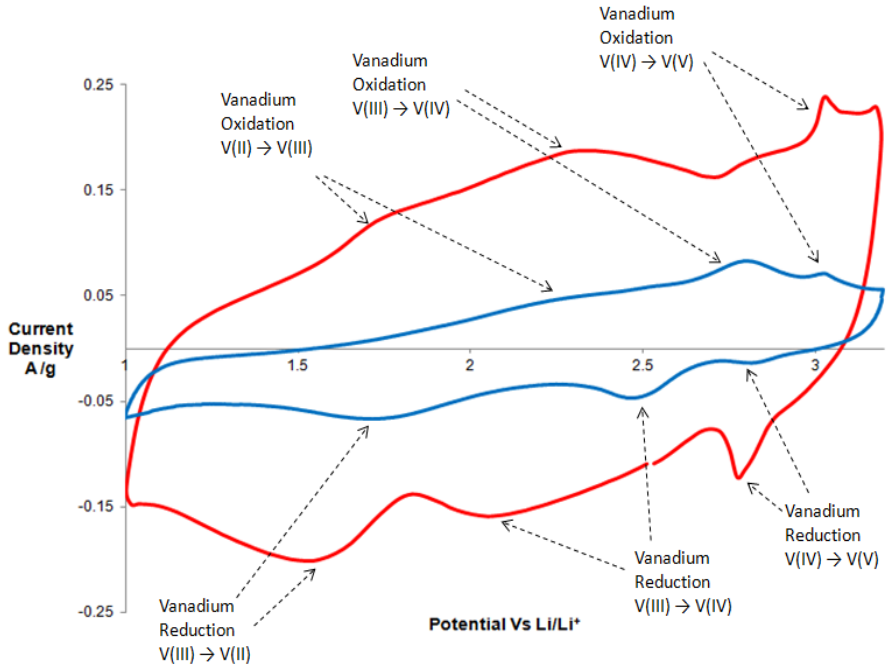

Figure 6.5: Cyclic voltammetry over a potential range of 1-3.2 V vs Li/Li^+ standard electrode potential V(IV)-25C-H_2(red) and VO_2 powder (blue) at a sweep rate of 0.5 mVs^{-1}

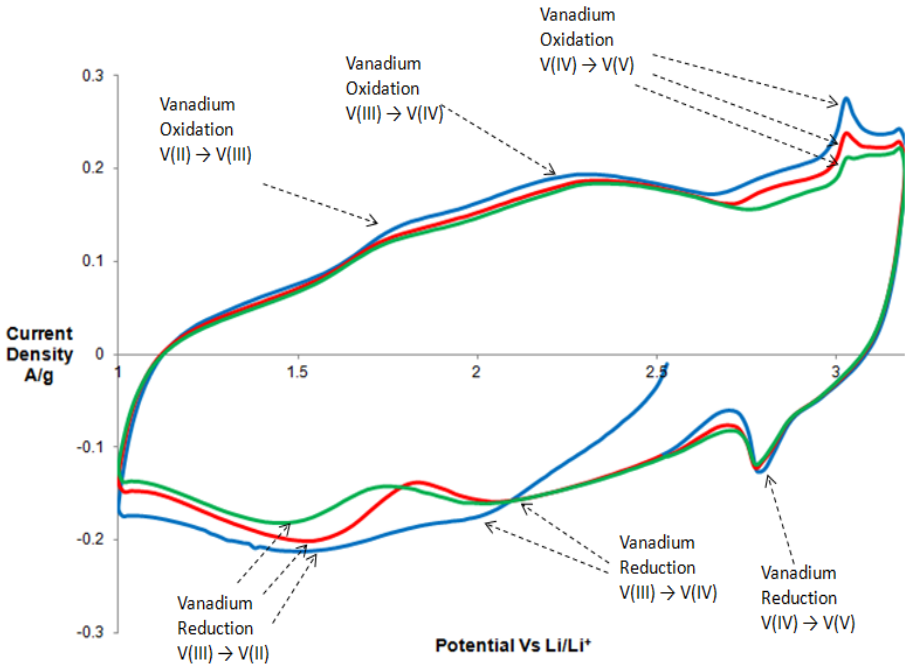

Figure 6.6: Cyclic voltammetry over a potential range of 1-3.2 V vs Li/Li^+ standard electrode potential V(IV)-25C-H_2 at a sweep rate of 0.5 mVs^{-1} 1st cycle(blue), 2nd cycle(red) and 3rd cycle (green)

Because V(IV)-25C-H_2 contains a variety of V oxidation states the further characterisation by electrochemical methods and possible exploitation for energy storage of the apparent redox flexibility of this material is warranted. Thus, the electrochemical properties of V(IV)-25C-H_2 were assessed using a variety of electrochemical methods. The potential window for this material is slightly different to those previously observed for V(IV) materials as V(IV)-25C-H_2 became unstable above 3.2 V and so measurements were unable to reach the maximum 4 V typically used for other compounds of vanadium.[293,305] For this reason we tested a VO_2 commercial powder standard by which to compare the electrochemical behaviour.

Cyclic voltammetry measurements of V(IV)-25C-H_2 and VO_2 were carried out at a variety of different sweep rates. Figure 6.5 shows the CV's of both V(IV)-25C-H_2 and the standard VO_2 powder at the lowest scan rate of 0.5 mVs^{-1}. The low scan rate displays the most accurate picture of redox processes occurring within the material. Figure 6.6 above shows the first three cycles of the CV of V(IV)-25C-H_2 measured at a 0.5 mVs^{-1} scan rate. The first cathodic sweep of V(IV)-25C-H_2 shows a single broad peak in the first cathodic sweep from 2.5-1 V, displaying no distinct features. This is explained by the amorphous nature of the material confirmed by the PXRD and XPS data revealing that the material is multivalent with oxidation states between V(0) and V(IV). The variety of different energy levels and the amorphous structure of the material produce the broad peak observed rather than resolved peaks at specific potentials. The reference material VO_2 (Figure 8.50) displays two peaks on the initial cathodic sweep at 2.45 and 1.7 V. The first peak is referenced as the insertion potential for Li^+ insertion into VO_2 reducing V(IV) to V(III).[293,295,305] In the first initial anodic sweep of VH-150 again the current produces a broad signal which can be interpreted as two broad peaks centred at 1.7 and 2.3 V, with the addition of a more resolved peak present at 3 V. The anodic sweep of VO_2 also produces three peaks at 2.3, 2.8 and 3.05 V. The best resolved peak at 2.8 V represents what is normally the V(III) to (V(IV) oxidation observed in VO_2 materials, suggesting the other peaks at 2.3 and 3.05 V in the VO_2 powder most likely represent oxidations from V(II) to (VIII) and V(IV) to V(V), respectively. This indicates that the same transitions occur in V(IV)-25C-H_2 but at lower potential values then that of the respective oxide. The second cycle produced a more informative picture of the electrochemical nature of the material. The cathodic sweep of V(IV)-25C-H_2 now displays three peaks centered at 2.7, 2.1 and 1.6 V. The first peak is well resolved whereas the two subsequent peaks are still broad but now show more resolved peaks

than previously. This is most likely due to the fact that more vanadium species are now present at the same oxidation state during cycling. The appearance of a small new peak at 2.85 V in the VO_2 powder on the second cathodic sweep confirms this new peak to be the reduction back of V(V) to V(IV). The comparison of V(IV)-25C-H_2 to the VO_2 reference allows the interpretation that the three peaks represent successive reductions from V(V) to V(II). At slightly lower potential values then those of the respective oxide. This is possibly due to the difference in ligands in V(IV)-25C-H_2 compared to the oxide in the standard, which have been shown to affect the redox potentials of a compound.

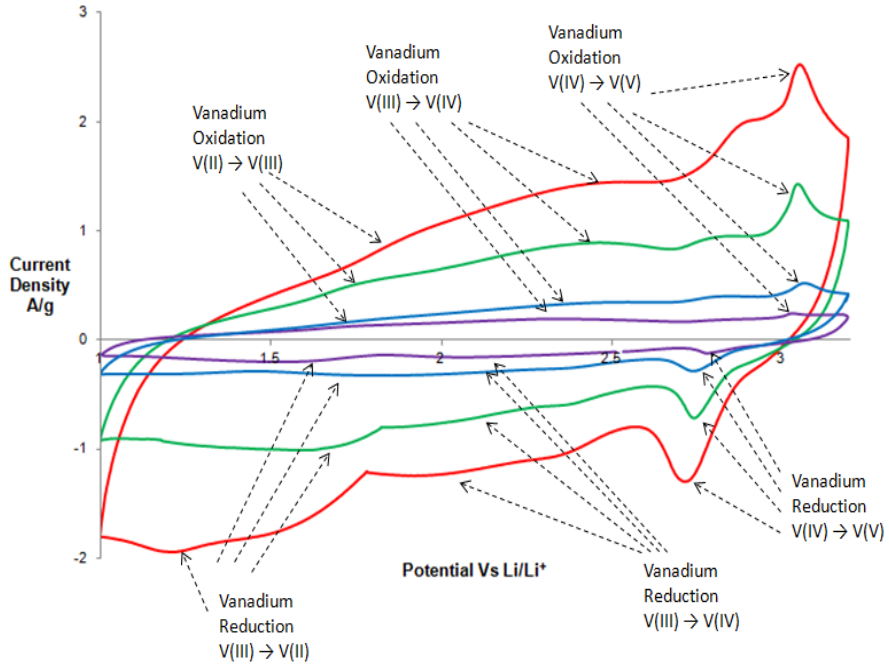

Figure 6.7: Cyclic voltammetry over a potential range of 1-3.2 V vs Li/Li^+ standard electrode potential at various sweep rates of V(IV)-25C-H_2 0.5 mVs^{-1} (purple), 1 mVs^{-1} (blue), 2 mVs^{-1} (green) and 5 mVs^{-1} (red)

Figure 6.7 shows the CV of V(IV)-25C-H_2 taken at a variety of different scan rates and it is clear that the current produced is approximately proportional to increase in sweep rate as by doubling the sweep rate, the current produced is almost doubled. The current is directly proportional to the sweep rate, this is indicating of a surface limited process typically seen in for capacitor responses to in an increase in sweep rate. Diffusion limited process typical for insertion based mechanisms, typically utilised by battery materials, are proportional to the square root of the sweep rate.[31]

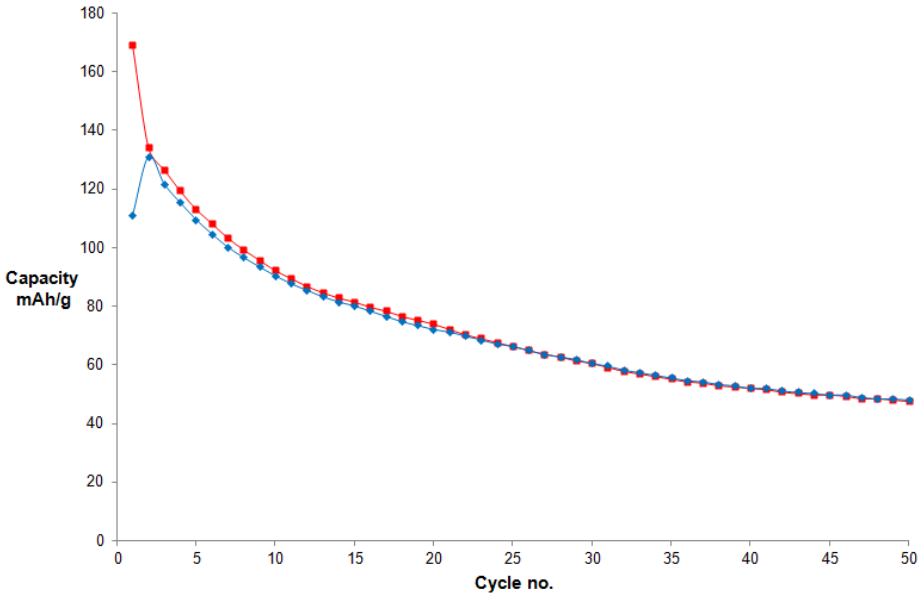

Figure 6.8: 50 cycles charge (red) and discharge (blue) capacity data for V(IV)-25C-H_2 at 1 mA.cm^{-2}

The capacity of V(IV)-25C-H_2 was assessed by galvanostatic charge discharge analysis over the course of 50 cycles and is shown above in Figure 6.8. V(IV)-25C-H_2 has an initial capacity of 111 mAh/g, which increases upon its first full charge to a peak capacity of 131 mAh/g. The reason for the increase in capacity after the first cycle is due to the oxidation of vanadium centers that where initially present in the lower oxidation states to higher oxidation states, allowing a higher concentration of lithium ions to be incorporated to balance the increased number of high oxidation state vanadium ions upon discharge. After carrying out 50 cycles, the capacity dropped by 64% to 47 mAh/g. These results indicate that despite showing an initial capacity comparable to previous published promising VO_2 cathode materials, the recyclability of the material is not sufficient to maintain its performance with repeated cycling. These capacities are not as high as most of the recorded examples of VO_2 and V_2O_3 which typically produce capacities around 160-250 mAh/g.[293,306–308] However, these materials have been developed in order to maximise their performance as a cathode material. When comparing these results to those of bulk VO_2, which produced capacities around 128 mAh/g dropping to 58 mAh/g at a lower current density,[309] this indicates an improvement shown by the use of the hydride ligand in the bulk state. Given the improvement relative to bulk VO_2 with better tailored morphologies, it is possible that the same could be achieved using the much lighter hydride ligand to produce improved capacity and recycling performance.

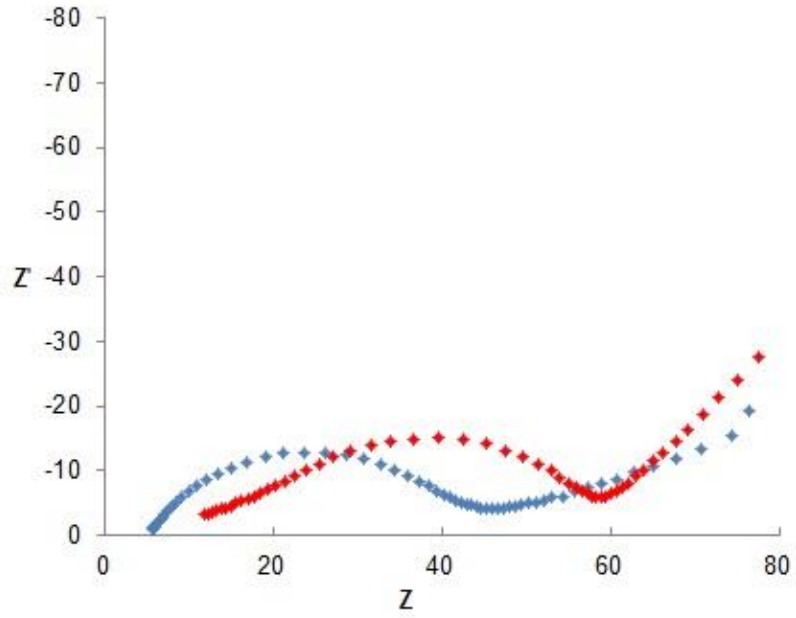

Figure 6.9: EIS spectra over the frequency range from 100 KHz to 0.01 Hz using a two electrode setup, using biased potentials equivalent to the open circuit potential of the cell, V(IV)-25C-H_2 prior initial discharge at 2.293 V vs Li/Li^+ ((blue) and Upon completion of 50^{th} discharge/charge cycle at 2.274 V vs Li/Li^+ (red)

The impedance measurements were all carried out over the frequency range from 100 KHz to 0.01 Hz using a two electrodes setup, using a biased potential equivalent to that of the open circuit potential of the cell, all open circuit potential values are listed in the Figure caption. Figures 6.9 and 8.51 show the Nyquist plots for both V(IV)-25C-H_2 and VO_2 respectively. They demonstrate the impedance spectra prior to initial discharge and after the final charge on completion of the 50 cycles. Both materials show a semicircle present at the high frequency region of plot, followed by a Warburg tail. The initial semicircle is of key importance as it indicates the charge transfer resistance of the material. The Warburg tail (W) is associated with lithium diffusion in the bulk of the active material. The high frequency intercept of the semicircle is related to the electrolyte resistance (R_e) and the diameter of the semicircles indicates the charge transfer resistance (R_{ct}) for the material. Using the diameter of the semicircles we calculated the initial values of R_{ct} to be 38.41 Ω and 44.39 Ω for V(IV)-25C-H_2 and VO_2 respectively, which rises to 46.67 Ω and 44.58 Ω after completing 50 cycles. This confirms that the V(IV)-25C-H_2 has a charge transfer resistance that is initially lower relative to that of our reference VO_2 powder but after recycling the resistance increases so that it is larger than the VO_2 commercial powder which barely increases after 50 cycles. This is possibly due to the formation of electrode/electrolyte interface layer, making the diffusion of ions across the separator more difficult. These improvements in electron conductivity are essential, as it

significantly affects the performance of the battery material. Improved electron conductivity allows the production of higher currents without losing capacity or cycle life. This is because the material is able to easily transport electrons to and from the vanadium centers allowing the charges to separate and recombine much more quickly and efficiently within the cathode.[45,46]

6.4 Conclusion

A non-stoichiometric vanadium hydride gel was prepared by thermal treatment of a solution of tetraphenyl vanadium (IV) at 100 °C followed by hydrogenation of the material in order to exploit the lightweight hydride ligand for improved energy storage. Characterisation of the material shows that it is amorphous and likely consists of vanadium hydride species in multiple oxidation states. The material is significantly less expensive to synthesise than TiH_3,[300] CrH_3 [299] and VH_3 materials previously reported by our group, though the material has a significantly low surface area of 2.2 m^2/g. The multivalent vanadium hydride gel possesses some redox activity and produces a capacitive like response to changes in sweep rate. With respect to capacity, although it possesses a reasonable peak capacity of 131 mAh/g at a discharge rate of 1 $mA.cm^{-2}$, the capacity decreases with repeated cycling until it reaches 47 mAh/g after 50 cycles. Therefore it does not present enough recyclability to be utilised as a useful secondary lithium battery material. Possibly if a more crystalline phase pure structure could be achieved, this could be a more effective battery cathode material with improved recyclability performance.

Chapter 7 : Discussion, Conclusions, and Recommendations

7.1 Research Conclusions

This thesis has investigated the synthesis of a series of composites to improve the electron conductivity of high surface area transition metal oxides, for applications as potential Li^+ battery electrode materials.

In Chapter Two an initial investigation was conducted on the as synthesised m-TiO_2 materials treated with TMS chloride. These were successfully impregnated with air-stable conducting polythiophene nanowires confirmed by both IR spectroscopy and solid state NMR. The characterisation demonstrated the retention of mesoporosity despite a large decrease in surface area with a significant degree of pore filling indicating that the material was not simply coated with polymer. The electrochemical properties of these composite materials were found to significantly improve the conductivity of the material (3.56×10^{-2} to 5.79 $mS.cm^{-1}$). Despite this the Li^+ storage capability of the material decreased significantly (301 to 75 mAh/g at 0.2 $mA.cm^{-2}$), this was attributed to limited Li^+ diffusion preventing access to the internal redox sites due to the pores being filled with polymer. This was the first time this approach had been used to create a conducting polythiophene transition metal oxide composite. Typical methods use a diluted solution of thiophene mixed with a solid host and the later addition of an oxidant to produce a composite of transition metal oxide coated with conducting polymer. This procedure led to polymer penetration through the interior of the pore structure of the material whilst maintaining the mesostructure and relatively high surface area.

Due to the poor Li^+ storage capabilities of the polythiophene composites, Chapter Three explored a variety of synthesis parameters to determine preferential conditions for a high performance polypyrrole composite material. Results showed that polymer content in excess of 5% is counterproductive because of the increase in density of the material without a significant improvement in conductivity, in addition to a larger decrease in surface area. The conductivity peaked at two orders of magnitude higher than the starting material (3.84×10^{-2} to 2.17 $mS.cm^{-1}$) but still increased most significantly at only 5% polymer content (1.04 $mS.cm^{-1}$). The 5% composite produced the best Li^+ storage capabilities with improved initial capacity

(139 to 170 mAh/g) and capacity retention (28.1 to 50.6%). Polymer content beyond 5% lead to a decrease in performance due to the increased density of the samples. The influence of pore size demonstrated that larger pores produced better capacity retention. The high initial capacity was attributed to the surface area of the material with higher initial capacities for materials possessing a higher surface area. This demonstrates that to obtain optimum performance the highest possible surface areas coupled with the largest improvements in conductivity are necessary.

As the long term cycling performance of these materials was still not sufficient to propose use as a Li^+ battery electrode material, in Chapter Four work using pyrrole composite was extended in an attempt to further improve capacity retention and initial capacity of the material. The use of a new strategy adopting a UV initiated polymerisation procedure to encourage a direct reaction between the two phases to produce a better interface. Results showed this procedure successfully impregnated polymer within the pores with an increase in surface area retention compared to chemical doping methods (48.8 to 86.5%). Electrochemical studies showed that low polymer content produced the best results when loaded for periods of 1 hour at standard conditions. Loading for less time is insufficient to improve conductivity and excess loading times lead to increase in density and loss of capacity and surface area. Peak capacities outperformed those made using chemical procedures (190 mAh/g) but still failed to produce high enough capacity retention to be a useful long-term battery electrode (21.9 to 46.3%). This was the first synthesis using a combination of this method of loading the monomer material into the host coupled with the less common method of photocatalysed polymerisation of polypyrrole. It demonstrated the advantages offered by this procedure of allowing a greater retention of surface area with concomitant improvement in performance. Downstream, this method may provide a convenient and inexpensive alternative to pyrolysis and graphene-based methods of improving charge transport for other battery materials being investigated.

After repeated attempts to improve conductivity using composites the utilise conducting polymers as a conducing additive, we attempted in Chapter Five to synthesize a composite using a sulfur donor agent to reduce the band gap of the oxide semiconductor. We were successfully able to synthesise transition meal oxysulfides using HMDST. This was carried out using various quantities of reagent and temperatures that would not damage the host structure. The presence of organic residues bonded to the surface after completion of the synthesis

hindered the optimum performance. The conductivity of the materials improved with the use of larger quantities of HMDST. This was further improved by increasing reaction temperatures up to 150 °C before deteriorating at 200 °C. Despite improved conductivity the surface area decreases significantly with increased amounts of reagent (527-66 m^2/g) and with higher temperatures (660-41 m^2/g) due largely to the increase in weight caused by more Ti-S-$(CH_3)_3$ groups bonded to the surface. This resulted in the loss of initial capacity (137-48 mAh/g). The materials improved cycling stability over 50 cycles with the best Li^+ storage performance made using large amounts of reagent at a lower temperature (111 to 77 mAh/g after 50 cycles). This strategy demonstrated vastly improved cycle life performance but requires further improvements in the synthesis to produce better overall performance. Ideally synthesis improvements would lead to an increased in the surface Ti-S-Ti sites with minimal organic residue blocking the pores and adding weight to the sample. These results demonstrated that this method of sulfur doping at lower temperatures achieved improving the conductivity of the host material without needing to reach the high temperatures typically involved in sulfur doping that would otherwise have damaged the structure.

As part of a side project during this PhD, in Chapter Six a non-stoichiometric vanadium hydride gel was prepared by thermal treatment of a solution of tetraphenyl vanadium (IV) at 100 °C followed by hydrogenation of the material to exploit the light weight of the hydrogen ligand for improved energy storage to that of its respective oxides. Characterisation demonstrated that the material was an amorphous vanadium hydride consisting of various vanadium oxidation states and possessing a surface area of only 2.2 m^2/g. This multivalent material demonstrated capacitive like responses to sweep rates and produced capacities of 131 mAh/g which decreased to 47 mAh/g after cycling so as yet it is not sufficient enough for use as a Li^+ battery cathode. Possibly if a more crystalline material could be obtained with a set structure the capacity performance and recyclability of the material could improve.

7.2 Further Work

In this work the electron conductivity of mesoporous Ti and Ta oxides has been improved by the use of conducting polymers and by sulfur doping, in an attempt to improve its performance as a Li^+ battery electrode material. These composites facilitated electron transport between the redox sites situated on the surface of the material allowing for more efficient electron transport

throughout the bulk material. These improvements in electron conductivity produced improved Li^+ storage properties in a number of cases, but unfortunately the performance was not fully optimised due to increases in weight of the material or pore blockage limiting the improvements in performance. The improved reaction kinetics of these materials might improve the capabilities in other redox based applications, such investigations were not undertaken due to time constraints for the publication of this thesis.

The results produced during the investigation of sulfur doping mesoporous oxides using HMDST were promising, however the capacity of the material was reduced due to the retention of excess amounts of residual organic upon completion of the synthesis. Further exploration of synthesis parameters and conditions may enable fine tuning of the synthesis in order to maximise the incorporation of surface sulfur sites with minimal retention of organic content after the completion of synthesis, thus maximising the benefits gained from improved conductivity with the minimal loss in performances due to increase in weight of the material and blocking of pores with residual organic. Another reason further exploration should be required is due to the strange results produced by the XPS analysis as it was not possible to fully assess the nature of the final compounds to a high degree of certainty. It would also be useful to fully assess the mechanism of the reactions taking place and using a closer examination of different synthesis conditions to observe the effect on the properties of the material. This material shows the most promise with regards to future work, due to its superior capacity retention properties. If the initial capacity of these materials can be it would produce significant improvements in its performance at a Li^+ battery electrode.

Further progression might also be made with continued development of the UV synthesis procedure, the positive results demonstrated by improved conductivity and surface area could be improved by the use of synthesis under vacuum conditions to minimise the influence of oxygen on the photochemistry taking place. This may improve the quantum yield of the synthesis in addition to allowing the monomer vapour to penetrate more deeply into the pores of the host, this could further improve electron transport deeper into the pores of the material. Deeper pore penetration into the pores could allow increased access to Ti surface sites deep within the pores of the material and could lead to further increasing both capacity retention and capacity of the material and therefore further improve the materials performance as a Li^+ battery electrode material.

Due do the shift in the focus of the thesis, the different material synthesised were subjected to different forms of analyses. The initial focus of the thesis being based around improvements in electron conductivity of mesoporous oxides with potential applications as a Li^+ battery electrode. The materials impedance was assessed using pellets, and the use of higher frequencies up to 1 MHz. Later the focus of the thesis changed solely to the utilisations of high surface area mesoporous oxides for the use in Li^+ battery electrode materials, therefore the impedance assessment was done in the form of a Li^+ battery cell and different to those of the initial materials tested. In future work it would be useful to directly compare the different materials made throughout the thesis using the same host material and use these to directly compare the performance of the different synthesis procedures using the more commonly used technique of potentiostatic impedance spectroscopy between 0.1 Hz-100 kHz using a Li^+ battery cell. By carrying out this assessment it would determine the effect of the different synthesis procedures on the performance of the material and to determine which of all the composite materials produces the best improvement of m-TiO_2 as a Li^+ battery electrode material.

Finally the improved materials should be investigated in other applications to determine if the improved electron transfer kinetics might improve the performance for applications such as photocatalysis and other areas of catalysis. It may also be beneficial to investigate the use of these high surface area materials for the application in dye-sensitised solar cells. This unfortunately was not able to be carried out in these studies due to the time restrictions. Even in their present state these materials have shown significant improvement in performance than was achieved by the starting material. In addition to this, different approaches were adapted and developed to improve the conductivity, allowing for retention of the surface area and porosity, which would otherwise have been lost using traditional methods. In this regard this thesis has achieved its aim in synthesising and characterising air stable polymer doped and electron conducting mesoporous oxysulfides, given their improvements in electron conductivity and Li^+ storage capabilities. These methods could be utilised by other materials in future research to hopefully improve their performance and thus lead to alternative approaches of processing energy storage materials in the place of simple solution based methods used previously.

Chapter 8 : Appendices

Appendix 1 Supplemental for Chapter 2 Synthesis and electrochemical properties of mesoporous titanium oxide with polythiophene nanowires in the pores

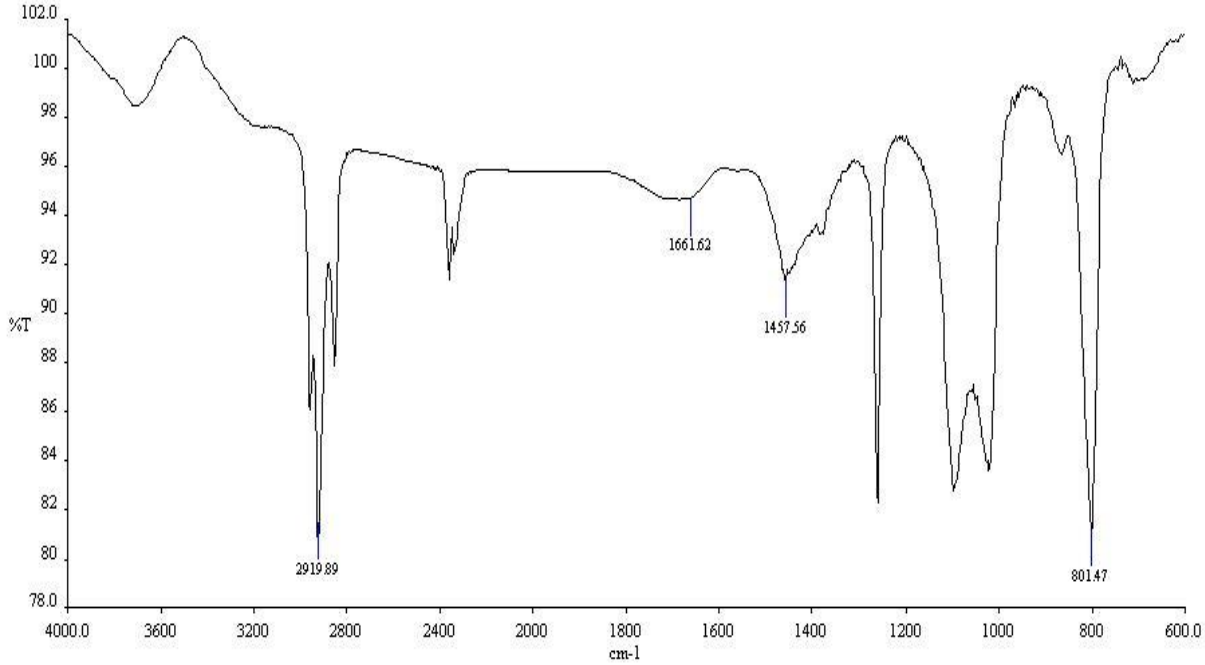

Figure 8.1: IR spectrum of thiophene in KBr

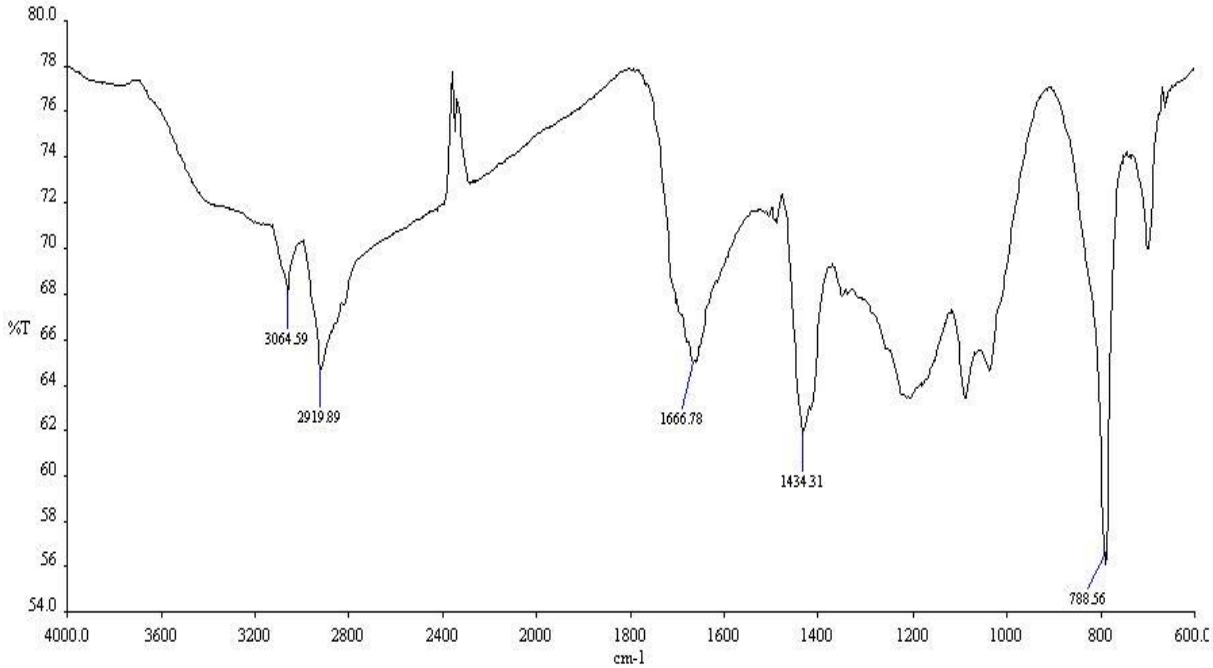

Figure 8.2: IR spectrum of polythiophene in KBr

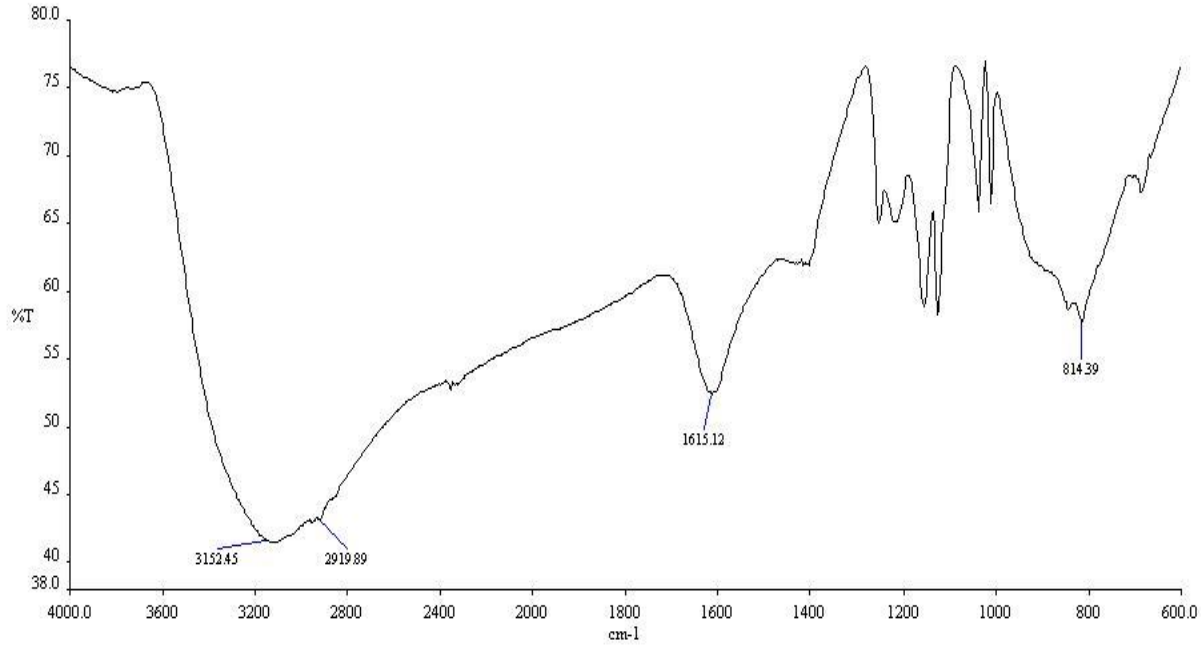

Figure 8.3: IR spectrum of m-TiO_2 TMS

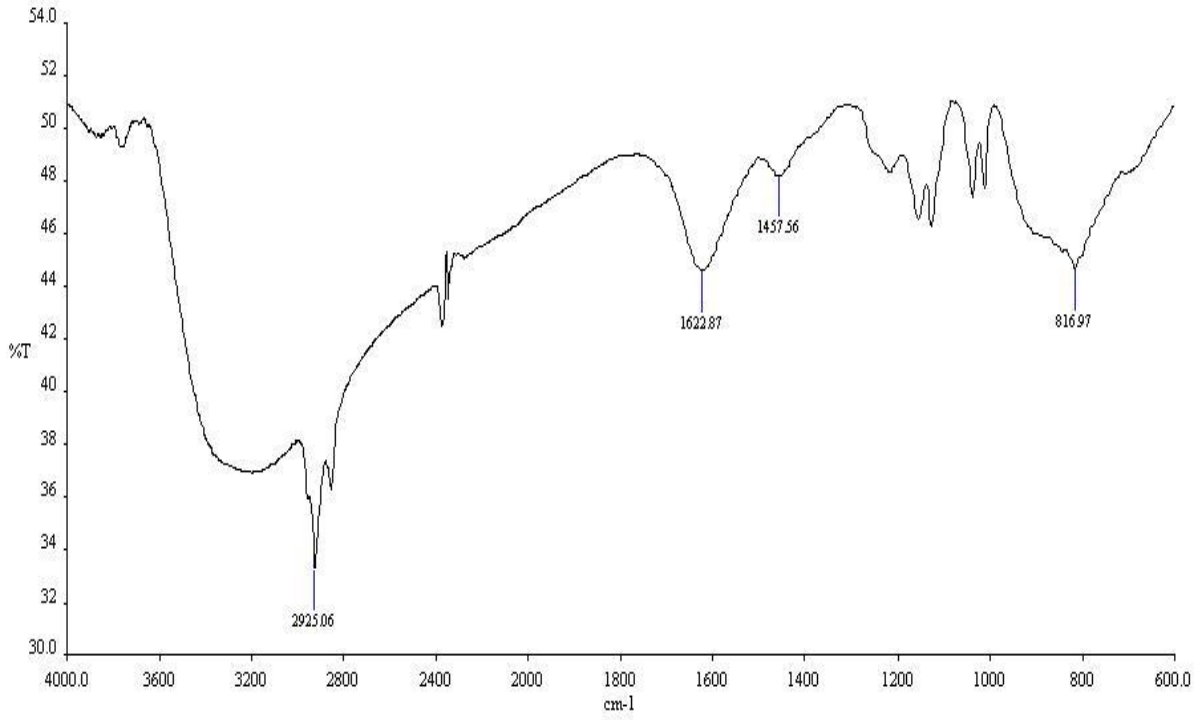

Figure 8.4: IR spectrum of m-Ti TMS loaded with thiophene vapour

Appendix 2 Supplemental for Chapter 3 Effect of Synthesis Parameters on the Electrochemical Properties of High-Surface-Area Mesoporous Titanium Oxide with Polypyrrole Nanowires in the Pores

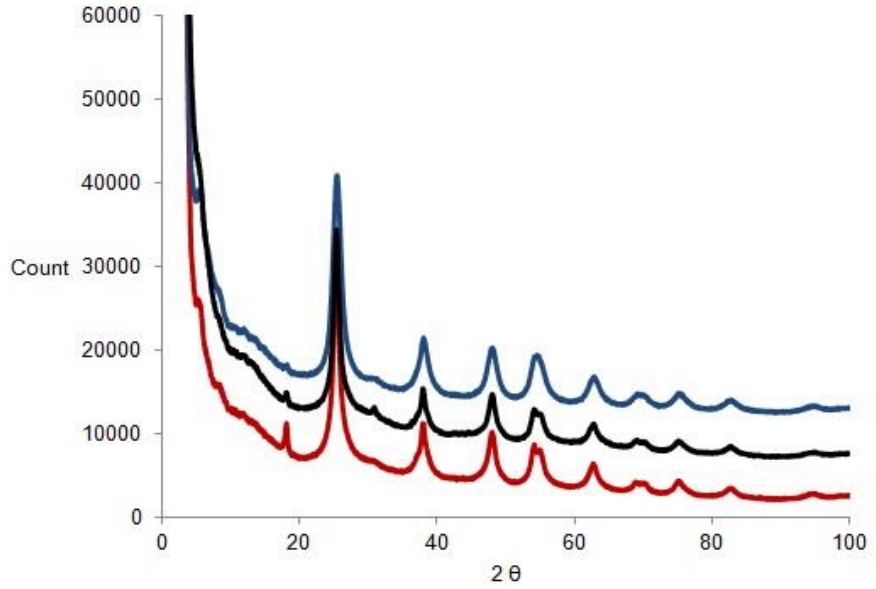

Figure 8.5: Powder X-ray diffraction pattern for samples C6PC (red), PC (5) (black) and C18PC (blue)

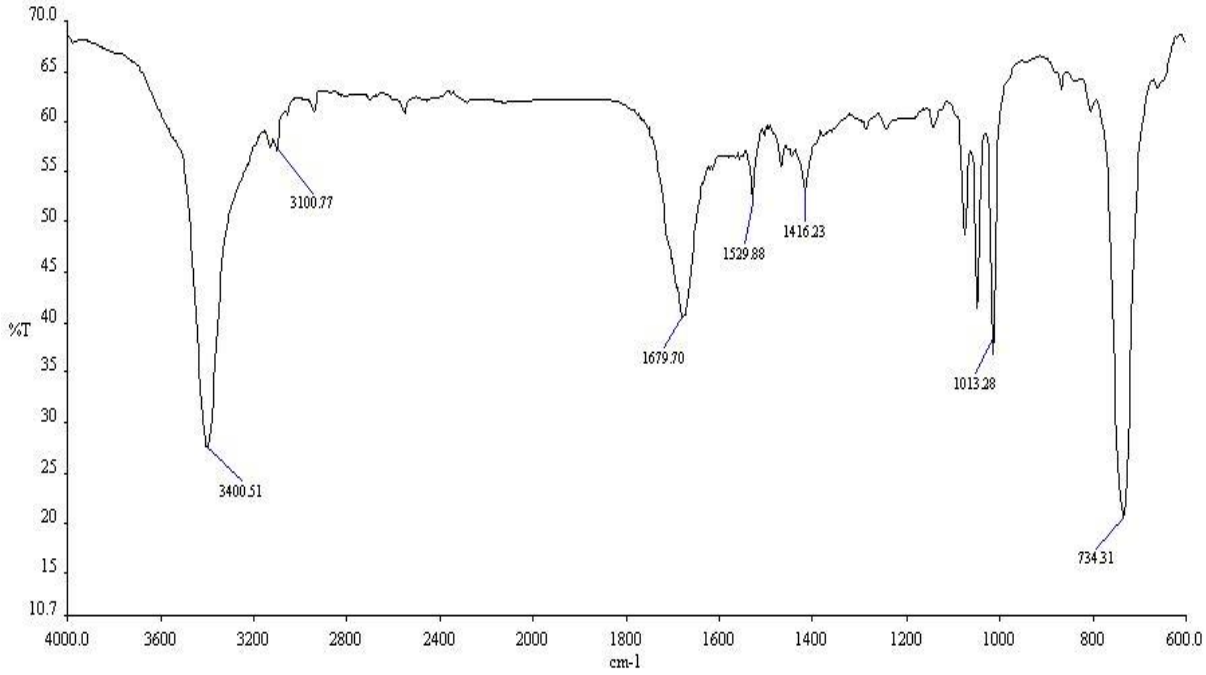

Figure 8.6: IR spectrum of pyrrole monomer in KBr

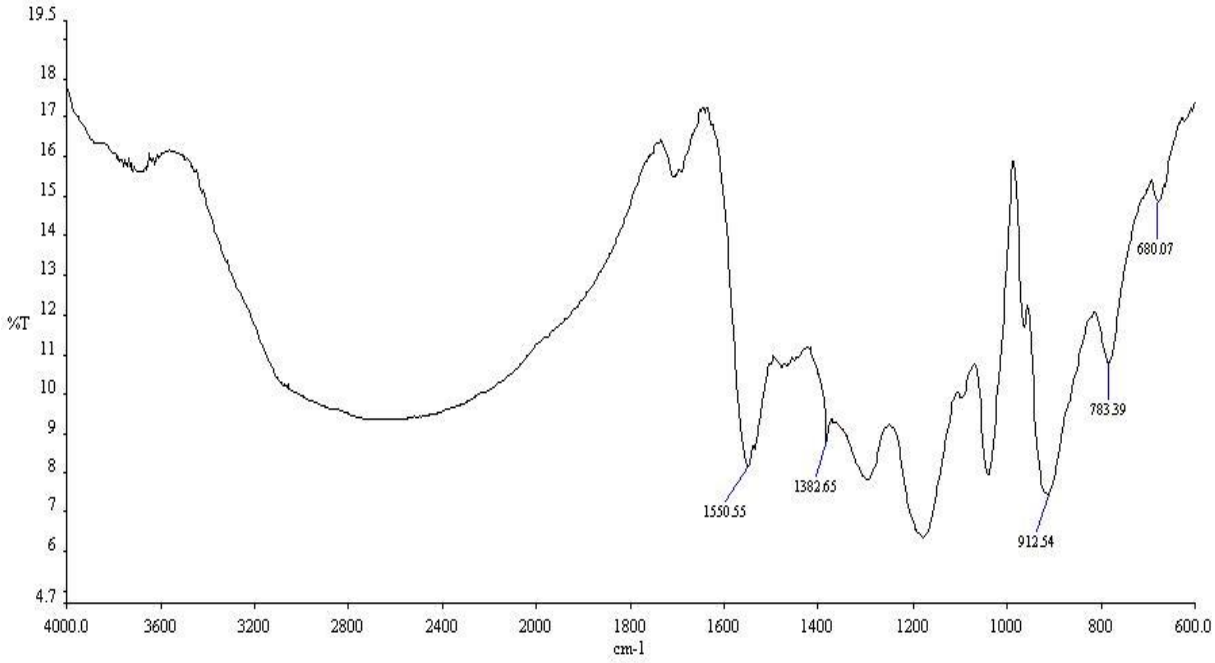

Figure 8.7: IR spectrum of polypyrrole in KBr

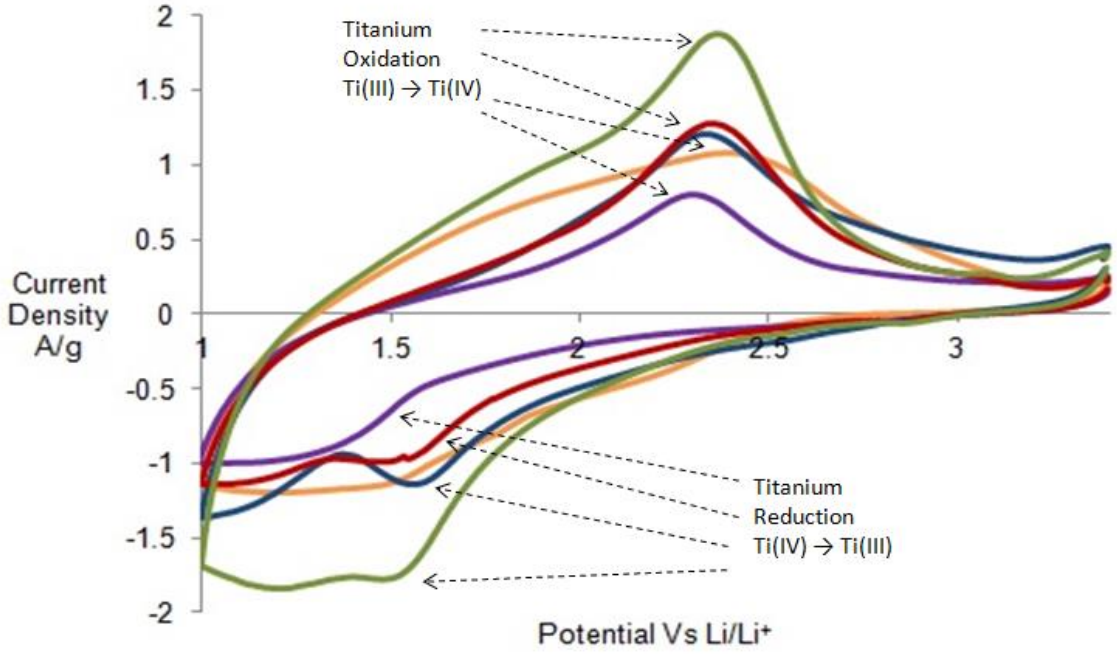

Figure 8.8: Cyclic voltammetry over a potential range of 1-3.4 V vs Li/Li^+ standard electrode potential at a sweep rates of 5 mVs^{-1} of samples C12 m-TiO_2 (orange), PC(5) (green), PC(10) (blue), PC(15) (red) and PC(30) (purple)

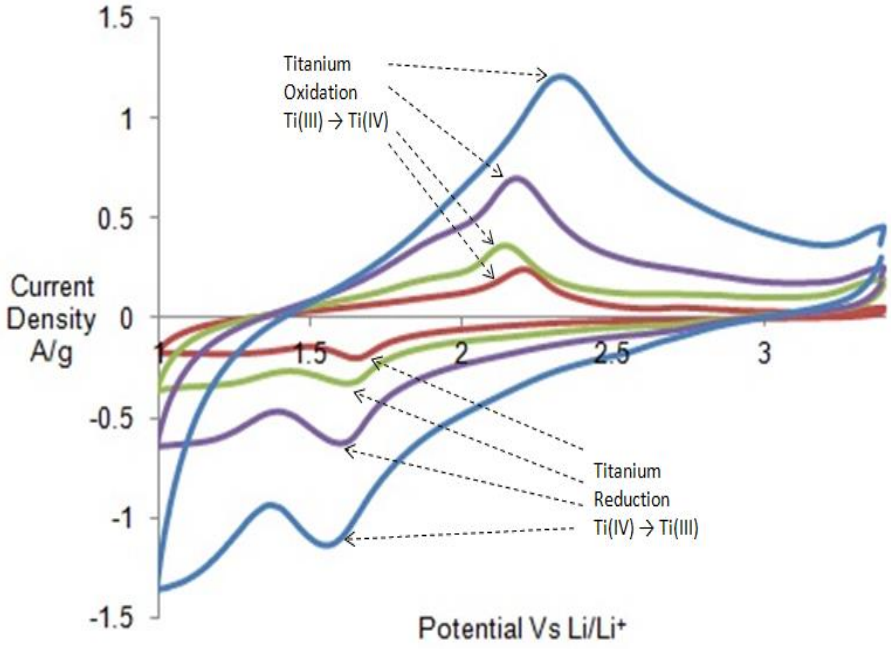

Figure 8.9: Cyclic voltammetry over a potential range of 1-3.4 V vs Li/Li^+ standard electrode potential at various sweep rates of PC(10) (blue) 5 mVs^{-1} (purple) 2 mVs^{-1}, (green) 1 mVs^{-1}, (red) 0.5 mVs^{-1}

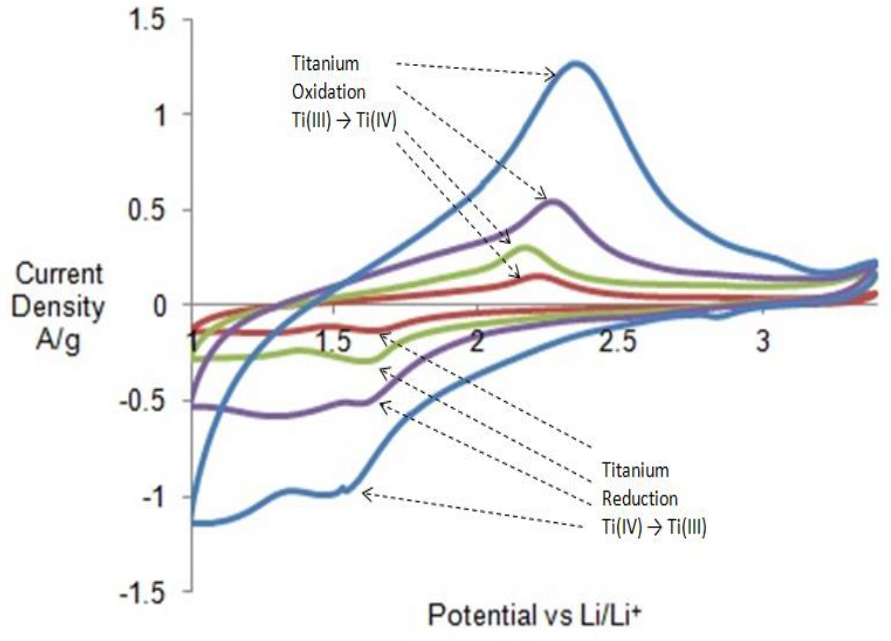

Figure 8.10: Cyclic voltammetry over a potential range of 1-3.4 V vs Li/Li^+ standard electrode potential at various sweep rates of PC(15) (blue) 5 mVs^{-1} (purple) 2 mVs^{-1}, (green) 1 mVs^{-1}, (red) 0.5 mVs^{-1}

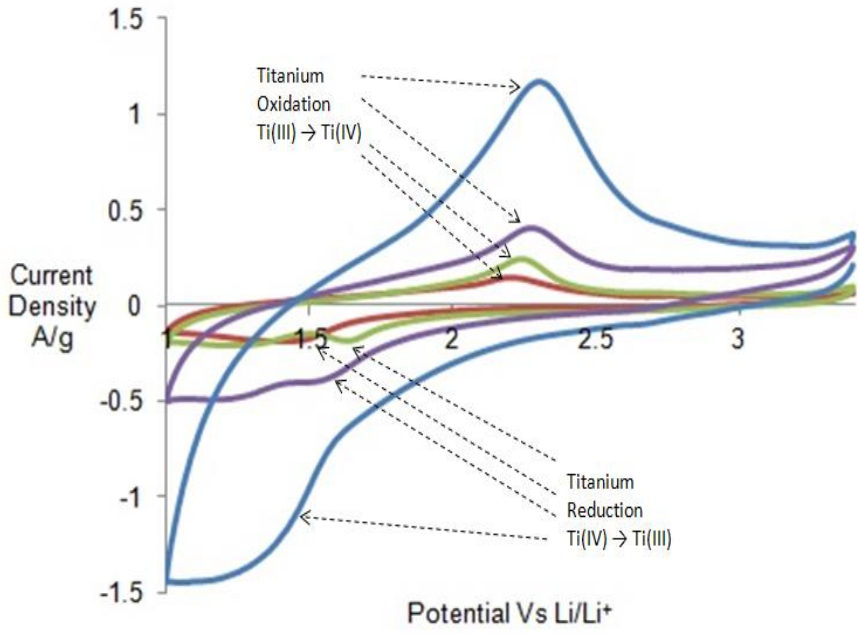

Figure 8.11: Cyclic voltammetry over a potential range of 1-3.4 V vs Li/Li^+ standard electrode potential at various sweep rates of PC(30) (blue) 5 mVs^{-1} (purple) 2 mVs^{-1}, (green) 1 mVs^{-1}, (red) 0.5 mVs^{-1}

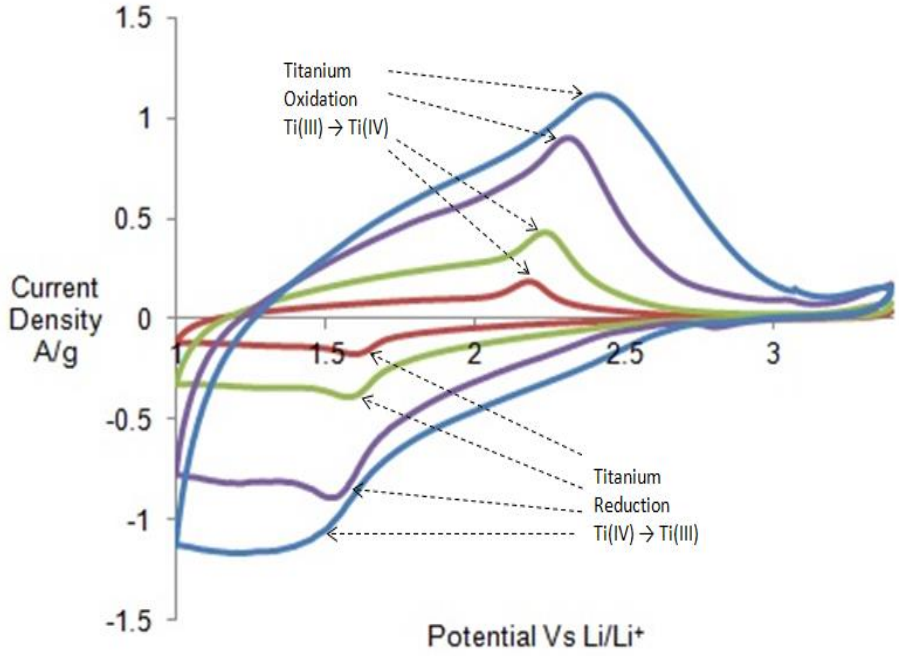

Figure 8.12: Cyclic voltammetry over a potential range of 1-3.4 V vs Li/Li^+ standard electrode potential at various sweep rates of C6 m-TiO_2 (blue) 5 mVs^{-1} (purple) 2 mVs^{-1}, (green) 1 mVs^{-1}, (red) 0.5 mVs^{-1}

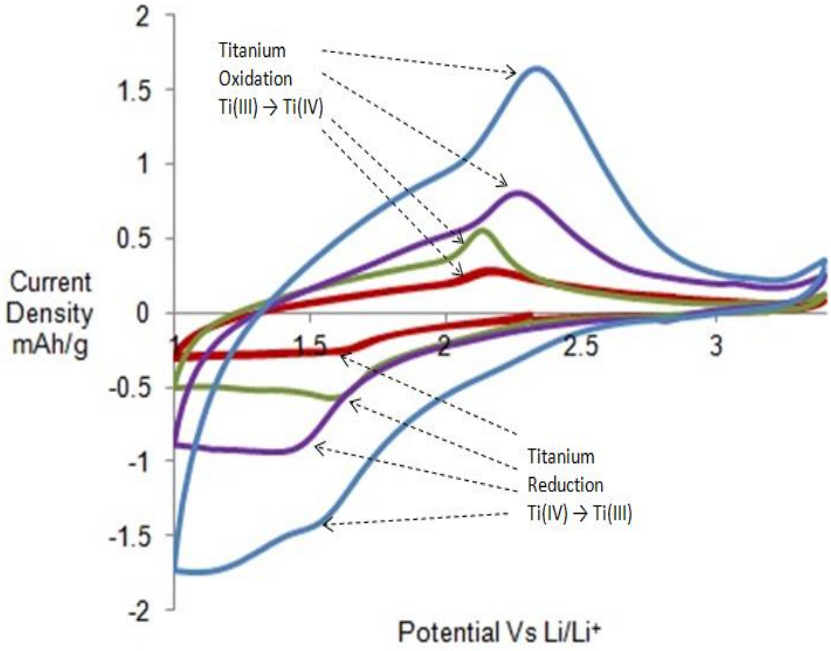

Figure 8.13: Cyclic voltammetry over a potential range of 1-3.4 V vs Li/Li^+ standard electrode potential at various sweep rates of C6PC (blue) 5 mVs^{-1} (purple) 2mVs^{-1}, (green) 1 mVs^{-1}, (red) 0.5 mVs^{-1}

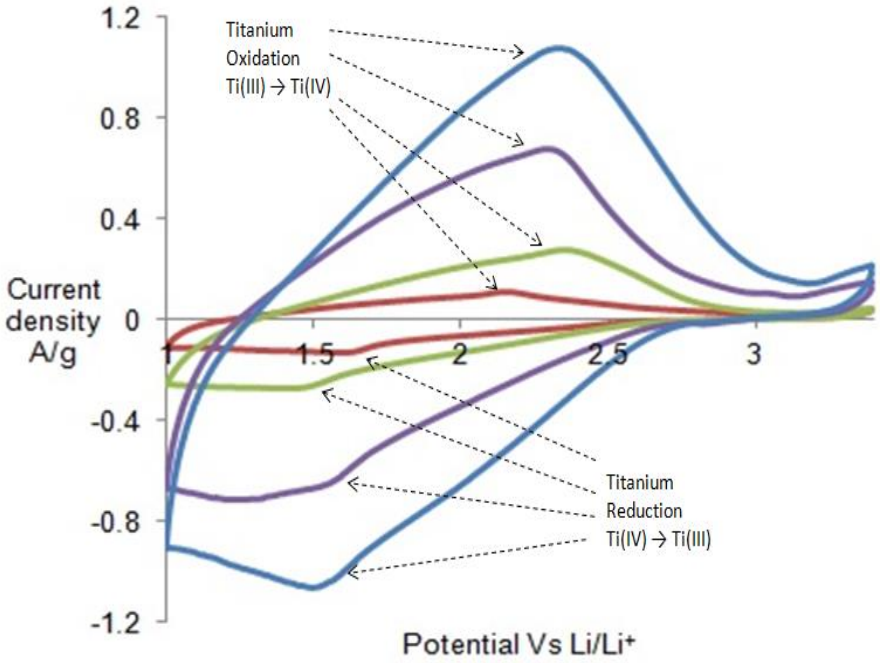

Figure 8.14: Cyclic voltammetry over a potential range of 1-3.4 V vs Li/Li^+ standard electrode potential at various sweep rates of C18 m-TiO_2 (blue) 5 mVs^{-1} (purple) 2 mVs^{-1}, (green) 1 mVs^{-1}, (red) 0.5 mVs^{-1}

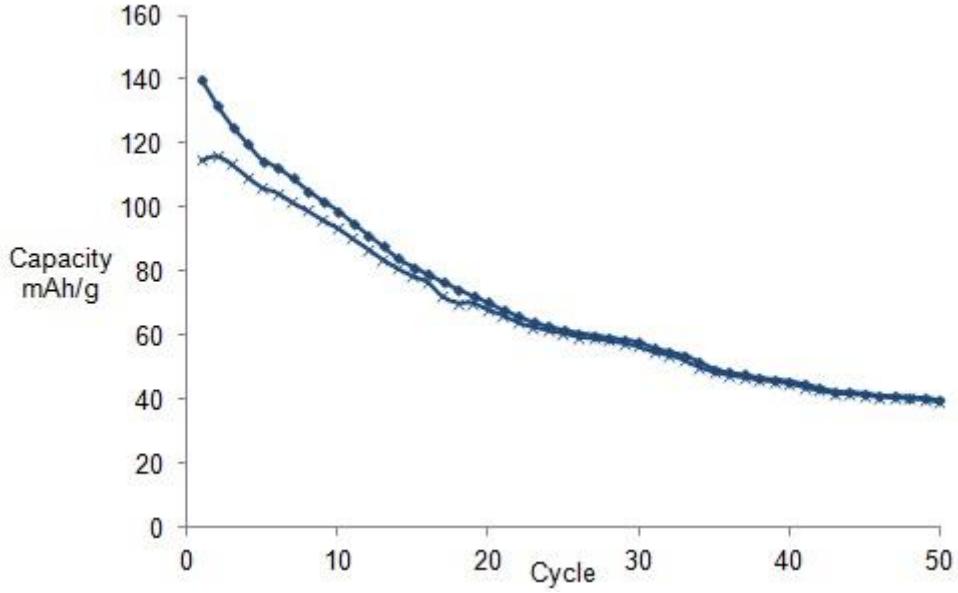

Figure 8.15: 50 Cycles charge (crosses) discharge (squares) capacity data for C12 m-TiO_2 at 1 mA.cm^{-2}

Appendix 3 Supplemental for Chapter 4 UV-Initiated Synthesis of Electroactive High Surface Area Ta and Ti Mesoporous Oxides Composites with Polypyrrole Nanowires within the Pores

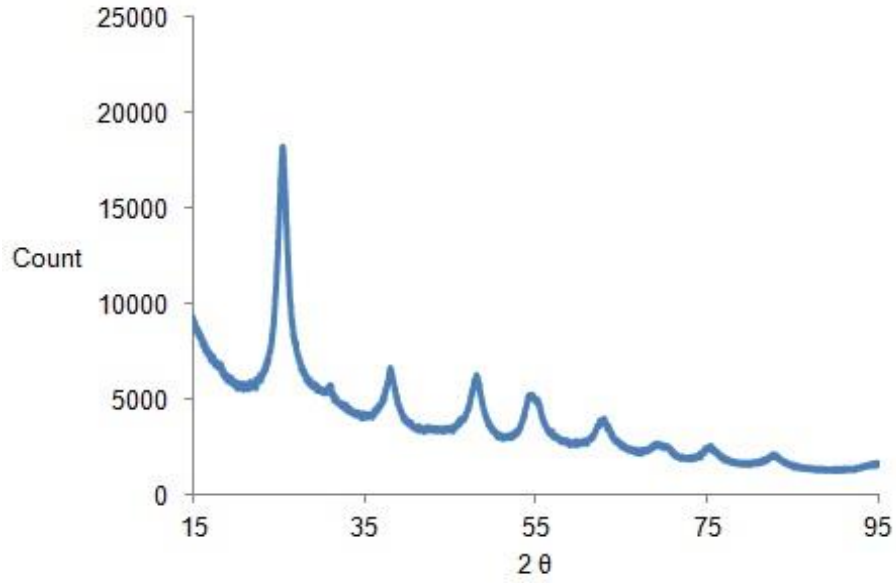

Figure 8.16: X-ray powder diffraction pattern at high angles for samples TiC 1

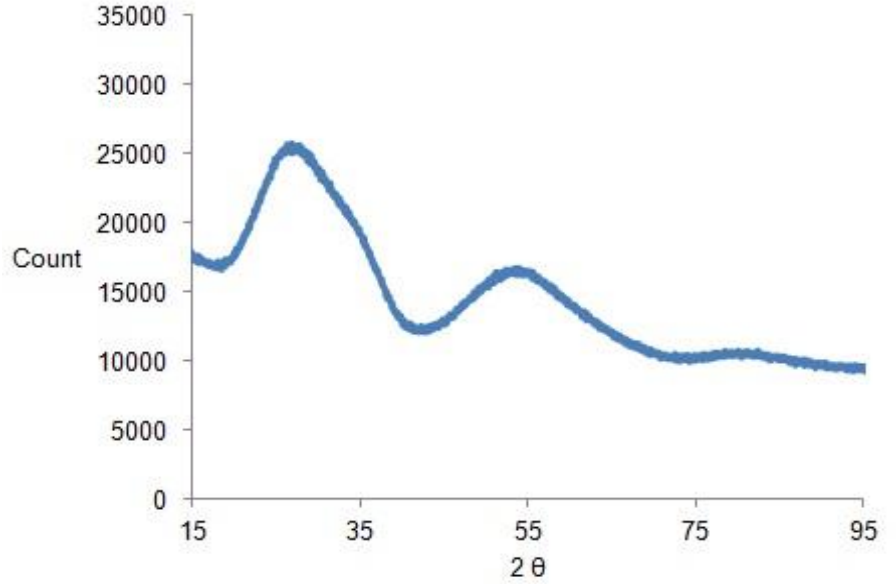

Figure 8.17: X-ray powder diffraction pattern at high angles for samples TaC

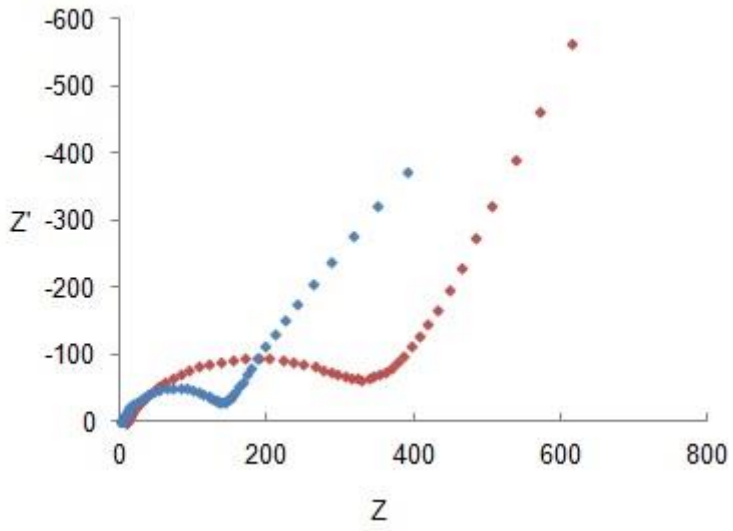

Figure 8.18: Nyquist plots over the frequency range from 100 KHz to 0.01 Hz using a two electrode setup, using biased potentials equivalent to the open circuit potential of the cell, m- Ta_2O_5 at 2.527 V vs Li/Li^+ (red) and TaC at 2.442 V vs Li/Li^+ (blue)

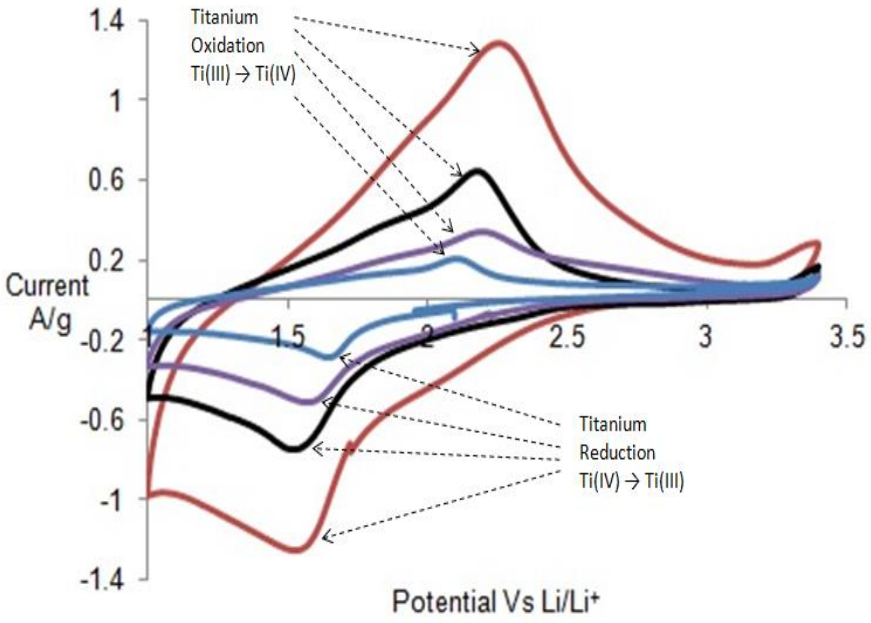

Figure 8.19: Cyclic voltammetry over a potential range of 1-3.4 V vs Li/Li^+ standard electrode potential at various sweep rates of TiC(0.5) at 0.5 mVs^{-1} (blue), 1mVs^{-1} (purple), 2 mVs^{-1} (black), 5 mVs^{-1} (red)

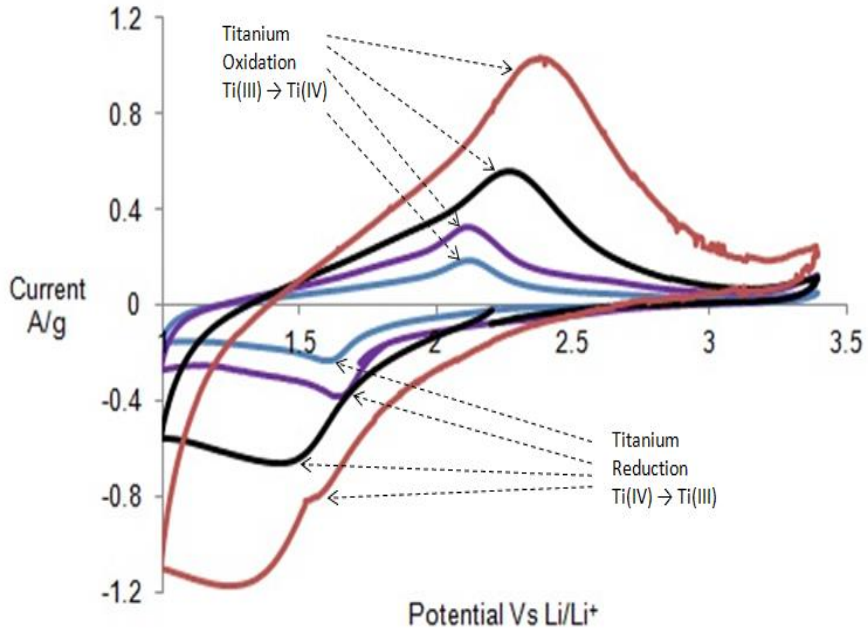

Figure 8.20: Cyclic voltammetry over a potential range of 1-3.4 V vs Li/Li^+ standard electrode potential at various sweep rates of TiC(2) at 0.5 mVs^{-1} (blue), 1mVs^{-1} (purple), 2 mVs^{-1} (black), 5 mVs^{-1} (red)

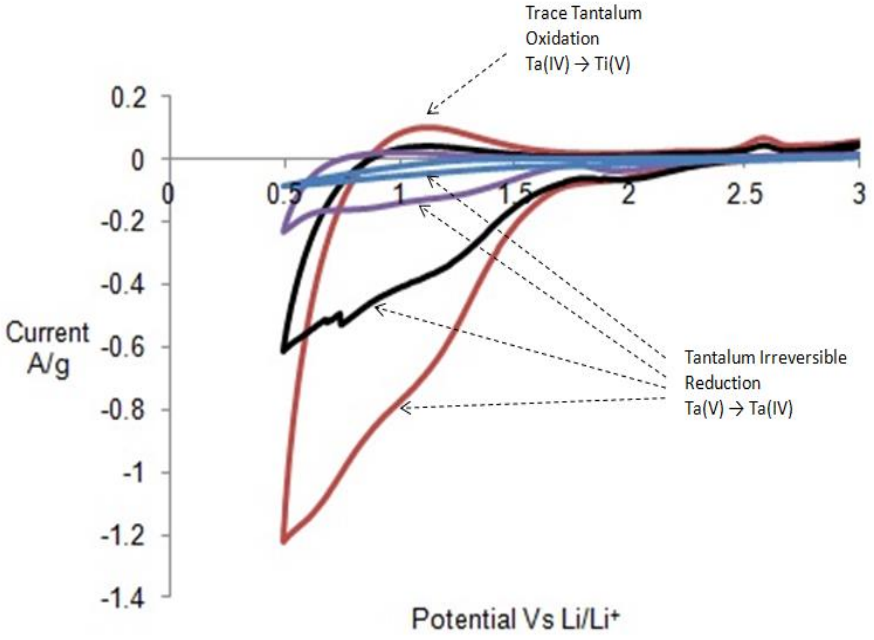

Figure 8.21: Cyclic voltammetry over a potential range of 1-3.4 V vs Li/Li^+ standard electrode potential at various sweep rates of Ta_2O_5 at 0.5 mVs^{-1} (blue), 1mVs^{-1} (purple), 2 mVs^{-1} (black), 5 mVs^{-1} (red)

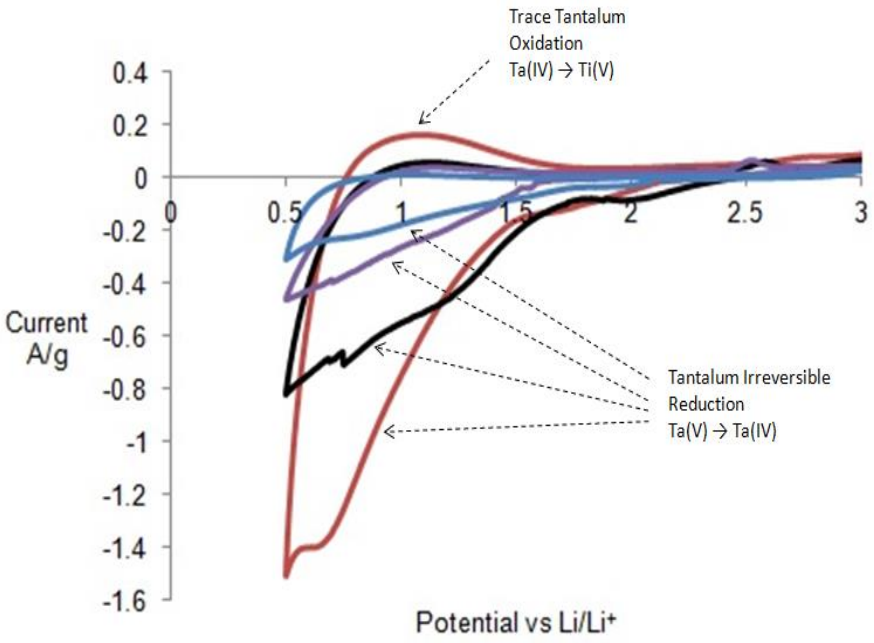

Figure 8.22: Cyclic voltammetry over a potential range of 1-3.4 V vs Li/Li^+ standard electrode potential at various sweep rates of TaC at 0.5 mVs^{-1} (blue), 1mVs^{-1} (purple), 2 mVs^{-1} (black), 5 mVs^{-1} (red)

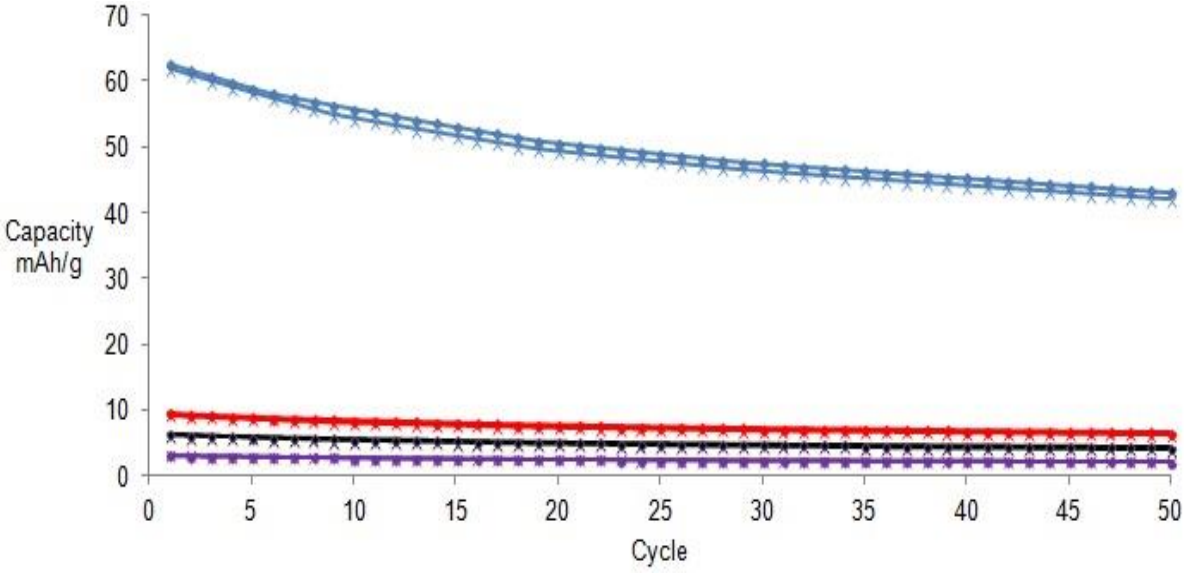

Figure 8.23: 50 Cycles charge (crosses) discharge (squares) capacity data for polypyrrole 100% (blue), 15% (red), 10% (black) and 5% (purple)

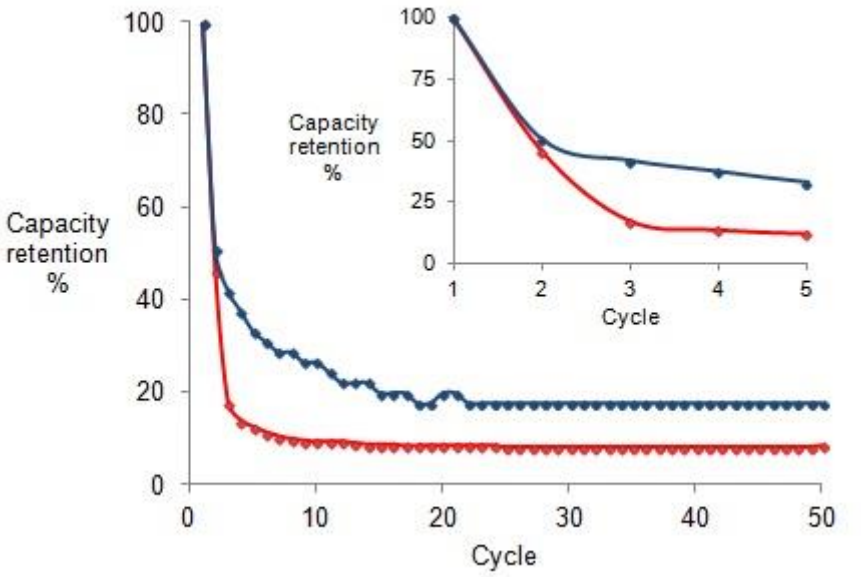

Figure 8.24: 50 Cycles (squares) capacity retention data for m-Ta_2O_5 (blue), TaC (red)

Appendix 4 Supplemental for Chapter 5 Low Temperature Synthesis and Electrochemical Properties of Mesoporous Titanium Oxysulfides

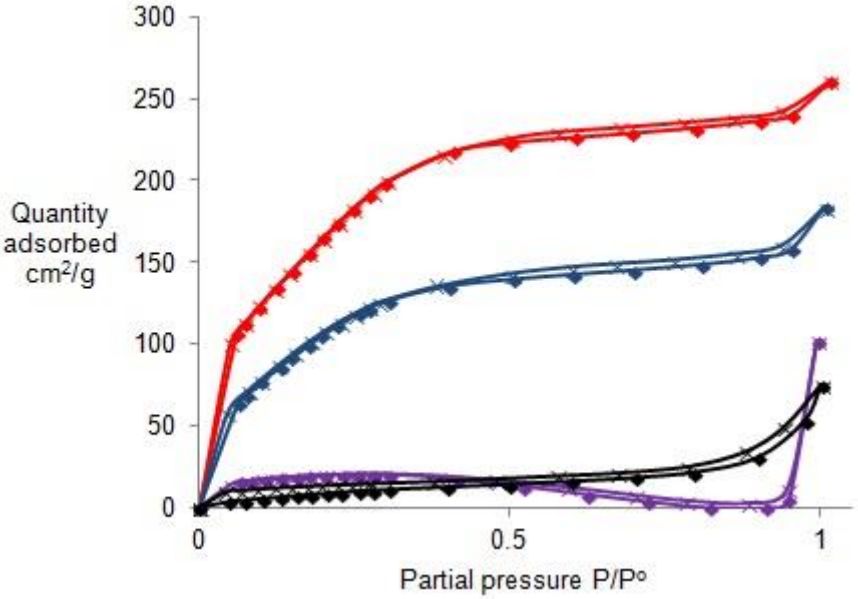

Figure 8.25: Nitrogen adsorption (crosses) and desorption (squares) for pristine m-TiO_2 (red), and composites synthesised at 100 °C (blue), 150 °C (purple) and 200 °C (black) with 3.5 mL of hexamethyldisilathiane (HMDST)

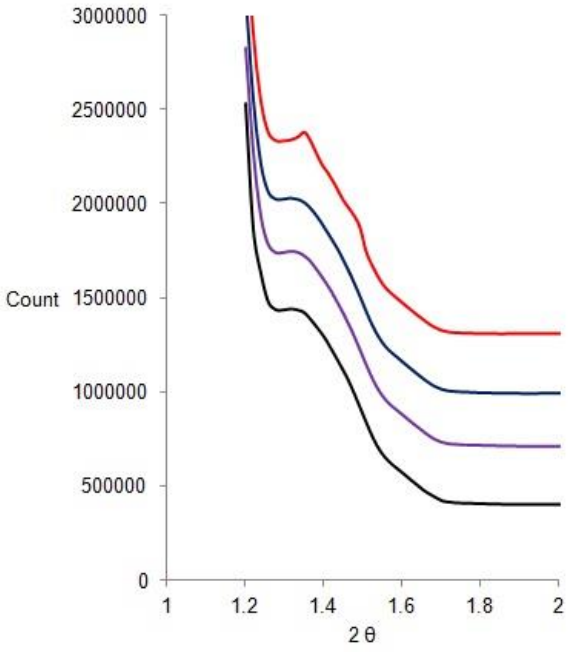

Figure 8.26: X-ray powder diffraction pattern at low angles for pristine m-TiO_2 (red) and composites synthesised at 100 °C (blue), 150 °C (purple) and 200 °C (black) with 3.5 mL of HMDST

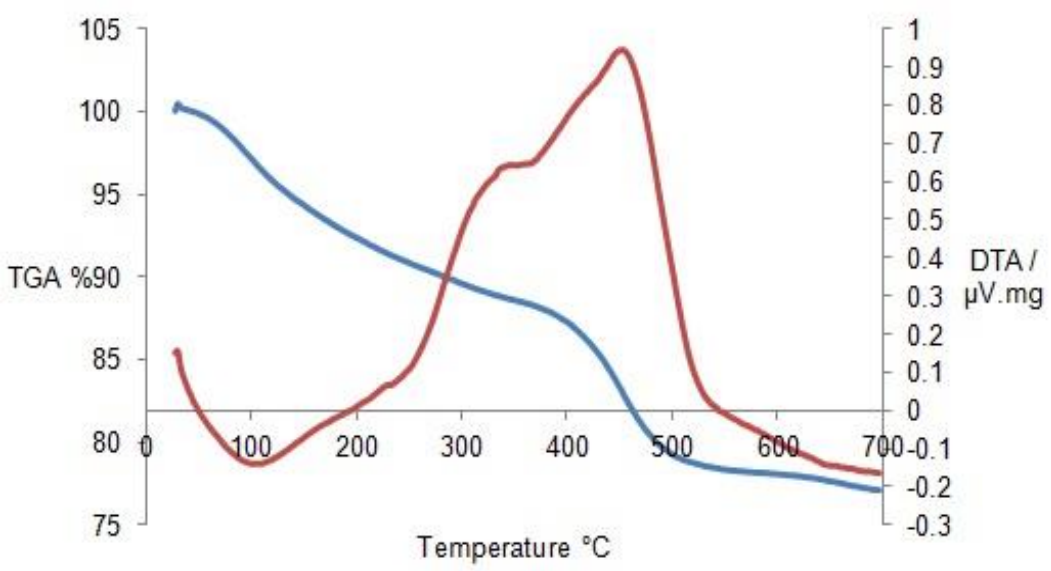

Figure 8.27: Thermogravimetric analysis (blue) and differential thermal analysis (red) plots for the composite made with 3.5 mL of HMDST at 100 °C

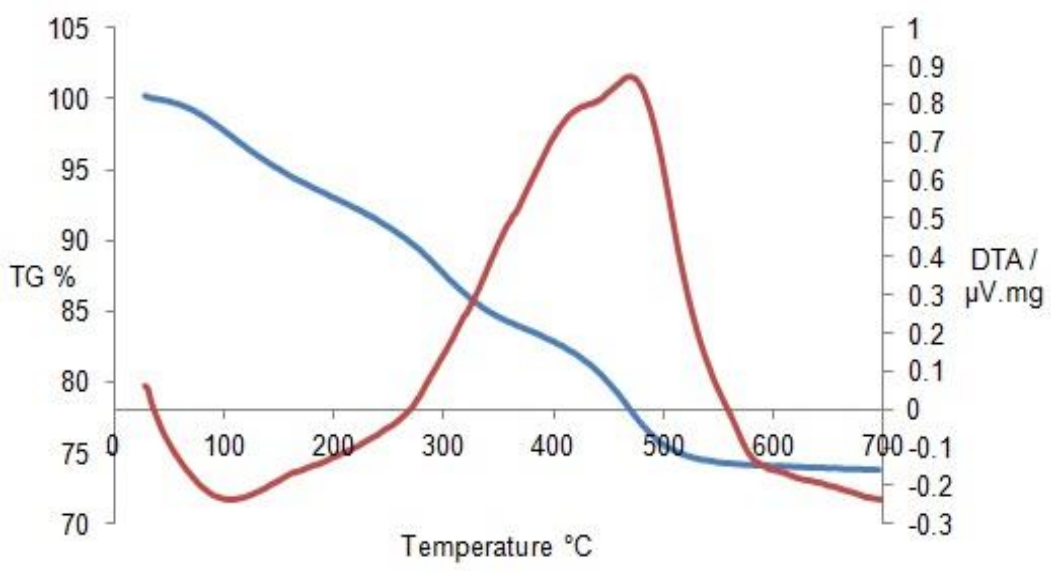

Figure 8.28: Thermogravimetric analysis (blue) and differential thermal analysis (red) plots for the composite made with 3.5 mL of HMDST at 200 °C

FTIR

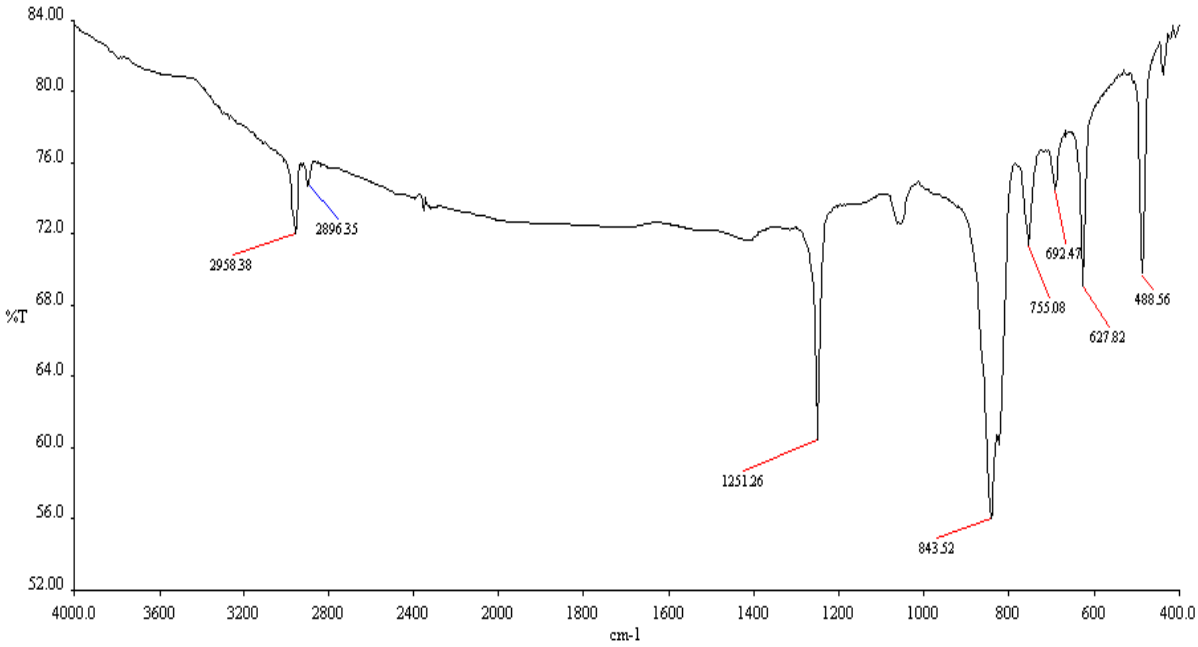

Figure 8.29: IR spectrum of hexamethyldisilathiane (HMDST)

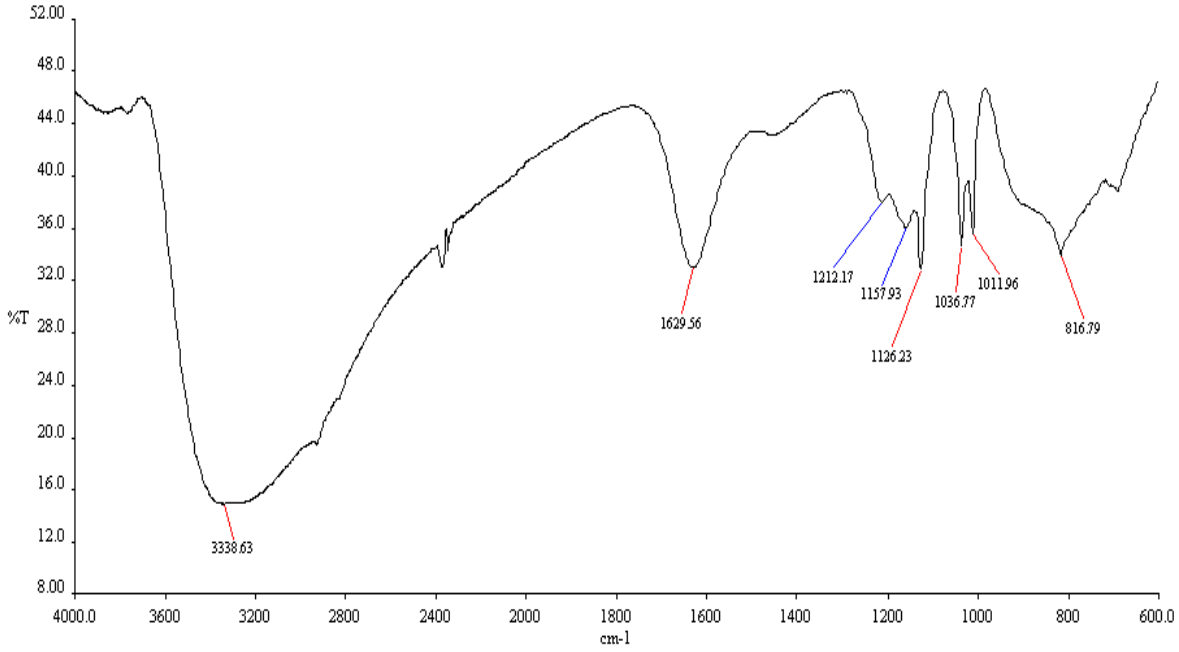

Figure 8.30: IR spectrum of m-TiO_2

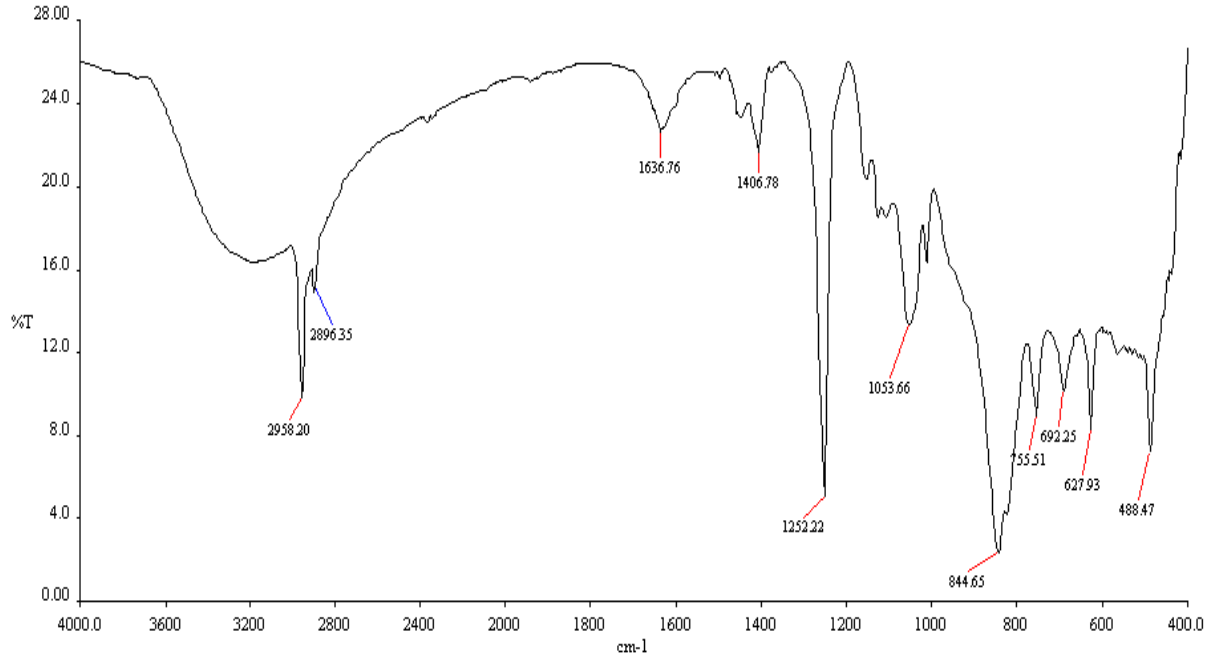

Figure 8.31: IR spectrum of HMDST loaded m-TiO_2

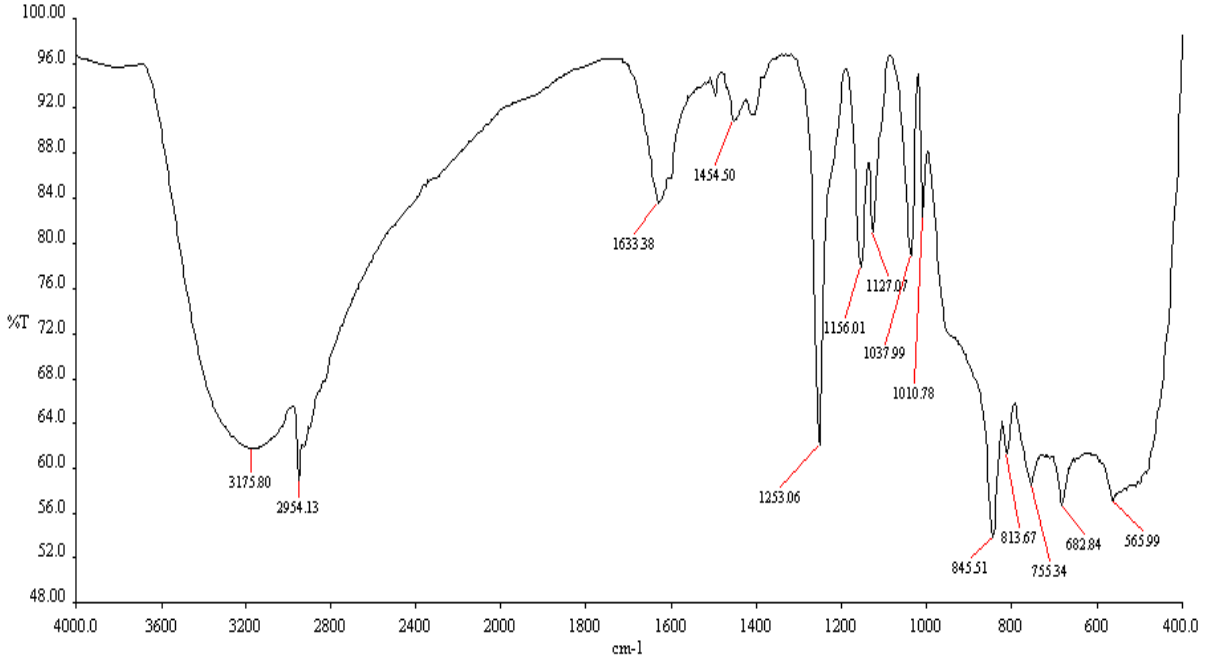

Figure 8.32: IR spectrum of composite made with 1.5 mL of HMDST at 150 °C

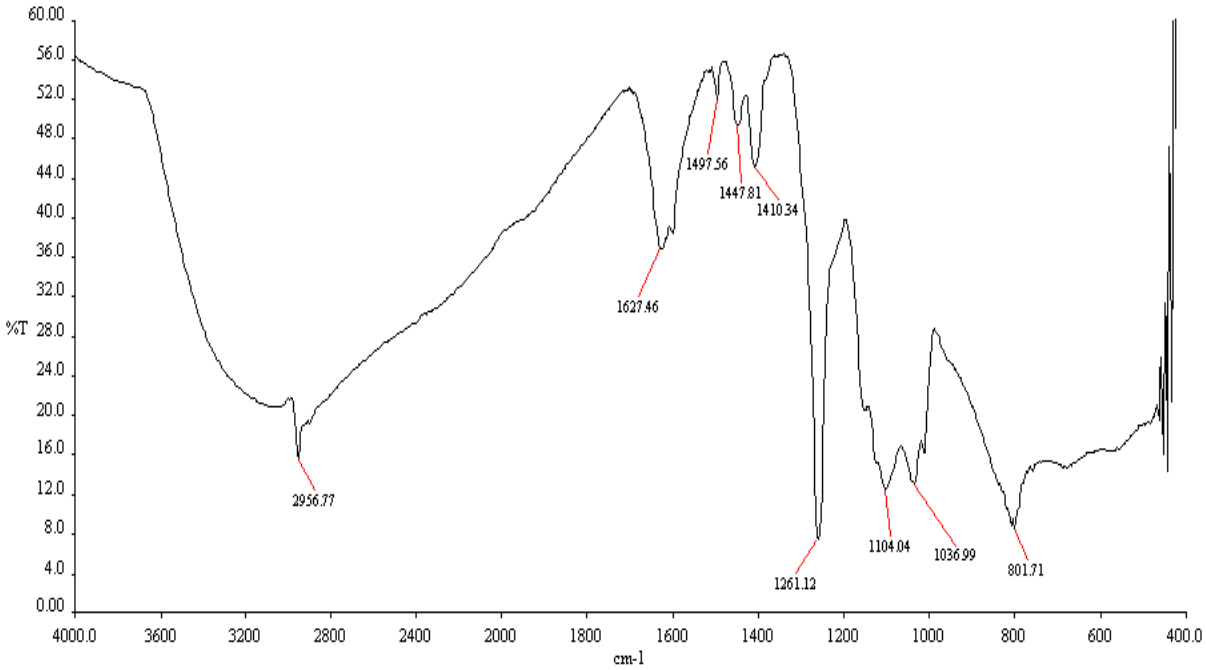

Figure 8.33: IR spectrum of sample made with 2.5 mL of HMDST at 150 °C

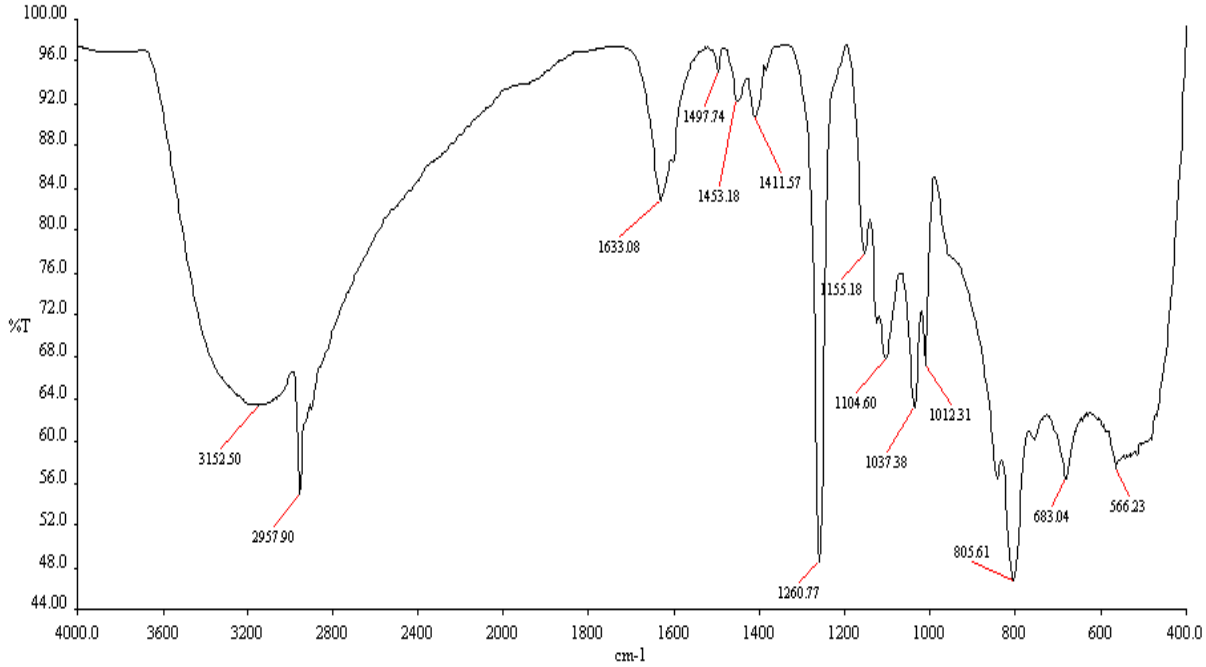

Figure 8.34: IR spectrum of composite made with 3.5 mL of HMDST at 150 °C

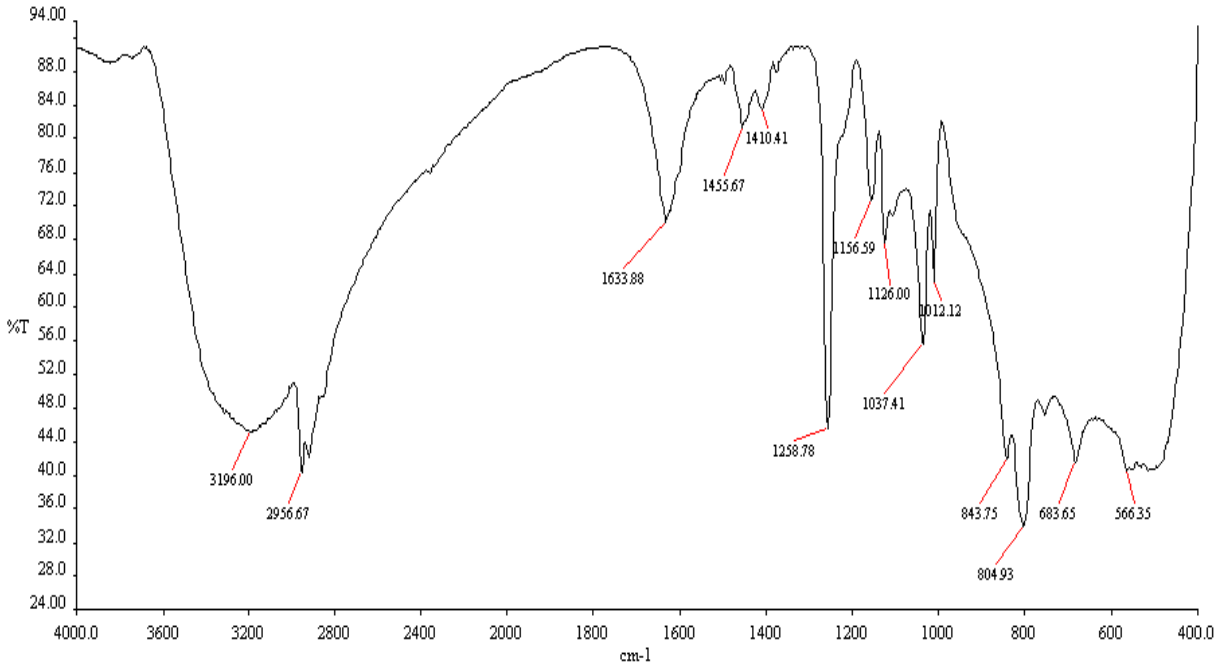

Figure 8.35: IR spectrum of composite made with 3.5 mL of HMDST at 100 °C

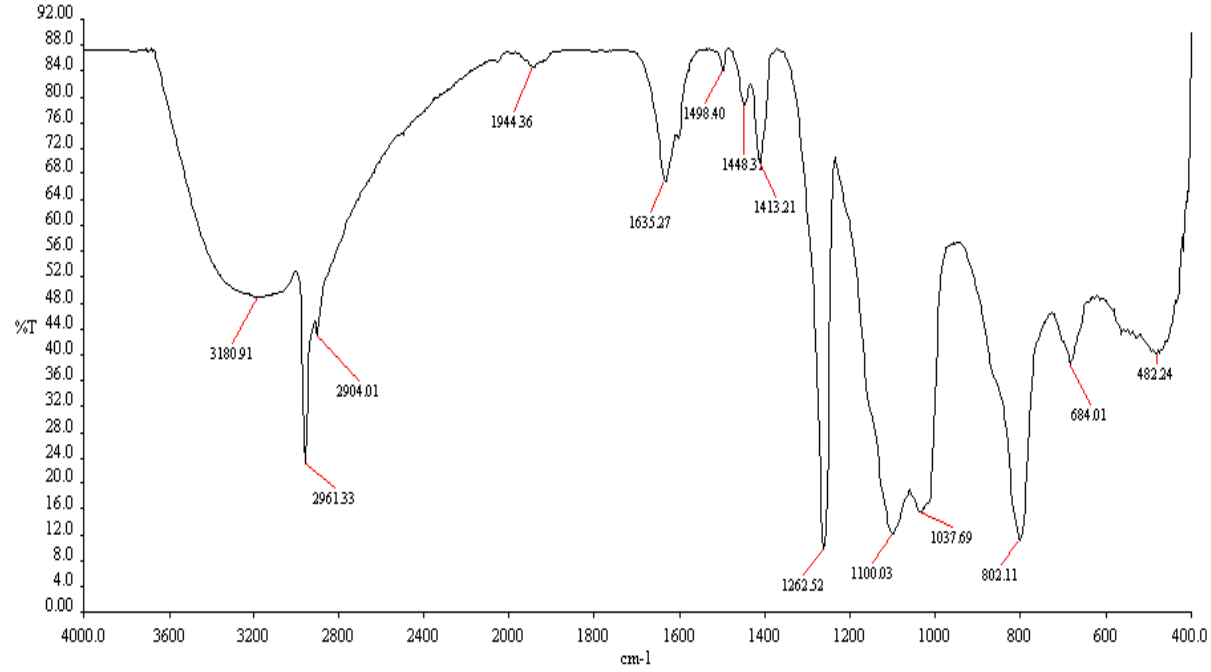

Figure 8.36: IR spectrum of composite made with 3.5 mL of HMDST at 200 °C

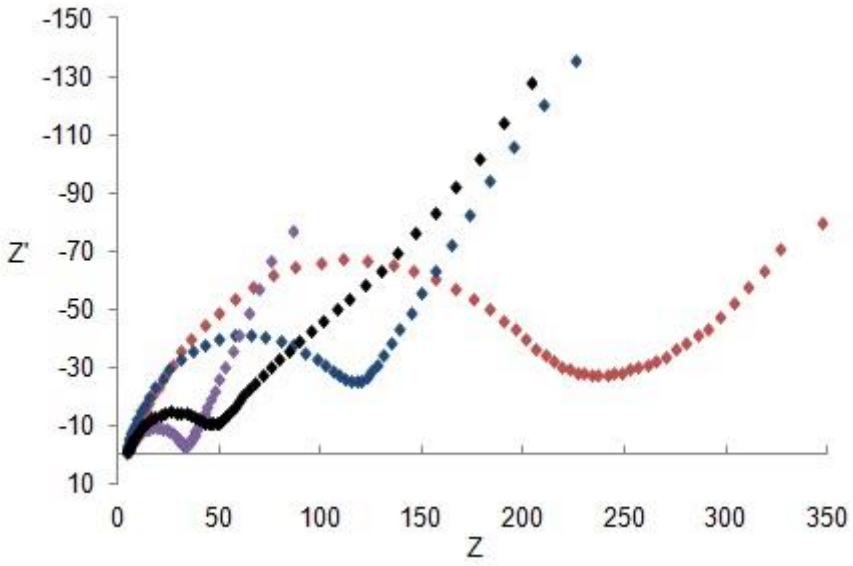

Figure 8.37: Nyquist Plot over the frequency range from 100 KHz to 0.01 Hz using a two electrode setup, using biased potentials equivalent to the open circuit potential of the cell, for pristine m-TiO_2 at 2.309 V vs Li/Li^+ (red) and composites synthesised at 100 °C at 2.512 V vs Li/Li^+ (blue), 150 °C at 2.394 V vs Li/Li^+ (purple) and 200 °C at 2.368 V vs Li/Li^+ (black) with 3.5 mL of HMDST

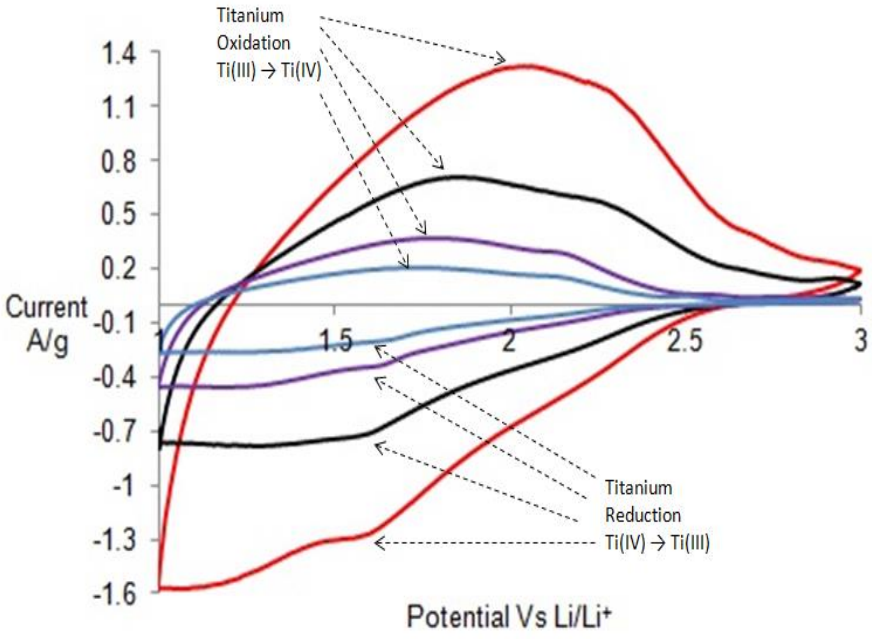

Figure 8.38: Cyclic voltammetry over a potential range of 1-3.4 V vs Li/Li^+ standard electrode potential at various sweep rates of composite synthesised with 1.5 mL of HMDST at 150 °C at 0.5 mVs^{-1} (blue), 1 mVs^{-1} (purple), 2 mVs^{-1} (black) and 5 mVs^{-1} (red)

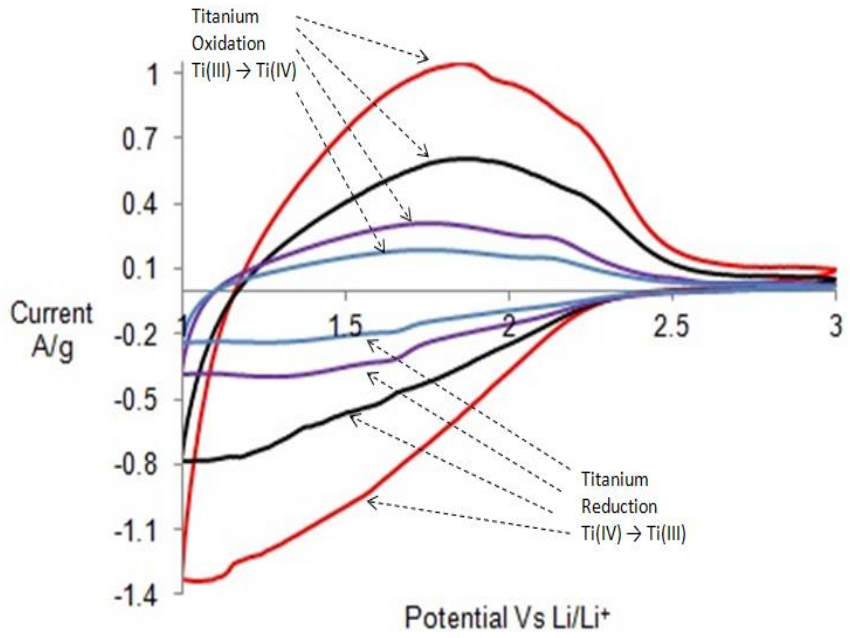

Figure 8.39: Cyclic voltammetry over a potential range of 1-3.4 V vs Li/Li^+ standard electrode potential at various sweep rates of sample synthesised with 2.5 mL of HMDST at 150 °C at 0.5 mVs^{-1} (blue), 1 mVs^{-1} (purple), 2 mVs^{-1} (black) and 5 mVs^{-1} (red)

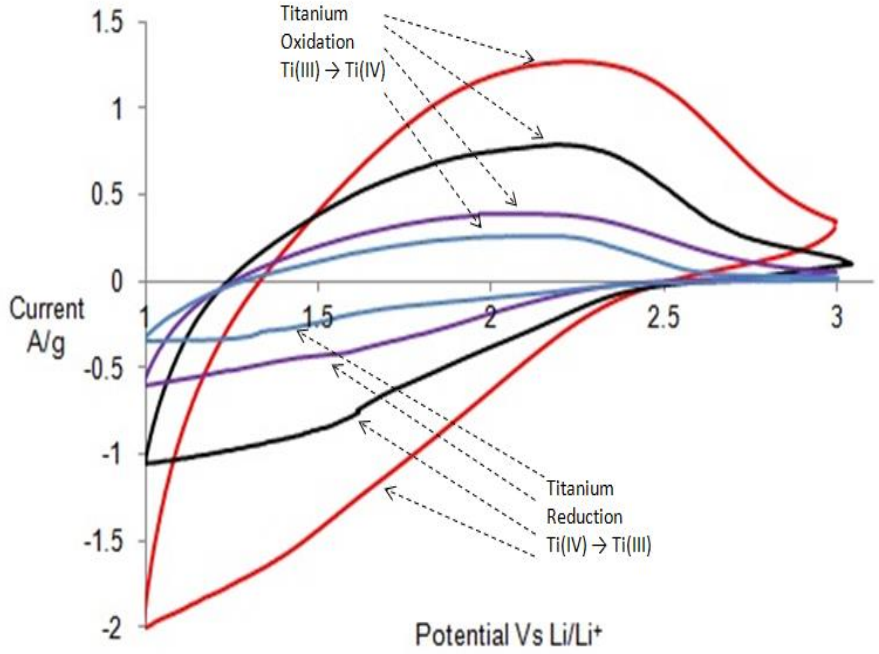

Figure 8.40: Cyclic voltammetry over a potential range of 1-3.4 V vs Li/Li^+ standard electrode potential at various sweep rates of pristine m-TiO_2 at 0.5 mVs^{-1} (blue), 1 mVs^{-1} (purple), 2 mVs^{-1} (black) and 5 mVs^{-1} (red)

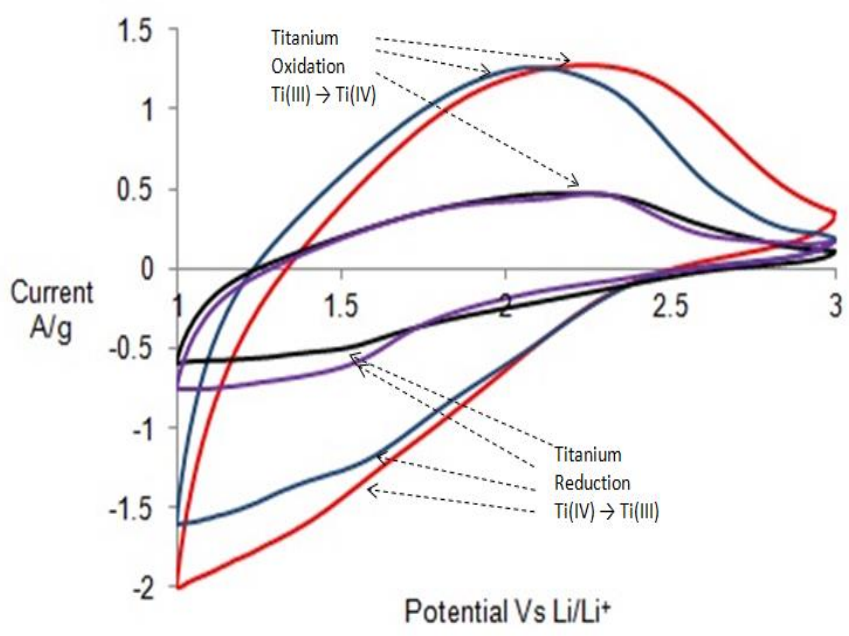

Figure 8.41: Cyclic voltammetry over a potential range of 1-3.4 V vs Li/Li^+ standard electrode potential at 5 mVs^{-1} for m-TiO_2 (red) and composites synthesised at 100 °C (blue), 150 °C (purple) and 200 °C (black) with 3.5 mL of HMDST

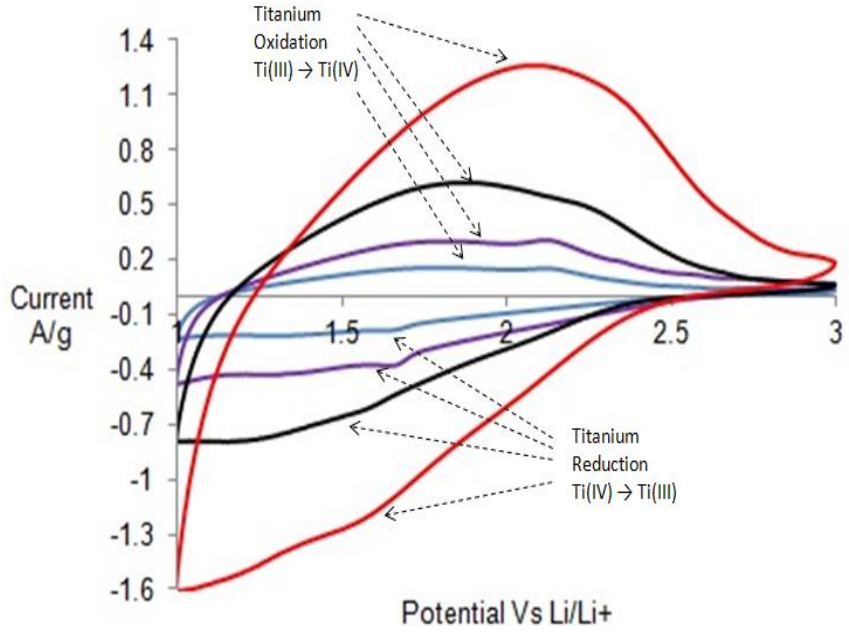

Figure 8.42: Cyclic voltammetry over a potential range of 1-3.4 V vs Li/Li^+ standard electrode potential at various sweep rates of sample synthesised with 3.5 mL of HMDST at 100 °C at 0.5 mVs^{-1} (blue), 1 mVs^{-1} (purple), 2 mVs^{-1} (black), 5 mVs^{-1} (red)

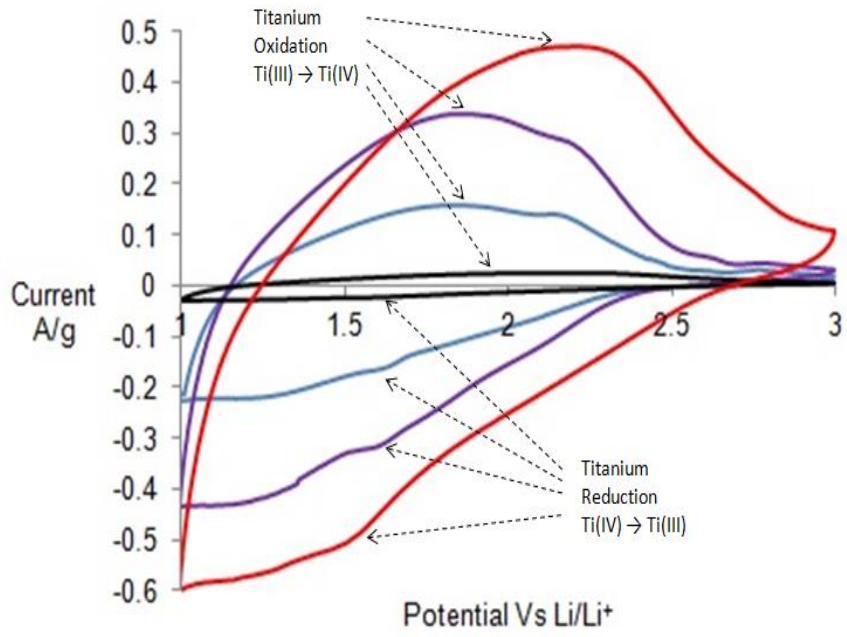

Figure 8.43: Cyclic voltammetry over a potential range of 1-3.4 V vs Li/Li^+ standard electrode potential at various sweep rates of sample synthesised with 3.5 mL of HMDST at 200 °C at 0.5 mVs^{-1} (blue), 1 mVs^{-1} (purple), 2 mVs^{-1} (black), 5 mVs^{-1} (red)

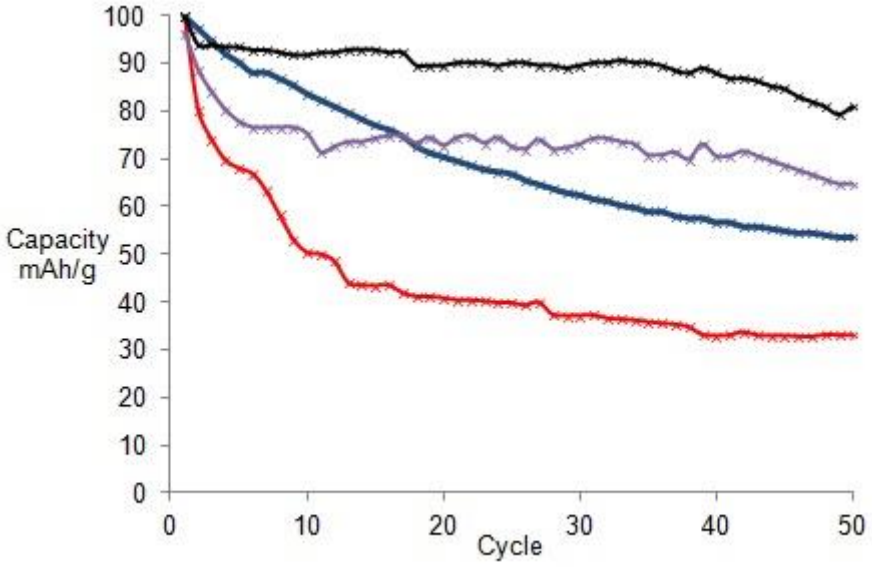

Figure 8.44: 50 Cycles discharge capacity retention data for m-TiO_2 (red) and composites synthesised with 1.5 mL (blue), 2.5 mL (purple), and 3.5 mL (black) of HMDST at 150 °C

Appendix 5 Supplemental for Chapter 6 Electrochemical and Hydrogen Storage Properties of Vanadium(IV) Hydride

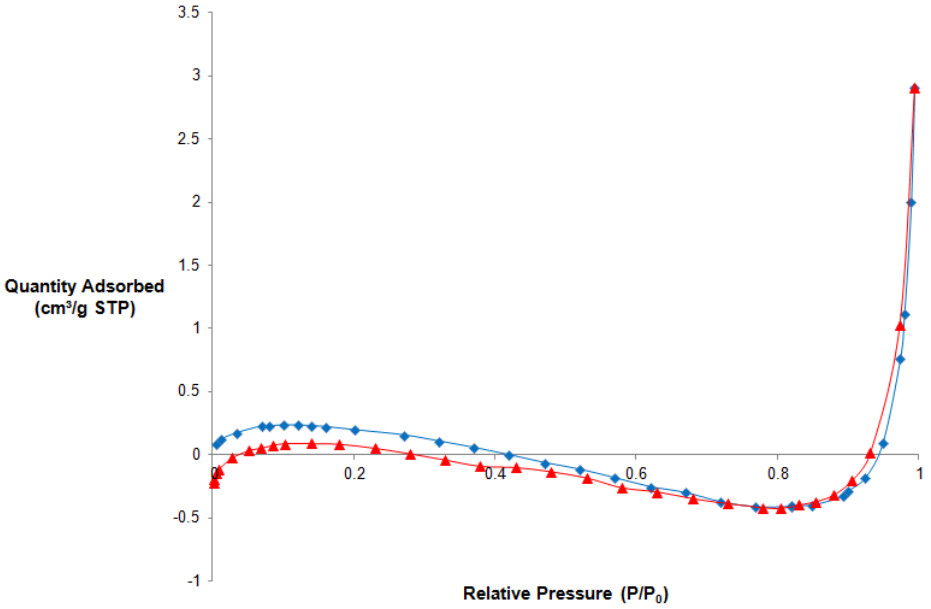

Figure 8.45: Nitrogen adsorption-desorption isotherm of V(IV)-100 recorded at 77K

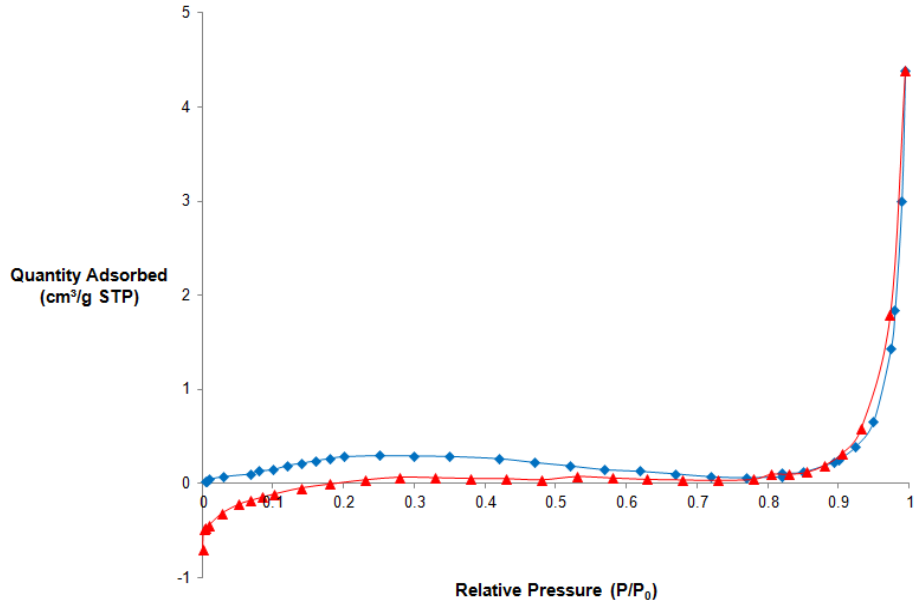

Figure 8.46: Nitrogen adsorption-desorption isotherm of V(IV)-25C-H_2 recorded at 77K

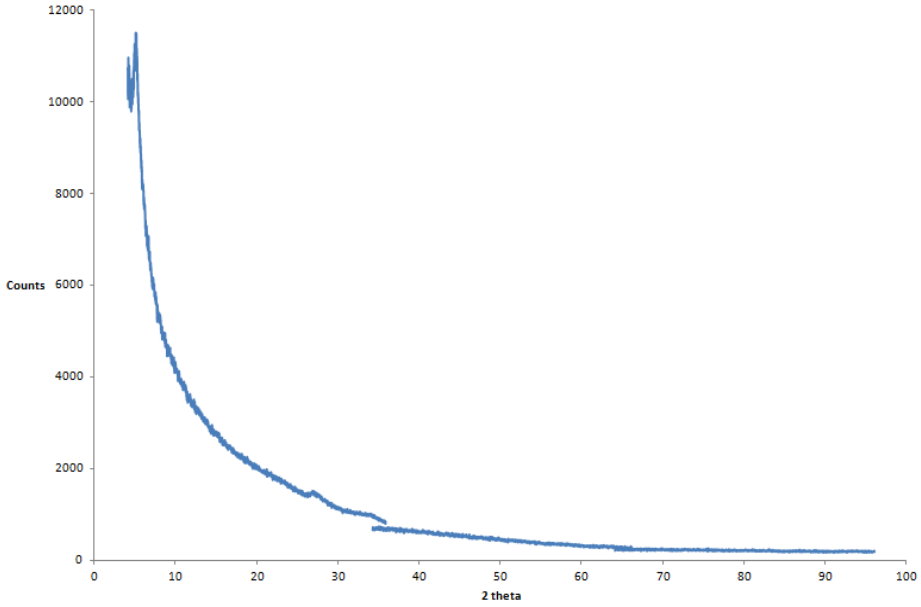

Figure 8.47: Powder x-ray diffraction of V(IV)-25C-H_2

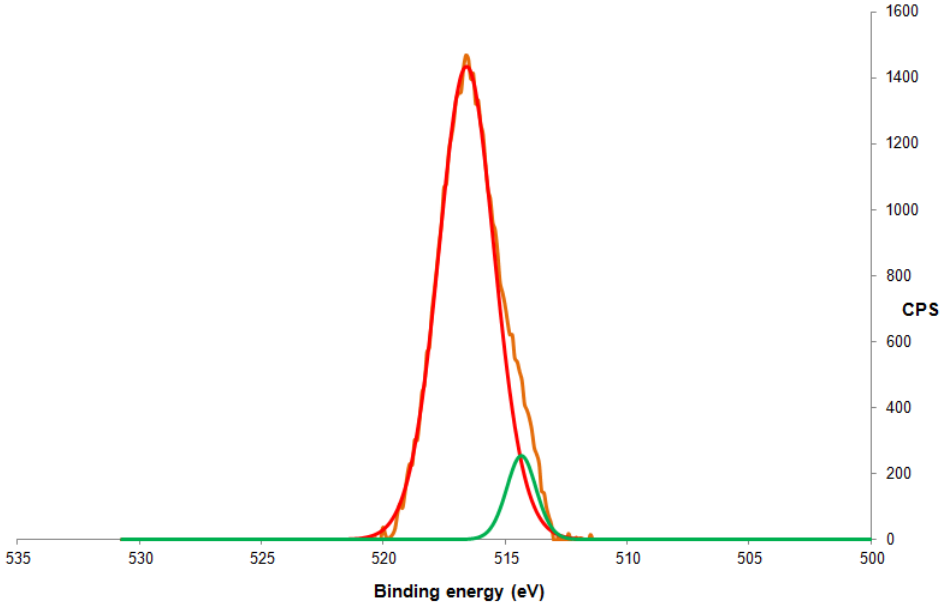

Figure 8.48: Baseline corrected peak fitting of vanadium 2p3/2 region of XPS of V(IV)-100

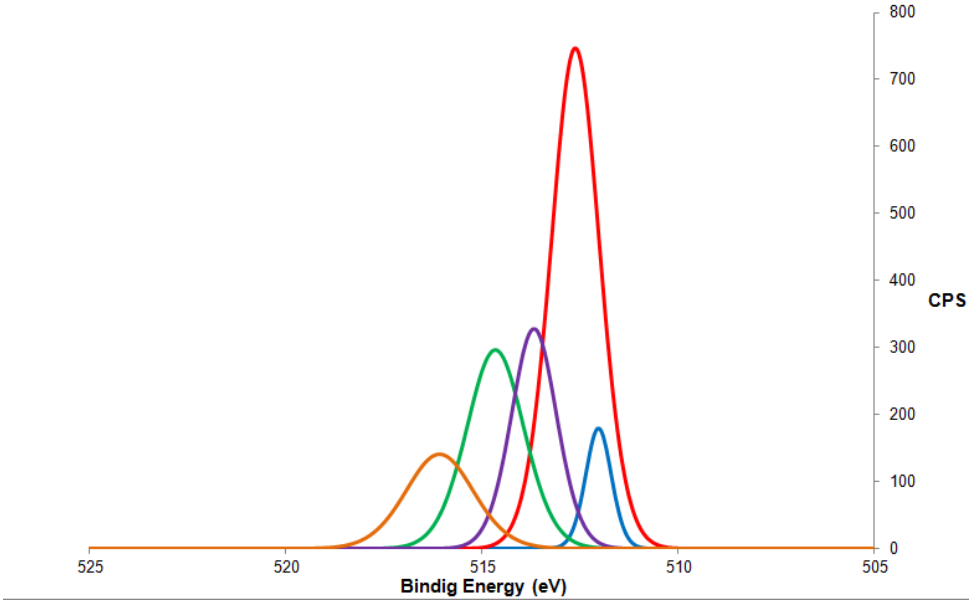

Figure 8.49: Baseline corrected peak fitting of vanadium 2p3/2 region of XPS of V(IV)-25C-H_2

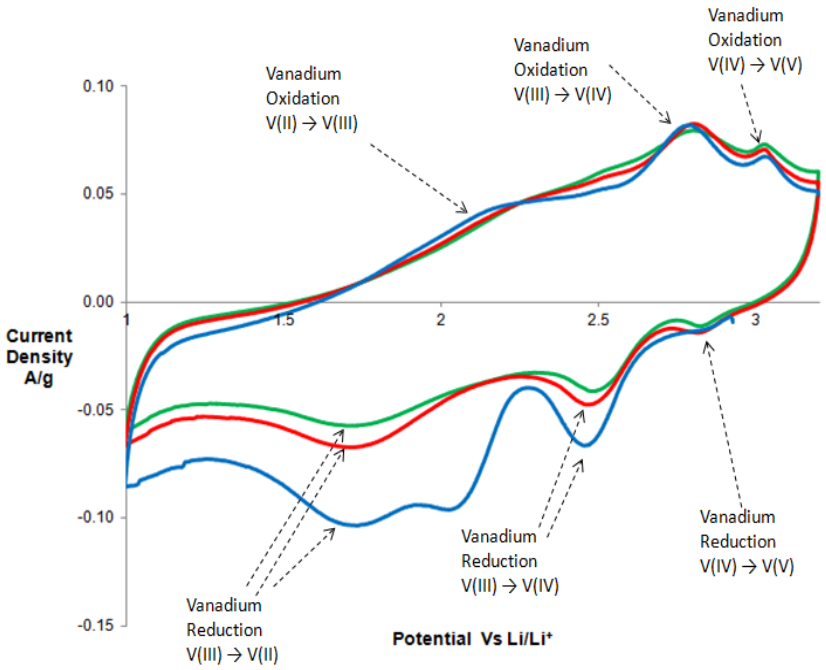

Figure 8.50: Cyclic voltammetry over a potential range of 1-3.2 V vs Li/Li^+ standard electrode potential VO_2 powder at a sweep rate of 0.5 mVs^{-1}: 1st cycle (blue), 2nd cycle (red) and 3rd cycle (green)

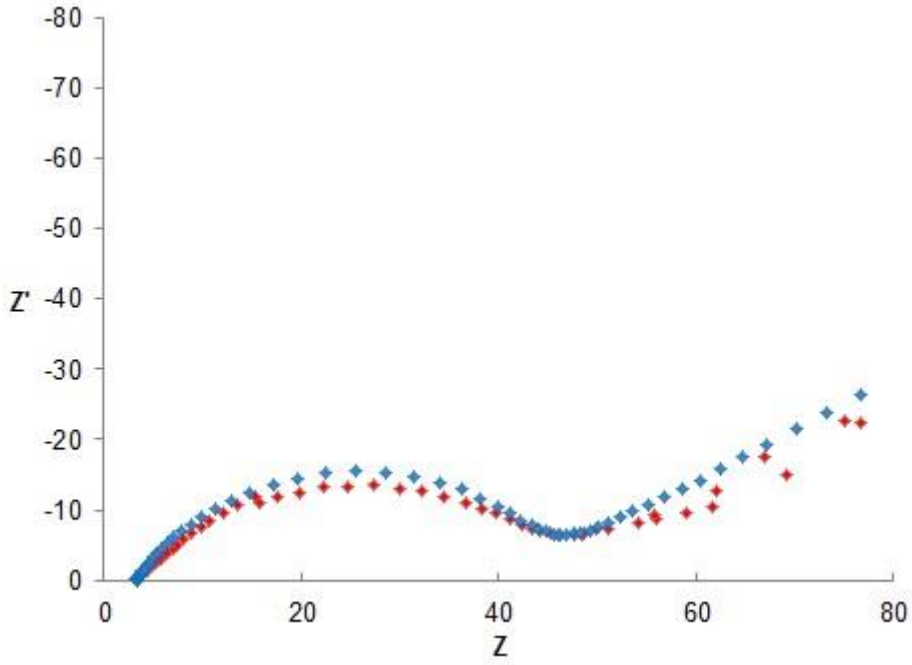

Figure 8.51: EIS spectra over the frequency range from 100 KHz to 0.01 Hz using a two electrode setup, using biased potentials equivalent to the open circuit potential of the cell, VO_2 prior initial discharge at 2.307 V vs Li/Li^+ ((blue) and Upon completion of 50^{th} discharge/charge cycle at 2.292 V vs Li/Li^+ (red)

Appendix 6 Copyright forms

Permission to reproduce a **Figure** from: Energy and Environmental Science 2014, 7, 5, 1597-1614

Order Completed

Thank you very much for your order.

This is a License Agreement between Luke Smith ("You") and Royal Society of Chemistry. The license consists of your order details, the terms and conditions provided by Royal Society of Chemistry, and the payment terms and conditions.

Get the printable license.

License Number	3674151365686
License date	Jul 22, 2015
Licensed content publisher	Royal Society of Chemistry
Licensed content publication	Energy & Environmental Science
Licensed content title	Pseudocapacitive oxide materials for high-rate electrochemical energy storage
Licensed content author	Veronica Augustyn,Patrice Simon,Bruce Dunn
Licensed content date	Mar 13, 2014
Volume number	7
Issue number	5
Type of Use	Thesis/Dissertation
Requestor type	academic/educational
Portion	figures/tables/images
Number of figures/tables/images	1
Distribution quantity	2
Format	print and electronic
Will you be translating?	no
Order reference number	None
Title of the thesis/dissertation	Synthesis and characterization of electron conducting mesoporous Nb, Ti and Ta oxysulfides
Expected completion date	Sep 2015
Estimated size	250
Total	0.00 GBP

ORDER MORE... CLOSE WINDOW

Permission to reproduce a **Figure** from: Energy and Environmental Science 2012, 5, 7, 7854-7863

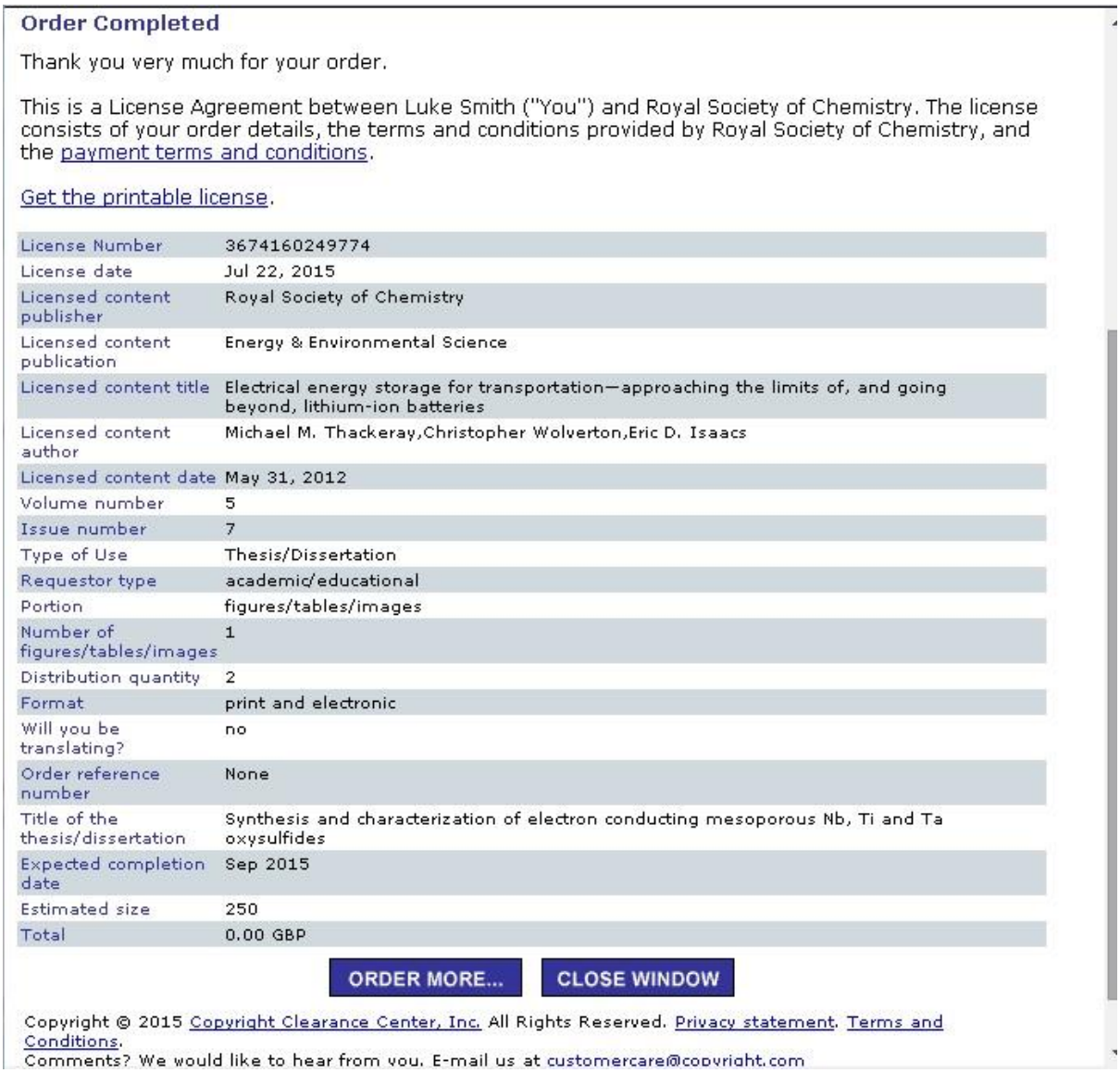

Order Completed

Thank you very much for your order.

This is a License Agreement between Luke Smith ("You") and Royal Society of Chemistry. The license consists of your order details, the terms and conditions provided by Royal Society of Chemistry, and the payment terms and conditions.

Get the printable license.

License Number	3674160249774
License date	Jul 22, 2015
Licensed content publisher	Royal Society of Chemistry
Licensed content publication	Energy & Environmental Science
Licensed content title	Electrical energy storage for transportation—approaching the limits of, and going beyond, lithium-ion batteries
Licensed content author	Michael M. Thackeray,Christopher Wolverton,Eric D. Isaacs
Licensed content date	May 31, 2012
Volume number	5
Issue number	7
Type of Use	Thesis/Dissertation
Requestor type	academic/educational
Portion	figures/tables/images
Number of figures/tables/images	1
Distribution quantity	2
Format	print and electronic
Will you be translating?	no
Order reference number	None
Title of the thesis/dissertation	Synthesis and characterization of electron conducting mesoporous Nb, Ti and Ta oxysulfides
Expected completion date	Sep 2015
Estimated size	250
Total	0.00 GBP

ORDER MORE... CLOSE WINDOW

Copyright © 2015 Copyright Clearance Center, Inc. All Rights Reserved. Privacy statement. Terms and Conditions.
Comments? We would like to hear from you. E-mail us at customercare@copyright.com

Permission to reproduce a **Figure** from: Energy and Environmental Science 2009, 2, 6, 638-654

Order Completed

Thank you very much for your order.

This is a License Agreement between Luke Smith ("You") and Royal Society of Chemistry. The license consists of your order details, the terms and conditions provided by Royal Society of Chemistry, and the payment terms and conditions.

Get the printable license.

License Number	3674160576750
License date	Jul 22, 2015
Licensed content publisher	Royal Society of Chemistry
Licensed content publication	Energy & Environmental Science
Licensed content title	Carbon nanotubes for lithium ion batteries
Licensed content author	Brian J. Landi,Matthew J. Ganter,Cory D. Cress,Roberta A. DiLeo,Ryne P. Raffaelle
Licensed content date	Apr 9, 2009
Volume number	2
Issue number	6
Type of Use	Thesis/Dissertation
Requestor type	academic/educational
Portion	figures/tables/images
Number of figures/tables/images	2
Distribution quantity	2
Format	print and electronic
Will you be translating?	no
Order reference number	None
Title of the thesis/dissertation	Synthesis and characterization of electron conducting mesoporous Nb, Ti and Ta oxysulfides
Expected completion date	Sep 2015
Estimated size	250
Total	0.00 GBP

ORDER MORE... CLOSE WINDOW

Permission to reproduce a **Figure** from: Nature Materials 2003, 2, 7, 464-467

Order Completed

Thank you very much for your order.

This is a License Agreement between Luke Smith ("You") and Nature Publishing Group ("Nature Publishing Group"). The license consists of your order details, the terms and conditions provided by Nature Publishing Group, and the payment terms and conditions.

Get the printable license.

License Number	3674161010938
License date	Jul 22, 2015
Licensed content publisher	Nature Publishing Group
Licensed content publication	Nature Materials
Licensed content title	Atomic resolution of lithium ions in LiCoO2
Licensed content author	Yang Shao-Horn,Laurence Croguennec,Claude Delmas,E. Chris NelsonandMichael A. O'Keefe
Licensed content date	Jul 1, 2003
Type of Use	reuse in a dissertation / thesis
Volume number	2
Issue number	7
Requestor type	academic/educational
Format	print and electronic
Portion	figures/tables/illustrations
Number of figures/tables/illustrations	1
High-res required	no
Figures	LiCoO2 structure
Author of this NPG article	no
Your reference number	None
Title of your thesis / dissertation	Synthesis and characterization of electron conducting mesoporous Nb, Ti and Ta oxysulfides
Expected completion date	Sep 2015
Estimated size (number of pages)	250
Total	0.00 GBP

ORDER MORE... CLOSE WINDOW

Permission to reproduce a **Figure** from: Chemical Society Reviews 2013, 42, 9, 2663-3670

Order Completed

Thank you very much for your order.

This is a License Agreement between Luke Smith ("You") and Royal Society of Chemistry. The license consists of your order details, the terms and conditions provided by Royal Society of Chemistry, and the payment terms and conditions.

Get the printable license.

License Number	3674180030009
License date	Jul 22, 2015
Licensed content publisher	Royal Society of Chemistry
Licensed content publication	Chemical Society Reviews
Licensed content title	The discovery of mesoporous molecular sieves from the twenty year perspective
Licensed content author	Charles T. Kresge,Wieslaw J. Roth
Licensed content date	Feb 21, 2013
Volume number	42
Issue number	9
Type of Use	Thesis/Dissertation
Requestor type	academic/educational
Portion	figures/tables/images
Number of figures/tables/images	1
Distribution quantity	2
Format	print and electronic
Will you be translating?	no
Order reference number	None
Title of the thesis/dissertation	Synthesis and characterization of electron conducting mesoporous Nb, Ti and Ta oxysulfides
Expected completion date	Sep 2015
Estimated size	250
Total	0.00 GBP

ORDER MORE... CLOSE WINDOW

Permission to reproduce a **Figure** from: Inorganic Chemistry 2001, 7, 5, 2088-2095

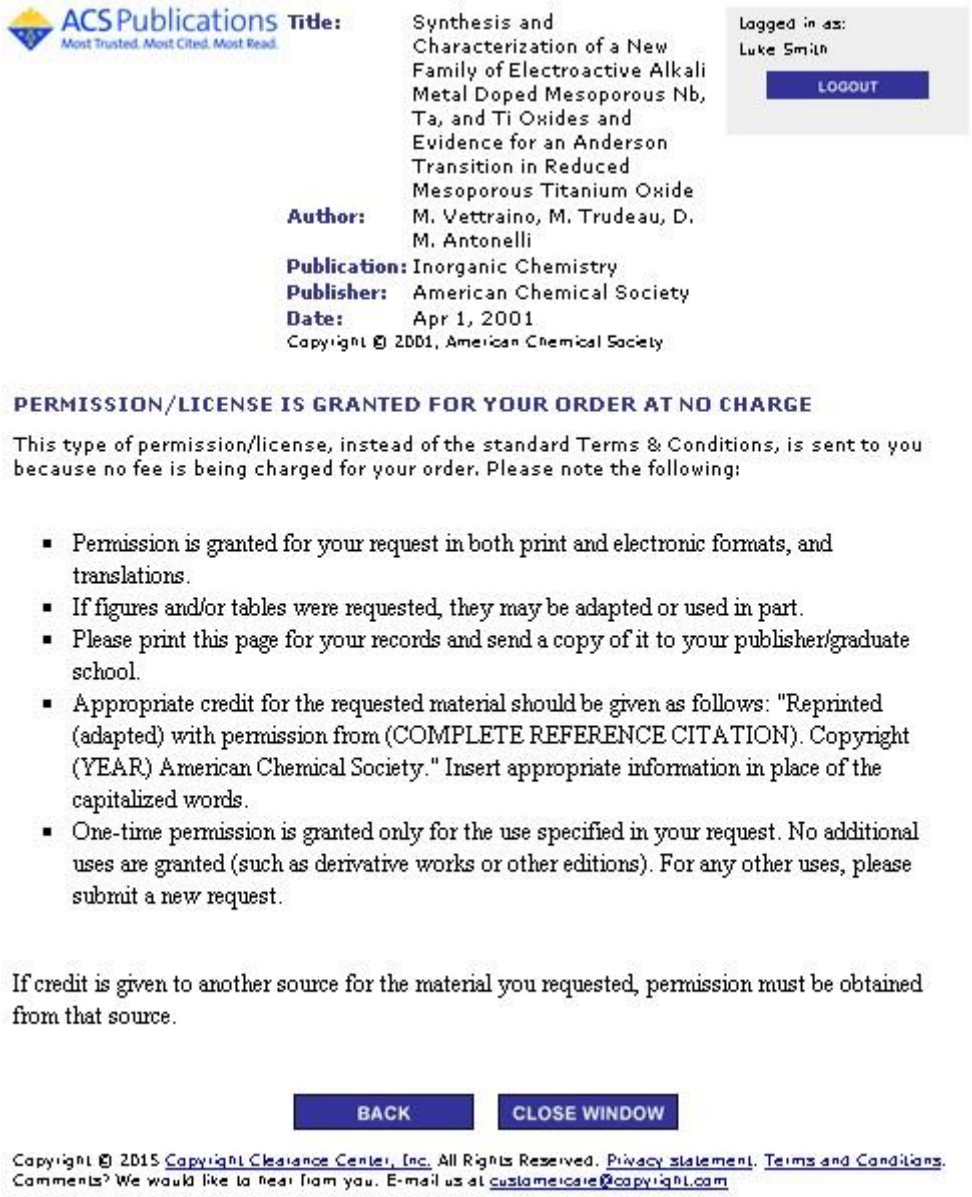

ACS Publications
Most Trusted. Most Cited. Most Read.

Title: Synthesis and Characterization of a New Family of Electroactive Alkali Metal Doped Mesoporous Nb, Ta, and Ti Oxides and Evidence for an Anderson Transition in Reduced Mesoporous Titanium Oxide

Author: M. Vettraino, M. Trudeau, D. M. Antonelli

Publication: Inorganic Chemistry

Publisher: American Chemical Society

Date: Apr 1, 2001

Copyright © 2001, American Chemical Society

Logged in as:
Luke Smith
LOGOUT

PERMISSION/LICENSE IS GRANTED FOR YOUR ORDER AT NO CHARGE

This type of permission/license, instead of the standard Terms & Conditions, is sent to you because no fee is being charged for your order. Please note the following:

- Permission is granted for your request in both print and electronic formats, and translations.
- If figures and/or tables were requested, they may be adapted or used in part.
- Please print this page for your records and send a copy of it to your publisher/graduate school.
- Appropriate credit for the requested material should be given as follows: "Reprinted (adapted) with permission from (COMPLETE REFERENCE CITATION). Copyright (YEAR) American Chemical Society." Insert appropriate information in place of the capitalized words.
- One-time permission is granted only for the use specified in your request. No additional uses are granted (such as derivative works or other editions). For any other uses, please submit a new request.

If credit is given to another source for the material you requested, permission must be obtained from that source.

BACK CLOSE WINDOW

Copyright © 2015 Copyright Clearance Center, Inc. All Rights Reserved. Privacy statement. Terms and Conditions.
Comments? We would like to hear from you. E-mail us at customercare@copyright.com

Permission to reproduce a **Figure** from: Chemical Communications 2014, 50, 41, 5413-5430

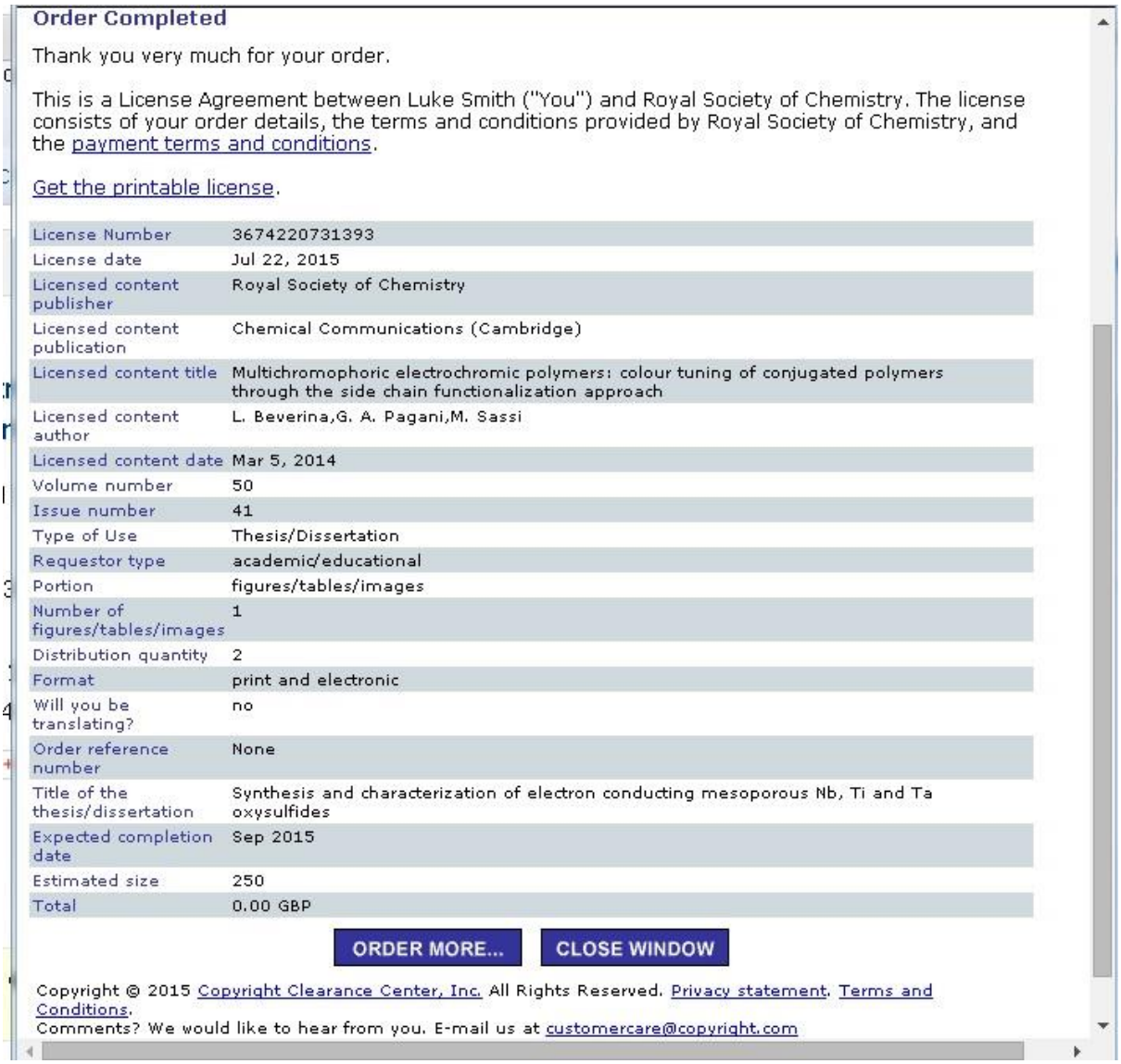

Order Completed

Thank you very much for your order.

This is a License Agreement between Luke Smith ("You") and Royal Society of Chemistry. The license consists of your order details, the terms and conditions provided by Royal Society of Chemistry, and the payment terms and conditions.

Get the printable license.

License Number	3674220731393
License date	Jul 22, 2015
Licensed content publisher	Royal Society of Chemistry
Licensed content publication	Chemical Communications (Cambridge)
Licensed content title	Multichromophoric electrochromic polymers: colour tuning of conjugated polymers through the side chain functionalization approach
Licensed content author	L. Beverina,G. A. Pagani,M. Sassi
Licensed content date	Mar 5, 2014
Volume number	50
Issue number	41
Type of Use	Thesis/Dissertation
Requestor type	academic/educational
Portion	figures/tables/images
Number of figures/tables/images	1
Distribution quantity	2
Format	print and electronic
Will you be translating?	no
Order reference number	None
Title of the thesis/dissertation	Synthesis and characterization of electron conducting mesoporous Nb, Ti and Ta oxysulfides
Expected completion date	Sep 2015
Estimated size	250
Total	0.00 GBP

ORDER MORE... CLOSE WINDOW

Permission to reproduce a **Figure** from: Journal of Materials Chemistry 2012, 22, 7, 3044-3052

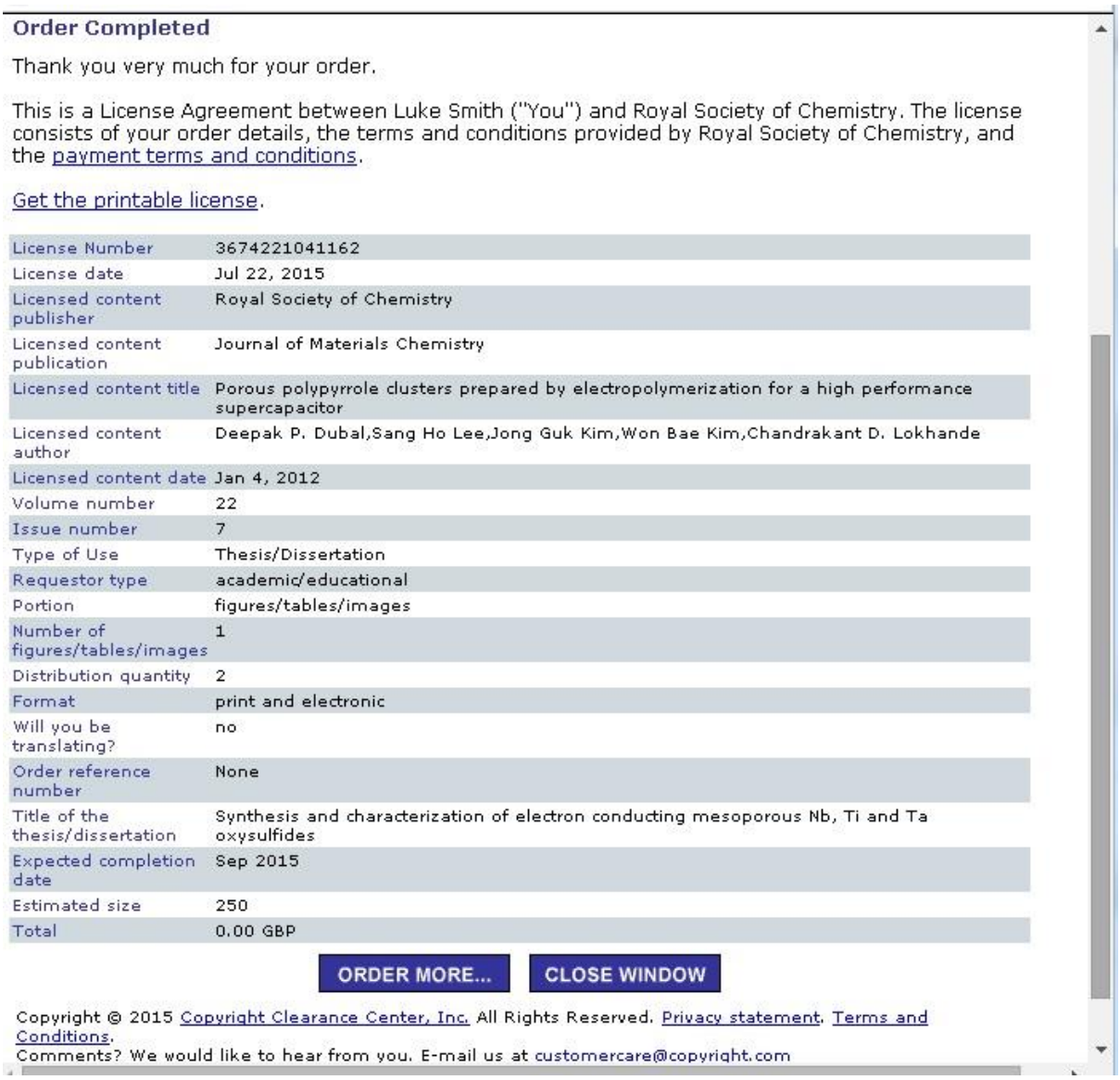

Order Completed

Thank you very much for your order.

This is a License Agreement between Luke Smith ("You") and Royal Society of Chemistry. The license consists of your order details, the terms and conditions provided by Royal Society of Chemistry, and the payment terms and conditions.

Get the printable license.

License Number	3674221041162
License date	Jul 22, 2015
Licensed content publisher	Royal Society of Chemistry
Licensed content publication	Journal of Materials Chemistry
Licensed content title	Porous polypyrrole clusters prepared by electropolymerization for a high performance supercapacitor
Licensed content author	Deepak P. Dubal,Sang Ho Lee,Jong Guk Kim,Won Bae Kim,Chandrakant D. Lokhande
Licensed content date	Jan 4, 2012
Volume number	22
Issue number	7
Type of Use	Thesis/Dissertation
Requestor type	academic/educational
Portion	figures/tables/images
Number of figures/tables/images	1
Distribution quantity	2
Format	print and electronic
Will you be translating?	no
Order reference number	None
Title of the thesis/dissertation	Synthesis and characterization of electron conducting mesoporous Nb, Ti and Ta oxysulfides
Expected completion date	Sep 2015
Estimated size	250
Total	0.00 GBP

ORDER MORE... CLOSE WINDOW

Copyright © 2015 Copyright Clearance Center, Inc. All Rights Reserved. Privacy statement. Terms and Conditions.
Comments? We would like to hear from you. E-mail us at customercare@copyright.com

Permission to reproduce a **Figure** from: Journal of Materials Chemistry 2000, 10, 5, 1251-1254

Order Completed

Thank you very much for your order.

This is a License Agreement between Luke Smith ("You") and Royal Society of Chemistry. The license consists of your order details, the terms and conditions provided by Royal Society of Chemistry, and the payment terms and conditions.

Get the printable license.

License Number	3674231444127
License date	Jul 22, 2015
Licensed content publisher	Royal Society of Chemistry
Licensed content publication	Journal of Materials Chemistry
Licensed content title	Microwave assisted preparation of binary oxide nanoparticles
Licensed content author	Oleg Palchik,Junjie Zhu,Aharon Gedanken
Licensed content date	Mar 29, 2000
Volume number	10
Issue number	5
Type of Use	Thesis/Dissertation
Requestor type	academic/educational
Portion	figures/tables/images
Number of figures/tables/images	1
Distribution quantity	2
Format	print and electronic
Will you be translating?	no
Order reference number	None
Title of the thesis/dissertation	Synthesis and characterization of electron conducting mesoporous Nb, Ti and Ta oxysulfides
Expected completion date	Sep 2015
Estimated size	250
Total	0.00 GBP

ORDER MORE... CLOSE WINDOW

Permission to reproduce a **Figure** from: Ebook Characterisation Techniques for Nanomaterials, 2008, page 211-218

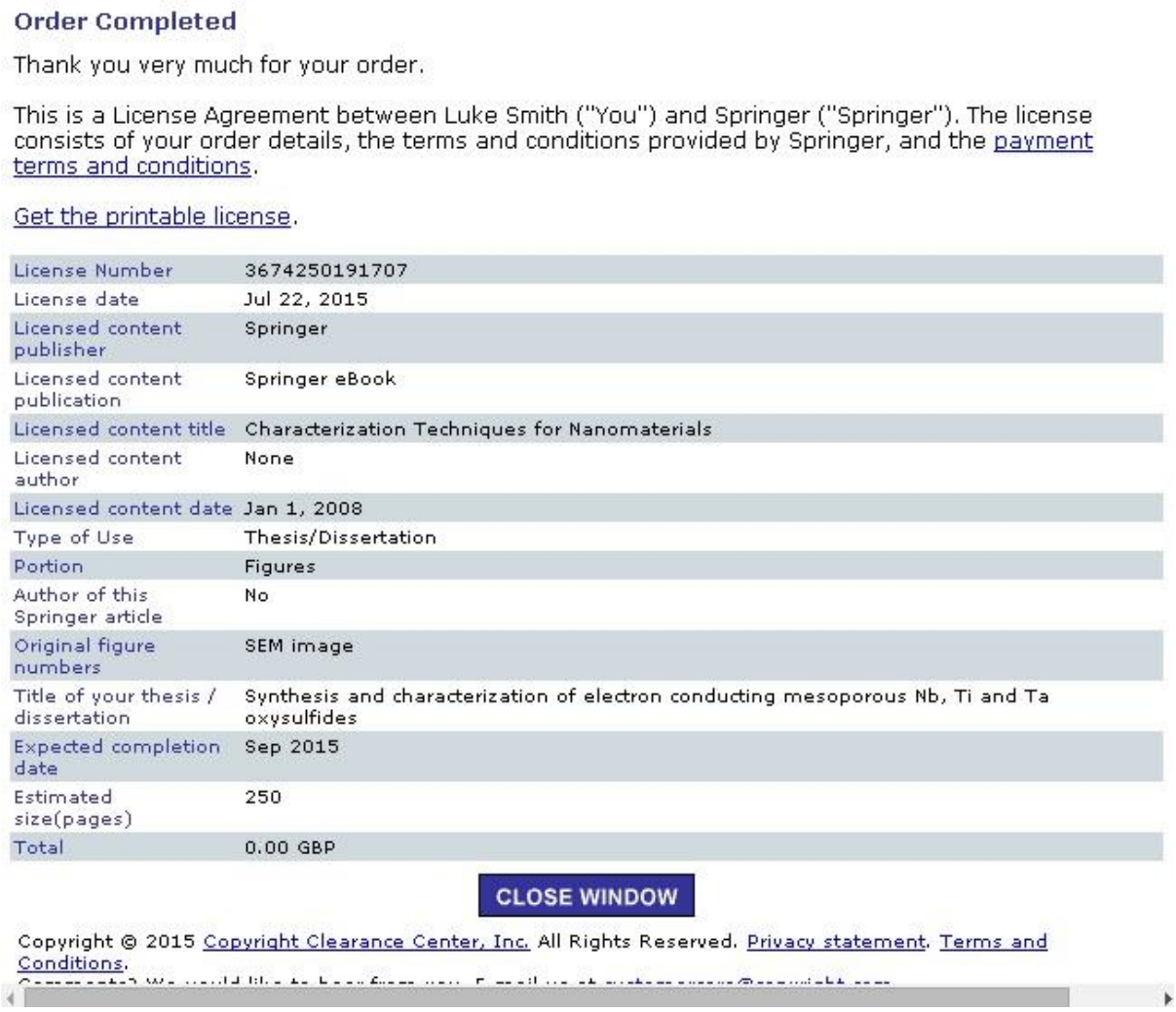

Order Completed

Thank you very much for your order.

This is a License Agreement between Luke Smith ("You") and Springer ("Springer"). The license consists of your order details, the terms and conditions provided by Springer, and the payment terms and conditions.

Get the printable license.

License Number	3674250191707
License date	Jul 22, 2015
Licensed content publisher	Springer
Licensed content publication	Springer eBook
Licensed content title	Characterization Techniques for Nanomaterials
Licensed content author	None
Licensed content date	Jan 1, 2008
Type of Use	Thesis/Dissertation
Portion	Figures
Author of this Springer article	No
Original figure numbers	SEM image
Title of your thesis / dissertation	Synthesis and characterization of electron conducting mesoporous Nb, Ti and Ta oxysulfides
Expected completion date	Sep 2015
Estimated size(pages)	250
Total	0.00 GBP

CLOSE WINDOW

Copyright © 2015 Copyright Clearance Center, Inc. All Rights Reserved. Privacy statement. Terms and Conditions.

Permission to reproduce a **Figure** from: RSC Advances 2015, 5, 17, 12782-12791

Order Completed

Thank you very much for your order.

This is a License Agreement between Luke Smith ("You") and Royal Society of Chemistry. The license consists of your order details, the terms and conditions provided by Royal Society of Chemistry, and the payment terms and conditions.

Get the printable license.

License Number	3674250754502
License date	Jul 22, 2015
Licensed content publisher	Royal Society of Chemistry
Licensed content publication	RSC Advances
Licensed content title	A new approach for the improved interpretation of capacitance measurements for materials utilised in energy storage
Licensed content author	Dimitrios K. Kampouris,Xiaobo Ji,Edward P. Randviir,Craig E. Banks
Licensed content date	Jan 23, 2015
Volume number	5
Issue number	17
Type of Use	Thesis/Dissertation
Requestor type	academic/educational
Portion	figures/tables/images
Number of figures/tables/images	1
Distribution quantity	2
Format	print and electronic
Will you be translating?	no
Order reference number	None
Title of the thesis/dissertation	Synthesis and characterization of electron conducting mesoporous Nb, Ti and Ta oxysulfides
Expected completion date	Sep 2015
Estimated size	250
Total	0.00 GBP

ORDER MORE... CLOSE WINDOW

Permission to reproduce the article in Microporous and Mesoporous materials 2014, 194, 52-59

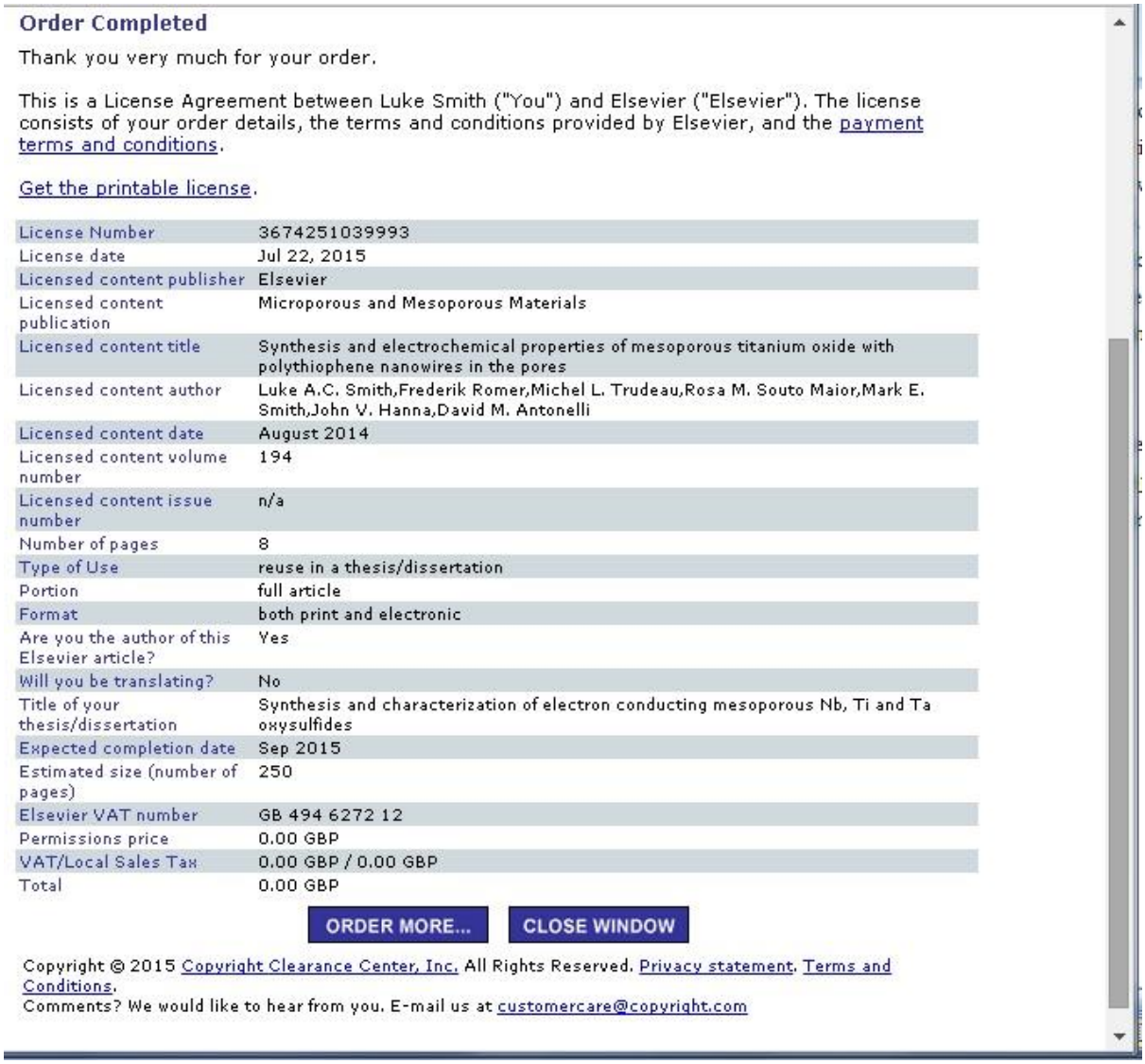

Order Completed

Thank you very much for your order.

This is a License Agreement between Luke Smith ("You") and Elsevier ("Elsevier"). The license consists of your order details, the terms and conditions provided by Elsevier, and the payment terms and conditions.

Get the printable license.

License Number	3674251039993
License date	Jul 22, 2015
Licensed content publisher	Elsevier
Licensed content publication	Microporous and Mesoporous Materials
Licensed content title	Synthesis and electrochemical properties of mesoporous titanium oxide with polythiophene nanowires in the pores
Licensed content author	Luke A.C. Smith,Frederik Romer,Michel L. Trudeau,Rosa M. Souto Maior,Mark E. Smith,John V. Hanna,David M. Antonelli
Licensed content date	August 2014
Licensed content volume number	194
Licensed content issue number	n/a
Number of pages	8
Type of Use	reuse in a thesis/dissertation
Portion	full article
Format	both print and electronic
Are you the author of this Elsevier article?	Yes
Will you be translating?	No
Title of your thesis/dissertation	Synthesis and characterization of electron conducting mesoporous Nb, Ti and Ta oxysulfides
Expected completion date	Sep 2015
Estimated size (number of pages)	250
Elsevier VAT number	GB 494 6272 12
Permissions price	0.00 GBP
VAT/Local Sales Tax	0.00 GBP / 0.00 GBP
Total	0.00 GBP

ORDER MORE... CLOSE WINDOW

Copyright © 2015 Copyright Clearance Center, Inc. All Rights Reserved. Privacy statement. Terms and Conditions.
Comments? We would like to hear from you. E-mail us at customercare@copyright.com

Permission to reproduce the article in ChemElectroChem 2014, 1, 12, 2153-2162

Your confirmation email will contain your order number for future reference.

Get the printable license.

License Number	3674251350167
License date	Jul 22, 2015
Licensed Content Publisher	John Wiley and Sons
Licensed Content Publication	ChemElectroChem
Licensed Content Title	Effect of Synthesis Parameters on the Electrochemical Properties of High-Surface-Area Mesoporous Titanium Oxide with Polypyrrole Nanowires in the Pores
Licensed Content Author	Luke A. C. Smith,Frederick Romer,Michel L. Trudeau,Mark E. Smith,John V. Hanna,David M. Antonelli
Licensed Content Date	Oct 21, 2014
Licensed Content Pages	10
Type of use	Dissertation/Thesis
Requestor type	Author of this Wiley article
Format	Print and electronic
Portion	Full article
Will you be translating?	No
Title of your thesis / dissertation	Synthesis and characterization of electron conducting mesoporous Nb, Ti and Ta oxysulfides
Expected completion date	Sep 2015
Expected size (number of pages)	250
Requestor Location	Luke Smith 9 Harlech Close Croesyceiliog CWMBRAN, United Kingdom np442qp Attn: Luke Smith
Billing Type	Invoice
Billing address	Luke Smith 9 Harlech Close Croesyceiliog CWMBRAN, United Kingdom np442qp Attn: Luke Smith
Total	0.00 GBP

ORDER MORE CLOSE WINDOW

REFERENCES

[1] B. Lee, C. S. Yoon, H. R. Lee, K. Y. Chung, B. W. Cho, S. H. Oh, *Sci. Rep.* **2014**, *4*, DOI 10.1038/srep06066.

[2] K. Young, C. Wang, L. Y. Wang, K. Strunz, in *Electr. Veh. Integr. Mod. Power Netw.* (Eds.: R. Garcia-Valle, J.A.P. Lopes), Springer New York, **2013**, pp. 15–56.

[3] D.-L. Fang, J.-C. Li, X. Liu, P.-F. Huang, T.-R. Xu, M.-C. Qian, C.-H. Zheng, *J. Alloys Compd.* **2015**, *640*, 82–89.

[4] R. Kötz, M. Carlen, *Electrochimica Acta* **2000**, *45*, 2483–2498.

[5] Y. Lei, Z.-H. Huang, Y. Yang, W. Shen, Y. Zheng, H. Sun, F. Kang, *Sci. Rep.* **2013**, *3*, DOI 10.1038/srep02477.

[6] S. F. Tie, C. W. Tan, *Renew. Sustain. Energy Rev.* **2013**, *20*, 82–102.

[7] D. M. Antonelli, *Microporous Mesoporous Mater.* **1999**, *30*, 315–319.

[8] H.-G. Jung, C. S. Yoon, J. Prakash, Y.-K. Sun, *J. Phys. Chem. C* **2009**, *113*, 21258–21263.

[9] M. Vettraino, M. Trudeau, D. M. Antonelli, *Inorg. Chem.* **2001**, *40*, 2088–2095.

[10] X. He, M. Trudeau, D. Antonelli, *Adv. Mater.* **2000**, *12*, 1036–1040.

[11] B. Ye, M. Trudeau, D. Antonelli, *Adv. Mater.* **2001**, *13*, 29–33.

[12] T. Christen, M. W. Carlen, *J. Power Sources* **2000**, *91*, 210–216.

[13] M. Sharma, G. I. N. Waterhouse, S. W. C. Loader, S. Garg, D. Svirskis, *Int. J. Pharm.* **2013**, *443*, 163–168.

[14] A. Nishino, *J. Power Sources* **1996**, *60*, 137–147.

[15] S. H. Lee, J.-S. Moon, M.-S. Lee, T.-H. Yu, H. Kim, B. M. Park, *J. Power Sources* **2015**, *281*, 77–84.

[16] X. Zhu, K. Shang, X. Jiang, X. Ai, H. Yang, Y. Cao, *Ceram. Int.* **2014**, *40*, 11245–11249.

[17] T. Tooming, T. Thomberg, H. Kurig, A. Jänes, E. Lust, *J. Power Sources* **2015**, *280*, 667–677.

[18] H. Teng, Y.-J. Chang, C.-T. Hsieh, *Carbon* **2001**, *39*, 1981–1987.

[19] J. Cho, S. Jeong, Y. Kim, *Prog. Energy Combust. Sci.* **2015**, *48*, 84–101.

[20] P.-Y. Chen, J. Qi, M. T. Klug, X. Dang, P. T. Hammond, A. M. Belcher, *Energy Env. Sci* **2014**, *7*, 3659–3665.

[21] K. T. Lee, J. Cho, *Nano Today* **2011**, *6*, 28–41.

[22] D. Wang, D. Choi, J. Li, Z. Yang, Z. Nie, R. Kou, D. Hu, C. Wang, L. V. Saraf, J. Zhang, et al., *ACS Nano* **2009**, *3*, 907–914.

[23] X. Lang, A. Hirata, T. Fujita, M. Chen, *Nat. Nanotechnol.* **2011**, *6*, 232–236.

[24] J.-K. Chang, W.-T. Tsai, *J. Electrochem. Soc.* **2003**, *150*, A1333–A1338.

[25] E. Frackowiak, F. Béguin, *Carbon* **2001**, *39*, 937–950.

[26] P. Simon, Y. Gogotsi, *Nat. Mater.* **2008**, *7*, 845–854.

[27] T. Brezesinski, J. Wang, S. H. Tolbert, B. Dunn, *Nat. Mater.* **2010**, *9*, 146–151.

[28] V. Augustyn, J. Come, M. A. Lowe, J. W. Kim, P.-L. Taberna, S. H. Tolbert, H. D. Abruña, P. Simon, B. Dunn, *Nat. Mater.* **2013**, *advance online publication*, DOI 10.1038/nmat3601.

[29] W. Xing, F. Li, Z. Yan, G. Q. Lu, *J. Power Sources* **2004**, *134*, 324–330.

[30] K.-W. Nam, S.-B. Ma, W.-S. Yoon, X.-Q. Yang, K.-B. Kim, *Electrochem. Commun.* **2009**, *11*, 1166–1169.

[31] J. Wang, J. Polleux, J. Lim, B. Dunn, *J. Phys. Chem. C* **2007**, *111*, 14925–14931.

[32] L. Ye, C. Wu, W. Guo, Y. Xie, *Chem. Commun.* **2006**, 4738–4740.

[33] B. E. Conway, V. Birss, J. Wojtowicz, *J. Power Sources* **1997**, *66*, 1–14.

[34] B. Vidyadharan, R. A. Aziz, I. I. Misnon, G. M. Anil Kumar, J. Ismail, M. M. Yusoff, R. Jose, *J. Power Sources* **2014**, *270*, 526–535.
[35] V. Augustyn, P. Simon, B. Dunn, *Energy Environ. Sci.* **2014**, *7*, 1597–1614.
[36] B. Diouf, R. Pode, R. Osei, *Renew. Energy* **2015**, *78*, 509–515.
[37] A. Ritchie, W. Howard, *J. Power Sources* **2006**, *162*, 809–812.
[38] A. Kondo, E. Nakamura, T. Kozawa, H. Abe, M. Naito, J. Yoshida, S. Nakanishi, H. Iba, *Adv. Powder Technol.* **2014**, *25*, 1280–1284.
[39] O. Rosas, J. Saunders, H. Castaneda, *Electrochimica Acta* **2013**, *113*, 77–86.
[40] J. Geder, H. E. Hoster, A. Jossen, J. Garche, D. Y. W. Yu, *J. Power Sources* **2014**, *257*, 286–292.
[41] Y. Li, J. Song, J. Yang, *Renew. Sustain. Energy Rev.* **2014**, *37*, 627–633.
[42] Y. Wang, B. Liu, Q. Li, S. Cartmell, S. Ferrara, Z. D. Deng, J. Xiao, *J. Power Sources* **2015**, *286*, 330–345.
[43] M. M. Thackeray, C. Wolverton, E. D. Isaacs, *Energy Environ. Sci.* **2012**, *5*, 7854–7863.
[44] W. Xu, V. V. Viswanathan, D. Wang, S. A. Towne, J. Xiao, Z. Nie, D. Hu, J.-G. Zhang, *J. Power Sources* **2011**, *196*, 3894–3899.
[45] M. S. Whittingham, *Chem. Rev.* **2004**, *104*, 4271–4302.
[46] C. Daniel, D. Mohanty, J. Li, D. L. Wood, in *AIP Conf. Proc.*, AIP Publishing, **2014**, pp. 26–43.
[47] S. Goriparti, E. Miele, F. De Angelis, E. Di Fabrizio, R. Proietti Zaccaria, C. Capiglia, *J. Power Sources* **2014**, *257*, 421–443.
[48] B. Scrosati, J. Garche, *J. Power Sources* **2010**, *195*, 2419–2430.
[49] N. Deprez, D. S. McLachlan, *J. Phys. Appl. Phys.* **1988**, *21*, 101.
[50] B. J. Landi, M. J. Ganter, C. D. Cress, R. A. DiLeo, R. P. Raffaelle, *Energy Environ. Sci.* **2009**, *2*, 638.
[51] N. Nitta, G. Yushin, *Part. Part. Syst. Charact.* **2014**, *31*, 317–336.
[52] M. Wissler, *J. Power Sources* **2006**, *156*, 142–150.
[53] Y. Lin, Z.-H. Huang, X. Yu, W. Shen, Y. Zheng, F. Kang, *Electrochimica Acta* **2014**, *116*, 170–174.
[54] K. Persson, V. A. Sethuraman, L. J. Hardwick, Y. Hinuma, Y. S. Meng, A. van der Ven, V. Srinivasan, R. Kostecki, G. Ceder, *J. Phys. Chem. Lett.* **2010**, *1*, 1176–1180.
[55] S.-L. Chou, J.-Z. Wang, J.-Z. Sun, D. Wexler, M. Forsyth, H.-K. Liu, D. R. MacFarlane, S.-X. Dou, *Chem. Mater.* **2008**, *20*, 7044–7051.
[56] J.-M. Tarascon, M. Armand, *Nature* **2001**, *414*, 359–367.
[57] N. Schweikert, A. Hofmann, M. Schulz, M. Scheuermann, S. T. Boles, T. Hanemann, H. Hahn, S. Indris, *J. Power Sources* **2013**, *228*, 237–243.
[58] C. H. Lee, S. J. Bae, M. Jang, *J. Power Sources* **2015**, *293*, 498–510.
[59] I. Hasa, R. Verrelli, J. Hassoun, *Electrochimica Acta* **2015**, *173*, 613–618.
[60] P. Wang, P. Li, T.-F. Yi, X. Lin, Y.-R. Zhu, L. Shao, M. Shui, N. Long, J. Shu, *J. Power Sources* **2015**, *293*, 33–41.
[61] X. Sun, Y. Xu, P. Ding, M. Jia, G. Ceder, *J. Power Sources* **2013**, *244*, 690–694.
[62] N. A. Milne, M. Skyllas-Kazacos, V. Luca, *J. Phys. Chem. C* **2009**, *113*, 12983–12995.
[63] W.-J. Zhang, *J. Power Sources* **2011**, *196*, 13–24.
[64] C. K. Chan, H. Peng, G. Liu, K. McIlwrath, X. F. Zhang, R. A. Huggins, Y. Cui, *Nat. Nanotechnol.* **2008**, *3*, 31–35.
[65] B. Das, M. V. Reddy, P. Malar, T. Osipowicz, G. V. Subba Rao, B. V. R. Chowdari, *Solid State Ion.* **2009**, *180*, 1061–1068.
[66] L. L. Gaines, R. M. Cuenca, *Costs of Lithium-Ion Batteries for Vehicles*, Argonne National Laboratory, Argonne, IL USA, **2000**.
[67] Z. Wang, Z. Wang, H. Guo, W. Peng, X. Li, *J. Alloys Compd.* **2015**, *626*, 228–233.

[68] Y. Shao-Horn, L. Croguennec, C. Delmas, E. C. Nelson, M. A. O'Keefe, *Nat. Mater.* **2003**, *2*, 464–467.
[69] K. A. Kurilenko, O. A. Shlyakhtin, O. A. Brylev, O. A. Drozhzhin, *Electrochimica Acta* **2015**, *152*, 255–264.
[70] J. Liang, D. Wu, M. Hu, Y. Tian, J. Wei, Z. Zhou, *Electrochimica Acta* **2014**, *146*, 784–791.
[71] J. Reed, G. Ceder, *Electrochem. Solid-State Lett.* **2002**, *5*, A145–A148.
[72] W.-S. Yoon, C. P. Grey, M. Balasubramanian, X.-Q. Yang, J. McBreen, *Chem. Mater.* **2003**, *15*, 3161–3169.
[73] N. Yabuuchi, Y.-T. Kim, H. H. Li, Y. Shao-Horn, *Chem. Mater.* **2008**, *20*, 4936–4951.
[74] K. Kang, Y. S. Meng, J. Bréger, C. P. Grey, G. Ceder, *Science* **2006**, *311*, 977–980.
[75] I. Belharouak, Y.-K. Sun, J. Liu, K. Amine, *J. Power Sources* **2003**, *123*, 247–252.
[76] S. Venkatraman, A. Manthiram, *Solid State Ion.* **2005**, *176*, 291–298.
[77] K. Amine, J. Liu, S. Kang, I. Belharouak, Y. Hyung, D. Vissers, G. Henriksen, *J. Power Sources* **2004**, *129*, 14–19.
[78] A. Yamada, M. Tanaka, K. Tanaka, K. Sekai, *J. Power Sources* **1999**, *81–82*, 73–78.
[79] H. Ikuta, K. Takanaka, M. Wakihara, *Thermochim. Acta* **2004**, *414*, 227–232.
[80] C. M. Julien, A. Mauger, K. Zaghib, H. Groult, *Inorganics* **2014**, *2*, 132–154.
[81] J. S. Chae, M. R. Jo, Y.-I. Kim, D.-W. Han, S.-M. Park, Y.-M. Kang, K. C. Roh, *J. Ind. Eng. Chem.* **2015**, *21*, 731–735.
[82] W. Wang, H. Liu, Y. Wang, C. Gao, J. Zhang, *Trans. Nonferrous Met. Soc. China* **2013**, *23*, 2066–2070.
[83] G. Cai, R. Guo, L. Liu, Y. Yang, C. Zhang, C. Wu, W. Guo, H. Jiang, *J. Power Sources* **2015**, *288*, 136–144.
[84] F. Fathollahi, M. Javanbakht, H. Omidvar, M. Ghaemi, *J. Alloys Compd.* **2015**, *627*, 146–152.
[85] G. R. Kiani, S. Boroomand, R. Khodabakhshi, M. Esmaeili, *Microelectron. Eng.* **2015**, *136*, 77–80.
[86] A. K. Padhi, K. S. Nanjundaswamy, J. B. Goodenough, *J. Electrochem. Soc.* **1997**, *144*, 1188–1194.
[87] Y. Wang, D. Zhang, X. Yu, R. Cai, Z. Shao, X.-Z. Liao, Z.-F. Ma, *J. Alloys Compd.* **2010**, *492*, 675–680.
[88] J. Molenda, *Funct. Mater. Lett.* **2011**, *4*, 107–112.
[89] N. Nitta, G. Yushin, *Part. Part. Syst. Charact.* **2014**, *31*, 317–336.
[90] Y. Li, X. Li, Z. Wang, H. Guo, T. Li, *Ceram. Int.* **2016**, *42*, 14565–14572.
[91] J. Qiu, C. Lai, Y. Wang, S. Li, S. Zhang, *Chem. Eng. J.* **2014**, *256*, 247–254.
[92] L.-Y. Wang, B. Xue, Y. Wu, N. Lun, Y.-X. Qi, Y.-J. Bai, *Electrochimica Acta* **2016**, *212*, 151–161.
[93] M. R. Jongerden, B. R. Haverkort, *Battery Modeling*, **2008**.
[94] A. G. Dylla, G. Henkelman, K. J. Stevenson, *Acc. Chem. Res.* **2013**, *46*, 1104–1112.
[95] S. Li, P. Xue, C. Lai, J. Qiu, M. Ling, S. Zhang, *Electrochimica Acta* **2015**, *180*, 112–119.
[96] C. Han, D. Yang, Y. Yang, B. Jiang, Y. He, M. Wang, A.-Y. Song, Y.-B. He, B. Li, Z. Lin, *J. Mater. Chem. A* **2015**, *3*, 13340–13349.
[97] S. Li, J. Qiu, C. Lai, M. Ling, H. Zhao, S. Zhang, *Nano Energy* **2015**, *12*, 224–230.
[98] Y. Shao, J. Xiao, W. Wang, M. Engelhard, X. Chen, Z. Nie, M. Gu, L. V. Saraf, G. Exarhos, J.-G. Zhang, et al., *Nano Lett.* **2013**, *13*, 3909–3914.
[99] M. Lübke, J. Shin, P. Marchand, D. Brett, P. Shearing, Z. Liu, J. A. Darr, *J. Mater. Chem. A* **2015**, *3*, 22908–22914.

[100] G. Armstrong, A. R. Armstrong, J. Canales, P. G. Bruce, *Chem. Commun.* **2005**, 2454–2456.
[101] J. Li, Z. Tang, Z. Zhang, *Chem. Phys. Lett.* **2006**, *418*, 506–510.
[102] H. D. Yoo, Y. Li, Y. Liang, Y. Lan, F. Wang, Y. Yao, *ChemNanoMat* **2016**, *2*, 688–691.
[103] U.S Advanced Battery Consortium, *USCAR: USABC Electric Vehicle Battery Test Procedures Manual*, **1996**.
[104] J. Liu, K. Song, P. A. van Aken, J. Maier, Y. Yu, *Nano Lett.* **2014**, *14*, 2597–2603.
[105] Y. J. Hong, M. Y. Son, Y. C. Kang, *Adv. Mater.* **2013**, *25*, 2279–2283.
[106] J. Shin, W.-H. Ryu, K.-S. Park, I.-D. Kim, *ACS Nano* **2013**, *7*, 7330–7341.
[107] H. Zhao, W. Yuan, G. Liu, *Nano Today* **2015**, *10*, 193–212.
[108] S. Wu, Y. Du, S. Sun, *Chem. Eng. J.* **n.d.**, DOI 10.1016/j.cej.2016.08.044.
[109] E. Bulut, M. Can, M. Özacar, H. Akbulut, *J. Alloys Compd.* **2016**, *670*, 25–34.
[110] C.-M. Park, H.-J. Sohn, *Electrochimica Acta* **2009**, *54*, 6367–6373.
[111] N. Liu, Z. Lu, J. Zhao, M. T. McDowell, H.-W. Lee, W. Zhao, Y. Cui, *Nat. Nanotechnol.* **2014**, *9*, 187–192.
[112] S. Cavaliere, *Electrospinning for Advanced Energy and Environmental Applications*, CRC Press, **2015**.
[113] S. H. Choi, Y. C. Kang, *ACS Appl. Mater. Interfaces* **2014**, *6*, 2312–2316.
[114] L. Chu, M. Li, X. Li, Y. Wang, Z. Wan, S. Dou, D. Song, Y. Li, B. Jiang, *RSC Adv.* **2015**, *5*, 49765–49770.
[115] A. S. Aricò, P. Bruce, B. Scrosati, J.-M. Tarascon, W. van Schalkwijk, *Nat. Mater.* **2005**, *4*, 366–377.
[116] Y.-H. Jin, S.-D. Seo, H.-W. Shim, K.-S. Park, D.-W. Kim, *Nanotechnology* **2012**, *23*, 125402.
[117] J. Jiang, Y. Li, J. Liu, X. Huang, C. Yuan, X. W. D. Lou, *Adv. Mater.* **2012**, *24*, 5166–5180.
[118] N. Mahmood, C. Zhang, F. Liu, J. Zhu, Y. Hou, *ACS Nano* **2013**, *7*, 10307–10318.
[119] R. Mukherjee, A. V. Thomas, A. Krishnamurthy, N. Koratkar, *ACS Nano* **2012**, *6*, 7867–7878.
[120] C. Zhang, N. Mahmood, H. Yin, F. Liu, Y. Hou, *Adv. Mater.* **2013**, *25*, 4932–4937.
[121] Z.-S. Wu, W. Ren, L. Xu, F. Li, H.-M. Cheng, *ACS Nano* **2011**, *5*, 5463–5471.
[122] X. Li, L. Fan, Z. Li, K. Wang, M. Zhong, J. Wei, D. Wu, H. Zhu, *Adv. Energy Mater.* **2012**, *2*, 425–429.
[123] X. Feng, *Nanocarbons for Advanced Energy Storage*, John Wiley & Sons, **2015**.
[124] Y. Sun, N. Liu, Y. Cui, *Nat. Energy* **2016**, *1*, 16071.
[125] Y. Wang, J. Wu, Y. Tang, X. Lü, C. Yang, M. Qin, F. Huang, X. Li, X. Zhang, *ACS Appl. Mater. Interfaces* **2012**, *4*, 4246–4250.
[126] N. Mahmood, C. Zhang, J. Jiang, F. Liu, Y. Hou, *Chem. – Eur. J.* **2013**, *19*, 5183–5190.
[127] N. Mahmood, C. Zhang, Y. Hou, *Small* **2013**, *9*, 1321–1328.
[128] Y. Tang, L. Hong, Q. Wu, J. Li, G. Hou, H. Cao, L. Wu, G. Zheng, *Electrochimica Acta* **2016**, *195*, 27–33.
[129] R. Alcántara, J. C. Jumas, P. Lavela, J. Olivier-Fourcade, C. Pérez-Vicente, J. L. Tirado, *J. Power Sources* **1999**, *81–82*, 547–553.
[130] R. Stoyanova, E. Zhecheva, L. Zarkova, *Solid State Ion.* **1994**, *73*, 233–240.
[131] K. M. Shaju, P. G. Bruce, *Adv. Mater.* **2006**, *18*, 2330–2334.
[132] Y.-K. Sun, S.-T. Myung, B.-C. Park, J. Prakash, I. Belharouak, K. Amine, *Nat. Mater.* **2009**, *8*, 320–324.
[133] G. Wang, H. Liu, J. Liu, S. Qiao, G. M. Lu, P. Munroe, H. Ahn, *Adv. Mater.* **2010**, *22*, 4944–4948.
[134] Y. Zhang, L. Wu, J. Zhao, W. Yu, *J. Electroanal. Chem.* **2014**, *719*, 1–6.

[135] J. Hu, J. Xie, X. Zhao, H. Yu, X. Zhou, G. Cao, J. Tu, *J. Mater. Sci. Technol.* **2009**, *25*, 405–409.
[136] H. C. Shin, W. I. Cho, H. Jang, *J. Power Sources* **2006**, *159*, 1383–1388.
[137] Y. Ge, X. Yan, J. Liu, X. Zhang, J. Wang, X. He, R. Wang, H. Xie, *Electrochimica Acta* **2010**, *55*, 5886–5890.
[138] Q. Lu, J. G. Chen, J. Q. Xiao, *Angew. Chem. Int. Ed.* **2013**, *52*, 1882–1889.
[139] Y. Yang, Z. Peng, G. Wang, G. Ruan, X. Fan, L. Li, H. Fei, R. H. Hauge, J. M. Tour, *ACS Nano* **2014**, *8*, 7279–7287.
[140] F. Zhang, L. Qi, *Adv. Sci.* **2016**, *3*, n/a-n/a.
[141] S. Kraas, A. Vijn, M. Falk, B. Ufer, B. Luerßen, J. Janek, M. Fröba, *Prog. Solid State Chem.* **2014**, *42*, 218–241.
[142] Q. Q. Xiong, H. Y. Qin, H. Z. Chi, Z. G. Ji, *J. Alloys Compd.* **2016**, *685*, 15–21.
[143] S. H. Ko, D. Lee, H. W. Kang, K. H. Nam, J. Y. Yeo, S. J. Hong, C. P. Grigoropoulos, H. J. Sung, *Nano Lett.* **2011**, *11*, 666–671.
[144] J. Jiang, Y. Li, J. Liu, X. Huang, *Nanoscale* **2011**, *3*, 45–58.
[145] J. Wang, Q. Zhang, X. Li, D. Xu, Z. Wang, H. Guo, K. Zhang, *Nano Energy* **2014**, *6*, 19–26.
[146] J. Liu, Y. Li, X. Huang, R. Ding, Y. Hu, J. Jiang, L. Liao, *J. Mater. Chem.* **2009**, *19*, 1859–1864.
[147] Z. Wang, F. Su, S. Madhavi, X. W. Lou, *Nanoscale* **2011**, *3*, 1618–1623.
[148] X. Yu, Z. Lu, G. Zhang, X. Lei, J. Liu, L. Wang, X. Sun, *RSC Adv.* **2013**, *3*, 19937–19941.
[149] K.-X. Wang, X.-H. Li, J.-S. Chen, *Adv. Mater.* **2015**, *27*, 527–545.
[150] Y. Li, B. Tan, Y. Wu, *Nano Lett.* **2008**, *8*, 265–270.
[151] H. Xia, Y. Wan, W. Assenmacher, W. Mader, G. Yuan, L. Lu, *NPG Asia Mater.* **2014**, *6*, e126.
[152] S. Saadat, J. Zhu, D. H. Sim, H. H. Hng, R. Yazami, Q. Yan, *J. Mater. Chem. A* **2013**, *1*, 8672–8678.
[153] J.-Y. Liao, D. Higgins, G. Lui, V. Chabot, X. Xiao, Z. Chen, *Nano Lett.* **2013**, *13*, 5467–5473.
[154] X. Wu, S. Zhang, L. Wang, Z. Du, H. Fang, Y. Ling, Z. Huang, *J. Mater. Chem.* **2012**, *22*, 11151–11158.
[155] H. Liu, Z. Hu, Y. Su, H. Ruan, R. Hu, L. Zhang, *Appl. Surf. Sci.* **2017**, *392*, 777–784.
[156] J. Wang, Q. Zhang, X. Li, B. Zhang, L. Mai, K. Zhang, *Nano Energy* **2015**, *12*, 437–446.
[157] J. Fan, G. Li, D. Luo, C. Fu, Q. Li, J. Zheng, L. Li, *Electrochimica Acta* **2015**, *173*, 7–16.
[158] P. Rozier, J. M. Tarascon, *J. Electrochem. Soc.* **2015**, *162*, A2490–A2499.
[159] C.-Y. Chen, H.-X. Li, M. E. Davis, *Microporous Mater.* **1993**, *2*, 17–26.
[160] M.-C. Silaghi, C. Chizallet, P. Raybaud, *Microporous Mesoporous Mater.* **2014**, *191*, 82–96.
[161] C. T. Kresge, W. J. Roth, *Chem. Soc. Rev.* **2013**, *42*, 3663–3670.
[162] E. Chomski, G. A. Ozin, *Adv. Mater.* **2000**, *12*, 1071–1078.
[163] D. M. Antonelli, J. Y. Ying, *Chem. Mater.* **1996**, *8*, 874–881.
[164] D. M. Antonelli, *Microporous Mesoporous Mater.* **1999**, *30*, 315–319.
[165] D. M. Antonelli, *Microporous Mesoporous Mater.* **1999**, *33*, 209–214.
[166] D. M. Antonelli, *Microporous Mesoporous Mater.* **1999**, *28*, 505–510.
[167] D. M. Antonelli, M. Trudeau, *Angew. Chem. Int. Ed.* **1999**, *38*, 1471–1475.
[168] M. Hussain, P. Akhter, N. Russo, G. Saracco, *Chem. Eng. J.* **2015**, *278*, 279–292.
[169] X. He, D. Antonelli, *Angew. Chem. Int. Ed.* **2002**, *41*, 214–229.

[170] Y. Noda, B. Lee, K. Domen, J. N. Kondo, *Chem. Mater.* **2008**, *20*, 5361–5367.
[171] Y. Takahara, J. N. Kondo, T. Takata, D. Lu, K. Domen, *Chem. Mater.* **2001**, *13*, 1194–1199.
[172] M. Vettraino, M. L. Trudeau, D. M. Antonelli, *Adv. Mater.* **2000**, *12*, 337–341.
[173] S. Murray, M. Trudeau, D. M. Antonelli, *Adv. Mater.* **2000**, *12*, 1339–1342.
[174] X. He, M. Trudeau, D. Antonelli, *Inorg. Chem.* **2001**, *40*, 6463–6468.
[175] B. Ye, M. L. Trudeau, D. M. Antonelli, *Adv. Mater.* **2001**, *13*, 561–565.
[176] M. J. Rosseinsky, *Chem. Mater.* **1998**, *10*, 2665–2685.
[177] B. Ye, M. Trudeau, D. Antonelli, *Chem. Mater.* **2001**, *13*, 2730–2741.
[178] M. Freund, B. Deore, *Self Doped Conducting Polymers*, Wiley, Canada, **2007**.
[179] P. A. Cox, *The Electronic Structure and Chemistry of Solids*, Clarendon Press, **1987**.
[180] T. Kamiya, H. Hosono, *Semicond. Sci. Technol.* **2005**, *20*, S92–S102.
[181] O. Rivero, F. Huerta, F. Montilla, C. Sanchis, E. Morallón, *Eur. Polym. J.* **2015**, *69*, 201–207.
[182] Y. Li, Ed. , *Organic Optoelectronic Materials*, Springer International Publishing, Cham, **2015**.
[183] R. Baumann, K. Lennarz, J. Bargon, *Synth. Met.* **1993**, *54*, 243–249.
[184] U. Riaz, C. Nwaoha, S. M. Ashraf, *Prog. Org. Coat.* **2014**, *77*, 743–756.
[185] Y.-J. Choi, K.-M. Kang, H.-S. Lee, H.-H. Park, *Thin Solid Films* **2015**, *583*, 226–232.
[186] H. K. Chitte, G. N. Shinde, N. V. Bhat, V. E. Walunj, *J. Sens. Technol.* **2011**, *1*, 47–56.
[187] J. M. Pringle, J. Efthimiadis, P. C. Howlett, J. Efthimiadis, D. R. MacFarlane, A. B. Chaplin, S. B. Hall, D. L. Officer, G. G. Wallace, M. Forsyth, *Polymer* **2004**, *45*, 1447–1453.
[188] J. H. Burroughes, D. D. C. Bradley, A. R. Brown, R. N. Marks, K. Mackay, R. H. Friend, P. L. Burns, A. B. Holmes, *Nature* **1990**, *347*, 539–541.
[189] K. A. Weerakoon, J. H. Shu, M.-K. Park, B. A. Chin, *J Solid State Sci Technol* **2012**, *12*, Q100–Q105.
[190] R. J. Waltman, J. Bargon, A. F. Diaz, *J. Phys. Chem.* **1983**, *87*, 1459–1463.
[191] A. B. C. D. S.Kelkar, *J Chem. Chem. Technol.* **2011**, *5*, 309–315.
[192] J. E. Frommer, *Acc. Chem. Res.* **1986**, *19*, 2–9.
[193] Z. Bao, A. J. Lovinger, *Chem. Mater.* **1999**, *11*, 2607–2612.
[194] M. E. Nicho, H. Hu, C. López-Mata, J. Escalante, *Sol. Energy Mater. Sol. Cells* **2004**, *82*, 105–118.
[195] R. D. McCullough, R. D. Lowe, *J. Chem. Soc. Chem. Commun.* **1992**, 70–72.
[196] R. D. McCullough, S. Tristram-Nagle, S. P. Williams, R. D. Lowe, M. Jayaraman, *J. Am. Chem. Soc.* **1993**, *115*, 4910–4911.
[197] K. S. Ryu, Y. Lee, K.-S. Han, M. G. Kim, *Mater. Chem. Phys.* **2004**, *84*, 380–384.
[198] K. Majid, R. Tabassum, A. F. Shah, S. Ahmad, M. L. Singla, *J. Mater. Sci. Mater. Electron.* **2008**, *20*, 958–966.
[199] X. Qiao, X. Wang, Z. Mo, *Synth. Met.* **2001**, *122*, 449–454.
[200] X. Qiao, X. Wang, X. Zhao, J. Liu, Z. Mo, *Synth. Met.* **2000**, *114*, 261–265.
[201] M. C. Gallazzi, C. Bertarelli, E. Montoneri, *Synth. Met.* **2002**, *128*, 91–95.
[202] Y. Bai, P. Qiu, Z. Wen, S. Han, *J. Alloys Compd.* **2010**, *508*, 1–4.
[203] P. Urbánek, A. di Martino, S. Gladyš, I. Kuřitka, A. Minařík, E. Pavlova, D. Bondarev, *Synth. Met.* **2015**, *202*, 16–24.
[204] D. P. Dubal, S. H. Lee, J. G. Kim, W. B. Kim, C. D. Lokhande, *J. Mater. Chem.* **2012**, *22*, 3044–3052.
[205] A. Chen, H. Wang, B. Zhao, X. Li, *Synth. Met.* **2003**, *139*, 411–415.
[206] I. Carrillo, E. Sanchez de la Blanca, J. L. G. Fierro, M. A. Raso, F. Acción, E. Enciso, M. I. Redondo, *Thin Solid Films* **2013**, *539*, 154–160.

[207] H. K. Chitte, G. N. Shinde, N. V. Bhat, V. E. Walunj, *J. Sens. Technol.* **2011**, *1*, 47–56.
[208] R. Ansari, *J. Chem.* **2006**, *3*, 186–201.
[209] Y. Yagci, F. Yilmaz, S. Kiralp, L. Toppare, *Macromol. Chem. Phys.* **2005**, *206*, 1178–1182.
[210] G. Wallace, P. Teasdale, G. Spinks, L. Kane-Maguire, *Conductive Electroactive Polymers: Intelligent Materials Systems*, CRC Press, **2002**.
[211] J. Xia, L. Chen, S. Yanagida, *J. Mater. Chem.* **2011**, *21*, 4644–4649.
[212] H. Zhao, L. Li, J. Yang, Y. Zhang, *J. Power Sources* **2008**, *184*, 375–380.
[213] E. Antolini, *Appl. Catal. B Environ.* **2009**, *88*, 1–24.
[214] K. H. An, S. Y. Jeong, H. R. Hwang, Y. H. Lee, *Adv. Mater.* **2004**, *16*, 1005–1009.
[215] F. Selampinar, L. Toppare, U. Akbulut, T. Yalçin, Ş. Süzer, *Synth. Met.* **1995**, *68*, 109–116.
[216] S. A. Waghuley, S. M. Yenorkar, S. S. Yawale, S. P. Yawale, *Sens. Actuators B Chem.* **2008**, *128*, 366–373.
[217] M. Penza, E. Milella, M. B. Alba, A. Quirini, L. Vasanelli, *Sens. Actuators B Chem.* **1997**, *40*, 205–209.
[218] P. M. George, D. A. LaVan, J. A. Burdick, C.-Y. Chen, E. Liang, R. Langer, *Adv. Mater.* **2006**, *18*, 577–581.
[219] L. Beverina, G. A. Pagani, M. Sassi, *Chem. Commun.* **2014**, *50*, 5413–5430.
[220] G. Inzelt, M. Pineri, J. W. Schultze, M. A. Vorotyntsev, *Electrochimica Acta* **2000**, *45*, 2403–2421.
[221] C.-G. Wu, T. Bein, *Chem. Mater.* **1994**, *6*, 1109–1112.
[222] Q.-T. Vu, M. Pavlik, N. Hebestreit, U. Rammelt, W. Plieth, J. Pfleger, *React. Funct. Polym.* **2005**, *65*, 69–77.
[223] D. M. Antonelli, J. Y. Ying, *Angew. Chem. Int. Ed. Engl.* **1995**, *34*, 2014–2017.
[224] Y. Zhu, S. Xu, L. Jiang, K. Pan, Y. Dan, *React. Funct. Polym.* **2008**, *68*, 1492–1498.
[225] L. Liu, F. Tian, X. Wang, Z. Yang, M. Zhou, X. Wang, *React. Funct. Polym.* **2012**, *72*, 45–49.
[226] Y. Furukawa, M. Akimoto, I. Harada, *Synth. Met.* **1987**, *18*, 151–156.
[227] F. Devreux, G. Bidan, A. A. Syed, C. Tsintavis, *J Phys* **1985**, *46*, 1595–1601.
[228] J. Tang, L. Kong, J. Zhang, L. Zhan, H. Zhan, Y. Zhou, C. Zhan, *React Funct Polym* **2008**, *68*, 1408–1413.
[229] D. D. Cunningham, L. Laguren-Davidson, H. B. Mark, C. Van Pham, H. Zimmer, *J Chem Soc Chem Commun* **1987**, *2*, 1021.
[230] P. Kovacic, K. N. McFarland, *J. Polym. Sci. Polym. Chem. Ed.* **1979**, *17*, 1963–1976.
[231] W. Sun, R. Hu, H. Liu, H. Zhang, J. Liu, L. Yang, H. Wang, M. Zhu, *Electrochimica Acta* **2016**, *191*, 462–472.
[232] S.-Q. Liu, S.-C. Li, K.-L. Huang, B.-L. Gong, G. Zhang, *J. Alloys Compd.* **2008**, *450*, 499–504.
[233] R. K. Rajput, *A Textbook of Electrical Engineering Materials (U.P. Technical University, Lucknow)*, Firewall Media, **2004**.
[234] S. S. Jeon, S. J. Yang, K.-J. Lee, S. S. Im, *Polymer* **2010**, *51*, 4069–4076.
[235] B. O. Skadtchenko, M. Trudeau, C.-W. Kwon, B. Dunn, D. Antonelli, *Chem. Mater.* **2004**, *16*, 2886–2894.
[236] L. A. C. Smith, F. Romer, M. L. Trudeau, R. M. Souto Maior, M. E. Smith, J. V. Hanna, D. M. Antonelli, *Microporous Mesoporous Mater.* **2014**, *194*, 52–59.
[237] S. Rapi, V. Bocchi, G. P. Gardini, *Synth. Met.* **1988**, *24*, 217–221.
[238] A. Y. H. Lo, R. W. Schurko, M. Vettraino, B. O. Skadtchenko, M. Trudeau, D. M. Antonelli, *Inorg. Chem.* **2006**, *45*, 1828–1838.
[239] B. Ye, M. Trudeau, D. Antonelli, *Chem. Mater.* **2002**, *14*, 2774–2781.

[240] C. H. Sun, X. H. Yang, J. S. Chen, Z. Li, X. W. Lou, C. Li, S. C. Smith, G. Q. (Max) Lu, H. G. Yang, *Chem. Commun.* **2010**, *46*, 6129.
[241] H. Eisazadeh, *World J. Chem.* **2007**, *2*, 67–74.
[242] N. Hassanzadeh, H. Omidvar, S. H. Tabaian, *Superlattices Microstruct.* **2012**, *51*, 314–323.
[243] J. Elguero, C. Marzin, J. D. Roberts, *J. Org. Chem.* **1974**, *39*, 357–363.
[244] D. J. Chadwick, in *Compr. Heterocycl. Chem.* (Eds.: A.R. Katritzky, C.W. Rees), Pergamon, Oxford, **1984**, pp. 155–200.
[245] X. Li, G. Jiang, G. He, W. Zheng, Y. Tan, W. Xiao, *Chem. Eng. J.* **2014**, *236*, 480–489.
[246] J. Wang, X. Ni, *Solid State Commun.* **2008**, *146*, 239–244.
[247] M. A. Fox, K. L. Worthen, *Chem. Mater.* **1991**, *3*, 253–257.
[248] C. Tao, L. Xu, J. Guan, *Chem. Eng. J.* **2013**, *229*, 371–377.
[249] F. Di Quarto, V. Figà, P. Bocchetta, M. Santamaria, *Electrochem. Solid-State Lett.* **2007**, *10*, H305–H308.
[250] L. A. C. Smith, F. Romer, M. L. Trudeau, M. E. Smith, J. V. Hanna, D. M. Antonelli, *ChemElectroChem* **2014**, *1*, 2153–2162.
[251] J. P. Turley, F. Romer, M. L. Trudeau, M. L. Dias, M. E. Smith, J. V. Hanna, D. M. Antonelli, *Microporous Mesoporous Mater.* **2014**, *190*, 284–291.
[252] S. Deivanayaki, V. Ponnuswamy, R. Mariappan, P. Jayamurugan, *Opt. - Int. J. Light Electron Opt.* **2013**, *124*, 1089–1091.
[253] T. C. Clarke, J. C. Scott, G. B. Street, *IBM J. Res. Dev.* **1983**, *27*, 313–320.
[254] F. Devreux, G. Bidan, A. A. Syed, C. Tsintavis, *J. Phys.* **1985**, *46*, 1595–1601.
[255] G. Q. Liu, H. T. Kuo, R. S. Liu, C. H. Shen, D. S. Shy, X. K. Xing, J. M. Chen, *J. Alloys Compd.* **2010**, *496*, 512–516.
[256] T.-F. Yi, B. Chen, Y.-R. Zhu, X.-Y. Li, R.-S. Zhu, *J. Power Sources* **2014**, *247*, 778–785.
[257] Q. Cao, H. P. Zhang, G. J. Wang, Q. Xia, Y. P. Wu, H. Q. Wu, *Electrochem. Commun.* **2007**, *9*, 1228–1232.
[258] B. Laskova, M. Zukalova, A. Zukal, M. Bousa, *J. Power Sources* **2014**, *246*, 103–109.
[259] H. Ren, R. Yu, J. Wang, Q. Jin, M. Yang, D. Mao, D. Kisailus, H. Zhao, D. Wang, *Nano Lett.* **2014**, *14*, 6679–6684.
[260] J. Chen, Z.-L. Tao, S.-L. Li, *Angew. Chem. Int. Ed.* **2003**, *42*, 2147–2151.
[261] M. S. Whittingham, R. R. Chianelli, *J. Chem. Educ.* **1980**, *57*, 569.
[262] M. S. Whittingham, *J. Electrochem. Soc.* **1976**, *123*, 315–320.
[263] J. L. Mohanan, S. L. Brock, *J. Non-Cryst. Solids* **2004**, *350*, 1–8.
[264] Q. Yao, I. U. Arachchige, S. L. Brock, *J. Am. Chem. Soc.* **2009**, *131*, 2800–2801.
[265] S. Bag, P. N. Trikalitis, P. J. Chupas, G. S. Armatas, M. G. Kanatzidis, *Science* **2007**, *317*, 490–493.
[266] R. Bissessur, J. Heising, W. Hirpo, *Chem. Mater.* **1996**, *8*, 318–320.
[267] A. E. Riley, S. H. Tolbert, *J. Am. Chem. Soc.* **2003**, *125*, 4551–4559.
[268] S. D. Korlann, A. E. Riley, B. S. Mun, S. H. Tolbert, *J. Phys. Chem. C* **2009**, *113*, 7697–7705.
[269] E. M. Rockafellow, L. K. Stewart, W. S. Jenks, *Appl. Catal. B Environ.* **2009**, *91*, 554–562.
[270] S.-H. Nam, T. K. Kim, J.-H. Boo, *Catal. Today* **2012**, *185*, 259–262.
[271] A. L. Let, D. E. Mainwaring, C. Rix, P. Murugaraj, *J. Non-Cryst. Solids* **2008**, *354*, 1801–1807.
[272] S.-C. Tsay, G. L. Yep, B.-L. Chen, L. C. Lin, J. R. Hwu, *Tetrahedron* **1993**, *49*, 8969–8976.

[273] C. J. Carmalt, C. W. Dinnage, I. P. Parkin, E. S. Peters, K. Molloy, M. A. Colucci, *Polyhedron* **2003**, *22*, 1255–1262.
[274] L. A. C. Smith, F. Romer, M. L. Trudeau, M. E. Smith, J. V. Hanna, D. M. Antonelli, *ChemNanoMat* **2015**, *1*, 276–284.
[275] Yongming Li,† Lucı´a Fernandez-Recio,‡ Peter Gerstel,† Vesna Srot,† Peter A. van Aken,† Gerhard Kaiser,† Marko Burghard,‡ and Joachim Bill, *Chem Mater* **2008**, *20*, 5593–5599.
[276] T. Hemraj-Benny, S. S. Wong, *Chem. Mater.* **2006**, *18*, 4827–4839.
[277] M. H. Lindic, H. Martinez, A. Benayad, B. Pecquenard, P. Vinatier, A. Levasseur, D. Gonbeau, *Solid State Ion.* **2005**, *176*, 1529–1537.
[278] G. Yang, Z. Yan, T. Xiao, *Appl. Surf. Sci.* **2012**, *258*, 4016–4022.
[279] P. V. R. K. Ramacharyulu, J. Praveen Kumar, G. K. Prasad, B. Sreedhar, *Mater. Chem. Phys.* **2014**, *148*, 692–698.
[280] M. M. Nasef, H. Saidi, H. M. Nor, M. A. Yarmo, *J. Appl. Polym. Sci.* **2000**, *76*, 336–349.
[281] C. V. J. Skipper, A. Hamaed, D. M. Antonelli, N. Kaltsoyannis, *J. Am. Chem. Soc.* **2010**, *132*, 17296–17305.
[282] R. Wu, G. Xia, S. Shen, F. Zhu, F. Jiang, J. Zhang, *Electrochimica Acta* **2015**, *153*, 334–342.
[283] R. B. King, *Coord. Chem. Rev.* **2000**, *200–202*, 813–829.
[284] X. Wang, L. Andrews, *J. Phys. Chem. A* **2003**, *107*, 570–578.
[285] G. A. Ozin, J. G. McCaffrey, *J. Am. Chem. Soc.* **1984**, *106*, 807–809.
[286] G. V. Chertihin, L. Andrews, *J. Phys. Chem.* **1995**, *99*, 12131–12134.
[287] A. E. S. Miller, C. S. Feigerle, W. C. Lineberger, *J. Chem. Phys.* **1986**, *84*, 4127.
[288] G. V. Chertihin, L. Andrews, *J. Am. Chem. Soc.* **1994**, *116*, 8322–8327.
[289] A. J. Maeland, T. R. P. Gibb, D. P. Schumacher, *J. Am. Chem. Soc.* **1961**, *83*, 3728–3729.
[290] J. J. Reilly, R. H. Wiswall, *Inorg. Chem.* **1970**, *9*, 1678–1682.
[291] X. Zhou, C. Cui, G. Wu, H. Yang, J. Wu, J. Wang, G. Gao, *J. Power Sources* **2013**, *238*, 95–102.
[292] C. Ban, N. A. Chernova, M. S. Whittingham, *Electrochem. Commun.* **2009**, *11*, 522–525.
[293] C. Nethravathi, B. Viswanath, J. Michael, M. Rajamath, *Carbon* **2012**, *50*, 4839–4846.
[294] N. Ganganagappa, A. Siddaramanna, *Mater. Charact.* **2012**, *68*, 58–62.
[295] Z. Chen, S. Gao, L. Jiang, M. Wei, K. Wei, *Mater. Chem. Phys.* **2010**, *121*, 254–258.
[296] W. Mowat, A. Shortland, G. Yagupsky, N. J. Hill, M. Yagupsky, G. Wilkinson, *J. Chem. Soc. Dalton Trans.* **1972**, 533–542.
[297] J. K. F. Buijink, A. Meetsma, J. H. Teuben, *Organometallics* **1993**, *12*, 2004–2005.
[298] H. D. Kaesz, R. B. Saillant, *Chem. Rev.* **1972**, *72*, 231–281.
[299] L. Morris, M. L. Trudeau, D. Reed, D. Book, D. M. Antonelli, *Phys. Chem. Chem. Phys.* **2015**, *17*, 9480–9487.
[300] T. K. A. Hoang, L. Morris, D. Reed, D. Book, M. L. Trudeau, D. M. Antonelli, *Chem. Mater.* **2013**, *25*, 4765–4771.
[301] V. I. Nefedov, Y. V. Salyn, G. Leonhardt, R. Scheibe, *J. Electron Spectrosc. Relat. Phenom.* **1977**, *10*, 121–124.
[302] B. Horvath, J. Strutz, J. Geyer-Lippmann, E. G. Horvath, *Z. Für Anorg. Allg. Chem.* **1981**, *483*, 181–192.
[303] R. J. Colton, A. M. Guzman, J. W. Rabalais, *J. Appl. Phys.* **1978**, *49*, 409–416.
[304] C. E. Myers, H. F. Franzen, J. W. Anderegg, *Inorg. Chem.* **1985**, *24*, 1822–1824.

[305] Q. Zhao, L. Jiao, W. Peng, H. Gao, J. Yang, Q. Wang, H. Du, L. Li, Z. Qi, Y. Si, et al., *J. Power Sources* **2012**, *199*, 350–354.
[306] C. V. Subba Reddy, E. H. Walker Jr., S. A. Wicker Sr., Q. L. Williams, R. R. Kalluru, *Curr. Appl. Phys.* **2009**, *9*, 1195–1198.
[307] W. Wang, B. Jiang, L. Hu, Z. Lin, J. Hou, S. Jiao, *J. Power Sources* **2014**, *250*, 181–187.
[308] M. M. Rahman, J.-Z. Wang, N. H. Idris, Z. Chen, H. Liu, *Electrochimica Acta* **2010**, *56*, 693–699.
[309] Q. Wang, J. Pan, M. Li, Y. Luo, H. Wu, L. Zhong, G. Li, *J. Mater. Sci. Technol.* **2015**, *31*, 630–633.